

NUMERICAL MODELLING
OF
HOMOGENEOUS AERATED-WATER WAVE IMPACTS

M. van der Eijk

NUMERICAL MODELLING
OF
HOMOGENEOUS AERATED-WATER WAVE IMPACTS

MARTIN VAN DER EIJK
NOVEMBER 2, 2018

TO OBTAIN THE DEGREE OF MASTER OF SCIENCE IN MARINE TECHNOLOGY AT THE DELFT
UNIVERSITY OF TECHNOLOGY

TO BE DEFENDED PUBLICLY ON THURSDAY NOVEMBER 15th, 2018 AT 3:00 PM

THESIS COMMITTEE:

DR. IR. J.J. HOPMAN
professor of Ship Design
DR. IR. M.J.B.M. POURQUIE
assistant professor of Fluid Mechanics
DR. IR. G.H. KEETELS
*assistant professor of Offshore and Dredging
Engineering*

SUPERVISOR:

DR. IR. P.R. WELLENS
assistant professor of Ship Hydromechanics

FACULTY OF MECHANICAL, MARITIME AND MATERIALS
ENGINEERING
MARINE AND TRANSPORT TECHNOLOGY
SHIP HYDROMECHANICS AND STRUCTURES

Abstract

A substantial part of structural damage for conventional vessels is caused by complex free surface events like slamming, breaking waves and green water. These events lead to the interaction of air and water where air can be entrained in water. The resulting air bubbles can considerably affect the evolution of the pressure caused by hydrodynamic impact loading. Besides a [cushioning effect](#) on the impact pressure and a possible [increase of the compressibility of the mixture higher than air](#), earlier documentation conclude that due to aeration the acting [forces can increase](#) due to long lasting time of the pressure and the [resonance](#) between oscillating air pockets & generated pressure waves. Nowadays, methods used to predict these forces, assume that the fluid is incompressible. This can lead to an [underestimation of the forces](#). *The aim of the graduation project is to evaluate the effect of a homogeneous mixture of water and air on the wave impact, specifically for a green water event.* Based on the documentation of the numerical method [COMFLOW](#), for the evaluation an [improved extended numerical solver](#) in FORTRAN and MATLAB is built.

COMFLOW is described as a robust finite volume method which can model these impact loadings by solving the governing laws -continuity equation and conservation of momentum- for a two-phase separated-flow using the first-order fractional step method and the second-order Adam-Bashforth timestepping scheme. Even with a coarse grid, a clear distinction between water and air can be maintained by combining the Volume-of-Fluid approach with the local height function and a constant line reconstructed free surface (SLIC-iVOF). However, the method is not capable to model the compressibility for a dispersed flow by assuming that inertial forces on the aeration are dominant: *a homogeneous mixture of air and water.*

In this report an extension is developed based on two volume fractions: the entrained air and air above the free surface, and Kapila's five-equation model. Considering the implementation and improvement of COMFLOW itself, the [representation of capillary forces is improved](#) by a new developed Continuum Surface Force (CSF) model for SLIC. Further, taking into account the transpose of the velocity gradient in the diffusive term, not done by COMFLOW, lead to [no significant underestimation of the viscosity](#) around the free surface for $Re=\mathcal{O}(35)$ and an error reduction of 2.7% for the 2D rising bubble. Besides the neglected term in the diffusive term, for the interpolation of the density around steep interfaces for SLIC, like wave impacts, the [cell-weighted averaging method leads to less spurious velocities](#) around the surface than the gravity-consistent averaging method used by COMFLOW. The last revised implementation is a [modified local height function](#), documented by COMFLOW as strictly mass conserving, which is made more strictly mass conserving due not overlapping of the heights.

The modelling of compression waves and bubble interaction is verified with the 1D shock tube and 2D helium shock bubble. For a simplified green water event, the results of the dam break tested for aeration levels 0.1, 1 and 5% showed that the effect of the [aeration after the impact is most relevant](#) and can achieve impact forces more than two times higher than the initial impact due to the combination of a plunging wave, mixing of water and air, air pocket oscillation and the longitudinal acoustic mode. [The effect of aeration becomes significant for \$Ma=\mathcal{O}\(0.10\)\$](#) . These observations are based on the dam break results with obstacle.

Preface

The last nine months were challenging but also the best part of my study career. I made many friends and learned a lot, especially debugging codes. Due to this project my interest to continue in the research area, especially in the computer physics, is even more increased. The satisfaction to see that the numerical results correspond with the analytical solutions, gives a boost to do more than needed. Therefore, I would say that this research is not the end of my student career but just a start.

One of the people who helped me the most in interesting myself in the topic is my supervisor Dr. Ir. P.R. Wellens. I am deeply grateful to my daily supervisor for helping, guiding and keeping me on track in the past nine months. Furthermore, I would like to thank him for the interesting and funny off-topic conversations.

I also wish to thank my friends, especially M. Boogaard, for reading my report critically and for the support they have shown during my study years. It was funny to see how obsessed they were getting with the bubbles I simulated. Besides, no friends is no fun.

Special thanks to the committee, Dr. Ir. J.J. Hopman, Dr. Ir. M.J.B.M. Pourquie and Dr. Ir. G.H. Keetels, for attending the graduation and judging my report. Thank you for your time.

I wish also to thank my family; dad, mother, brother and sister in law but also the family of my mother and girlfriend, for supporting me not only during my graduation but during my entire life in every situation.

Last but not least, I am deeply grateful to my girlfriend for being patient with me; love you.... and to the bubbles, still not annoying to see them pulsating on my screen.

I hope I can arouse your interest while reading the report.

November 2, 2018

Martin van der Eijk

Table of contents

Abstract	i
Preface	iii
Tables	ix
Figures	xi
Symbols	xv
1 General introduction	1
2 Literature review	5
2.1 Introduction	5
2.2 Air pocket	6
2.2.1 Pressure development	6
2.2.2 Oscillations	7
2.3 Entrained air	9
2.3.1 Compressibility of the mixture	9
2.3.2 Effect on impact	11
2.3.3 Air bubble rates	12
2.3.4 Scaling	13
2.4 Green water loading	14
2.5 Physical relevance	16
2.5.1 Relative velocity	16
2.5.2 Sea-state	17
2.6 Numerical model	18
2.6.1 ComFLOW	20
2.6.2 Extension	21
2.7 Conclusion	22
3 One-phase VoF model	23
3.1 Introduction	23
3.2 Governing Equations	23
3.3 Numerical Model	25
3.3.1 Continuity equation	25
3.3.2 Navier-Stokes equation	26
3.3.3 Solution method	28
3.4 Free surface displacement	30
3.4.1 Volume-of-Fluid method	30
3.4.2 Local height function	34

3.4.3	Free surface boundary conditions	35
3.5	Conclusion	36
4	Multiphase VoF model	37
4.1	Introduction	37
4.2	Governing equations	38
4.3	Numerical model	39
4.3.1	Convective term	40
4.3.2	Diffusive term	42
4.3.3	Solution method	44
4.3.4	Reduction of unsteady density term	46
4.3.5	Reduction of convective density term	47
4.3.6	Negative pressures	47
4.3.7	Gas pressure in surface cell	47
4.3.8	Density at cell edge	48
4.4	Surface tension	51
4.4.1	Interpolation of the pressure	52
4.4.2	CSF-model	52
4.4.3	Implementation of CSF-model	54
4.5	Simulations	55
4.5.1	1D water piston	56
4.5.2	Standing gravity wave	57
4.5.3	2D oscillating planar rod	60
4.5.4	Standing capillary wave	62
4.5.5	2D rising bubble	63
4.5.6	Dam break case	67
4.6	Conclusion	72
5	Double fraction VoF model	75
5.1	Introduction	75
5.2	Principle	76
5.3	Comparison with Multiphase model	77
5.4	Numerical model: <i>Extension</i>	78
5.4.1	Material derivative density	79
5.4.2	Transport equation	79
5.4.3	Convective density term	84
5.4.4	Equation of state	84
5.4.5	Constant mass fraction	85
5.4.6	Sequence of calculation	86
5.5	1D Shock tube	86
5.5.1	Separated fluids	87
5.5.2	Mixture	89
5.5.3	Reflection	90
5.6	2D Shock bubble interaction	92
5.7	Dam break case	97
5.7.1	Propagation of the water	98
5.7.2	Dam break at real scale	98
5.7.3	Compressible versus Incompressible	100
5.8	Conclusion	102

6	Dam break simulations	103
6.1	Introduction	103
6.2	Numerical setup	103
6.3	Comparison of models	105
6.4	Comparison of Results	105
6.4.1	Pressures	106
6.4.2	Oscillations	110
6.4.3	Forces & Moments	111
6.4.4	Free surface dynamics	113
7	Conclusion	117
8	Recommendations	119
	Appendix A Impact types	121
	Appendix B Models	125
B.1	Overview Numerical models	125
B.2	Analytic estimation of impact pressure	127
B.2.1	Shock wave model	127
B.2.2	Models for Wagner type pressure	127
B.2.3	Models for transition type pressure	128
B.2.4	Models for Bagnold type pressure	128
B.3	Filling flow model	129
	Appendix C Green water loading	131
C.1	Effect of ship motions & environment	131
C.2	Numerical simulations	131
C.3	Longitudinal force	132
C.4	Limiting range of dam break	132
	Appendix D Free surface displacement	133
D.1	Donor-Acceptor method	133
D.2	Local height function	135
D.3	Flux limiter	137
	Appendix E Dam break results	139
E.1	Original VOF model	139
E.2	Air pocket oscillation	140
	Appendix F Discretization Multiphase model	143
F.1	Poisson equation	143
F.2	New velocity	145
	Appendix G Extended model	147
G.1	Derivation transport equation	147
G.2	CFL-controller	148
G.3	Acoustics of the mixture	149
G.4	Shock bubble	151
	Bibliography	153

Tables

4.1	Limit on CFL number by convection diffusion equation [149].	44
4.2	Cell-edge densities multiplied by the gravity and the direction of the dashed line for fig. 4.4.	50
4.3	2D rising bubble simulations and benchmark values.	65
4.4	High frequency and low frequency oscillations in pressure at the wall.	72
5.1	Initial conditions and gas properties for the shock bubble interaction simulation.	93
5.2	Resulting velocities in $[m/s]$ for 2D helium cylinder.	95
5.3	Dam break simulations at model scale with different amount of aeration.	98
5.4	Dam break simulations at real scale with different amount of aeration.	99
5.5	High frequency and low frequency oscillations in pressure at the wall; step size of $1[Hz]$	101
6.1	Simulations dam break case with obstacle	104
6.2	Pressure impulse acting on the obstacle and the wall.	109
6.3	Dominant frequency oscillations for $t=2.2-3.0[s]$	110
6.4	Dominant frequency oscillations for $t=4.8-6.0[s]$	111
6.5	Maximum and minimum forces and moments.	113
6.6	Maximum water height at wall and obstacle.	115

Figures

2.1	Two-phase flow phenomena for a breaking wave [149].	5
2.2	Typical pressure development over time [149].	8
2.3	Density and speed of sound change versus aeration.	10
2.4	Dam break freeboard exceedance [17].	15
3.1	Discretization notation continuity equation.	25
3.2	Discretization notation horizontal momentum.	26
3.3	Interface orientation near the wall.	31
3.4	Donor-Acceptor method in horizontal direction for δF_e	33
3.5	The local height function for updating the free surface.	34
3.6	The effect of the local height function (LHF) on mass conservation (loss due to droplets) for a standing wave 64x64.	35
4.1	Discretization convective term control volume.	40
4.2	Effect of density ratio.	42
4.3	Interpolation of pressure	48
4.4	Gravity consistent averaging method for SLIC.	50
4.5	Gravity-consistent averaging (max. $0.4[m/s]$) versus Cell-weighted averaging (max. $1e^{-9}[m/s]$)	51
4.6	Surface tension in case of a bubble	53
4.7	The choice of κ for the CSF-model.	54
4.8	Falling water mass in 1D	56
4.9	Results of incompressible and compressible air for the 1D water piston.	57
4.10	Convergence study for 1D water piston.	58
4.11	Standing wave comparison for cell-weighted and gravity-consistent averaging method at $x=0.5[m]$	58
4.12	Standing wave simulation parameters.	59
4.13	Standing wave simulation for $H_0=0.08[m]$ and $H_0=0.04[m]$ at $x=0.5[m]$	60
4.14	Standing wave simulation measured at $x=0.5[m]$, $\zeta_{a,0}=0.3[m]$	60
4.15	Pressure and diameter of the bubble over time compared with ANSYS; dotted line is method 1 for the diffusive term.	61
4.16	Diameter of the air rod over time compared with the water rod.	62
4.17	Volume fraction (right) against time compared with ANSYS CFX (left); (a) 0.01[s], (b) 0.05[s], (c) 0.09[s], (d) 0.13[s].	62
4.18	Pressure against time compared with ANSYS (left); (a) 0.49[s], (b) 0.51[s], (c) 0.67[s], (d) 0.75[s], (e) 0.79[s].	62
4.19	Comparison of two CSF-models.	63
4.20	Properties of the CSF-model.	64
4.21	Flow domain for 2D rising bubble.	64
4.22	Rising bubble results for the original method.	66

4.23	Mean velocity comparison of diffusive models for 80×240	66
4.24	Snapshots of the 2D rising bubble in order of time for three different incompressible simulations.	67
4.25	Snapshots of the 2D rising bubble through interface in order of time with surface tension $\sigma = 24.5[\text{N/m}]$	67
4.26	Change and convergence of 2D dam over time in height (h) and length (l) using non-dimensional values.	69
4.27	Setup 2D dam break case.	69
4.28	The results of the present model for the dam break case compared with experimental results of MARIN in the column (a) and numerical results of Wemmenhove et al. (2010) in the column (b).	70
4.29	Fast Fourier transform of the entrapped air pocket.	72
5.1	Extended model principle	76
5.2	Illustration of the effect of pressure on mixture.	78
5.3	Calculation sequence of the variables for compressible double fraction model during a time step.	86
5.4	Different stages by shock tube for same liquid [38].	87
5.5	The effect of flux limiter and results of shock tube in separated fluids on $t=0.25[\text{s}]$ for $dt=1 \cdot 10^{-4}[\text{s}]$ and $N=800$	89
5.6	Shock in fluid mixture at $t = 55.137 \cdot 10^{-5}[\text{s}]$	91
5.7	Reflected shock front in order of time for 400 elements.	92
5.8	Shock bubble interaction setup.	93
5.9	Illustration of different pressure waves at the interface of the cylinder.	93
5.10	Velocity notation shock cylinder; continuous lines: present model, figures: model of Quirk and Karni (1996)	95
5.11	Schematic drawing of the waves inside the Helium bubble corresponding with fig. 5.12(b)-(d) [80]; dotted line is relatively weak pressure waves, dark line is strong pressure waves.	96
5.12	Sequence of images of the density in $[\text{kg}/\text{m}^3]$ from (a) $32[\mu\text{s}]$, (b) $52[\mu\text{s}]$, (c) $62[\mu\text{s}]$, (d) $72[\mu\text{s}]$, (e) $82[\mu\text{s}]$ till (f) $102[\mu\text{s}]$ for from left to right; Haas and Sturtevant (1987) , Quirk and Karni (1996) , and the present model.	96
5.13	Sequence of images of the density in $[\text{kg}/\text{m}^3]$ from (g) $245[\mu\text{s}]$, (h) $427[\mu\text{s}]$ till (i) $\approx 600[\mu\text{s}]$ computational / $674[\mu\text{s}]$ experimental for from left to right; Haas and Sturtevant (1987) and the present model.	97
5.14	Pressure and propagation of the water with aeration.	99
5.15	Impact pressure for aerated water in dam break case at real scale.	100
5.16	Compressible model compared with incompressible multiphase model for dam break case.	100
6.1	Setup dam break case of MARIN 3D experiment; cross sign: measure point pressure, grey area: measure acting force, arrow: measure water height.	104
6.2	The comparison of the one-phase model and the fully compressible model for the dam break case with obstacle.	106
6.3	The evolution of the distribution of pressure for all β values; the first row represents the pressure on the wall, the second row at the front of the obstacle, and the third row at the back of the obstacle.	107
6.4	Pressures measured during the simulation in time; subscripts ",1" and ",2" represent time periods given in table 6.5.	108
6.5	The initial entrapped air pocket and the effect of the returning jet on P_6 and P_7	111

6.6	The forces and moment measured during the simulation for β_0 in time; subscripts "1" and "2" represent time periods given in table 6.5.	112
6.7	Behavior of the mixture in time.	114
A.1	Classification of breaking wave impact type according to Oumeraci et al. (1992).	122
B.1	Collision of a wave on a vertical wall [145].	128
B.2	Illustration of idealized configuration of the filling flow [113].	129
D.1	Most common situations during a simulation of a free surface flow.	134
D.3	Four examples of mass loss due to overlapping of local height functions.	136
D.4	Calculation of fraction at the cell face; blue: second-order upwind, orange: first-order upwind.	137
E.1	Continuous lines are experimental results of [90], dotted lines are simulation results $H = 0.3[m]$	139
E.2	Continuous lines are experimental results of H1 and H4 [90], dotted lines are simulation results $H = 0.3[m]$	139
E.3	Continuous lines are experimental results of H2 and H3 [90], dotted lines are simulation results $H = 0.3[m]$	140
E.4	Illustration of air pocket oscillation.	141
G.1	The pressure field in $[Pa]$ for from left to right; Quirk and Karni (1996) and the present model at time (a) $32[\mu s]$, (b) $62[\mu s]$ and (c) $82[\mu s]$	152
G.2	The fraction field for from left to right; Quirk and Karni (1996) and the present model at time (a) $32[\mu s]$, (b) $62[\mu s]$, (c) $82[\mu s]$ and (d) $230[\mu s]$	152

Symbols

The next list describes several symbols and abbreviations that will be used later within the body of the document

Physics Constants

π	Constant value Pi	3.14159[–]
g	Gravity constant	9.81[kg/m ³]
k_a	Constant value of Oumeraci et al. (1995)	5.35[m/s]

Bibliography

ϵ	Clearance of incoming flow	[–]
κ_a	Air thickness coefficient	[–]
κ_l	Impact height function	[–]
κ_m	Added mass correction factor	[–]
$\boldsymbol{\tau}$	Shear stress tensor	[kg/ms ²]
ρ_s	Density of structure	[kg/m ³]
\mathbf{s}	Position of free-surface	[–]
\mathbf{T}	Stress tensor	[kg/ms ²]
θ	Attack angle of wave front	[°]
ζ	Curvature of wave front surface	[°]
C_d	Drag coefficient	[–]
CD	Chart Datum	[m]
D	Diameter of air pocket	[m]
E_s	Elastical modulus of structure	[kg/ms ²]
f_0	Natural oscillation frequency	[1/s]
f_l	Longitudinal acoustic frequency	[1/s]
f_t	Transverse acoustic frequency	[1/s]
H	Wave height	[m]
h	Freeboard exceedance or water depth	[m]
h'	Height of dam	[m]
H_{SWL}	Height of still water line	[m]
K	Effective thickness of water mass	[–]
L	Length domain/added water mass	[m]
R	Radius of air pocket	[m]
S	Height of frontal area of structure	[m]
T	Period	[s]
U	Velocity of approaching wave front (u_0)	[m/s]

Numerical Model

α	Compressibility factor	[ms ² /kg]
----------	------------------------	-----------------------

β	Air content in mixture	[–]
δx	Horizontal length of edge of cell	[m]
δy	Vertical length of edge of cell	[m]
γ	Adiabatic ratio of specific heats	[–]
\hat{H}	Right hand side of transport eq. (5.13)	
κ	Curvature	[1/m]
λ	Wave length	[m]
μ	Dynamic viscosity	[kg/(ms)]
$\nabla \cdot$	Divergence operator	[1/m]
∇	Gradient operator	[1/m]
ν	Kinematic viscosity	[m ² /s]
ω	Frequency ($2\pi/f$)	[rad/s]
ϕ	Momentum velocity	[m/s]
$\Psi(r)$	Function depending on flux limiter	[–]
ρ	Density	[kg/m ³]
$\rho_{l,0}$	Initial liquid density	[kg/m ³]
σ	Surface tension	[kg/s ²]
\mathbf{F}	Body forces vector [g_x, g_y] ^T	[m/s ²]
\mathbf{n}	normal vector of cell face	[m]
\mathbf{u}	Velocity vector [u, v] ^T	[m/s]
\mathbf{x}	Domain position vector [x, y] ^T	[m]
\tilde{C}	Term in the Poisson eq. (5.22)	
\tilde{u}	Intermediate velocity	[m/s]
A	Volume fraction of liquid in mixture	[–]
A_p	Area of air pocket	[m ²]
c	Speed of sound	[m/s]
dt	Time step numerical simulation	[s]
d	Distance from center to free surface	[m]
d_c	Center distance between two cells	[m]
F	Fraction water of mixture	[–]
F	Measured force	[kg · m/s ²]
H	Height function	[m]
I	Impulse	[kg/ms]
K	Right hand side of transport eq. (5.8)	
k	Wave number	[1/m]
k_d	Artificial diffusion coefficient	[–]
L	Domain length	[m]
M	Measured moment	[kg · m ² /s ²]
m	Mass flux	[m ² /s]
n	Mode of oscillation	[–]
P	Measured pressure	[kg/ms ²]
p	Pressure of aggregated fluid	[kg/ms ²]
p_0	Atmospheric pressure (p_{atm})	[kg/ms ²]
S	Boundary of control volume, cell face	[m]
s	Position of free surface defined by $s(\mathbf{x},t)=0$	[m]
t	Time	[s]
t_{ris}	Rise time of the pressure	[s]
V	Volume of control volume	[m ²]
y	Mass fraction of aeration	[–]

Superscript

<i>*</i>	Intermediate step
<i>L</i>	Left side of cell face
<i>n</i>	Time level
<i>R</i>	Right side of cell face
<i>T</i>	Transpose

Subscript

0	Initial or natural condition
<i>a</i>	Air
<i>adv</i>	Advective term
<i>avg</i>	Average
<i>c</i>	Center of control volume
<i>div</i>	Divergence term
<i>e</i>	East face of control volume
<i>ee</i>	East face outside control volume
<i>f</i>	Face side
<i>FS</i>	Free surface
<i>g</i>	Gas, often aerated
<i>h</i>	Horizontal
<i>i</i>	Horizontal coordinate or specific fluid
<i>int</i>	Interface
<i>j</i>	Vertical coordinate
<i>jet</i>	Jet along the vertical wall
<i>l</i>	Water, often mixed with air
<i>max</i>	Maximum value
<i>n</i>	North face of control volume
<i>nn</i>	North face outside control volume
<i>o</i>	Obstacle
<i>p</i>	Air pocket
<i>s</i>	South face of control volume
<i>s</i>	Structure
<i>ss</i>	South face outside control volume
<i>v</i>	Vertical
<i>w</i>	Propagating fluid of interest, often mixture of water
<i>w</i>	West face of control volume
<i>ww</i>	West face outside control volume
<i>x</i>	Horizontal direction
<i>y</i>	Vertical direction

Abbreviations

<i>AF</i>	Additional Fluid
<i>BgN</i>	Bagnold number
<i>CFL</i>	Courant Friedrich Lewy number
<i>CSF</i>	Continuum Surface Force
<i>CV</i>	Control Volume
<i>Eö</i>	Eötvös number
<i>Fn</i>	Froude number

<i>FPSO</i>	Floating Production Storage and Offloading vessel
<i>JONSWAP</i>	Joint North Sea wave project
<i>LHF</i>	Local Height Function
<i>MARIN</i>	Maritime Research Institute Netherlands
<i>PLIC</i>	Piecewise Linear Interface Construction
<i>Re</i>	Reynolds number
<i>SLIC</i>	Simple Line Interface Calculation
<i>SVOF</i>	Simplified Volume-of-Fluid
<i>VoF</i>	Volume-of-Fluid
<i>WLIC</i>	Weighted Linear Interface Calculation

1 | General introduction

The severity of the waves is increasing, leading to higher design loads for sea-going vessels and offshore structures. Hydrodynamic impact loading account for 10% of structural damage for conventional ships [147]. The structure experiences an increase of large motions and violent waves coming onto the deck, called green water events. Especially for Floating Production Storage and Offloading vessels (FPSO's), Tension-Leg Platforms (TLP's), and Single Point Anchor Reservoirs (SPAR's) the green water can damage the sensitive equipment on the deck.

Besides green water events, other complex free surface events are also important for the survival of the vessels, like slamming, sloshing and splashing. These events can significantly damage the structure which can even lead to flooding of compartments. The processes which are responsible for such damages are still not fully understood. Due to the complexity of these wave impacts, a lot of different local physical processes can be experienced, which are hard to predict.

Nowadays, these physical processes are predicted by numerical methods, which often assume water to be incompressible. One of the analytical equations to predict green water forces is developed by Buchner (2002).

During a breaking wave event, a considerable quantity of air can be entrapped over a few meters beneath the free surface. Values up to 14.4% at real scale are measured and can sustain for a couple of wave periods [21]. These processes are recognized by the white caps in a stormy ocean. The air entrainment drastically modifies the compressibility of the fluid with more than one order of magnitude. The fluid can even be more compressible than air. This can result in a *cushioning effect on the initial impact pressure* but also to pressure gradients of large amplitude and a long lasting time of the pressure. This results in an *underestimation of the acting forces* [118].

A small amount of aeration can drastically *affect the dynamics of the impact*, like oscillation frequencies, and lead to generation of seaward forces on the structure due to sub-atmospheric pressures.[14, 22]. The presence of air may arise the question if the water still can be assumed as incompressible.

The aim of the graduation project is to evaluate the effect of a homogeneous mixture of water and air on the wave impact, specifically for a green water event.

For this evaluation, the physics behind the oscillations of air pockets and the compressibility of aerated water need to be well understood. Further, the earlier documentation of numerical methods, analytical models, and experiments taking into account the effect of aeration on the impact need to be reviewed. The physical relevance of aeration needs to be evaluated.

The numerical method COMFLOW need to be implemented, extended and validated to account for the compressible effects of aeration. The original method COMFLOW is implemented based on earlier documentation [78, 149]. During the process of implementation, the steps to

implement the method are reviewed again and improved when necessary.

A wave impact happens in a short time period. To capture the impact, a small time step as well as a dense grid is needed. Numerical models using high-order interpolation result in very high computational costs. Therefore, a robust model like COMFLOW is suitable to model these impacts. The multiphase model incorporated in the simulation method is based on the compressible Navier-Stokes equations which describe the motion of an aggregated fluid, the liquid and gas phase, with varying properties. Although the multiphase model of COMFLOW is appropriate for the simulation of two-phase flows in the limit of separated-phase flows, it is not suitable for cases of dispersed phase flows [117]. The model is not able to predict the compressibility of two fluids. During the graduation period the core of the COMFLOW method is reproduced and extended to a method, which can deal with a dispersed flow. This is done by using the numerical computer environments FORTRAN and MATLAB.

The extended model, called the compressible double fraction Volume-of-Fluid (VoF) model, is based on the multifluid approach. A fixed Cartesian grid is used where the variables are staggered. The model is based on Kapila's five-equation model [73]. The convective terms are predicted using the second-order upwind scheme and the time integration is based on the second-order Adams-Bashforth scheme. To solve the pressure and the velocity, the explicit fractional step method is used. To describe the free surface a modified VoF method, originally introduced by Hirt and Nichols (1981), is used where the interface is represented by piecewise constant lines (SLIC). The free surface displacement method is extended with the local height function for improved accuracy of the free surface. To account for the aeration, a third phase is defined by assuming a homogeneous mixture and a constant air-mass fraction. All fluids are assumed as compressible resulting in a new transport equation.

Report structure

The report starts with a [Literature review](#) in chapter 2. In this review, the general pressure distribution over time by a wave impact is explained. After that, the possible effects of air on the wave loads at real scale and model scale are discussed in. This is separated in two phenomena; the [Air pocket](#) in section 2.2 and [Entrained air](#) in section 2.3. The need for numerical methods to predict the forces is highlighted.

The event [Green water loading](#) and the difficulty to predict this loading are explained. An analytical equation is derived in section 2.4 for the dam break case to predict the forces. A dam break is a simplified green water event.

Besides the effect of air, the [Physical relevance](#) in section 2.5 is confirmed. It needs to be verified that compressible effects of entrained air can be experienced at real scale events. The chapter ends with the [Derivation of the multifluid model](#), the background of COMFLOW, and a conclusion.

Hereafter, in chapter 3, the [One-phase VoF model](#) documented by Kleefsman et al. (2005) is implemented. The method is explained briefly. The original [Free surface displacement](#) algorithm is discussed in section 3.4 together with the [Local height function](#). Furthermore, the scheme of the fractional step method, to solve the system of equations, is elaborated in section 3.3.3.

In chapter 4, the [Multiphase VoF model](#), documented by Wemmenhove (2008), is in short discussed and compared with the one-phase model. The one-phase model is altered to get the multiphase Navier-Stokes solver.

Besides the implementation of the original method, the method is modified with respect to the modelling of the [Surface tension](#) in section 4.4. Furthermore, the gravity-consistent averag-

ing method is compared with the cell-weighted averaging method for the [Density at cell edge](#) for SLIC in section [4.3.8](#) and the effect of neglecting terms in the [Diffusive term](#) is discussed in section [4.3.2](#).

For this model, different kind of section [4.5](#) are done for verification in section [4.5](#). With the 1D water piston case, the representation of the compressible effects of air is tested. Standing wave simulations can be used to assess the performance of the numerical model for free surface waves. Further, the CSF-model is tested for the oscillating 2D planar rod to show that the model can give an accurate distinction between both phases and an accurate representation of the capillary forces. Hereafter, the 2D rising bubble case is used to look if the original method is improved with respect to modelling the viscosity. In the end, the results for 2D dam break case are compared with experimental data and the original method.

For the [Double fraction VoF model](#) in chapter [5](#), the extension is made based on the multiphase model. In this chapter it is discussed how to add the effect of aeration to the discretization of the governing equations. The principle and the difference between the multiphase model and the extension are elaborated. For this model a [Modified local height function](#) and a new [Transport equation](#), discussed in section [5.4.2](#) and section [5.4.2](#), are used.

To verify that the model can represent the compressibility for a fluid as well as a mixture, a [1D Shock tube](#) in section [5.5](#) for separated and mixed fluid is simulated. For this case a grid convergence study is done. Besides the 1D shock tube, the [2D Shock bubble interaction](#) with helium in section [5.6](#) is used as 2D verification of the extension by comparing the results with analytical, numerical, and experimental results. For the [Dam break case](#) in section [5.7](#), the extended model is tested for a dispersed flow with a separated phase and compared with the original method and the analytical model. This is done at real scale as well as experimental scale in section [5.7](#).

After the validation, [Dam break simulations](#) with an obstacle are done in chapter [6](#). The new-developed model is compared with the one-phase model. This comparison is done by measuring the water height at certain places. Also, the impact pressures on the dam and the wall are measured.

For the aerated compressible simulations, the wave impact and free surface dynamics are analyzed and compared with other results of other investigations. The behavior of the trapped air pocket and the oscillation frequencies are highlighted and compared with other documented results.

In the end, a [Conclusion](#) is described in chapter [7](#) based on the all the simulations results and some [Recommendations](#) are prescribed in chapter [8](#). This must show whether the effect of aeration is significant and if it is possible to extend the method COMFLOW.

2 Literature review

2.1 Introduction

Before the explanation of the numerical method used to model the effect of entrained air, it need to be understood which kind of phenomena can be expected during a wave impact. A number of flow phenomena can happen around a breaking wave against a structure. The two-phase phenomena for a breaking wave are illustrated in fig. 2.1. A distinction between three groups is made:

- Air pocket
- Bubble cloud
- Spray

The largest physical feature is the [Air pocket](#), discussed in section 2.2. Due to the overtopping of the wave, either due to the wave steepness or the presence of a ship, air pockets can be entrapped [149]. This feature has, in general, a short lifetime compared to the other features.

The smaller air pockets, called bubbles, can be entrained during the impact or wave breaking. The air pocket can fragment in many bubbles which results in [Entrained air](#) in the water. The bubbles are grouped in clouds and have a longer lifetime than the air pocket, up to several wave periods [96, 149]. This feature is discussed in section 2.3.

The last feature called spray is located above the free surface. The spray consists of water particles instead of air. The feature is only visible after a large scale during wave breaking. The effect of spray on the impact is negligible [149]. Therefore, the focus will be on air pockets and bubbles. From a numerical perspective, the air pocket is represented by multiple grid cells while the size of a bubble is smaller than one grid cell.

The current state of investigations concerning the influence of air in water on the wave impact

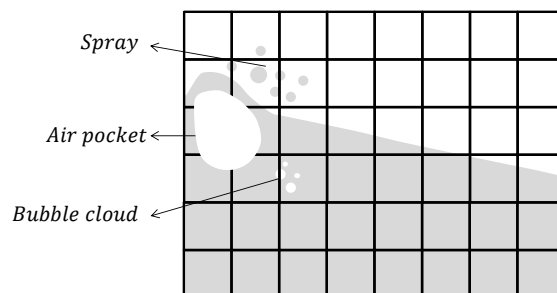


Figure 2.1: Two-phase flow phenomena for a breaking wave [149].

is reviewed in section 2.2 and section 2.3. This concerns the pressure development changed by air, the different phenomena during an impact and the physical relevance of air at real and model scale.

Hereafter, an introduction to [Green water loading](#) is given and an analytical model to approximate the impact pressure is derived in section 2.4. The [Physical relevance](#) of aeration at real scale as well as model scale is evaluated in section 2.5.

Furthermore, for the numerical model, the [Derivation of the multifluid model](#) is given in section 2.6. The model used by [ComFLOW](#) is explained more in depth and a short introduction of the extension is given. The chapter wraps up with a section 2.7 of the literature review where the relevance of aerated-water wave impact is confirmed.

2.2 Air pocket

The distinction made in fig. 2.1 between air pocket and entrained air, can be related to the cell size. When the bubble can be represented by multiple cells, it is defined as an air pocket. The entrained air is harder to track compared with the air pocket, because no free surface can be defined. Often entrained air is produced by a fragmented air pocket. Note that the effect of an air pocket on the impact can also be caused by entrained air, but often to a lesser extent.

In this section, the effect of an air pocket on the [Pressure development](#) is discussed in section 2.2.1. Besides the cushioning effect on the impact, an air pocket can give sub-atmospheric pressures due to [Oscillations](#), described in section 2.2.2.

2.2.1 Pressure development

When a breaking wave hits a vertical wall, an air pocket can be entrapped. The size of the air pocket depends on many parameters. It is found by Plumerault et al. (2012) that the size slightly increases with the breaking distance relative to the structure. However, the aeration level hardly influences the size of the air pocket. During the impact, the air pocket has an ascending movement before it stabilizes. The maximum pressure can be found at the wall at the elevation of the low end of the entrapped air pocket. The resultant impact loads highly depend on the position of the breaking point of the wave.

According to Wemmenhove (2008), there are four different stages in the pressure development where two peaks occur. These stages are illustrated in fig. 2.2. The first stage is caused due to the compressibility of the air. An air pocket is going to be entrapped which gives a cushioning effect on the pressure peak [21]. The pressure can decrease with the amount of air entrapped but increases the pressure rise time [21, 37, 61]. Further, Bürger et al. (1989) found that a wave impact with a very thin lens shape air pocket results in the highest pressure at the wall. In another investigation, the same result was found [6]. Another example is the work of Oumeraci et al. (1995) who found that a large air pocket results in the highest pressures, while with a small air pocket the largest overall forces are found.

In the investigation of Bredmose et al. (2009) it is found that the entrapment of a small pocket of air gives the highest impact pressure. Further, there is a possibility that the magnitude of the impact force and impulse increase by entrapment of air due to the increase in spatial and temporal extent of the impact. This can happen, even though the presence of air may reduce the magnitude of pressure.

The results given by Obhrai et al. (2005) showed that the air pocket increases the spatial extent and duration of the pressure which could result in a larger impulse being applied to the structure. However, without an air pocket, the pressures were higher. Also, other investiga-

tions found that an air pocket increases the impulse due to re-bounce [14, 154].

The first peak in fig. 2.2 is caused by the wave crest hitting the wall [127]. This peak is called the impact pressure. The second peak is caused by the water being accelerated to slow down at the wall as it falls back, primarily due to the gravity force [149]. This peak is called the reflective pressure or the quasi-hydrostatic pressure [22]. During stage 4 air can be entrained from the air pocket. While the first peak is important for short-term damage, the reflective pressure is of importance for the long-term damage. The peak is lower but last longer. This can also have an influence on the next incoming wave [149]. The effect of the air pocket is smaller on the second peak [154].

The pressure over time differs a lot for different impact types. The one illustrated in fig. 2.2 is the most general one. Given in the report of Vink (1997), the pressure distribution is similar to a wave impact where a small air pocket is entrapped due to a vertical wave. This one is called the transition type wave impact or flip-through impact [145]. This is the most severe impact case [31]. An in-depth explanation of the impact types is given in appendix A.

When the air pocket grows, there will be a second impact pressure. Further, low-frequency force oscillations can be found between the impact pressure and reflective pressure. This one is called the Bagnold type wave impact [145]. The existence of two impact pressures is caused due to a greater air pocket. The first impact pressure, called the hammer shock, is caused by the wave crest hitting the wall. The second pressure peak, immediately after the initial impact called a compressive shock, is caused due to the maximum compression of the air pocket [127]. In the results of Plumerault (2009) it is shown that the air content in water influences the second peak but hardly affects the first peak. The effect of the breaking distance is neglectable and the natural frequency of air pocket is of importance for the second peak.

The low-frequency oscillations after the impact pressure are caused by the cyclic compressions and expansions of the trapped air pocket under the highly transient pressure fields. This is related to the eigenfrequency of the air pocket which depends on the size [127]. The low-frequency oscillations were found to correlate well with the amount of entrained air [107]. Negative gauge peak pressures can be found in this type of impact. These are caused due to the effect that the trapped air is so much compressed that in re-expanding it throws the water mass back with a velocity that pressure drops below the atmospheric pressure [127]. The oscillations are illustrated in fig. 2.2 as a dotted line.

These low-frequency oscillations are likely to be dynamically amplified when the damped eigenfrequency of the structure is in the same range and can be more severe than one peak excitation force. The frequencies are for example in the same range as for caisson breakwaters and can influence the stability of the structure [145]. More information about oscillations is given in the next paragraph.

2.2.2 Oscillations

In the previous paragraph, it was established that the natural frequency of the air pocket can have a significant effect on the pressure. An entrapped air pocket will interact with the surrounding fluid while it is in a pulsating motion. The fluid energy is alternately stocked and released which gives pressure oscillations. The potential energy of the air pocket is significant compared to the total energy of the impacting fluid: up to 15% [118]. The natural frequency (f_0) of an air pocket, assuming a spherical bubble with an adiabatic pulsation, is given by the

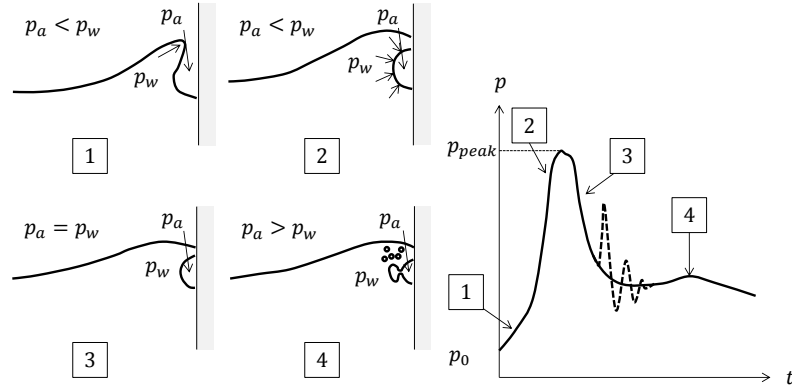


Figure 2.2: Typical pressure development over time [149].

equation [88]:

$$f_0 = \frac{1}{2\pi R_0} \sqrt{\frac{3\gamma p_0}{\rho_{w,0}}}, \quad (2.1)$$

where the density $\rho_{w,0}$ depends on the aeration level β . Further, the parameters γ , R_0 , and p_0 are the specific heats ratio, the initial radius, and the atmospheric pressure, respectively. However, the air pocket is often not spherical. Therefore, Oumeraci et al. (1992) proposes a simple way to calculate the natural oscillation frequency:

$$f_0 = \frac{k_a}{2R_0}, \quad (2.2)$$

where $k_a=5.35[\text{m/s}]$, a constant obtained by Oumeraci et al. (1995). The frequency of the pressure oscillation decreases with β and the breaking distance D [118]. This is explained by the increase of the air pocket by an increase of D .

Besides the frequency of pulsation of the air pocket, also the domain frequencies can be of importance. The walls can reflect pressure waves which can give amplifications. For the longitudinal (f_l) and transverse (f_t) acoustic mode, the natural frequencies are approximated by:

$$\begin{aligned} f_l &= \frac{c_{w,0}}{2L}, \\ f_t &= \frac{c_{w,0}}{2H_{SWL}}, \end{aligned} \quad (2.3)$$

where L is the length of the domain and H_{SWL} the height of the still waterline in $[m]$. Further, c represents the speed of sound in $[m/s]$. The transverse mode may correspond with the reflection of the pressure wave on the base of the structure leading to destabilizing forces [118]. Note that it is an approximation of the speed of sound because the speed of sound is not constant over the height.

The work of Plumerault et al. (2012) showed that a distinction can be made between two regions. The first region is the front of the air pocket. In this region, the pressure fluctuations are related to the oscillations of the air pocket. Further, there can be an influence of the transverse acoustic mode which depends on the air content. The second region is below, where the transverse acoustic mode is dominant. The air pocket oscillation is dominant over the transverse acoustic wave in forces and moments. Values of pressure lower than the atmospheric pressure,

called sub-atmospheric pressure, can be found due to an oscillating air pocket [14, 22]. The oscillating forces and moment experienced by the wall increase with a decreasing air content. The breaking distance has a limited influence on pressures, forces, and moments [116].

Recent computations by Plumerault (2009) indicate that when the reflected pressure waves at the seabed are in phase with the pulsation of the air pocket, pressures higher than those caused by the initial impact may occur due to resonance.

2.3 Entrained air

It is known that air can be entrained by successive breaking events at the impact zone. This lead to bubbles in the water. This is visible in situation 4 in fig. 2.2 where the air pocket crumbles into smaller bubbles. However, the question arises what the effect is of this entrained air.

As mentioned before, the simulation method COMFLOW is not capable to model the aeration. Due to the air entrained, the properties of the air-water mixture changes, like compressibility. The [Compressibility of the mixture](#) is related to its sound speed. This is discussed in section 2.3.1. Further, it is discussed which kind of [Air bubble rates](#) can be expected at real scale as well as model scale and what the [Scaling](#) effect is.

2.3.1 Compressibility of the mixture

The compressibility (α) of a bubbly mixture depends on the change in volume caused by a difference in pressure, where the volume is related to the density. Furthermore, the relation between the speed of sound and pressure is [113, 141]:

$$\frac{d\rho_w}{dp} = \frac{1}{c_w^2}, \quad (2.4)$$

where ρ_w and c_w are the density and speed of sound of the mixture, respectively. Both, the compressibility and the speed of sound, are related to the pressure. The following relation between compressibility and speed of sound is derived:

$$\alpha = \frac{1}{\rho_w c_w^2}. \quad (2.5)$$

Assuming that the entrained air hardly affect the density ρ_w , the compressibility α increases due to the presence of air. The non-dimensional Mach number can indicate the relevance of compressibility:

$$Ma = \frac{u}{c_w}, \quad (2.6)$$

where u is the speed of the fluid in [m/s].

To derive a simple expression for the speed of acoustic waves in a bubbly mixture (c_w), no relative velocity between the bubbles and the liquid is assumed. Further, a pressure equilibrium at the boundary of the bubbles and no interaction between the bubbles is assumed. This leads to a homogeneous mixture [141, 153]. This assumption is only valid when the frequency of the pressure wave is well below the resonant frequency of the largest bubble in the mixture.

The mass of gas in the mixture remains constant and an adiabatic behavior is assumed. An adiabatic behavior means that compression happens so fast that no heat is transferred between air and the water. To have an isothermal flow, compression would have to be slow enough for heat transfer with air at constant temperature [21]. According to Peregrine and Thais (1996) the effect of choosing an adiabatic flow is small. This is elaborated in section 2.3.2.

The density of the mixture (ρ_w) can be found, using the volume fraction of air (β) in the mixture:

$$\rho_{w,0} = (1 - \beta_0)\rho_{l,0} + \beta_0\rho_{g,0}, \quad (2.7)$$

where ρ_g and ρ_l are the densities of the air and water in the mixture in $[kg/m^3]$, respectively. According to Wood (1941), the following expression for the speed of sound of the mixture at atmospheric pressure p_0 can be established by also assuming no capillary and dissipative effects:

$$\frac{1}{\rho_{w,0}c_{w,0}^2} = \frac{\beta_0}{\rho_{g,0}c_{g,0}^2} + \frac{1 - \beta_0}{\rho_{l,0}c_{l,0}^2}. \quad (2.8)$$

The equation is verified by experiments [152]. According to eq. (2.8), an air content of 5% gives a speed of sound of $52.5[m/s]$ which is up to 7 times(!) lower than the speed of sound of air ($\approx 350[m/s]$). The reason for this is that the density in eq. (2.5) hardly changes while the compressibility increases. The graph illustrating eq. (2.8) is shown in fig. 2.3. The formula

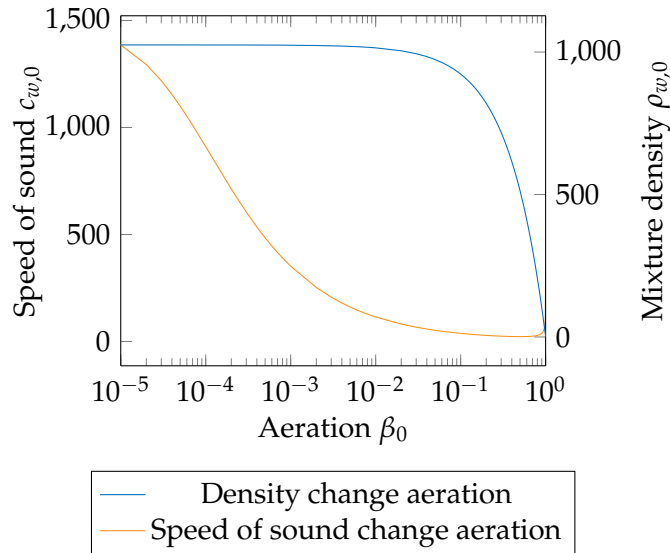


Figure 2.3: Density and speed of sound change versus aeration.

of Wood (1941) can also be written as function of the air mass fraction $y = m_g/m$, where m_g is the mass of air and m the mass of the mixture in a control volume. Using the equations $\beta_0\rho_{g,0} = y\rho_{w,0}$ and $(1 - \beta_0)\rho_{l,0} = (1 - y)\rho_{w,0}$, for a given pressure p_0 [118]:

$$\begin{aligned} \rho_{w,0} &= \frac{\rho_{g,0}\rho_{l,0}}{y\rho_{l,0} + (1 - y)\rho_{g,0}}, \\ \beta_0 &= \frac{y\rho_{l,0}}{(1 - y)\rho_{g,0} + y\rho_{l,0}}, \\ \frac{1}{c_{w,0}^2} &= \left(\frac{\rho_{g,0}\rho_{l,0}}{(1 - y)\rho_{g,0} + y\rho_{l,0}} \right)^2 \left(\frac{y}{\rho_{g,0}^2 c_{g,0}^2} + \frac{1 - y}{\rho_{l,0}^2 c_{l,0}^2} \right). \end{aligned} \quad (2.9)$$

From fig. 2.3 it can be concluded that the speed of sound for an air-water mixture is not necessarily between the speed of sound of water and air. The minimum speed can be found at $\beta_0 = 0.5006$ which gives $23.76[m/s]$. Due this speed reduction, pressure gradients can last longer in time. The pressure relaxation time is conversely proportional to the sound speed [118].

2.3.2 Effect on impact

Aeration of the water, like an entrapped air pocket, can influence the pressure dynamics of the flow. Bullock et al. (2001) did drop tests and laboratory wave tests where the results show that entrained air reduces the maximum impact pressures and increase rise times for both experiments. The cushioning effect becomes more important when the voids ratio and the violence of the impact increases.

An analytical approach, called filling flow model and derived by Peregrine and Thais (1996), can be used to estimate the pressure at the surface of a confined space where jets can occur. This is similar to a flip-through impact. However, for small values of air content, the effect is not as dramatic as suggested by the filling flow model. The filling flow model is described in appendix B.3.

Bredmose et al. (2009) performed a numerical study of aerated violent wave impacts by an incompressible potential-flow model and a novel compressible-flow model which accommodates both entrained and trapped air. This was done for a flip-through impact and a plunging breaker. The results show that high aeration levels of above 5% can give sub-atmospheric pressures, which can lead to the generation of destabilizing seaward forces on parts of the structure. Pressure waves propagates down to the base of the wall which will be reflected at the sea bed. This can yield high pressures on the structure. The same results are obtained by Bullock et al. (2007).

Due to the high aeration level, the speed of sound reduction is great. The speed of sound for the previous maximum pressure can be low enough to propagate to the foot of the structure. This can give a vertical gradient in upward direction. This results in a lifting force exerted on the structure. The lifting force decreases with the air content while for increasing the breaking distance the lifting force increases.

With the same model different impacts with low or high aeration level are analyzed at real scale [15]. For all the impact types investigated -high and low aerated impact and flip-through impact- the maximum pressure, force and rise time of the impulse decrease with the initial aeration level due to the cushioning effect of aerated water. Further, the pressure reduction increases with the violence of the impact. This is conformable with the filling model of Peregrine and Thais (1996). The effect of aeration can also be significant for the air pocket oscillations as shown in eq. (2.3). At a certain level of aeration, leading to a low speed of sound, resonance can happen between the air pocket oscillation and the returning pressure wave from the seabed.

Bullock et al. (2007) performed large scale regular wave tests on vertical and sloping walls. They concluded that due to both high and low aeration levels, high pressures of the same magnitude can occur. The aeration does not seem to influence the magnitude. Further, Bullock et al. (2007) concluded from numerical and analytic studies that the potential benefit of aeration, like the cushioning effect, decreases when the impact pressure increases. Even if the pressure for a high aeration impact is lower, the force is not necessarily lower than due to low aeration impact. Low aeration impact gives more spatially localized pressure maxima with a shorter rise time and maximum duration compared to high aeration. When the pressure gradient last longer, the forces on an object increases which would result in a greater displacement of the object. This means that in an incompressible case the displacement is underestimated when aeration is involved [118]. The aeration of the water influences the pressure development by the impact. However, the effect on the free surface dynamics is negligible [116].

Plumerault (2009) who developed a three fluid model to represent the acoustic properties of the air-water mixture well, found that the air content decreases the air pocket size and does

not affect the free surface dynamics. Further, the results of the model also showed that the pressure is hardly affected by the air content. The speed of high pressure propagating down to the bottom is affected by the air content. It affects the synchronous aspect of the pressure oscillations between the bottom and free surface, and the oscillation of the air pocket. These results correspond with the results of large scale tests of Bullock et al. (2007).

2.3.3 Air bubble rates

Measurements are needed of the average amount of aeration in water in violent conditions to know if compressible effects of the bubble mixture can occur. It is complicated to estimate the amount of air under a breaking wave. This results in a variety of values.

Deane and Stokes (2002) found that two mechanisms control the numbers and size of bubbles. One of the mechanisms is fragmentation of the air pocket while the second is due to impact of the jet. A distinction can be made using the Hinze scale. The Hinze scale is the scale of emergent critical balance between fluid straining and elastic restoring forces [46].

Bubbles can be observed down to a depth of the order of 10[m] and usually located within 1 or 2[m] of the ocean surface [138]. Lamarre and Melville (1995) did measurements in the ocean using short acoustic pulses traveling from a transmitting to a receiving hydrophone. The speed of sound is measured and using eq. (2.8) of Wood (1941), the air volume fractions is calculated. For a wind of 8[m/s] at the surface of the ocean, volume fractions at 0.5[m] under the surface of 10^{-5} are found and at 1[m] depth 10^{-6} .

Field measurements of the Atlantic waves were done by Bullock et al. (2001) to find "atmospheric" values of aeration. After impact, the void ratios for a CD (Chart Datum) of 9.1[m] was 14.4% and for a CD of 5.5[m] was 7.9%. These measurements are based on 50 sets of data recordings of 20 minutes with a significant wave height of 2.4[m] and mean water level at 5.4[m] measured at a distance of 350[m] of the Admiralty Breakwater at the France coast. The maximum impact velocity was around 20[m/s].

Besides the field measurements, also a laboratory model of the Admiralty Breakwater is made. For sea water, at model scale, the void ratio reaches 3.1% averaged over 200 wave period. They concluded that the air content in the ocean is generally greater than the air content in model tests. This indicates that aeration is subject to a scale effect. Some offshore structures can operate up to a CD of 320[m] [66]. This means high initial aeration values could be found in the operational area of the offshore structures.

It is also found by Bullock et al. (2001) that a large amount of entrained air does not necessarily prevent high pressure values with short rise time. For the void fraction at the position of the highest pressure found during the measurements, a value of 28% was estimated which was equivalent to 55% void at atmospheric pressure.

The theoretical shape of the vertical profile of air fraction beneath the free surface is determined by Buckingham (1997). It varies in depth but is independent on the horizontal range. The vertical profile is determined by the nature of turbulent diffusion. This process transports the gas down into the deep. This corresponds with a void fraction following an inverse-square profile. It is assumed that there is an uniform injection of air through the sea surface. However, a model like this is inadequate to describe the bubble plumes generated by breaking [118]. A combination of a short-term exponential profile ending with a longer-live inverse square profile is suggested.

Peregrine and Thais (1996) said that when waves are frequently breaking, the air content is

likely to be higher than 1%. However, looking to the literature found, it is not possible to conclude clearly what the amount of bubbles should be beneath the free surface. Some mention "very high" fractions whereas others mention "very low" ones [118]. This can depend on the different mechanisms. Namely, the mechanisms for large scale entrainments, jet intrusions and crushing of air cavities can be found. On small scale, bubble formation of breaking of very thin filaments of air and gathering of large bubbles can be found [34].

2.3.4 Scaling

Entrained air is usually associated with a reduction in impact pressure due to the cushioning effect of the air. However, a trapped air pocket can lead to an increase of the pressure impulse exerted on the wall [15]. This effect is likely to be scale dependent but no studies have yet been conducted.

The design of structures is often based on model tests. Using the Froude law, the forces can be determined. The Froude law scales the ratio between inertial and gravitational forces. However, when entrained air needs to be taken into account, Froude scaling can lead to wrong results [15]. The Froude law assumes no influence of viscosity, surface tension and air. However, when air gets entrapped and the Froude scaling is used, the dynamics of the fluid pressure relative to the atmospheric pressure and the compressibility of air is not accounted for. The level of aeration often increases with the scale [15, 21]. The Froude scaling overestimates the values using small models. This can lead to an overestimation of more than 10% [21].

Besides the Froude scaling, to scale the compressible effects, the ideal is that the ratio of inertial force to elastic force to remain the same. [21]: the Cauchy law scaling. The results showed a gross underestimation of the maximum pressure and an overestimation of the rise time. Using this scaling law, the impulse is reduced while the model implies that it should be conserved which makes this scaling law not reliable. It is found that the pressure impulse decreases when the level of aeration increases.

Blenkinsopp and Chaplin (2011) said that going from the model scale to the real scale, entrained air bubbles need to travel a longer distance to escape from the water which lead to an increase of aeration. This can be scaled directly with the length scale, while the wave period scales with the square root of the length scale. This leads to an increase of the ambient level of aeration.

Looking to the non-dimensional analysis done by Bredmose et al. (2015), a breaking free surface gravity wave against a vertical wall on a certain fixed instant of time before impact is used. It is concluded that Froude scaling is not accurate enough to scale for small models. The maximum pressure is a function of:

$$\frac{p_{max} - p_0}{\rho_w g h} = f \left(\frac{\tilde{h}(x)}{h}, \frac{\mathbf{s}}{h}, \frac{\mathbf{u}(\mathbf{x})}{\sqrt{g h}}, \beta_0(\mathbf{x}), \frac{p_0}{\rho_w g h}, \frac{\rho_{a,0}}{\rho_w}, \gamma \right), \quad (2.10)$$

based on fig. 2.2 where \tilde{h} is the waterdepth as function of the distance to the vertical wall, h the waterdepth at the vertical wall relative to the still waterline, \mathbf{s} the position of the free surface, and $\beta_0(\mathbf{x})$ the volume fraction of air depending on the position. When scaling to the real scale, the first two terms of eq. (2.10) will not change and neither the last two terms. The third term can be scaled when the velocity field scales as the square root of the length, resulting in Froude scaling. Deducing eq. (2.10) using Froude scaling, the maximum pressure remains function of:

$$\frac{p_{max} - p_0}{\rho_w g h} = f \left(\beta_0(\mathbf{x}), \frac{\rho_w u_0^2}{p_0} \right), \quad (2.11)$$

using a reference velocity u_0 from $\mathbf{u}(\mathbf{x})$.

The Bagnold model is many times used for a trapped pocket air. This scaling model is based on the 1D piston experiment where a mass of water is released and compresses a volume of air that was initially at atmospheric pressure [6]. This case is illustrated in fig. 4.8. It is only decelerated due to a pressure difference. Mitsuyasu (1967) and Lundgren (1969) extended this model to account for air leakage during compression. Takahashi et al. (1985) used this model to predict the maximum pressure beneath bridge decks. In this experiment the air can be trapped. They noted that the maximum pressure is function of the Bagnold number (BgN) as can be seen in eq. (2.11):

$$BgN = \frac{\rho_w K u_0^2}{p_0 D}, \quad (2.12)$$

where K is the thickness of the water mass effectively contributing to the impact. Bredmose and Bullock (2008) extended this model to 2D and 3D axisymmetric air pockets and showed that the Bagnold number is directly proportional to the length scale where the hydrodynamics is scalable by the Froude law. This means the parameters K , u_0 and D do not have to be determined. With the Bagnold-Mitsuyasu model, they found an encouraging level of agreement.

Lafeber et al. (2012) found a good match with the Bagnold-Mitsuyasu scaling law for the Froude scaled wave flume impacts at two scales.

As discussed in section 2.3.3, the aeration levels on model scale are smaller than at real scale. This means that it is harder to experience compressible effects during model tests than in the field. Also for the cases simulated with the extended model in chapter 5, these compressible effects are not experienced. However, due to the difference in density the oscillations of the air pocket results in a change in the free-surface dynamics as well as the impact pressure.

2.4 Green water loading

In rough seas large amount of water can invade the ship's deck. The water on the deck can impact, often flip-through impact, with other structures on the deck and can significantly damage them. This highly non-linear effect is called the green water effect. The flow of green water is a complex process. Due to bow slamming in head waves, water can come onto the deck.

However, ships do not always encounter head waves. They also encounter waves at 15 to 30 degrees [17]. Offshore structures like FPSO's cannot change their heading. This means that not only at the bow water can come onto the deck but also on the side of the ship [16]. When this happens, it is likely to cause damage. Green water caused damage on several FPSO's typically at midship and further aft in non-heading waves [143]. Most of the time only small structures are damaged. As a result, these structures can cause safety problems. Further, the crew on the deck can be in danger due to green water.

Green water loadings are hard to predict. The knowledge about the complex physics of green water from the sides onto the deck is limited. Namely, the relative wave motion along the side is non-linear, which is the result of non-linearities in incoming waves and in the reflection of the waves on the ship [17]. When water comes onto the deck from the side due to the relative wave motion, a fast transverse flow occurs on the deck. Interesting to see is that it does not travel with the velocity of the motion of the wave crest in the longitudinal direction. It is a non-linear and complex phenomenon, which means that it cannot be solved with linear wave theory [19]. This makes the number of methods limited. According to Buchner (2002) a typical sequence can be observed during a green water event:

- First the relative motion of the wave exceeds the freeboard level.
- This results in water spilling onto the deck with a certain velocity and height.
- This is called green water. It forms a high-velocity water jet.
- The green water impacts on a structure on deck like an impinging jet.

During the impact, a distinction can be made between three stages. The *first* stage is the impact stage where the highest pressure peak takes place. In this stage, an impinging jet along the structure can be observed. The *second* stage is the quasi-static loading. This is when the kinetic energy of the water is almost out of the fluid and a large amount of water has built up against the structure. The *third* stage is the plunging water stage where water falls back onto the deck and generates a second pressure peak. These pressure peaks depend on the velocity squared, like in the equation of the impact pressure for breaking waves in appendix B.2. Before the impact stage, small pressure peaks could be observed due to fast thin water jets in front of the main amount of water.

When the water flow comes onto the deck, shown in fig. 2.4, it can be simplified to a vertical wall of water height h where the ship does not move. The vertical wall is taken away when the time is larger than zero and water flows into the dry area. This is also called the dam breaking problem where the water behind the vertical wall is given by the dotted lines [17]. This case is in this report often used as validation, like in section 4.5.6.

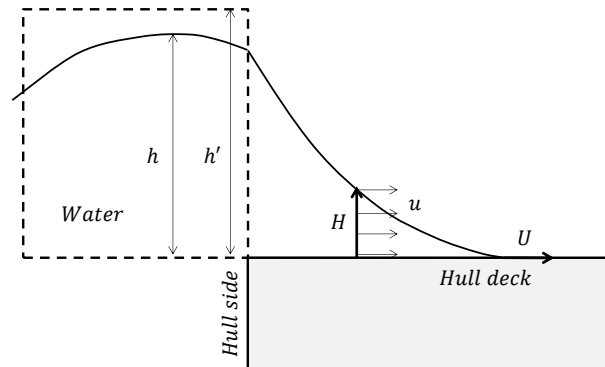


Figure 2.4: Dam break freeboard exceedance [17].

The dam break problem can be used to do an estimation of the load levels on slender structures on the deck. However, the actual flow compared to the dam break is more complex. The ship deck does move, the height of the freeboard exceedance varies in time, the initial velocity as like for the dam break is not necessarily zero and is influenced by wave kinematics and run up effects. The dam break still can help to understand the green water effects [18]. As explained before, the water can come onto the deck at the bow but also at the side of the ship. For both cases, the dam breaking problem can help to understand the physics. When the water comes onto the deck from the side of the ship, a fast transverse flow occurs [17].

Using shallow water flow assumptions -constant density, absence of shock waves and horizontal scale dominant- the water height as a function of the time (t) and horizontal position (y) from the initial dam position with height h' can be found. The height of the initial dam depends on the freeboard exceedance (h) and is higher due to the difference in velocity in the real case. Note that this equation is not applicable for $t = 0$ [133]:

$$H(y, t) = \left(\frac{-y}{3\sqrt{gt}} + \frac{2}{3}\sqrt{h'} \right)^2. \quad (2.13)$$

For the dam break it is assumed that the amount of water behind the hull side is infinite. The speed of the wave front for the dam breaking problem is equal to $U = 2\sqrt{gh'}$. However, the speed of the water particles is different [133]:

$$\begin{aligned} u(y, t) &= \frac{2}{3} \left(\frac{y}{t} + \sqrt{gh'} \right), \\ u(H) &= 2 \left(\sqrt{gh'} - \sqrt{gH} \right). \end{aligned} \quad (2.14)$$

Knowing that the velocity distribution is constant over the height, the force per meter depth exerted on a slender structure can be calculated with $F = \frac{1}{2}C_d\rho_w Su^2H$, where C_d is the drag coefficient and S the height of the frontal area of the structure. The force (F) and the moment (M) can be calculated with:

$$F(H) = 2C_d\rho_w gS(h' - 2\sqrt{h'H} + H)H, \quad (2.15)$$

$$M(H) = C_d\rho_w gS(h' - 2\sqrt{h'H} + H)H^2. \quad (2.16)$$

The equation for the force shows that a maximum can be found. A thin layer of water yields a higher velocity while the height H decreases. By differentiating over H the maxima can be found for the force as well as for the moment.

In appendix C, the effect of ship motions, environmental conditions, and longitudinal forces on green water loading are discussed. Furthermore, limiting scenarios of the dam break problem are discussed.

2.5 Physical relevance

In eq. (2.8) it is shown that a small amount of aeration significantly changes the speed of sound of the mixture. Further, in section 2.3.3 it is shown that the air bubbles rates found in the field as well as during experiments at model scale can reduce the speed of sound of the mixture far below the speed of sound of only air.

However, to verify that compressible effects need to be taken into account during numerical simulations, [Relative velocity](#) between the wave impact and the structure is needed. Further, the effect of the [Sea-state](#) is discussed.

2.5.1 Relative velocity

To compress a fluid, the immersion velocity and/or the relative wave velocity need to be in the order of the speed of sound in the fluid. Field measurements are done of the immersion velocity at the bow of a ship by Hodgson and Barltrop (2003) using transducers on the bow. This is done in the Atlantic to the West of the Shetland Isles. In this region, the sea state had a significant wave height of 14[m] and a peak period of 15[s] [54]. The length of the ship used for the measurements is 245[m]. A distinction is made between instantaneous slamming and progressive slamming. By progressive slamming, the pressure front travels upward over the plate. A traditional pressure development over time is shown up to immersion velocities of 100[m/s]. The rise time increases with the size of the area while the pressure impulse remains constant. This is called progressive slamming where the mean value of the immersion velocity is around 45[m/s] [146]. When the immersion velocities are higher than 100[m/s], only short sharp slams occur. This is called instantaneous slamming where the duration of the load is independent of the target size and thus the immersion velocity.

Another investigation is done by Wang et al. (2002). The slamming pressures and structural responses are calculated for three selected plate panels on an FPSO with a length of 230[m]. Using the JONSWAP wave spectrum of the sea by the West Shetland Isles, the maximum relative vertical velocity at the bow is found to be 15.5[m/s]. The sea has similar environmental conditions as the North Atlantic open sea. In the Gulf of Mexico, the vertical relative velocity at the bow was 12.5[m/s] at its maximum. Note that by the impact the water is accelerated which gives higher velocities of the flow along the bow.

The measurements in the Atlantic waves by Bullock et al. (2001), discussed in section 2.3.3, are done by a breakwater where an average speed of impact of 20[m/s] is found.

Further, Elhimer et al. (2017) did experiments using an air-water mixture for determining the slamming loads during a cone water entry. They concluded that when the Mach number is bigger than 0.3, the slamming coefficient depends on the Mach number and on the void fraction. Also, Plumerault et al. (2012) concluded that it was possible to reach Mach numbers higher than 0.3 during the simulation of a breaking third order Stokes wave capturing a small air pocket. Peregrine and Thais (1996) determined the Mach number on the inflow velocity and found that even impacts with an inflow velocity of a Mach number of 0.3 could give compressible effects.

Looking to the velocities of wave impact relative to the structures, in the field for an aeration level of 5% and the lowest velocity found, a Mach number of 0.24 can easily be reached. When a relative speed of 15.75[m/s] is reached, a Mach number of higher than 0.3 is found. Note that at model scale, this velocity is harder to reach due to the scaling effect of aeration discussed in section 2.3.3 and section 2.3.4.

2.5.2 Sea-state

For laboratory tests, often fresh water is used. However, at real scale like the ocean, there is sea water which has different properties. For example, the difference in density of sea water and fresh water could have an effect on the impact pressure. The unit mass of salt water is bigger than the unit mass of fresh water. However, according to Bullock et al. (2001) it is not necessarily true that the impact pressure will be bigger for an impact with salt water.

Bullock et al. (2007) did regular and irregular wave tests to measure the behavior of a breaker in fresh water and in sea water. The results showed that in both tests the maximum pressure for fresh water averaged over 200 wave periods is higher than for sea water. However, the duration of impact is longer for sea water than for fresh water. The impulse loading remained nearly the same.

The results also showed that during the impact air is entrained in the water. Bubbles formed in fresh water tend to be larger than the bubbles in sea water. Further, they also tend to coalesce more easily. This can be explained by the effect of salinity in water. Scott (1975) was the first one who found that salinity is inversely related to the size of air bubbles. The exudates of marine organisms have a similar effect as the salinity. Slauenwhite and Johnson (1999) concluded that the bubble production is greater in sea water than in fresh water. The bubble production is not just a simple function and depends on many parameters like ionic strength, surface tension, structure breaking/making ability and density.

When the size of the bubbles is bigger, the buoyancy force also will be bigger. This means that in fresh water the bubbles persist for a shorter amount of time. Bullock et al. (2001) found that at the model scale the bubbles withstand in fresh water for one wave period while in salt for several wave periods. For the regular wave test, for example, the average void ratio after 200 wave period was for sea water 3.1% and for fresh water 0.2%. In section 2.3 it was

concluded that aeration is a subject to a scale effect which makes it difficult to scale from laboratory tests with fresh water to real scale with sea water.

According to Morris et al. (2000) from 1995 to 2000, based on 25 FPSO's located on the UK Continental Shelf and in the Norwegian waters, a near linear increase of bow green water occurrence with increasing significant wave height is found. In this period, 17 green water and 2 wave slam incidents are identified on 12 FPSO's were 26 areas of damage is classified. An average of incidents per year of 0.21 to 0.28 is found. At the sides a freeboard exceedance of 4[m] occurred on 75% of the FPSO's while 15% had experienced a freeboard exceedance of higher than 10[m]. As discussed in section 2.4, the freeboard exceedance is related to the initial height for the dambreak case where the height of the initial dam is higher. Using eq. (2.14), this results in a velocity of at least 20[m/s].

Besides the results of the past, it is predicted by Bertin et al. (2013) that the significant wave height will increase over the whole North Atlantic Ocean, reaching a value of 0.01[m/yr], due to rise in wind speed. This result implies that the change of freeboard exceedance will increase in the future, resulting in an increase of compressible effects of the air-water mixture.

2.6 Numerical model

In this section, a more in depth information is given about the background of the numerical method [ComFLOW](#), where the model developed in this report is based on. Hereafter, a short introduction to the extended model is given.

The section starts with the [Derivation of the multifluid model](#). In appendix B.1, a very short overview of numerical and analytical approaches used for the prediction of wave breaking is reviewed.

Derivation of the multifluid model

Before discussing the numerical method COMFLOW, the governing equations are elaborated as well as how to solve these on macroscopic level. The derivation is documented by Plumerault (2009).

If we are at a scale which is small enough to consider phases as not mixed and assume that a phase i can be described as a continuum, the integral form of the governing equations can be written as:

$$\begin{aligned} \frac{\partial \rho_i}{\partial t} + \nabla \cdot (\rho_i \mathbf{u}_i) &= 0, \\ \frac{\partial \rho_i \mathbf{u}_i}{\partial t} + \nabla \cdot (\rho_i \mathbf{u}_i \mathbf{u}_i^T) &= \nabla \cdot \mathbf{T}_i + \rho_i \mathbf{F}_i, \end{aligned} \tag{2.17}$$

where \mathbf{T} is the stress tensor, containing the normal stresses, like pressure, and the shear stresses $-p\mathbf{I} + \boldsymbol{\tau}$. Further, \mathbf{F} is the body force vector. Note that the first equation is called the continuity equation and the second equation represents the conservation of momentum. Besides these two equations, also an equation for the conservation of energy exists. The conservation of energy for every phase is left out of scope. For the topic discussed in this report, we are not interested in thermodynamic properties of the fluid. The assumption of barotropic fluid is made which means that the pressure in fluid i only depends on the density of fluid i .

Besides these equations at the continuum level, the fluids need to be separated by an interface. This interface indicates a jump in mass and momentum. The jump in momentum can

be caused by the surface tension and in mass due to a difference in velocity of the fluid and the interface. To indicate the presence of a phase on microscopic level, an additional function $s_i(\mathbf{x}, t)$ is needed. When the phase is at time t in location \mathbf{x} , the value of the function is equal to one, otherwise it will be equal to zero. Because this additional function is related to the phase i , the material derivative along the interface is equal to zero $\frac{Ds_i}{Dt} = 0$. Only at the interface, a gradient of the function s_i can be found similar to a Dirac vector function [118].

To go from the microscopic scale to the macroscopic scale, the equations need to be averaged over a volume using the procedure of Drew (1983). The conservation equations given in eq. (2.17) can only be valid in areas where the fluid i is present. This can be done by multiplying eq. (2.17) with the function s_i . The interfacial source term, representing the creation of fluid i on macroscopic level due to mass transfer across the interface at the microscopic level [39], needs to be added to eq. (2.17). This causes also a momentum transfer (\mathbf{M}) due to the mass transfer (Γ) [118]. These terms are explained more in detail by Drew (1983). This results in the following equations:

$$\begin{aligned} \frac{\partial \langle s_i \rho_i \rangle}{\partial t} + \nabla \cdot \langle s_i \rho_i \mathbf{u}_i \rangle &= \Gamma_i, \\ \frac{\partial \langle s_i \rho_i \mathbf{u}_i \rangle}{\partial t} + \nabla \cdot \langle s_i \rho_i \mathbf{u}_i \mathbf{u}_i^T \rangle &= \nabla \cdot \langle s_i \mathbf{T}_i \rangle + \langle s_i \rho_i \mathbf{F}_i \rangle + \mathbf{M}_i, \end{aligned} \quad (2.18)$$

where $\langle \rangle$ represents the averaging operator. By averaging the function s_i over a volume, at macroscopic level this can be indicated as a volume fraction F_i . During the procedure, the interfacial force density is neglected. It is also assumed that there is no mass transfer at the interface, like due to chemical reactions or evaporation, and the interfacial pressure of the fluids are equal. This result in the following equations for example a two fluid model where $F_2 = 1 - F_1$:

$$\begin{aligned} \frac{\partial F}{\partial t} + \mathbf{u}_{int} \cdot \nabla F &= 0, \\ \frac{\partial F \rho_1}{\partial t} + \nabla \cdot (F \rho_1 \mathbf{u}_1) &= 0, \\ \frac{\partial (1-F) \rho_2}{\partial t} + \nabla \cdot ((1-F) \rho_2 \mathbf{u}_2) &= 0, \\ \frac{\partial F \rho_1 \mathbf{u}_1}{\partial t} + \nabla \cdot (F \rho_1 \mathbf{u}_1 \mathbf{u}_1^T) + \nabla (F p_1) &= \\ p_{int} \nabla F + \nabla \cdot (F \boldsymbol{\tau}_1) + F \rho_1 \mathbf{F}_1, \\ \frac{\partial (1-F) \rho_2 \mathbf{u}_2}{\partial t} + \nabla \cdot ((1-F) \rho_2 \mathbf{u}_2 \mathbf{u}_2^T) + \nabla ((1-F) p_2) &= \\ -p_{int} \nabla (1-F) + \nabla \cdot ((1-F) \boldsymbol{\tau}_2) + (1-F) \rho_2 \mathbf{F}_2, \end{aligned} \quad (2.19)$$

where p_{int} is the interface pressure related to the surface tension. It is proposed by Chantepedrix (2004) that the amount of equations can be reduced with the assumption of no-slip between the phases. This strong assumption leads to neglecting the Archimedes effect for gas bubble on subgrid level dispersed in a fluid. Further, the assumption that the pressure of the phases are instantaneously equal leads to not taking into account the acoustical effect in gas bubbles on subgrid level. Filling in the no-slip condition in the momentum equations and summing them, leads to the "mixture density" $\rho = F \rho_1 + (1-F) \rho_2$. In the report the mixture density is noted as ρ_w . Note that this is not necessarily a real mixture of fluids. The fluids can be immiscible. The

pressure still depends on both densities and both mass conservation equations are still needed:

$$\begin{aligned}
\frac{\partial F}{\partial t} + \mathbf{u} \cdot \nabla F &= 0, \\
\frac{\partial F \rho_1}{\partial t} + \nabla \cdot (F \rho_1 \mathbf{u}) &= 0, \\
\frac{\partial (1-F) \rho_2}{\partial t} + \nabla \cdot ((1-F) \rho_2 \mathbf{u}) &= 0, \\
\frac{\partial \rho \mathbf{u}}{\partial t} + \nabla \cdot (\rho \mathbf{u} \mathbf{u}^T) + \nabla p &= \nabla \cdot ((1-F) \boldsymbol{\tau}_2 + F \boldsymbol{\tau}_1) + F \rho_1 \mathbf{F}_1 + (1-F) \rho_2 \mathbf{F}_2,
\end{aligned} \tag{2.20}$$

where the "mixture pressure" is $\rho = F \rho_1 + (1-F) \rho_2$. Note that the pressure of the phases are assumed barotropic and pressure equilibria is assumed ($p_1 = p_2$). The surface tension will be added later again as body force in section 4.4.3. This assumption leads to convenient mathematical properties such as hyperbolicity of the system [118].

The viscous term can also be simplified. It is assumed that each fluid is a Newtonian fluid and the compressible term (the divergence term) can be neglected. This can be done when the viscous term is small compared to the convective term, like for violent wave impacts. Using a "mixture dynamic viscosity" the term can be simplified. The momentum equation can be simplified to:

$$\begin{aligned}
\frac{\partial F}{\partial t} + \mathbf{u} \cdot \nabla F &= 0, \\
\frac{\partial F \rho_1}{\partial t} + \nabla \cdot (F \rho_1 \mathbf{u}) &= 0, \\
\frac{\partial (1-F) \rho_2}{\partial t} + \nabla \cdot ((1-F) \rho_2 \mathbf{u}) &= 0, \\
\frac{\partial \rho \mathbf{u}}{\partial t} + \nabla \cdot (\rho \mathbf{u} \mathbf{u}^T) + \nabla p &= \nabla \cdot (\mu (\nabla \mathbf{u} + (\nabla \mathbf{u})^T)) + \rho \mathbf{F}.
\end{aligned} \tag{2.21}$$

2.6.1 ComFLOW

The numerical method COMFLOW is developed by the University of Groningen and is used as a guideline for the model developed in this report. The model used in COMFLOW is based on the Navier-Stokes equations and originally made to simulate liquid sloshing on board a spacecraft [53]. The method solves the momentum equation and continuity equation. It models a viscous incompressible liquid free-surface flow in and around arbitrary geometries. At the free surface continuity of stresses is imposed; effects of capillarity are included. Also liquid-solid body interaction is included in COMFLOW. A major application in the maritime area concerns the prediction of hydrodynamic wave loading on ships and offshore platforms [108]. An accurate description of the free surface is therefore important. The numerical method is known as a well-validated robust numerical tool for the offshore industry to study complex free surface problems.

Earlier applications of the numerical method COMFLOW were in the simulation of sloshing on board of a spacecraft by Gerrits (2001), but also in medical science Loots (2003). Nowadays a major application can be found in the maritime industry to study hydrodynamic wave loading by Fekken et al. (1999), but also flow in anti-roll tanks [140].

One-phase model

The first version of COMFLOW is based on the single fluid Navier-Stokes equations that describe the flow for an incompressible viscous fluid. The equations are discretized on a fixed

structured Cartesian grid using the finite volume method just for the incompressible fluid. The air is treated as void space. The computational domain is given by the free surface, inflow and outflow boundaries. For displacing the free surface, the Volume-of-Fluid (VoF) method is used. This is based on the original VoF method developed by Hirt and Nichols (1981). Later, the VoF method is combined with a local height function. This resulted in a strictly mass conserving method according to Kleefsman et al. (2005). This is elaborated in chapter 5. This model is only capable to simulate the incompressible water of fig. 2.1 where the effect of air is neglected.

The equations described in eq. (2.21) are solved for the liquid. This means that only one continuity equation needs to be solved. Further, the fluid is assumed incompressible which results in a more simplified momentum equation as discussed in chapter 3. Also the transport equation is modified to make use of the donor-acceptor method.

Multiphase model

The incompressible single fluid model for wave impacts did not allow for a precise description of the dynamics of the pressure field induced by impact [149]. For higher accuracy, a two-phase model is developed by Wemmenhove (2008). By modeling this flow, the free surface is no longer the boundary of the calculation domain which results in a discontinuity at the free surface between two phases. The advantage of the two-phase model is the ability to simulate entrapped air pockets and the compressibility of air. Entrapped air has a cushioning effect by violent wave impacts but also can increase the impact peaks due to pressure oscillations [116]. In this model, the water phase is assumed incompressible, while the air phase is assumed compressible using an adiabatic equation of state. The liquid and gas phase is described as one aggregated fluid with varying properties. Problems with the boundary conditions at the free surface vanish by including the second phase. The shock effects were not included in the compressible flow model since he argued that local flow velocities hardly exceed the speed of sound.

When looking to the equations given in eq. (2.21), the two continuity equations are combined into an equation of conservation of mass for the "mixture". The multiphase model satisfies the conservation of liquid and the total mass. This means that the model is conservative in case of using the conservative governing equations. This is described in chapter 4.

2.6.2 Extension

Although the multiphase model is appropriate for the simulation of two-phase flows in the limit of separated-phases, it was not suitable for cases with a compressible dispersed flow [117]. The model is not able to predict the acoustic properties of an air-water mixture. Wave impact is a case where mixing of separated-phases happens. After impact, a presence of air can be found within the water. This can be represented by the multiphase model developed by Plumerault (2009).

To model the compressibility of an air-water mixture, a three fluid model is developed by Plumerault (2009). In the multiphase model, a second volume fraction is added that represents the presence of air dispersed in water. This gives an additional equation of state for the liquid. The method of Plumerault (2009) calculates the aeration level based on the pressure equilibria and no-slip conditions between the phases. The presented model in this report is different in that regard.

2.7 Conclusion

The influence of air in water during water impact and the pressure distribution over time for different kind of impacts were discussed based on documentation of the past. The effect of air on the impact was discussed in section 2.2 for an air pocket and section 2.3 for air entrainment. *It can be concluded that based on the earlier documentation about this subject, air entrainment needs to be modelled to prevent underprediction of the impact.*

Documentation of the past, described in section 2.2 and section 2.3, showed that air affects the impact:

- Cushioning effect on the initial impact. However, this effect decreases with the violence of the impact. Therefore, the aeration hardly affects on large scale the impact.
- The pressure rise time increases. This can lead to higher forces due entrapping air pockets. For aeration, the forces are still often decreasing.
- The air content does not affect the free surface dynamics before the impact.
- An increase of impulse and forces due oscillations. The frequencies of the domain as well as the air pocket can lead to resonance. These frequencies are affected by the aeration.
- Due to oscillations, sub-atmospheric pressures can be experienced.
- The rise time of the impulse decreases.
- The effect of air entrainment is the same as for an air pocket but to a lesser extent.

Many investigations proved already that the effect of aeration in sea water is significant and needs to be modelled for real scales. However, it is not yet implemented in a similar numerical model as COMFLOW and specifically used for green water events.

It is shown with eq. (2.5) that the compressibility of a mixture of air and water increases with a decreasing speed of sound. The compressibility of a mixture can be an order *higher* than of air. The relevance of aerated water by impact is confirmed by data of field measurements around the Shetland Islands in section 2.3.3, giving a atmospheric level of aeration up to 14.4%. The speed of sound can be in the order of the relative wave velocity, resulting in a Mach number higher than 0.3. This is discussed in section 2.5, where for this Mach number compressible effects can be expected.

In section 2.3.3, it is shown that for atmospheric conditions at model scale, an aeration level of 3.1% can be experienced. It is concluded in section 2.5.2 that aeration is a subject to scale effect, increasing the need for numerical methods for real scale simulations.

Besides the effect of air on the impact, in eq. (2.15) an analytical approximation of green water loading for an incompressible fluid is given. It is shown in section 2.4 that the dam break problem can be used as a simplification of a green water event.

The next step is to implement the basis of the CFD method COMFLOW, the one-phase model, which only models the incompressible water [78]. This model is needed to show what differences the assumptions of incompressibility can give in the results.

3 | One-phase VoF model

3.1 Introduction

To get a first-insight in modelling a water wave impact, in this chapter only the main component water, illustrated in fig. 2.1, is modelled. This corresponds with the first version of COMFLOW, discussed in section 2.6.1.

The first work on this numerical method has been carried out by Gerrits (2001), Fekken (2004), and Kleefsman et al. (2005). This method solves the governing equations given in eq. (2.21) for a single-phase: the liquid. The air phase is assumed as void and is not modelled. This means that the effect of entrapment of air pocket, illustrated in fig. 2.1, is neglected in this chapter. This leads to a reduction of the computational costs where only a part of the domain has to be solved. The core of the numerical method, which neglect moving bodies and apertures, is described in this chapter.

For the flow domain a fixed Cartesian grid is used where the variables are staggered. The boundaries are described as impenetrable. The equations are discretized in space using the finite volume method. To represent the free surface, the **VoF method** introduced by Hirt and Nichols (1981) is used. The free surface is represented by piecewise constant lines where the interface is parallel to one of the coordinate axes (**SLIC**), discussed in section 3.4.1. This is combined with the local height function to prevent detaching non-physical bubbles, called flotsam.

The method documented by Kleefsman et al. (2005) is explained and reproduced using MATLAB. The VoF method developed by Hirt and Nichols (1981) is explained in detail. Incomplete documentation how to **represent a jet along a wall** is clarified in section 3.4.1. The full report of the validation and verification results, developed by Kleefsman et al. (2005), can be read in Eijk van der (2018).

In section 3.2, the **Governing Equations** are given, assuming the fluid is incompressible and Newtonian. Hereafter, in section 3.3, the **Numerical Model** is elaborated. The governing equations are discretized and the boundary conditions for the domain are given. Furthermore, the solution method is discussed. After solving the system, the free surface can be displaced, **Free surface displacement** algorithm is discussed in section 3.4. This algorithm combined with the **Local height function** in section 3.4.2. The chapter ends with a **Conclusion** in section 3.5.

3.2 Governing Equations

To describe the flow of an incompressible Newtonian fluid in a given Cartesian domain, the conservation laws of physics are needed. These laws are the continuity equation and the Navier-Stokes equations, describing the conservation of mass and conservation of momentum,

respectively. The air is assumed as empty so the governing equations are solved for a single-phase flow. The equations are only solved in the liquid-filled part of the domain. It is assumed that the control volume (V_f) is time invariant. The continuity equation in a conservative form:

$$\oint_{\partial V_f} \mathbf{u} \cdot \mathbf{n}_f dS_f = 0, \quad (3.1)$$

where $\mathbf{u} = (u, v)^T$ are the velocity components in planar coordinates, ∂V_f the boundary of the control volume, and \mathbf{n}_f is the normal at the cell face S_f . Boldface symbols denote vectors. The momentum equation is:

$$\int_{V_f} \frac{\partial \mathbf{u}}{\partial t} dV_f + \oint_{\partial V_f} \mathbf{u} \mathbf{u}^T \cdot \mathbf{n}_f dS_f = -\frac{1}{\rho} \oint_{\partial V_f} p \mathbf{n} dS_f + \nu \oint_{\partial V_f} \nabla \mathbf{u} \cdot \mathbf{n}_f dS_f + \int_{V_f} \mathbf{F} dV_f, \quad (3.2)$$

where ρ is the water density and ν the kinematic viscosity. Both values are assumed constant which results in a simplification of the viscous term compared to eq. (2.21). Further, p is the pressure of the aggregated fluid, ∇ is the gradient operator, and $F = [g_x, g_y]$ the external body force. An example of an external body force is gravity. Temperature variations are neglected and energy is conserved [78]. Due to the incompressibility and constant viscosity, the energy equation is decoupled from the system and is not needed. Furthermore, as noted in section 2.6, for wave impacts there is no interest in thermodynamic properties.

The boundary conditions are needed to solve the governing equations. The boundaries can be separated into two kinds of area; the walls and the free surface. Without these conditions, the system cannot be solved.

In the context of the application, it can be assumed that the shear stress at the wall is not important due to the violence of the flow. An impact happens in a short time period where there is no time to develop the boundary layer. No mesh refinement is needed along the wall [64]. Therefore, a free-slip boundary condition is used at the four walls of the computational domain with $N \times M$ cells. The boundary layer scales with $\delta \sim \sqrt{vt}$ [81], which makes it valid to assume free-slip. This is achieved by using ghost cells where the velocity in the center of the face is equal to the ghost cell behind the wall. These cells can be described as cells behind the wall, which do not contribute directly to the flow in the domain but help with achieving the boundary conditions at the wall. This indicates that the walls cause no shear stress. More details about ghost cells can be found in other documentation [41, 118]. Further, no penetration conditions are applied to the walls, known as the Dirichlet boundary condition. For impenetrable walls, the initial velocity of the ghost cell orthogonal to the wall is equal to zero.

Also a boundary condition has to be applied at the wall for the pressure. The pressure gradient normal to the wall should be equal to zero. This means that the pressure in the ghost cell has to be defined as equal to the adjacent cell by doing a constant extrapolation.

The separation layer between the water and air is called the free surface. At the free surface the normal and tangential forces need to be balanced [41]:

$$\mu \left(\frac{\partial u_n}{\partial t} + \frac{\partial u_t}{\partial n} \right) = 0, \quad (3.3)$$

$$-p_{FS} + 2\mu \frac{\partial u_n}{\partial n} = -p_0 + \sigma \kappa, \quad (3.4)$$

where u_n and u_t are the normal and tangential component of the velocity, respectively. The displacement of the free surface can be described by the material derivative of s when the

position of the free surface is given by $s(\mathbf{x},t)=0$. This is also described in section 2.6, eq. (2.21). This results in the following transport equation on macroscopic level:

$$\frac{DF}{Dt} = \frac{\partial F}{\partial t} + (\mathbf{u} \cdot \nabla)F = 0. \quad (3.5)$$

3.3 Numerical Model

The governing equations are solved numerically on a domain which has a fixed Cartesian grid. The governing equations need to be solved for every cell containing water. The discretization is based on a staggered grid using the finite volume method. This means that the velocities are defined at the cell faces. Further, the pressure is defined at the cell center.

Cell labeling is needed to make a distinction between cells which are filled or empty. With the cell labeling, a sharp interface can be produced. The cells which are empty but can be filled by water are labeled E(mpty). The adjacent cells containing fluid are labeled S(urface). All the other cells are labeled as F(luid). This means that it is not possible that an F-cell is connected with an E-cell. Note that the F-cell is not necessarily completely filled. A velocity between an F and S-cell is called an FS-velocity [78]. The FS-, FF- and SS-velocities are determined by solving the momentum equation. Velocities between S- and an E-cell are found by constant extrapolation of the interior velocities, independent of the surface orientation. Sometimes an EE-velocity is needed to solve the convective and diffusive term, which is also done by doing constant extrapolation in the perpendicular direction of the free surface.

The [Continuity equation](#) is discretized in section 3.3.1. Hereafter, the [Navier-Stokes equation](#) is discretized in steps.

3.3.1 Continuity equation

The continuity equation is given in eq. (3.1). When this equation is satisfied, there is no mass loss in the domain. The discretization is done in two dimensions and over the squared cell itself, with parameters shown in fig. 3.1. The discretization of the continuity equation is given in eq. (3.6):

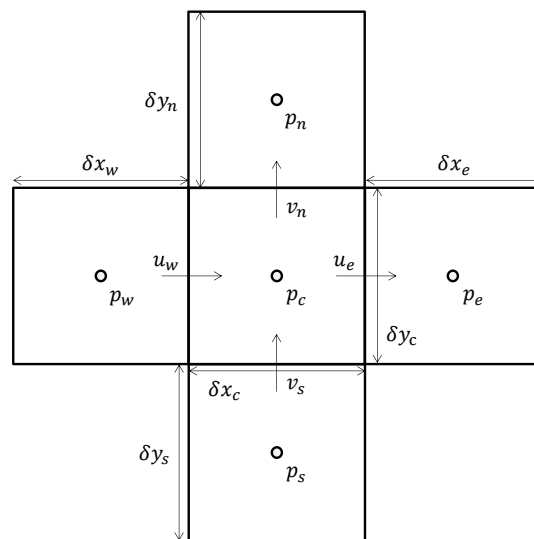


Figure 3.1: Discretization notation continuity equation.

$$(u_e - u_w)\delta y_c + (v_n - v_s)\delta x_c = 0. \quad (3.6)$$

Note that the dimensions are a property of the cell. This equation satisfies incompressibility of the fluid.

3.3.2 Navier-Stokes equation

The Navier-Stokes equation is discretized in the manner shown in fig. 3.2. This is done to solve the conservative momentum equation for Fluid cells and to get the fluxes needed for the free surface displacement. This figure only explains for the momentum discretization in the horizontal direction. The control volume surrounds a velocity that is defined at a cell face. The momentum equation in the horizontal direction is solved over the control volume illustrated by the dotted line. For the momentum equation in the horizontal direction, the horizontal neighboring cells are needed. The momentum discretization in the vertical direction, the upper and lower neighboring cells are needed. Note that the control volume is different for the continuity equation. The discretization for the momentum equation in the horizontal direction is explained in the following section for every term, in the order of eq. (3.2).

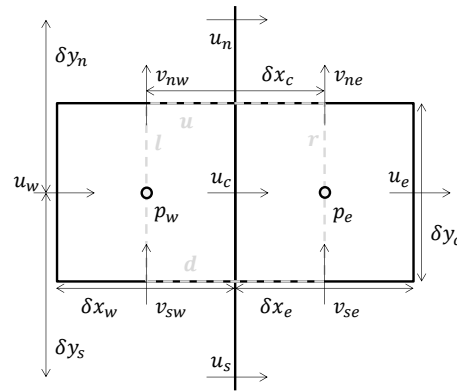


Figure 3.2: Discretization notation horizontal momentum.

Unsteady term

The volume integral of the time derivative is the first term shown in eq. (3.2). The midpoint rule is used to discretize the integral over space. This results for the discretization in the horizontal direction in:

$$\int_{V_f} \frac{\partial u}{\partial t} dV_f \approx \frac{\partial u_c}{\partial t} \delta x_c \delta y_c, \quad (3.7)$$

where u_c is the central velocity, δx_c is equal to $\frac{1}{2}(\delta x_w + \delta x_e)$ and y_c the height of the control volume. Note that for the momentum equation in vertical direction the δy_c is equal to $\frac{1}{2}(\delta y_n + \delta y_s)$ and x_c is equal to the width of the cell.

Convective term

The convective term is the second term shown in eq. (3.2). This is a closed boundary integral, like the continuity equation. The integral represents a scalar velocity ϕ , which is advected with the velocity vector \mathbf{u} . This has to be evaluated at all boundaries of the control volume. The

result of the integral can be seen as a mass flux multiplied by the scalar velocity. The convective term for the horizontal momentum:

$$\oint_{\partial V_f} u(\mathbf{u} \cdot \mathbf{n}_f) dS_f \approx \sum_{f=u,r,l,d} \phi_f m_f = m_r \frac{u_e + u_c}{2} + m_u \frac{u_n + u_c}{2} - m_l \frac{u_c + u_w}{2} - m_d \frac{u_c + u_s}{2}, \quad (3.8)$$

where m_r , m_l , m_u and m_d are the mass fluxes through the right, left, upper and lower boundary [78], and $\phi_f = u_f$ the horizontal momentum velocity. The mass fluxes are given by using the first-order upwind scheme [41]:

$$m_r = \begin{cases} u_e, & \text{if } m_r < 0 \\ u_c, & \text{if } m_r > 0 \end{cases}$$

$$m_l = \begin{cases} u_w, & \text{if } m_l > 0 \\ u_c, & \text{if } m_l < 0 \end{cases}$$

$$m_u = \begin{cases} u_n, & \text{if } m_u < 0 \\ u_c, & \text{if } m_u > 0 \end{cases}$$

$$m_d = \begin{cases} u_s, & \text{if } m_d > 0 \\ u_c, & \text{if } m_d < 0 \end{cases}$$

For the momentum equation in vertical direction the same scheme can be found where $\phi_f = v_f$. A wave impact happens in a small time interval and to capture the impact well, a dense mesh is needed. This makes it valid to use a first-order upwind scheme where the truncation error depends on the cell size. Further, a dense grid is needed to capture the impact. A dense grid decreases the truncation error.

Diffusive term

The diffusion term is the fourth term in eq. (3.2). The term can be written as a volume integral in horizontal direction:

$$\nu \int_{V_f} \nabla \cdot \nabla u dV_f, \quad (3.9)$$

where ν is assumed constant. Looking to eq. (2.21), the laplacian of the velocity vector can be derived using the incompressibility assumption ($\nabla \cdot \mathbf{u} = 0$) and the constant dynamic viscosity discussed in section 4.3.2:

$$\begin{aligned} \mu \nabla \cdot (\nabla \mathbf{u} + \nabla \mathbf{u}^T) &= \mu \nabla \cdot \nabla \mathbf{u} + \mu \nabla \cdot (\nabla \mathbf{u})^T \\ &= \mu \nabla \cdot \nabla \mathbf{u} + \mu \nabla (\nabla \cdot \mathbf{u}) \\ &= \mu \Delta \mathbf{u}. \end{aligned} \quad (3.10)$$

To discretize this volume integral, the midpoint rule is used. This is written for a two dimensional grid as the sum of the second order derivatives in horizontal and vertical direction of the velocity in horizontal direction [41, 78]. The inner derivative (first derivative) is applied on the cell faces r, l, u, d and the outer gradient is applied on the center of the volume.

$$\nu \int_{V_f} \nabla \cdot \nabla u dV_f \approx \nu \delta x_c \delta y_c \left(\frac{1}{\delta x_c} \left(\frac{u_e - u_c}{\delta x_e} - \frac{u_c - u_w}{\delta x_w} \right) + \frac{1}{\delta y_c} \left(\frac{u_n - u_c}{\delta y_n} - \frac{u_c - u_s}{\delta y_s} \right) \right). \quad (3.11)$$

For a non-uniform grid, this discretization is first order accurate. The diffusion term in convection-dominated simulations is not of importance [78]. For the momentum equation in vertical direction, all the horizontal velocities change into vertical velocities. Further, the dimensions of the control volume changes.

Pressure term

The pressure term is the third term in eq. (3.2). The discretization is done based on the notations given in fig. 3.2. The boundary integral in the x-momentum equation is discretized in the following manner:

$$\frac{1}{\rho} \oint_{\partial V_f} p n_x dS \approx \frac{1}{\rho_c} (p_e - p_w) \delta y_c, \quad (3.12)$$

where p_e and p_w are the center pressures of the eastern and western cell, respectively. These pressures are assumed constant everywhere in the cell. For the momentum equation in the vertical direction, the difference between the pressures of the northern and southern cell is taken, multiplied by the distance between those centers δx_c .

External body force

In this report, the external body force only consists of gravity. However, it is possible to let the gravity act $g = (g_x, g_y)^T = (0, -9.81)^T [ms^{-2}]$ in the horizontal and vertical direction. This can be helpful to find faults in the code of the numerical model and the free surface displacement. The external body force is represented by the last term in eq. (3.2). Using the Gauss' divergence theorem, the volume integral is written as a boundary integral. The discretization of this integral in horizontal direction is:

$$\int_{V_f} \nabla(g_x x_c) dV_f = \oint_{\partial V_f} (g_x x_c) \mathbf{n}_f dS_f \approx g_x \delta y_c \delta x_c. \quad (3.13)$$

Note that for the momentum equation in vertical direction, the size of the control volume changes and the gravity acting in vertical direction is needed (g_y).

3.3.3 Solution method

To solve the governing equations numerically, a discretization in time is needed. Further, the continuity equation and the momentum equation are correlated. They need to be solved in a way that both are conserved. To solve the equations, [Stability](#) is needed to ensure that the calculation converges to a solution.

Unsteady term

The discretizations of the equations in time and motion are explained. The conservation laws are discretized in time using the forward Euler method. A first-order method is used, because the overall accuracy is determined by the first-order accuracy of the free surface displacement algorithm [78]. The first-order forward Euler method has the following form:

$$\Phi^{n+1} = \Phi^n + \delta t f(\Phi^n), \quad (3.14)$$

where n indicates the time step and δt is the time step size. The forward Euler integration is compatible with the time integration method used in the evolution of the VoF-function [41].

Solution method

The used solution method is needed to conserve mass and momentum by doing an iteration step. To solve the conservative equations given in eq. (3.1) and eq. (3.2), the fractional step method is used [28, 63]. This pressure correction scheme, also called the projection method, is

a simple first-order algorithm which makes it popular. The solution method will not change for the model in the report. The equations to solve are, in differential form [41]:

$$\begin{aligned} \nabla \cdot \mathbf{u}^{n+1} &= 0, \\ \frac{\mathbf{u}^{n+1} - \mathbf{u}^n}{\delta t} + \frac{1}{\rho} \nabla p^{n+1} &= \mathbf{R}^n, \end{aligned} \quad (3.15)$$

where \mathbf{R} contains the convective term, diffusive term, and external body force:

$$\mathbf{R}^n = -(\mathbf{u}^n \cdot \nabla) \mathbf{u}^n + \nu \nabla \cdot \nabla \mathbf{u}^n - \nabla \mathbf{g}. \quad (3.16)$$

For the fractional step method an intermediate velocity $\tilde{\mathbf{u}}$ is calculated from the momentum equation whereby the pressure term is simply omitted. This leads to complete decoupling of the intermediate velocity field:

$$\tilde{\mathbf{u}}^n = \mathbf{u}^n + \delta t \mathbf{R}^n. \quad (3.17)$$

The next step is to solve the pressure of the next time step. This pressure can be calculated using the Poisson equation. This equation can be found by taking the divergence of the momentum equation. This leads to a divergence free velocity field and satisfies the continuity equation:

$$\nabla \cdot \nabla p^{n+1} = \frac{\rho_c}{\delta t} \nabla \cdot \tilde{\mathbf{u}}^n. \quad (3.18)$$

The discretization is given by Hirsch (2007), using the notation of fig. 3.1:

$$\frac{1}{\delta x_c} \left(\frac{p_e^{n+1} - p_c^{n+1}}{(\delta x_e + \delta x_c)/2} - \frac{p_c^{n+1} - p_w^{n+1}}{(\delta x_c + \delta x_w)/2} \right) + \frac{1}{\delta y_j} \left(\frac{p_n^{n+1} - p_c^{n+1}}{(\delta y_n + \delta y_c)/2} - \frac{p_c^{n+1} - p_s^{n+1}}{(\delta y_c + \delta y_s)/2} \right) = Q_c, \quad (3.19)$$

where:

$$Q_c = \frac{\rho_c}{\delta t} \left(\frac{\tilde{u}_e^n - \tilde{u}_w^n}{\delta x_c} + \frac{\tilde{v}_n^n - \tilde{v}_s^n}{\delta y_c} \right). \quad (3.20)$$

This equation can be written in the linear form $\overline{\overline{A}} \mathbf{p} = \mathbf{Q}$. The size of the square matrix $\overline{\overline{A}}$, containing the constant values, is $(N+2) \times (M+2)$. The increase in size of the matrix is caused by the ghost cells where also a pressure needs to be defined to prevent singularity. The matrix contains five diagonals for the inner domain. When the matrix does not contain any free surface boundary conditions, the sum of the rows of the matrix is equal to zero which should satisfy mass conservation. The diagonal solver for sparse matrices in MATLAB is used to solve the Poisson equation.

The new velocity in horizontal direction can be calculated with the following formula, using the notations of fig. 3.2:

$$\frac{u_c^{n+1} - \tilde{u}_c^n}{\delta t} \delta y_c \delta x_c = \frac{1}{\rho} (p_e^{n+1} - p_w^{n+1}) \delta y_c. \quad (3.21)$$

According to Chang et al. (2002), for the scheme now used a "splitting" error is made. The pressure is calculated in a different step than the new velocity. When both steps are calculated with the density at the old time level, this splitting error appears in the momentum equation and discrete continuity is satisfied exactly (no divergence error). In case of using an iterative solver, the convergence error can lead to mass creation/destruction.

Stability

Stability is needed to ensure that the code converges. Regarding explicit time integration and convection, the velocity should not travel in a single time step over the whole cell. This stability criterion is called the Courant Friedrich Lewy (CFL) condition [41]:

$$CFL = \frac{|\mathbf{u}|\delta t}{h} \leq 1, \quad (3.22)$$

where h is δx or δy depending on the component of the velocity vector. An additional stability criterion comes from the diffusive term in one spatial dimension. The diffusion per single time step should not be bigger than approximately one cell [64]:

$$\frac{2\nu\delta t (\delta x^2 + \delta y^2)}{V^2} \leq 1. \quad (3.23)$$

Note that these criteria indicate that when the cell size (V) decreases, the time step has to decrease. Typically, δt is chosen equal to one-fourth to one-third of the minimum cell transit time [64]. The pseudo code for the CFL-controller is given in appendix G.2.

3.4 Free surface displacement

After the governing equations are solved numerically, the free surface displacement can be calculated using the velocities of the new time step. The free surface displacement is needed to represent the wave impact and the movement of the water by the impact. For this, the VoF method in combination with the local height function is used.

First, the [Volume-of-Fluid method](#) is discussed in section 3.4.1, how to represent the interface and displace the fluid. Hereafter, the [Local height function](#) is discussed in section 3.4.2 to maintain a "sharp" free surface. Furthermore, for the [Free surface boundary conditions](#) need to be implemented and are discussed in section 3.4.3.

3.4.1 Volume-of-Fluid method

The VoF method is needed to represent the free surface in a sharp manner. Further, it is needed to predict the free surface displacement. Using a piecewise constant reconstruction of the [Interface](#) (SLIC), a fast computation of the free surface displacement and the [Advancing F in time](#) can be done. In combination with a local height function and a dense mesh, a sharp free surface can be represented which is strictly mass conserving. The combination with the local height function makes it more efficient and even as accurate as using the piecewise linear orientation of the interface [149]. The original VoF method developed by Hirt and Nichols (1981), is discussed first. After that, the local height function is discussed in section 3.4.2.

The F value in this report indicates the filling rate of water of a certain cell. The value of F should be between zero and one. A cell filled more than one is not possible when the fluid is assumed incompressible.

Interface

To determine the slope of the free surface in a cell, single valued functions H_y and H_x have to be determined. The surface can be represented as a single valued function. To approximate these functions [64] the following equations are evaluated. For the calculation, the notations in

fig. 3.1 are used:

$$H_{y,c} = F_s \delta y_s + F_c \delta y_c + F_n \delta y_n, \quad (3.24)$$

$$H_{x,c} = F_w \delta x_w + F_c \delta x_c + F_e \delta x_e, \quad (3.25)$$

where H can be seen as a local height function. The derivatives of these height functions need to be compared to find the interface orientation:

$$\frac{\partial H_{y,c}}{\partial x} = \frac{H_{y,e} - H_{y,w}}{\frac{1}{2} \delta x_e + \delta x_c + \frac{1}{2} \delta x_w}, \quad (3.26)$$

$$\frac{\partial H_{x,c}}{\partial y} = \frac{H_{x,n} - H_{x,s}}{\frac{1}{2} \delta y_n + \delta y_c + \frac{1}{2} \delta y_s}. \quad (3.27)$$

When the absolute value of eq. (3.26) is smaller than the absolute value of eq. (3.27), the surface orientation is horizontal. When eq. (3.27) is negative, the fluid lies below the surface:

$$\left| \frac{\partial H_{y,c}}{\partial x} \right| < \left| \frac{\partial H_{x,c}}{\partial y} \right| = \begin{cases} \frac{\partial H_{x,c}}{\partial y} < 0 & S \\ \frac{\partial H_{x,c}}{\partial y} > 0 & N \end{cases} \quad (3.28)$$

$$\left| \frac{\partial H_{y,c}}{\partial x} \right| > \left| \frac{\partial H_{x,c}}{\partial y} \right| = \begin{cases} \frac{\partial H_{y,c}}{\partial x} < 0 & E \\ \frac{\partial H_{y,c}}{\partial x} > 0 & W \end{cases} \quad (3.29)$$

The notations S(outh), N(orth), E(ast) and W(est) indicate the side which is filled with fluid.

Adjacent to the wall, it is difficult to calculate the surface orientation of a surface cell; ghost cells are needed. An example is shown in fig. 3.3 where the orientation of cell 9 is calculated and the ghost cells are involved. Using the method described in Hirt & Nichols (1981), H for the ghost cells should be zero. However, this implies that surface cell 9, shown in in fig. 3.3, would have a horizontal surface orientation. A more natural way would be that the free surface of cell 9 is vertical oriented and can be filled as shown in fig. 3.3 by the dotted line.

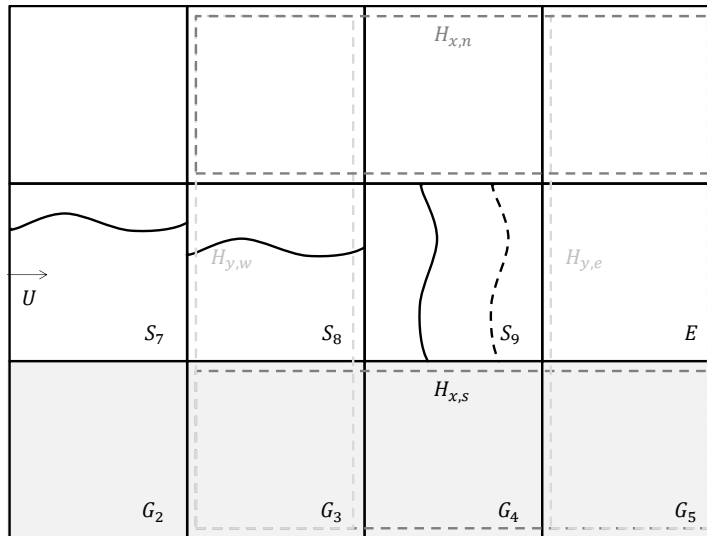


Figure 3.3: Interface orientation near the wall.

To achieve this, e.g. at the bottom wall, the ghost cells have to be filled at a filling rate bigger than zero. Assuming an uniform grid, this implies that:

$$\left| \frac{\partial H_{y,8}}{\partial x} \right| < \left| \frac{\partial H_{x,8}}{\partial y} \right| \quad \& \quad \frac{\partial H_{x,8}}{\partial y} < 0, \quad (3.30)$$

$$\left| \frac{(F_4 + F_9 - F_2 - F_7)\delta y}{2\delta x} \right| < \left| \frac{(-F_2 - F_3 - F_4)\delta x}{2\delta y} \right| \quad \& \quad \frac{(-F_2 - F_3 - F_4)\delta x}{2\delta y} < 0, \quad (3.31)$$

and:

$$\left| \frac{\partial H_{x,9}}{\partial y} \right| < \left| \frac{\partial H_{y,9}}{\partial x} \right| \quad \& \quad \frac{\partial H_{y,9}}{\partial x} < 0, \quad (3.32)$$

$$\left| \frac{(-F_3 - F_4 - F_5)\delta x}{2\delta y} \right| < \left| \frac{(F_5 - F_3 - F_8)\delta y}{2\delta x} \right| \quad \& \quad \frac{(F_5 - F_3 - F_8)\delta y}{2\delta x} < 0. \quad (3.33)$$

Assume that all filling rates are positive and the filling rates in the inner domain are not larger than one. To simplify the equation, F_4 is assumed as zero. This results in $-F_5 = F_3 > 3.001 \frac{\delta x}{\delta y}$.

Assuming that the remaining ghost cells adjacent to the F-cells have a filling rate of one, the surface orientation of other surface cells are not affected. This is also verified for the corners of the inner domain and vertical walls. This method is applied when the next inner-cell has been labeled as E(mpty), see fig. 3.3. Note that this method is for a grid where $\delta y \leq \delta x$.

Advancing F in time

After defining the interface and solving the governing equations, fraction F is advanced in time. To advect and conserve the incompressible fluid in time, the VoF function has to be used [41]:

$$\frac{\partial F}{\partial t} + \mathbf{u} \cdot \nabla F = 0, \quad (3.34)$$

which yields with the simplified equation for mass conservation of water:

$$\begin{aligned} \frac{\partial(F\rho_w)}{\partial t} + \nabla \cdot (\mathbf{u}\rho_w F) &= 0, \\ F \frac{D\rho_w}{Dt} + \rho_w \frac{DF}{Dt} + \rho_w F \nabla \cdot \mathbf{u} &= 0, \\ \frac{\partial F}{\partial t} + \mathbf{u} \nabla \cdot (F) &= 0. \end{aligned} \quad (3.35)$$

Note that the assumption of incompressibility is forcefully implemented in the transport equation; $\mathbf{u} \cdot \nabla F = \nabla \cdot (\mathbf{u}F)$. Using this relation, the staggered velocities can still be used. The differential equation can be discretized:

$$\begin{aligned} F_c^{n+1} &= F_c^n - \frac{u_e F_{i+\frac{1}{2},j} - u_w F_{i-\frac{1}{2},j}}{\delta x_c} - \frac{v_n F_{i,j+\frac{1}{2}} - v_s F_{i,j-\frac{1}{2}}}{\delta y_c}, \\ &= \frac{\delta F_e + \delta F_n - \delta F_w - \delta F_s}{\delta x_c \delta y_c}, \end{aligned} \quad (3.36)$$

where the notation of fig. 3.1 is used for the discretization. Here the flux δF_e in horizontal direction is calculated as:

$$\delta F_e = u_e^{n+1} F_{i+\frac{1}{2},j} \delta y_c dt. \quad (3.37)$$

This convection scheme can lead to smearing of the VoF function in partially filled cells. This is due to the interpolation. The free surface loses his definition [144].

To solve this problem, the donor-acceptor method of Hirt & Nichols (1981) is used, illustrated in fig. 3.4. This method makes use of downwind and upwind difference schemes. The meaning of $F_{i+\frac{1}{2},j}$ is decided by the donor-acceptor method F_{AD} .

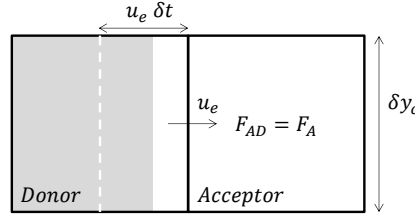


Figure 3.4: Donor-Acceptor method in horizontal direction for δF_e

The fluid field in the next time step can be found by:

$$F_c^{n+1} = F_c^n - \frac{1}{\delta x_c \delta y_c} \sum_{f=n,w,s,e} \delta F_f. \quad (3.38)$$

The expression for the amount fluid transported through a cell face in one time step is:

$$\delta F_f = \pm \delta S_f (\text{MIN} (F_{AD} |u_f \delta t| + AF, F_D \delta x_D)), \quad (3.39)$$

were S_f is the length of the cell face (δx , δy). The pm sign determines if the flux is out or into the cell. The MIN operator is needed to prevent that the donor cell can transport more than it contains. The additional fluid (AF) operator is to take the situation into account that the amount of void to be transported exceeds the amount the donor cell contains. The additional fluid is equal to:

$$AF = \text{MAX} ((1 - F_{AD}) |u_f \delta t| - (1 - F_D) \delta x_D, 0.0), \quad (3.40)$$

where x_D is the length of the donor/upwind cell parallel to the velocity u_f through the face. Further, F_A and F_D are the fractions of the area which is transported through the cell face of the acceptor cell and donor cell, respectively. Subscript A means that the cell is an acceptor/downwind cell. The cell which get fluid is the acceptor cell. The value of F_{AD} depends on the situation.

$$F_{AD} = \begin{cases} \textcircled{1} F_A \\ \textcircled{2} F_D \end{cases} \quad (3.41)$$

①: F_{AD} is equal to F_A when the cell upstream of the donor cell is empty or when the acceptor cell is empty, independent of the surface orientation. This indicates that the donor cell first must fill before a downwind empty cell can be filled. Further, when the free surface, defined in the donor cell, moves normal to itself, F_{AD} is also equal to F_A .

②: When cells are completely filled or empty, the donor cell approximation is used ($F_{AD} = F_D$). Further, when the fluid doesn't move normal to the interface, F_{AD} is equal to F_D .

The donor-acceptor method is applied on the whole inner domain. This includes the displacement of the fluid in cells which are labelled as E(mpty) or F(luid). Note that the free surface displacement is solved after calculating the new velocity. Further, note that the amount of fluid transported is always subtracted or added to the donor cell fluid, even when $F_{AD} = F_A$. All possible situations for the free surface displacement are illustrated in appendix D.1.

3.4.2 Local height function

The donor-acceptor method of Hirt and Nichols (1981) has two main drawbacks. It loses or gains mass due to rounding the VoF function to a value between one and zero. Further, the appearance of flotsam and jetsam (small droplets disconnecting from the surface).

To solve these drawbacks, the donor-acceptor method is combined with a local height function. These height functions depend on the orientation of the surface in a cell. When horizontally oriented, the height function is H_y , see eq. (3.24). By a vertical oriented surface, the height function is H_x , given in eq. (3.25). The local height function in combination with a piecewise constant reconstructed free surface has low computational costs. The free surface is still sharp in a coarse mesh and the numerical method is documented as strictly mass conserving.

To find the free surface displacement, the flux through every cell face still has to be calculated. However, instead of updating the cells separately, the height function has to be updated. After the height function is updated, the water is redistributed depending on its original surface orientation. Note that only cells labelled as an S-cell have a local height function. The other cells are updated individually. An example of a couple of local height functions are shown in fig. 3.5. Note that the adjacent ghost cells at the wall have to be filled completely. When the ghost cell is included in the height function, it remains completely filled ($F = 1$) after the update.

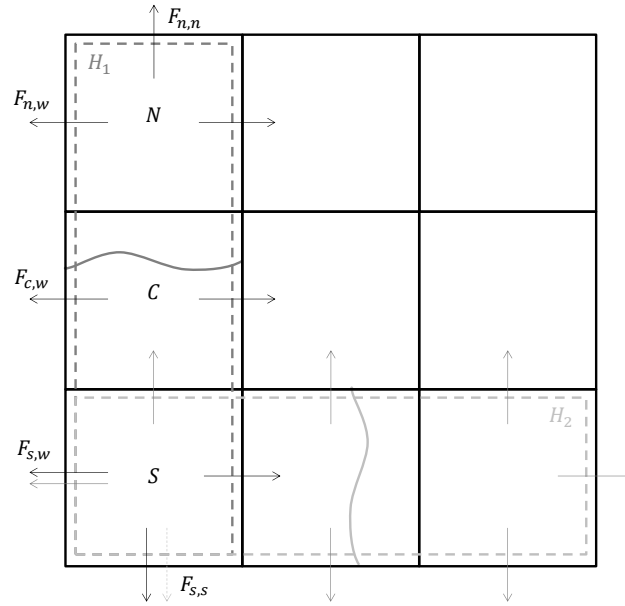


Figure 3.5: The local height function for updating the free surface.

To update the height function for S_8 in fig. 3.3:

$$H_1^{n+1} = H_1^n - \frac{\delta F_{n,e} + \delta F_{n,n} + \delta F_{n,w} + \delta F_{c,e} + \delta F_{c,w} + \delta F_{s,e} + \delta F_{s,s} + \delta F_{s,w}}{\delta x_c}, \quad (3.42)$$

where the fluxes δF are illustrated in fig. 3.5. The beneficial effect of the height function is shown in fig. 3.6. The local height function is strictly mass conserving and does not result in droplets for the standing gravity wave case.

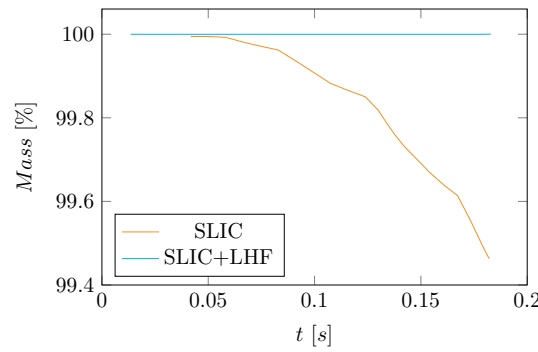


Figure 3.6: The effect of the local height function (LHF) on mass conservation (loss due to droplets) for a standing wave 64x64.

3.4.3 Free surface boundary conditions

For the free surface, still boundary conditions needs to be defined to solve the governing equations. The section 3.4.3 need to be defined for S-cells. Furthermore, the phenomenon [Surface tension](#) is introduced.

Pressure at free surface

To satisfy the continuity equation, the pressures and velocities have to be known in cells containing fluid. In cells containing a free surface, the pressure is specified at the free surface. To measure up to this pressure, linear extrapolation is done between the pressure defined at the surface (p_{FS}) and the pressure inside the fluid (p_F). The line connecting between the centers of p_S and p_F should be preferably such that it is closest to the normal of the free surface. Furthermore, the viscosity and therefore the shear stress are neglected [78]. It is assumed there is no-slip between the fluids resulting in one unique velocity. Solving the pressure in the S-cell is done with the equation:

$$\frac{p_S - p_F}{d_c} = \frac{p_{FS} - p_F}{d}, \quad (3.43)$$

$$p_S = \left(1 - \frac{d_c}{d}\right) p_F + \frac{d_c}{d} p_{FS},$$

where the pressure of the F(luid) cell have to be solved with the Poisson equation eq. (3.19). The fraction d_c/d , using the notation in fig. 3.1, is equal to:

$$\frac{d_c}{d} = \frac{\delta y_n + \delta y_c}{2F_n \delta y_n + \delta y_c}. \quad (3.44)$$

The defined pressure at the free surface p_{FS} is equal to eq. (3.4).

Surface tension

A discontinuous tension, called surface tension, between two fluids is obtained due to the cohesive forces between molecules down into a liquid. The surface becomes under tension due to the imbalanced forces caused by adhesion and cohesion. This tension makes it harder for an object to move through the interface. Surface tension makes it acquire the least surface area possible.

To implement surface tension σ , the curvature κ needs to be calculated in every surface cell.

To calculate the mean curvature, the local height function, based on the surface orientation, is used. The curvature for a horizontal oriented free surface can be calculated with the equation:

$$\kappa = \frac{1}{\delta x_c} \left(\frac{\partial H_{y,e}/\partial x}{\sqrt{1 + (\partial H_{y,e}/\partial x)^2}} - \frac{\partial H_{y,w}/\partial x}{\sqrt{1 + (\partial H_{y,w}/\partial x)^2}} \right), \quad (3.45)$$

where:

$$\frac{\partial H_{y,e}}{\partial x} = \frac{H_{y,e} - H_{y,c}}{\frac{1}{2}(\delta x_e + \delta x_c)} \quad \text{and} \quad \frac{\partial H_{y,w}}{\partial x} = \frac{H_{y,c} - H_{y,w}}{\frac{1}{2}(\delta x_w + \delta x_c)}. \quad (3.46)$$

The notations are illustrated in fig. 3.3. At the walls the curvature is assumed in this report as neutral. The height function of the ghost cell is equal to the adjacent height function of the surface cell.

3.5 Conclusion

In this chapter the core of the one-phase VoF model of Kleefsman et al. (2005) is reproduced. This model is verified and validated for the well-known dam break case and the standing gravity wave, described by Eijk van der (2018).

In this report, it is shown that the discretized governing equations used, are solved right and can be applied on the dam break case as well as on the standing wave case. A [convergence](#) of $\mathcal{O}(\delta x^{1.14})$ in space and $\mathcal{O}(\delta t^{0.97})$ in time is found for the 2D dam break problem using the L2-norm. This corresponds with the first-order fractional step method, upwinding or downwinding free surface displacement algorithm, and first-order upwind scheme in section 3.3. The first-order free surface displacement algorithm determines the overall accuracy.

Further, in appendix D.2, it is shown for a standing wave that using a local height function makes the model strictly mass conserving. In section 3.4.1, the implementation of the orientation of a wave front along a wall by using ghost cells is in detail explained.

The results of the [dam break problem](#) are compared with the experimental results of Lobovsky et al. (2014) [108]. The results of the 2D dam break case can be found in appendix E.1. A similar setup of the dam break case is illustrated in fig. 4.27. The magnitude of the impact pressure is overpredicted at the base of the wall and underpredicted at the middle of the wall.

Taking into account the presence of air leads to a cushioning effect on the pressure. The next step is to implement a two-phase model of Wemmenhove (2008) to take air entrapment into account. For violent wave impacts, this could increase the accuracy of predicting the impact pressure.

4 | Multiphase VoF model

4.1 Introduction

In the one-phase model, not every physical phenomenon is included. Therefore, a multiphase model is developed by Wemmenhove (2008) which corresponds with the second version of COMFLOW described in section 2.6.1. This multiphase model is capable of taking into account the effects of air entrapment and compressibility of air, like the air pocket in fig. 2.1. The entrapment of air pocket can lead to a more violent impact than modelled by the one-phase model [14, 23, 111]. This is discussed in section 2.2. The one-phase model can overpredict the initial impact pressure due to the cushioning effect, but can also underpredict the forces due to the air pocket oscillations.

The flow is still governed by the Navier-Stokes equations using the [aggregated fluid](#) approach. The model treats both phases as one mixture with varying properties and uses one continuity and one momentum equation instead of two. An aggregated fluid model generally leads to a continuous velocity field and a sharp interface between fluids. For the compressible air, an equation of state is introduced to close the system of equations [149]. Compared with the one-phase model of chapter 3, no extrapolation around the free surface of the pressure and velocity is needed anymore and the full domain is solved. The free surface reconstruction remains the same as for the one-phase fluid model (SLIC). The model is implemented in FORTRAN as well as MATLAB.

Besides describing the multiphase model developed by Wemmenhove (2008), the steps to implement the method are [reviewed and improved](#) when necessary. The model is tested for the gravity-consistent averaging method of Wemmenhove (2008) for SLIC to calculate the density at the cell faces in section 4.3.8. Further, the effect of the incompressibility assumption on the viscous term done by Wemmenhove (2008) is discussed in section 4.3.2.

The chapter starts with the [Governing equations](#) given in section 4.2, which are quite similar to the governing equations for the one-phase model. Hereafter, in section 4.3, the [Numerical model](#) is described and the system of equations are discretized. The Poisson equation is derived for the multiphase model. Besides the Poisson equation, additional corrections and interpolation for the Poisson equation are discussed.

In section 4.4, different models for the modelling of the [Surface tension](#) are discussed. This is completely different than the implementation of the surface tension for the one-phase fluid model. Hereafter, a verification and validation of the multiphase model is described by doing [Simulations](#) in section 4.5. Besides the verification of the method to model capillary forces, the free surface displacement algorithm and the representation of a oscillating air pocket is verified. The chapter wraps up in section 4.6 with a [Conclusion](#) about the improvements of the

original method and simulation results.

4.2 Governing equations

The mass conservation is again applied on an arbitrary volume V_f with boundary S_f . The equation to satisfy mass conservation is different than eq. (3.1) for the one-phase model. The unsteady term is not equal to zero anymore due to the compressibility of air:

$$\int_{V_f} \frac{\partial \rho}{\partial t} dV_f + \oint_{\partial V_f} (\rho \mathbf{u}) \cdot \mathbf{n} dS_f = 0, \quad (4.1)$$

where \mathbf{u} is the velocity vector and ρ the density of the aggregated fluid. Using Gauss' divergence theorem for the boundary integral, the mass conservation in conservative partial-differential form:

$$\frac{\partial \rho}{\partial t} + \nabla \cdot (\rho \mathbf{u}) = 0. \quad (4.2)$$

The momentum equation in integral form is also applied to an arbitrary volume V_f with boundary S_f :

$$\begin{aligned} \int_{V_f} \frac{\partial(\rho \mathbf{u})}{\partial t} dV_f + \oint_{\partial V_f} \rho \mathbf{u} (\mathbf{u} \cdot \mathbf{n}_f) dS_f + \oint_{\partial V_f} p \mathbf{n}_f dS_f \\ - \oint_{\partial V_f} (\mu (\nabla \mathbf{u} + \nabla \mathbf{u}^T) - \frac{2}{3} \mu \nabla \cdot \mathbf{u}) \mathbf{n}_f dS_f - \int_{V_f} \rho \mathbf{F} dV_f = 0, \end{aligned} \quad (4.3)$$

where p is the pressure, μ is the dynamic viscosity and \mathbf{F} body forces. Note that the dynamic viscosity is not anymore constant in the domain. Again by applying Gauss' theorem, the momentum equation in conservative partial-differential form:

$$\frac{\partial(\rho \mathbf{u})}{\partial t} + \nabla \cdot (\rho \mathbf{u} \mathbf{u}) + \nabla p - \nabla \cdot (\mu (\nabla \mathbf{u} + \nabla \mathbf{u}^T) - \frac{2}{3} \mu \nabla \cdot \mathbf{u}) - \rho \mathbf{F} = 0. \quad (4.4)$$

Compared with the one-phase model, the non-constant density cannot be taken outside the divergence terms.

For the free surface displacement, eq. (3.5) remains the same as for the one-phase model. The fluid dynamics are now calculated in all open cells, instead of only cells containing water, which makes the boundary conditions that are applied for the free surface of the one-phase flow in section 3.4.3 obsolete [149]. The boundary conditions at the wall for the closed domain remains the same as for the one-phase model. The walls remain impenetrable. Further, free-slip along the walls is assumed. The requirements for the conservative kinetic energy balance is described in Wemmenhove (2008).

Note that with eq. (4.2), in contrast to eq. (2.21) and the one-phase model, only the total mass is conserved and not the phases separately. However, due to the assumption of incompressible water and the use of a conservative transport equation, the water is conserved. This implies that when total mass is conserved and the water, the air also is conserved. This property is clarified in section 5.4.2. It is described by Kleefsman et al. (2005) that the local height function, as for the one-phase model, need to be applied for every Surface cell to prevent non-physical bubbles, and be strictly mass conserved when meeting the CFL-criteria.

4.3 Numerical model

Again, as described in section 3.3, a fixed Cartesian grid is used where the variables are staggered. Further, apertures are not taken into account. The same cell labeling as discussed in section 3.3, is used to make a distinction between cells which are filled or empty. However, for the multiphase model the governing equations are solved for every cell in the domain instead for only F-cells. The discretization of the continuity equation in time by using the forward Euler scheme:

$$\frac{\rho^{n+1} - \rho^n}{dt} + \mathbf{u}^n \cdot \nabla \rho^n + \rho^n \nabla \cdot \mathbf{u}^{n+1} = 0, \quad (4.5)$$

where the first two terms concern the compressibility of the mixture fluid. The last term contains the velocity at the next time step. This velocity is needed so that the momentum equation can be substituted into the continuity equation by taking the divergence. This is elaborated in section 4.3.3. The same was done for the one-phase model in section 3.3.3.

The multiphase model is only discretized in 2D and 1D. The same control volume is used as for the continuity equation of the one-phase model, illustrated in fig. 3.1. With first-order accuracy, the discretization is:

$$\delta x_c \delta y_c \left(\frac{\rho_c^{n+1} - \rho_c^n}{dt} + u_c^n \cdot (\nabla \rho)_c^n \right) + \rho_c^n \left(\delta y_c (u_e^{n+1} - u_w) + \delta x_c (v_n^{n+1} - v_s^{n+1}) \right) = 0, \quad (4.6)$$

where the density of the cell center is:

$$\rho_c = F_c \rho_l + (1 - F_c) \rho_{g,c}.$$

The term ρ_l represents the density of the liquid and $\rho_{g,c}$ the density of the gas in the corresponding cell. Note that when the cell is divergence free, the sum of the compressible terms is equal to zero.

For the conservative momentum equation, the same control volume as for the one-phase model is used for the discretization, given in fig. 3.2. When the momentum equation is conservative it can handle discontinuous velocity field caused by a shock wave due to density difference. The non-conservative momentum equation can model only continuous velocity field and the shock wave only as a compression wave. It introduces an artificial viscosity. However, it will reduce the computational costs significantly, as explained in section 4.3.1, and therefore the non-conservative form is solved during the simulations in this report. The conservative form is given by

$$\frac{1}{\rho^n} \frac{\rho^{n+1} \mathbf{u}^{n+1} - \rho^n \mathbf{u}^n}{dt} + \frac{1}{\rho^n} \nabla \cdot (\rho^n \mathbf{u}^n \mathbf{u}^n) + \frac{1}{\rho^n} \nabla p^{n+1} - \frac{1}{\rho^n} \nabla \cdot (\mu^n (\nabla \mathbf{u}^n + (\nabla \mathbf{u}^n)^T)) - \frac{2}{3} \mu^n \nabla \cdot \mathbf{u}^n - \mathbf{F}^n = 0, \quad (4.7)$$

while the non-conservative momentum equation is given by:

$$\frac{\mathbf{u}^{n+1} - \mathbf{u}^n}{dt} + \nabla \cdot (\mathbf{u}^n \mathbf{u}^{nT}) + \frac{1}{\rho^n} \nabla p^{n+1} - \frac{1}{\rho^n} \nabla \cdot (\mu^n (\nabla \mathbf{u}^n + (\nabla \mathbf{u}^n)^T)) - \frac{2}{3} \mu^n \nabla \cdot \mathbf{u}^n - \mathbf{F}^n = 0, \quad (4.8)$$

where the density is defined in the center of a cell. The density is presented in the continuity equation. In the following paragraphs every term is separately discussed and discretized using fig. 3.2. The unsteady term, the gravity term and the pressure term remain the same as for the one-phase model in section 3.3.2.

Using the control volume, illustrated in fig. 4.1, the scheme is:

$$\begin{aligned}
\text{conv}_x = & u_{ee} \left(-\frac{1}{4}m_{rr} + \frac{1}{4}|m|_{rr} \right) \\
& + u_e \left(\frac{1}{2}m_r + \frac{1}{4}m_{rr} + \frac{1}{4}m_{ci} - \frac{1}{2}|m|_r - \frac{1}{2}|m|_{rr} \right) \\
& + u_c \left(\frac{1}{2}m_r - \frac{1}{2}m_l + \frac{1}{4}|m|_{rr} + |m|_{ci} + \frac{1}{4}|m|_{ll} \right) \\
& + u_w \left(-\frac{1}{2}m_l - \frac{1}{4}m_{ll} - \frac{1}{4}m_{ci} - \frac{1}{2}|m|_l - \frac{1}{2}|m|_{ll} \right) \\
& + u_{ww} \left(\frac{1}{4}m_{ll} + \frac{1}{4}|m|_{ll} \right),
\end{aligned} \tag{4.11}$$

$$\begin{aligned}
\text{conv}_y = & u_{nn} \left(-\frac{1}{4}m_{uu} + \frac{1}{4}|m|_{uu} \right) \\
& + u_n \left(\frac{1}{2}m_u + \frac{1}{4}m_{uu} + \frac{1}{4}m_{cj} - \frac{1}{2}|m|_u - \frac{1}{2}|m|_{uu} \right) \\
& + u_c \left(\frac{1}{2}m_u - \frac{1}{2}m_d + \frac{1}{4}|m|_{uu} + |m|_{cj} + \frac{1}{4}|m|_{dd} \right) \\
& + u_s \left(-\frac{1}{2}m_l - \frac{1}{4}m_{ll} - \frac{1}{4}m_{cj} - \frac{1}{2}|m|_l - \frac{1}{2}|m|_{ll} \right) \\
& + u_{ss} \left(\frac{1}{4}m_{dd} + \frac{1}{4}|m|_{dd} \right).
\end{aligned} \tag{4.12}$$

The mass fluxes are given by:

$$\begin{aligned}
m_{ci} &= \rho_c u_c \delta y_c, \\
m_{cj} &= \frac{1}{2} \left(\frac{1}{2}(\rho_{nw} v_{nw} + \rho_{sw} v_{sw}) \delta x_w + \frac{1}{2}(\rho_{ne} v_{ne} + \rho_{se} v_{se}) \delta x_e \right), \\
m_r &= \frac{1}{2}(\rho_e u_e + \rho_c u_c) \delta y_c, \\
m_{rr} &= \rho_e u_e \delta y_c, \\
m_u &= \frac{1}{2}(\rho_{ne} v_{ne} \delta x_e + \rho_{nw} v_{nw} \delta x_w), \\
m_{uu} &= \frac{1}{2} \left(\frac{1}{2}(\rho_{ne} v_{ne} \delta x_e + \rho_{nw} v_{nw} \delta x_w) + \frac{1}{2}(\rho_{nne} v_{nne} \delta x_e + \rho_{nnw} v_{nnw} \delta x_w) \right)
\end{aligned}$$

The convective term for momentum in the horizontal direction is equal to:

$$\frac{1}{\rho} \oint_{\partial V_f} \mathbf{u}(\rho \mathbf{u} \cdot \mathbf{n}_f) dS_f = \frac{1}{\rho_c} (\text{conv}_x + \text{conv}_y). \tag{4.13}$$

It is important to note that *two* columns of neighbouring ghost cells are needed at the boundary of the domain. The extra column will have the same velocities as the neighbouring ghost cell.

Due to the fraction $\frac{1}{\rho_c}$, a density ratio can be found in the convection when the conservative momentum equation is solved. At the free surface between air and water, this ratio can be 1:1,000. For a fluid configuration shown in fig. 4.2, the density ratio ρ_r/ρ_c gives a multiplication of the convective term by a factor of 500 for water and air.

$$\frac{1}{\rho_c} m_r \phi_c = \frac{\rho_r}{\rho_c} \frac{u_c + u_w}{2} u_c \approx 500(u_r u_c). \tag{4.14}$$

This may lead to high flow velocities u^{n+1} around the free surface, which could lead to lower time steps due to the stability criteria given in section 3.3.3. This cannot only happen in the primary direction, but also in the secondary direction [149]. In case of solving the non-

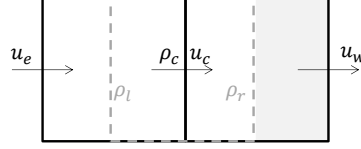


Figure 4.2: Effect of density ratio.

conservative momentum equation, the density ratio is omitted. This means that solving the non-conservative momentum equation, given in eq. (4.8), leads to lower computational costs.

4.3.2 Diffusive term

The volume integral of the diffusive term, the fourth term of eq. (4.3):

$$\frac{1}{\rho} \int_{V_f} \nabla \cdot \left(\mu \left(\nabla \mathbf{u} + \nabla \mathbf{u}^T \right) - \frac{2}{3} \mu \nabla \cdot \mathbf{u} \right) dV_f. \quad (4.15)$$

This volume integral can be solved in many ways [53, 63, 78, 118]. All methods assume, like is explained for eq. (2.21), that the divergence term of eq. (4.15) can be neglected. Two methods are compared for the 2D rising bubble case described in section 4.5.5.

The 2D rising bubble case is done for incompressible fluids. This indicates that $\nabla \cdot (\nabla \mathbf{u})^T = 0$. However, the dynamic viscosity is not constant around the free surface, resulting in $\nabla \cdot (\mu (\nabla \mathbf{u})^T) \neq 0$, using eq. (3.10).

Method 1

The first method neglects the term $(\nabla \mathbf{u})^T$ and is used by the original method of Wemmenhove (2008) and Plumerault (2009). For the 2D rising bubble case this results in an error around the free surface, illustrated in fig. 4.23.

To discretize eq. (4.15), the control volume shown in fig. 3.2 is used. When discretizing the equation, values of the viscosity at velocity locations u_n , u_e , u_s and u_w to compute $(\nabla \mathbf{u})^T$ are needed which is according to Wemmenhove (2008) outside the control volume. The values of viscosity can deviate significantly, especially near the free surface. The discretization is given by:

$$\begin{aligned} & \frac{1}{\rho_c} \int_{V_f} \nabla \cdot (\mu \nabla \mathbf{u}) dV_f \\ &= \frac{1}{\rho_c} \delta x_c \delta y_c \left(u_w \left(\frac{\mu_l}{\delta x_w \delta x_c} \right) + u_e \left(\frac{\mu_r}{\delta x_e \delta x_c} \right) + u_n \left(\frac{\mu_u}{\delta y_n \delta y_c} \right) + u_s \left(\frac{\mu_d}{\delta y_s \delta y_c} \right) \right. \\ & \quad \left. + u_c \left(-\frac{\mu_l}{\delta x_w \delta x_c} - \frac{\mu_r}{\delta x_e \delta x_c} - \frac{\mu_u}{\delta y_n \delta y_c} - \frac{\mu_d}{\delta y_s \delta y_c} \right) \right) \quad (4.16) \end{aligned}$$

The term is discretized for the momentum in horizontal direction. This can be done in a similar way for the momentum in vertical direction.

Method 2

The second method is described by Hirsch (2007) for a collocated grid. This method is transformed to a staggered grid to find the discretization for the control volume, illustrated in fig. 3.2. The difference compared with the first method is that the term $(\nabla \mathbf{u})^T$ is included in the discretization. The divergence term in eq. (4.15) is still neglected. This results in a term $\nabla \cdot (\mu(\nabla \mathbf{u} + \nabla \mathbf{u}^T))$ for the diffusive term. In matrix-form:

$$\nabla \cdot \left(\mu \begin{bmatrix} \frac{\partial u}{\partial x} & \frac{\partial u}{\partial y} \\ \frac{\partial v}{\partial x} & \frac{\partial v}{\partial y} \end{bmatrix} + \mu \begin{bmatrix} \frac{\partial u}{\partial x} & \frac{\partial v}{\partial x} \\ \frac{\partial u}{\partial y} & \frac{\partial v}{\partial y} \end{bmatrix} \right). \quad (4.17)$$

The eq. (4.17) can be simplified to the following matrix:

$$\begin{bmatrix} \frac{\partial}{\partial x} \left(\boxed{2} \mu \frac{\partial u}{\partial x} \right) + \frac{\partial}{\partial y} \left(\mu \frac{\partial u}{\partial y} + \boxed{\mu \frac{\partial v}{\partial x}} \right) \\ \frac{\partial}{\partial x} \left(\mu \frac{\partial v}{\partial x} + \boxed{\mu \frac{\partial u}{\partial y}} \right) + \frac{\partial}{\partial y} \left(\boxed{2} \mu \frac{\partial v}{\partial y} \right) \end{bmatrix} = \begin{bmatrix} \frac{\partial}{\partial x} \tau_{xx} + \frac{\partial}{\partial y} \tau_{xy} \\ \frac{\partial}{\partial x} \tau_{yx} + \frac{\partial}{\partial y} \tau_{yy} \end{bmatrix}, \quad (4.18)$$

The boxed terms are added compared with the first method. The equation can be discretized for the momentum in horizontal direction:

$$\begin{aligned} \frac{1}{\rho} \int_{V_f} \nabla \cdot (\mu(\nabla \mathbf{u} + \nabla \mathbf{u}^T)) dV_f &= \frac{1}{\rho_c} \delta x_c \delta y_c \left(\frac{\tau_{xx,i+\frac{1}{2},j} - \tau_{xx,i-\frac{1}{2},j}}{\delta x_c} + \frac{\tau_{xy,i,j+\frac{1}{2}} - \tau_{xy,i,j-\frac{1}{2}}}{\delta y_c} \right) \\ &= \frac{1}{\rho_c} \delta x_c \delta y_c \left(2u_w \left(\frac{\mu_l}{\delta x_w \delta x_c} \right) + 2u_e \left(\frac{\mu_r}{\delta x_e \delta x_c} \right) + u_n \left(\frac{\mu_u}{\delta y_n \delta y_c} \right) + u_s \left(\frac{\mu_d}{\delta y_s \delta y_c} \right) \right. \\ &\quad \left. + u_c \left(-2 \frac{\mu_l}{\delta x_w \delta x_c} - 2 \frac{\mu_r}{\delta x_e \delta x_c} - \frac{\mu_u}{\delta y_n \delta y_c} - \frac{\mu_d}{\delta y_s \delta y_c} \right) \right. \\ &\quad \left. + \frac{1}{\delta x_c \delta y_c} (\mu_u (v_{ne} - v_{nw}) + \mu_d (v_{sw} - v_{se})) \right), \quad (4.19) \end{aligned}$$

where the last term, containing the vertical velocities, rises from the derivative $\left(\frac{\partial v}{\partial x} \right)_{i,j \pm \frac{1}{2}}$.

The dynamic viscosities at the top (μ_u) and bottom (μ_d) of the momentum cell are found by linear interpolation between the corner point viscosity values μ_{nw} , μ_{ne} , μ_{sw} and μ_{se} . These corner point values are found by doing an interpolation between the adjacent pressure points where the dynamic viscosities are found by harmonic averaging. For example, for the dynamic viscosity at the top boundary of the momentum cell $(i+1, j+\frac{1}{2})$ [118]:

$$\mu_{i+1,j+\frac{1}{2}} = \frac{\mu_{i+1,j+1} \mu_{i+1,j} (\delta y_{j+1} + \delta y_j)}{\delta y_j \mu_{i+1,j+1} + \delta y_{j+1} \mu_{i+1,j}}. \quad (4.20)$$

For computing the local average viscosity in cell center $(i+1, j)$:

$$\mu_{i+1,j} = (1 - F_{i+1,j}) \mu_g + F_{i+1,j} \mu_l, \quad (4.21)$$

where μ_l is the dynamic viscosity of the liquid (water) and μ_g the dynamic viscosity of the gas (air).

For the diffusive term, *method 2* is used in the following simulations based on the results in fig. 4.23. The pressure term, the third term in eq. (4.3), is discretized in the same way is in

eq. (3.12) for the one-phase model. The gravity body force is also discretized in the same way as in eq. (3.13). However, compared with the one-phase model, for the multiphase model the surface tension is also described as a force acting on a volume. The vector \mathbf{F} consists of the gravity and capillary forces; $\mathbf{F} = \mathbf{F}_g + \frac{1}{\rho}\mathbf{F}_\sigma$ where $\mathbf{F}_\sigma = -\sigma\kappa\mathbf{n}\delta_\Gamma - (\nabla\sigma)\delta_\Gamma$. The δ_Γ is a delta function concentrated on the surface interface Γ . The discretization of the capillary body force is elaborated in section 4.4.

When convection and diffusion are absent and the surface tension is neglected, the pressure gradient ($\frac{1}{\rho}\nabla p$) should match the gravity vector \mathbf{g} . When this is not fulfilled, spurious velocities occur around the free surface. Further, the pressure term has to be discretized in the same way as the gravity term [53]. Both requirements impose a restriction on the cell edge density ρ_c [149]. This will be highlighted in section 4.3.8.

4.3.3 Solution method

For solving the governing equations, a solution method is needed. This should be done in a way that mass and momentum are conserved. The conservation of energy is not solved in this model, because the thermodynamic properties of the fluid is not where we are interested in.

For the one-phase model, a forward Euler time discretization is used, illustrated in eq. (3.14). However, combining the forward Euler time discretization with the second-order upwind scheme leads to stability problems.

It is proven by Wemmenhove (2008), for a convection diffusion equation where the diffusive number is assumed small, the CFL-number restriction for a forward Euler scheme combined with a second-order upwind scheme is lower than for the second-order upwind scheme combined with the second-order Adams-Bashforth time discretization. The limit of the CFL-number is given in table 4.1 for all four combinations. Here d is the diffusive number which is equal to $\frac{2kdt}{(\delta x)^2}$, where k is the diffusion coefficient. To decrease the amount of artificial vis-

	1st order upwind	2nd order upwind
Forward Euler	$1 - d \approx 1$	$\sqrt{d} \ll 1$
Adams Bashforth	$\frac{1}{2} - d \approx \frac{1}{2}$	$\frac{1}{4} - \frac{1}{2}d \approx \frac{1}{4}$

Table 4.1: Limit on CFL number by convection diffusion equation [149].

cosity and maintain numerical stability, the second-order upwind scheme combined with the Adams-Bashforth time discretization is used. The Adams-Bashforth scheme is illustrated:

$$\phi^{n+1} = \phi^n + dtf \left(\frac{3}{2}\phi^n - \frac{1}{2}\phi^{n-1} \right). \quad (4.22)$$

This scheme is used for the convective and diffusive term of the momentum equation. When using the Adams-Bashforth scheme for the discretized non-conservative momentum equation:

$$\begin{aligned} \mathbf{u}^{n+1} + dt \frac{1}{\rho^n} \nabla p^{n+1} = \mathbf{u}^n + dt \mathbf{F}^n - \frac{3}{2} dt \\ \left(\frac{1}{\rho^n} \nabla \cdot (\rho^n \mathbf{u}^n \mathbf{u}^n) - \frac{1}{\rho^n} \nabla \cdot (\mu^n \nabla \mathbf{u}^n) \right) + \frac{1}{2} dt \\ \left(\frac{1}{\rho^{n-1}} \nabla \cdot (\rho^{n-1} \mathbf{u}^{n-1} \mathbf{u}^{n-1}) - \frac{1}{\rho^{n-1}} \nabla \cdot (\mu^{n-1} \nabla \mathbf{u}^{n-1}) \right), \quad (4.23) \end{aligned}$$

and using the forward Euler scheme for the discretized continuity equation:

$$\rho^{n+1} + dt\rho^n \nabla \cdot \mathbf{u}^{n+1} = \rho^n - dt\mathbf{u}^n \cdot \nabla \rho^n, \quad (4.24)$$

where n and $n + 1$ indicates the previous time level and the next time level, respectively. Because the pressure is calculated for the next time step, it can be placed at the left hand side of the equation. This can be simplified using the intermediate velocity step $\tilde{\mathbf{u}}$ as done in eq. (3.17) for the one-phase model:

$$\begin{aligned} \tilde{\mathbf{u}} = \mathbf{u}^n + dt\mathbf{F}^n + \frac{3}{2}dt \left(-\frac{1}{\rho^n} \nabla \cdot (\rho^n \mathbf{u}^n \mathbf{u}^n) + \frac{1}{\rho^n} \nabla \cdot (\mu^n \nabla \mathbf{u}^n) \right) \\ - \frac{1}{2}dt \left(-\frac{1}{\rho^{n-1}} \nabla \cdot (\rho^{n-1} \mathbf{u}^{n-1} \mathbf{u}^{n-1}) + \frac{1}{\rho^{n-1}} \nabla \cdot (\mu^{n-1} \nabla \mathbf{u}^{n-1}) \right) \end{aligned} \quad (4.25)$$

The fractional step method used for the one-phase model, is also used for the multiphase model. The reason that the second-order Adams-Bashforth is used, is to increase the stability for the second-order upwind scheme. The accuracy in time remains first-order due to using the fractional step method of Chorin (1968). It's proven by Rannacher (1991) that, due to the enforced Neumann boundary condition on the pressure, the scheme is not fully first-order and the error irreducible. This means that the application of the first-order forward Euler scheme has the same accuracy in time as the application of the second-order Adams-Bashforth scheme.

For solving the pressure in the next time step, the same method is used as for the one-phase model in eq. (3.19). By taking the divergence of the conservative momentum equation, eq. (4.7), and substituting this in the continuity equation for the velocity of the new time step, eq. (4.24), the pressure can be solved:

$$dt \nabla \cdot \left(\frac{1}{\rho^n} \nabla p^{n+1} \right) = \frac{1}{\rho^n} \frac{\rho^{n+1} - \rho^n}{dt} + \frac{\mathbf{u}^n}{\rho^n} \cdot \nabla \rho^n - \nabla \cdot \left(\frac{\mathbf{u}^n}{\rho^n} (\rho^{n+1} - \rho^n) \right) + \nabla \cdot \tilde{\mathbf{u}}^n. \quad (4.26)$$

Comparing this with the one-phase flow in eq. (3.19), the terms $\frac{1}{\rho^n} \frac{\rho^{n+1} - \rho^n}{dt}$ and $\frac{\mathbf{u}^n}{\rho^n} \cdot \nabla \rho^n$ come from the continuity equation and the term $\nabla \cdot \left(\frac{\mathbf{u}^n}{\rho^n} (\rho^{n+1} - \rho^n) \right)$ comes from the conservative momentum equation. The last term contains density values inside the divergence operator as the discretization is kept conservative [149]. In this report, the non-conservative momentum equation is solved which simplifies eq. (4.26) by taking out the *stroked term*.

This equation is solved in the same way as for the Poisson equation of the one-phase model, eq. (3.19). The diagonal solver for sparse matrices in MATLAB is used to solve this linear system.

When the pressure is found, the new velocity can be calculated with the following equation:

$$\mathbf{u}^{n+1} = \tilde{\mathbf{u}} - \frac{1}{\rho^n} \left(\mathbf{u}^n \rho^{n+1} - \mathbf{u}^n \rho^n \right) - dt \frac{1}{\rho^n} \nabla p^{n+1}. \quad (4.27)$$

To solve eq. (4.26) explicitly, the right hand side has to consist only of terms on time level n . This means that the density on the next time level has to be transferred to the left hand side of the equation. This is done with an equation of state by assuming a barotropic relation and is discussed in the following section 4.3.4.

The free surface displacement remains the same as for the one-phase model. The local height function combined with the donor-acceptor method is used in this model as discussed in section 3.4.2.

In case of solving the non-conservative momentum equation, section 4.3.5 can be skipped. Note that this method is developed by Wemmenhove (2008). However, not every aspect described by Wemmenhove (2008) is used in the model, like a density correction for the gas density. The full discretization of the multiphase model, using the conservative momentum equation and forward Euler time stepping scheme, is given in appendix F.

4.3.4 Reduction of unsteady density term

The Poisson equation, given in eq. (4.26), needs to be rewritten in a form that it can be solved. The equation still consists of two unknowns at the next time level ($n + 1$).

The water is assumed as incompressible while the air is assumed as compressible. This means that the unsteady and density gradient terms can be reduced. These terms together represent the Lagrangian material derivative of the density, which should be equal to zero for an incompressible flow. This results in the following Poisson equation:

$$dt \nabla \cdot \left(\frac{1}{\rho^n} \nabla p^{n+1} \right) = (1 - F^n) \frac{1}{\rho^n} \left(\frac{\rho_a^{n+1} - \rho_a^n}{dt} + \mathbf{u}^n \cdot \nabla \rho_a^n \right) - \nabla \cdot \left(\frac{\mathbf{u}^n}{\rho^n} (\rho^{n+1} - \rho^n) \right) + \nabla \cdot \tilde{\mathbf{u}}^n. \quad (4.28)$$

To find the air density of the next time level, an equation of state is used. Assuming the flow as barotropic; $\rho_a = f(p)$, the polytropic equation of state is used. The advantage compared to the sound propagation equation of state, the input of the equation of state are no gradients of the pressure and density [149]. The polytropic equation:

$$p^{n+1} = p_0 \left(\frac{\rho_a^{n+1}}{\rho_{a,0}} \right)^\gamma, \quad (4.29)$$

where γ is the adiabatic ratio of specific heats, which is equal to 1.4 for pure air. As reference pressure (p_0) and density ($\rho_{a,0}$), the atmospheric values are used. When the pressure and density of the previous time step (p^n and ρ_a^n) are used as reference values, this leads to 'drift' in the pressure in time due to small errors in the iteration when solving the conservative momentum equation [149].

For the unsteady density term a linearization is done, using the Newton approximation. This is done to eliminate the exponent $\frac{1}{\gamma}$ stemming from the polytropic equation:

$$f(x_1) = f(x_0) + (x_1 - x_0) f'(x_0). \quad (4.30)$$

The denser the grid resolution, the more accurate the approximation. Note that for modelling a wave impact, a dense mesh is needed to represent the free surface accurately. For the approximation, the equation of state is needed for the derivative. This leads to the following approximation [149]:

$$\begin{aligned} \rho_a^{n+1} &= \frac{\rho_{a,0}}{p_0^{\frac{1}{\gamma}}} (p^*)^{\frac{1}{\gamma}} + (p^{n+1} - p^*) \frac{\rho_{a,0}}{p_0^{\frac{1}{\gamma}}} \frac{1}{\gamma} (p^*)^{\frac{1}{\gamma}-1} \\ &= \rho_a^* + (p^{n+1} - p^*) \frac{\rho_a^*}{\gamma p^*}, \end{aligned} \quad (4.31)$$

where p^* is the recent pressure value found from the previous pressure iteration. This is equal to the pressure of the previous time step. Further, the term ρ_a^* is the density calculated using the pressure of the previous iteration p^* . The pressure term of the new time level needs to be transported to the left hand side of the Poisson equation. This to calculate the pressure implicitly. The unsteady density term becomes:

$$(1 - F^n) \frac{1}{\rho^n} \frac{\rho_a^{n+1} - \rho_a^n}{dt} = (1 - F^n) \frac{1}{\rho^n} \frac{1}{dt} \left(\frac{\rho_a^*}{\gamma p^*} (p^{n+1} - p^*) - \rho_a^n \right). \quad (4.32)$$

The density gradient term in the Poisson equation consists of known values so no modification is required. The Poisson equation is solved in the control volume fig. 3.1. The velocity is needed in the cell center. This velocity is found by using the central averaging method.

4.3.5 Reduction of convective density term

The convective density term, the third term in eq. (4.26), contains also a density term of the next time level. However, in this term there is no time step in the denominator. For the pressure iteration this term is estimated with the pressure of the previous iteration. Further, for the fraction, the previous time step is used.

$$\begin{aligned} \nabla \cdot \left(\frac{\mathbf{u}^n}{\rho^n} (\rho^{n+1} - \rho^n) \right) &= \nabla \cdot \left(\frac{\mathbf{u}^n}{\rho^n} (1 - F^n) \left(\frac{\rho_{a,0}}{p_a t m^{\frac{1}{\gamma}}} (p^*)^{\frac{1}{\gamma}} - \rho_a^n \right) \right) \\ &= \nabla \cdot \left(\frac{\mathbf{u}^n}{\rho^n} (1 - F^n) (\rho_a^* - \rho_a^n) \right). \end{aligned} \quad (4.33)$$

When the new pressure is calculated, also new densities are needed in the iteration. This means that, in case of solving the conservative momentum equation, an iteration is needed to find the new pressure level.

4.3.6 Negative pressures

When the pressure becomes negative, this will result in an imaginary density due to the equation of state in eq. (4.29). These negative pressure can be caused by pocket oscillations, partially and fully filled cells with gas. To treat negative pressures, the gas density needs to be limited by modifying the equation of state. This does not lead to undesirable modifications of the Poisson matrix [149]. The gas density is calculated after the new pressure.

$$\rho_a^* = \begin{cases} \rho_{a,0} \left(\frac{p^*}{p_0} \right)^{\frac{1}{\gamma}}, & \text{if } p^* \geq p_0 \\ \rho_{a,0} \left(1 + \frac{2}{\pi} \arctan \left(\frac{\pi}{2} \frac{p^* - p_0}{p_0} \right) \right)^{\frac{1}{\gamma}}, & \text{if } p^* < p_0 \end{cases} \quad (4.34)$$

4.3.7 Gas pressure in surface cell

To calculate the air density in a cell, the pressure is needed in that particular cell to solve the equation of state. However, in Surface cells the gas pressure might be different than the pressure of the cell center.

When the air pressure is assumed equal to the pressure of the cell center, this might lead to an overestimation of the pressure due to the extra pressure caused by the hydrostatic effect of the liquid layer. This leads to an overestimation of the gas density and so underestimated gas

densities elsewhere in the domain due to mass conservation [149].

To correct this effect, an interpolation method is needed, which is only used in cells where the gravitational force has a component perpendicular to the free surface. When the filling ratio (F) is smaller than 0.5, the interpolation is not necessary and the air pressure is assumed equal to the pressure of the cell center. This calculation is part of the iteration to calculate the new pressure. The interpolation method is dependent on the pressure and the air density. First, the

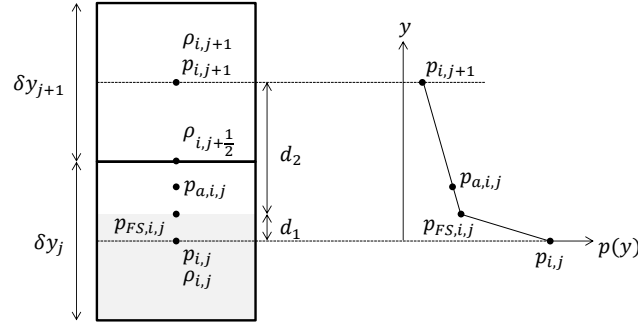


Figure 4.3: Interpolation of pressure

pressure at the free surface need to be found for fig. 4.3:

$$p_{FS,i,j} = \frac{(\delta y_j + \frac{1}{2}\delta y_{j+1} - F_{i,j}\delta y)\rho_{a,i,j}p_{i,j} + (F_{i,j}\delta y - \frac{1}{2}\delta y)\rho_w p_{i,j+1}}{(\delta y_j + \frac{1}{2}\delta y_{j+1} - F_{i,j}\delta y)\rho_{a,i,j} + (F_{i,j}\delta y - \frac{1}{2}\delta y)\rho_w} \quad (4.35)$$

The pressure of the air can be found by doing the following interpolation:

$$p_{a,i,j} = \frac{(\frac{1}{2}\delta y_j - \frac{1}{2}F_{i,j}\delta y_j)p_{i,j+1} + (\frac{1}{2}\delta y_{j+1} + \frac{1}{2}\delta y_j - \frac{1}{2}F_{i,j}\delta y_j)p_{FS,i,j}}{\frac{1}{2}\delta y_{j+1} + \delta y_j - F_{i,j}\delta y_j} \quad (4.36)$$

This is similar for the other free surface normal directions. This pressure can be used for p^* in the equation of state in eq. (4.34). This interpolation method is not used at the boundaries of the domain.

4.3.8 Density at cell edge

The density at the cell edge is needed for two terms; the diffusive term and the pressure gradient term. However, there are multiple ways to calculate these densities. The calculation of densities at the cell edges can lead to serious errors, leading to spurious velocities [149]. This is caused by the imbalance of the pressure gradient and the body force. Therefore two methods are discussed; the **Cell-weighted** averaging method and the **Gravity-consistent** averaging method.

Cell-weighted

The cell-weighted averaging method is the most obvious method used for calculating the density at the cell edge. This method makes use of the data of two complete cells, while the gravity-consistent averaging method will make use of only just two half cells. In horizontal direction, the density at the cell edge is found by simple averaging between the density of the neighbouring cells:

$$\rho_{i,j+\frac{1}{2}} = \frac{\delta y_j \rho_{i,j} + \delta y_{j+1} \rho_{i,j+1}}{\delta y_j + \delta y_{j+1}}. \quad (4.37)$$

Note that with this method no information is needed of the orientation of the free surface. While this is an easy method to implement, it is shown by several numerical methods that this method leads to spurious velocities around the free surface [51, 59, 124, 151].

Gravity-consistent

The gravity-consistent averaging method is developed by Wemmenhove (2008). Assuming that the momentum equation only consists of the pressure gradient and the body force (hydrostatic case), these should be in equilibrium. This means that both terms need to be discretized in the same way. The equation $\nabla \times (\rho \mathbf{F}) = 0$ can be found from the momentum equation, knowing that the curl of a gradient is zero for the pressure term. To fulfill this requirement, the density around the free surface needs to be interpolated in the following way, called the gravity-consistent averaging method, using the notation of fig. 4.3. With the gravity-consistent averaging method, non-physical spurious velocities at the free surface should be prevented [149]. However, it is not clear if it also is applicable for a piecewise constant line representation of the free surface.

In case of a surface cell with an adjacent empty cell, also called an SE-edge. According to the gravity-consistent averaging method, the density need to be calculated in the following way:

$$\rho_{i,j\pm\frac{1}{2}} = \frac{d_1 \rho_{w,i,j(-1)} + d_2 \rho_{a,i,j(+1)}}{d_1 + d_2}, \quad (4.38)$$

where the \pm , (-1) and $(+1)$ depends on the filling ratio:

$$d_1 = \begin{cases} F_{i,j} \delta y_j - \frac{1}{2} \delta y_j, & \text{if } F_{i,j} > 0.5 \\ \frac{1}{2} \delta y_{j-1} + F_{i,j} \delta y_j, & \text{if } F_{i,j} < 0.5 \end{cases}$$

$$d_2 = \begin{cases} \frac{1}{2} \delta y_{j+1} + \delta y_j - F_{i,j} \delta y_j, & \text{if } F_{i,j} > 0.5 \\ \frac{1}{2} \delta y_j - F_{i,j} \delta y_j, & \text{if } F_{i,j} < 0.5 \end{cases}$$

In case of FS- and SE-cells, using the case illustrated in fig. 4.3 where $F_{i,j} > 0.5$:

$$\rho_{i,j-\frac{1}{2}} = \frac{\delta y_j \rho_{w,i,j} + \delta y_{j-1} \rho_{i,j-1}}{\delta y_j + \delta y_{j-1}}, \quad (4.39)$$

where the density is calculated at a FS-edge. In a similar way, the density for an SE-edge can be calculated when $F_{i,j} < 0.5$.

Note that the interpolation is done between the air and water density of that particular cell and not the total averaged density. The same can be done for north, east and west filled cells.

For fluids cells and empty cells with no adjacent surface cell, called EE-edges or FF-edges, the cell-weighted averaging method in eq. (4.37) is used. These edges are assumed as a homogeneous mixture because the orientation of the phase is not defined. An F-cell does not have to be completely filled.

Comparison of methods

The two interpolation methods can give only different results at the free surface. Where the gravity-consistent averaging method is dependent on the orientation of the free surface, the cell-weighted averaging method is not. This lead into an increase of effort for the gravity-consistent method to calculate the density at the cell edge. However, it should lead to non-spurious velocities at the free surface. In this subsection, the method is compared with the

	Gravity-Consistent	Cell-Weighted
$(\rho g_y \cdot n)_1$	-10,000	-7,500
$(\rho g_x \cdot n)_2$	-10	-2,500
$(\rho g_y \cdot n)_3$	10	2,500
$(\rho g_x \cdot n)_4$	5,000	7,500

Table 4.2: Cell-edge densities multiplied by the gravity and the direction of the dashed line for fig. 4.4.

cell-weighted averaging method to see if it is applicable for SLIC.

When two free surfaces are represented in the momentum cell, the distance between air and water can be used for the interpolation, like in eq. (4.38). Note that for example for a surface cell which is horizontally oriented, and an adjacent surface cell which is vertically oriented, two parts of water can exist. The interface is represented by a constant line so the normal vector is in line with the coordinate axis.

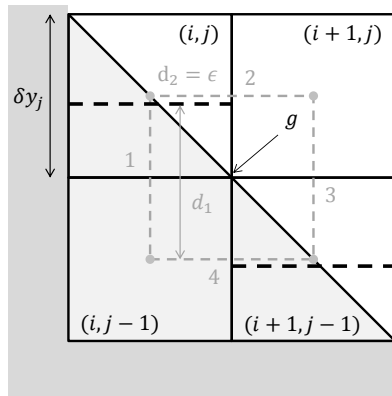


Figure 4.4: Gravity consistent averaging method for SLIC.

When the $\oint \nabla p$ is equal to zero, the case is gravity consistent [149]. Using the momentum equation, this is equal to the sum of ρg of all densities at the cell edges. In case of a gravity vector of $g = [-10, -10]^T [m/s^2]$ and the set up of fig. 4.4, interpolation makes this case not gravity consistent for the gravity-consistent averaging method. The value ρF for every cell face density of the dashed line in fig. 4.4 is given in table 4.2. When using the high-order method, piecewise linear interface construction (PLIC), the method is gravity consistent. When using the cell-weighted averaging method for the density combined with SLIC, it is gravity consistent in case of fig. 4.4.

Besides using SLIC, it is mentioned in chapter 3 that the surface cell adjacent to the wall has an orientation perpendicular to the wall. In that case, both methods are gravity consistent.

When looking to a situation containing at least 3×3 cells, a similar situation as fig. 4.4 is found. In cases where the height difference between the two Surface cells is bigger than $\frac{\delta y}{2}$ and both surface cells have a fraction level of higher (or lower) than 0.5, the gravity-consistent method is not gravity consistent. This means that for cases with steep slopes of water, the gravity-consistent method does not work with SLIC. Further, the method is orientation-dependent which can give a destabilizing density gradient for a steep free surface. An example is the

standing gravity wave discussed in section 4.5.2. With the gravity-consistent averaging method an increase in wave amplitude, relative to the initial amplitude, was found for non-breaking waves. This corresponds with an energy increase due to the spurious velocities at the free surface.

This is also proven for the case illustrated in fig. 4.5 where the Surface cells are filled with $F = 0.5$. The domainsize is $1[m] \times 1[m]$ and the gridsize 30×30 . The effect of density inter-

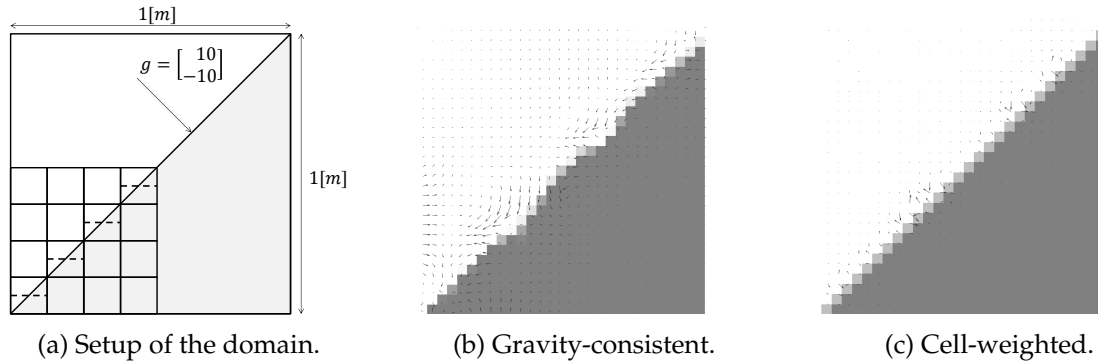


Figure 4.5: Gravity-consistent averaging (max. $0.4[m/s]$) versus Cell-weighted averaging (max. $1e^{-9}[m/s]$)

polation on the results is significant. *The choice is made to use cell-weighted averaging method which seems more gravity consistent for SLIC and reduces the computational costs. However, note that the spurious velocities remain visible. It can be seen that the velocities for the cell-weighted averaging method, after 3[s], are up to 10^8 less high than for the explained gravity-consistent averaging method. The maximum velocity reached using the gravity-consistent averaging method is $0.4[m/s]$, while when using the cell-weighted averaging method the maximum speed is $1e^{-9}[m/s]$. For an higher-order interface tracking method than SLIC, the gravity-consistent averaging method will perform better.*

Adding obstacle

For the dam break simulation in chapter 6, an obstacle in the domain is placed, representing a superstructure on deck which is hit by green water. This obstacle is used to measure impact pressures and forces.

Adding the obstacle to the domain, this block does not have apertures. This means that the cells are not cutted by the obstacle. The walls of the block will have the same pressure as the neighbouring cells in the internal fluid domain to have a zero pressure gradient over the wall. The pressure at the corners of the obstacle is equal to the average pressure of the neighboring cells in the flow domain. The internal velocities are assumed equal to zero. Further, along the walls free-slip boundary condition is applied.

4.4 Surface tension

How to take into account the capillary forces is not document in the report of Wemmenhove (2008). The surface tension is the pressure jump across the surface, as explained in section 4.4. It is described for the one-phase model in section 3.4.3 [78]. Therefore, in this section this model is tested for the multiphase model [25] and compared with a developed Continuum

Surface Force (CSF) model.

A CSF-model describes the surface tension as a body force [11]. This is also done by the CFD-method for ANSYS FLUENT. It is shown that this kind of model lead to less spurious velocities for the modelling of the capillary forces in multiphase flows [1] than the model used for the one-phase model where the pressure is extrapolated by using the boundary condition described in eq. (3.4). At the end of the section a new developed CSF-model for SLIC is implemented. The curvature (κ) is calculated in the same way as in eq. (3.45) for the one-phase model. This calculated made use of the local height function.

4.4.1 Interpolation of the pressure

The pressure on the free surface can be calculated in the same way as for the one-phase model. The boundary condition on the free surface is given in eq. (3.4). The pressure in the bubble compared with the one-phase model is not equal to the atmospheric pressure p_0 . By omitting the shear term (no-slip condition) and substituting for p_0 an internal pressure in the domain, the boundary condition of the free surface can be found for the multiphase model [25]. In case of fig. 4.6, this is:

$$p_{FS} = p_{i,j} - \sigma\kappa, \quad (4.40)$$

where κ is the curvature calculated with eq. (3.45). To implement this boundary condition, an interpolation is needed, as for the one-phase model. Using trigonometry, the following equation can be used in case of fig. 4.6 where the water volume fraction $F_{i,j} < 0.5$:

$$\begin{aligned} \frac{p_{i,j} - p_{i,j-1}}{d} &= \frac{p_{FS} - p_{i,j-1}}{dc}, \\ \frac{p_{i,j} - p_{i,j-1}}{d} &= \frac{p_{i,j} - \sigma\kappa - p_{i,j-1}}{dc}, \\ \left(1 - \frac{dc}{d}\right) p_{i,j} - \left(1 - \frac{dc}{d}\right) p_{i,j-1} &= -\frac{dc}{d} \sigma\kappa. \end{aligned} \quad (4.41)$$

Substituting for the pressure in cell (i, j) , the derivative of the pressure in the positive vertical direction for cell $(i, j - 1)$:

$$\nabla_{i,j-\frac{1}{2}} p = \frac{p_{i,j} - \sigma\kappa - p_{i,j-1}}{d}, \quad (4.42)$$

where d is equal to $d = \frac{1}{2}\delta y_{j-1} + F_{i,j}\delta y_j$. By redefining the derivative of the pressure described by Chan and Street (1970), the surface tension can be modelled. Note that for $F_{i,j} > 0.5$, the boundary condition for the free surface changes to $p_{FS} = p_{i,j} + \sigma\kappa$.

When looking to the situation illustrated in fig. 4.6, the derivative $\nabla_{j-\frac{1}{2}} p$ of cell (i,j) has to be changed as well as the derivative $\nabla_{j+\frac{1}{2}} p$ of cell $(i,j-1)$. However, when $F_{i,j} > 0.5$, the derivative $\nabla_{j-\frac{1}{2}} p$ of cell $(i,j+1)$ and the derivative $\nabla_{j+\frac{1}{2}} p$ of cell (i,j) have to be changed.

4.4.2 CSF-model

The other method is based on the method of Brackbill et al. (1992), which is a continuum method where the surface tension is prescribed as a volume force employing the divergence theorem. This body force term, also noted at the end of section 4.3.2, is added to the momentum equation in eq. (4.8). The same is true for the normal vector:

$$\mathbf{F}_\sigma = \frac{1}{\rho} \sigma \left(-\nabla \cdot \frac{\nabla F}{|\nabla F|} \right) \nabla F. \quad (4.43)$$

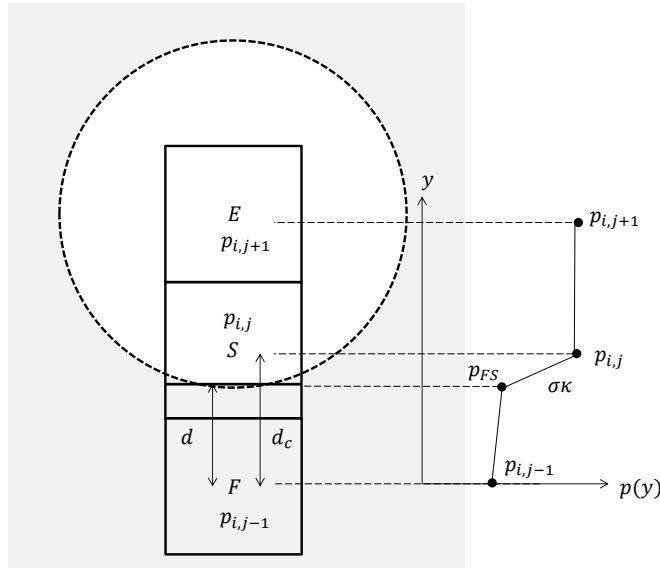


Figure 4.6: Surface tension in case of a bubble

This equation can be simplified to:

$$\mathbf{F}_\sigma = -\frac{1}{\rho} \sigma \kappa \nabla F. \quad (4.44)$$

The control volume is based on the staggered variables as illustrated in fig. 3.2. The body force term is added to the intermediate velocity \tilde{u} of the Poisson equation in eq. (4.26).

The discretization of eq. (4.44) is based on the position of the interface. When there is an interface in the control volume, this will affect the velocity vector \mathbf{u} in both directions. This means that the orientation of the free surface is not important for the discretization. The discretization in horizontal direction:

$$\int_V \mathbf{F}_\sigma^n dV = -\frac{1}{\rho_{i+\frac{1}{2},j}^n} \sigma \kappa^n (F_{i+1,j}^n - F_{i,j}^n) \delta y_j. \quad (4.45)$$

Note that for the density $\rho_{i+\frac{1}{2},j}^n$, the density in the center of the control volume is meant. According to Tang et al. (2004), the CSF-model needs to be coupled with an accurate transport scheme giving a sharp interface to decrease the intensity of the spurious velocities, like the second-order scheme PLIC. The method to estimate the normal vector often dictates overall accuracy and performance of the CSF-model. The CSF-model is known to induce spurious velocities near the interface. This can cause no exact representation of the momentum jump condition at the interface; the pressure and the viscous stress forces do not balance the capillary force. In case of a static or translating problem, the curl of the momentum equation where the pressure is balanced by the capillary forces, should satisfy [1]:

$$\nabla \kappa \times \nabla F = 0. \quad (4.46)$$

Results of Abadie et al. (2015) show that the heightfunction curvate calculation is in particular interesting for the case of near-static bubbles or oscillating bubbles. There is no exact balance found between capillary forces and pressure but the spurious currents are lower when the curvature is calculated in eq. (3.45) instead of using no height function. In that case, the leading error is caused by the advection term and not the accuracy of the curvature.

In this model the first-order SLIC is used which means that the model is robust in predicting the position of the interface, the curvature and the normal vector. This means that the spurious

currents can be bigger than in case of using PLIC.

Comparing the methods for the surface tension, only with the last method it is succeeded to make from an initial planar rod a bubble, see section 4.5.3. The first method could not maintain the the interface of the rod due to spurious velocities and is orientation dependent, like the gravity-consistent averaging method. Therefore, *the CSF-model is used in this report.*

4.4.3 Implementation of CSF-model

The implementation of the CSF-model needs some special attention. The delta function δ_Γ is equal to $|\nabla F|$ and the surface tension coefficient is assumed constant [83]. The resulting capillary force is $\mathbf{F}_\sigma = -\sigma\kappa\nabla F$. Further, the control volume consist of two half cells where both cells can have a surface orientation with a certain curvature. Here $\kappa_{i,j}$ is the curvature in the center of the cell (i,j) .

In the model used by Baraldi et al. [7], based on the approach of Brackbill et al. [11], the following equation is used for the momentum in horizontal direction

$$x \cdot \left(\int_V \frac{1}{\rho^n} \mathbf{F}_\sigma^n dV \right) = -\frac{1}{\rho_{i+\frac{1}{2},j}^n} \sigma \left(\frac{\kappa_{i+1,j}^n + \kappa_{i,j}^n}{2} \right) (F_{i+1,j}^n - F_{i,j}^n) \delta y_j. \quad (4.47)$$

In this model they make use of an PLIC-orientation. When using the SLIC-orientation, in some cases the curvature κ is underestimated. This is illustrated in fig. 4.7. In the left upper corner cell, there is no free surface which results into a curvature of zero defined in that cell center. The orientation of the capillary force \mathbf{F}_σ is described in eq. (3.45). Further, the grey area indi-

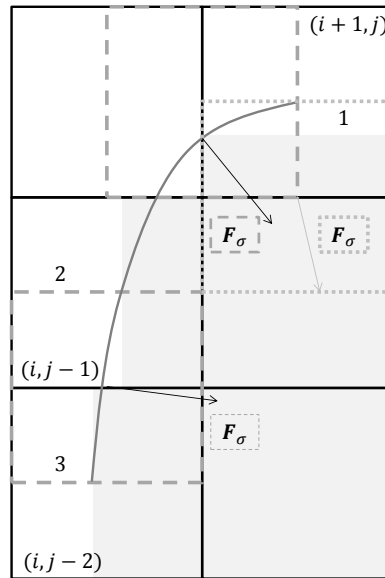


Figure 4.7: The choice of κ for the CSF-model.

cates the fluid. The full line could be the representation of the free surface in reality. In case of the horizontal dashed control volume, using eq. (4.47) to estimate the curvature, leads to an underestimation. The curvature would be two times smaller than the curvature of cell 1.

Instead of using this averaging method, two adjacent columns of three cellheight are used,

similar to the height function. This results in a curvature for cell 1:

$$\kappa_{i+\frac{1}{2},j}^n = \frac{\kappa_{i+1,j}^n + \kappa_{i,j-1}^n}{2}, \quad (4.48)$$

where $\kappa_{i,j-1}$ is the curvature of cell 2. In case of no adjacent cell where the curvature is defined, the curvature $\kappa_{i+\frac{1}{2},j}$ will be equal to $\kappa_{i+1,j}$ like used by Hernández et al. (2008). This is similar to upwinding or downwinding the curvature.

For the dotted vertical control volume by cell 1, the curvature is also underestimated using eq. (4.47). The capillary force is smeared out over two control volumes while just one control volume contains the interface.

To prevent smearing out, for this case the value of $\kappa_{i+1,j-\frac{1}{2}} = \kappa_{i+1,j}$ where the interface is in the control volume. The capillary force of eq. (4.47) applied on the dotted control volume in vertical direction is equal to:

$$y \cdot \int_V \mathbf{F}_\sigma^n dV = -\sigma \kappa_{i+1,j} \frac{F_{s,i+1,j}^n - F_{s,i+1,j-1}^n}{\frac{1}{2}(\delta y_j + \delta y_{j-1})}. \quad (4.49)$$

For the curvature between cell 2 and 3, the averaging method in Eq. (4.47) is used.

The results of the model used by Baraldi et al. (2014) are compared with the presented model in fig. 4.19. The wave amplitude converges for both methods by increasing the grid resolution. However, the method Baraldi et al. (2014) gives a phase delay relative to the analytical solution.

4.5 Simulations

After implementing the multiphase model in COMFLOW, the model needs to be verified to show that it converges to the true solution. This is part of the quantification of total uncertainty and establishing the numerical accuracy of a simulation for model validation purposes. It needs to be shown that the equations are solved right and the global error decreases [42]. This will be done by doing simulations of a couple of cases; 1D water piston, standing gravity wave, 2D oscillating rod, standing capillary wave, rising bubble, and the dam break case. Every case is needed to demonstrate the capabilities of the model.

With the [1D water piston](#) in section 4.5.1, the model is tested if it can model the compressibility of air. This case can show if the model can handle oscillations of an entrapped air pocket during violent free surface events. Hereafter, the simulation results of the standing wave is discussed. Standing wave simulations can be used to assess the performance of the numerical model for free surface waves. Besides the [Standing gravity wave](#) in section 4.5.2, also the [Standing capillary wave](#) is simulated in section 4.5.4. With this case, the convergence of the new developed CSF-model, discussed in section 4.4, can be shown. In section 4.5.3, the [2D oscillating planar rod](#) is also part of the verification of the CSF-model used. The results for this case shows that the surface tension of entrapped air pockets can be well modelled. The [2D rising bubble](#) in section 4.5.5 shows, besides the convective, gravity, and capillary term, also the diffusive term is well modelled for an air pocket. At the end, with the [Dam break case](#) in section 4.5.6, the propagation of the water is tested as well as the impact pressure. The 2D numerical results are compared with the 3D experimental results of MARIN. With this case, it can be shown that the model is able to simulate a violent free surface event.

4.5.1 1D water piston

For the 1D water piston the set up is shown in fig. 4.8. This set up is also used by Wemmenhove (2008). The water is initially at rest. This case corresponds with an entrapped air pocket due to a wave impact which starts to oscillate. The diffusive effects and surface tension forces are neglected. The gravity vector points downwards which results in an accelerating

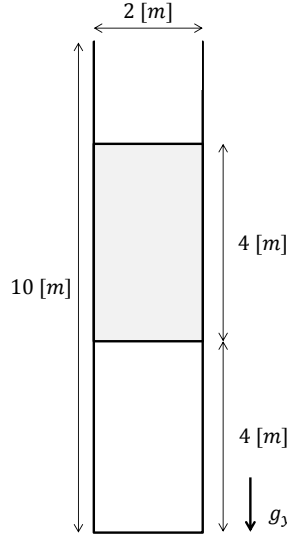


Figure 4.8: Falling water mass in 1D

water mass. When this happens, a volume of air is entrapped. The top of the flow domain is open and the atmospheric pressure is prescribed. The input parameters are: $\rho_w=1,000[kg/m^3]$, $\rho_a=1[kg/m^3]$, $\gamma=1$ and $g=10[m/s^2]$. A fixed time step of 0.01[s], 0.005[s] and 0.0025[s] is used.

This case is done for the incompressible two-phase flow as well as for the compressible two-phase flow. According to Wemmenhove (2008), for the incompressible two-phase flow the air phase is incompressible which results in no movement of the water piston. A steady state should be found due to pressure equilibrium.

For the compressible two-phase flow, an oscillatory motion of the water mass compressing the air should be observed. On the long term, the air phase will be equal to the hydrostatic pressure at the bottom of the water mass and the water piston will be at rest. The oscillation amplitude decreases due to loss of energy by physical and artificial viscosity of the air [149]. The pressure distribution at steady state for the incompressible two-phase isentropic flow is shown in fig. 4.9a.

The same pressure is found at the bottom of the flow domain as by Wemmenhove (2008). The pressure distribution is equal to ρgh . The gradient of the pressure in fig. 4.9a is determined by the density. The pressure at the bottom should be equal to $(10 - 8)\rho_a g + (8 - 4)\rho_w g + (4 - 0)\rho_a g = 40,060[Pa]$. In case of the compressible two-phase flow, using the relation for an isotropic flow ($\gamma=1$) of an ideal gas, the final position of the water mass can be found:

$$\begin{aligned}
 p_0 V_{a,0}^\gamma &= p_1 V_{a,1}^\gamma \\
 V_{a,0} &= \frac{100}{140} 4 \approx 2.86[m].
 \end{aligned}
 \tag{4.50}$$

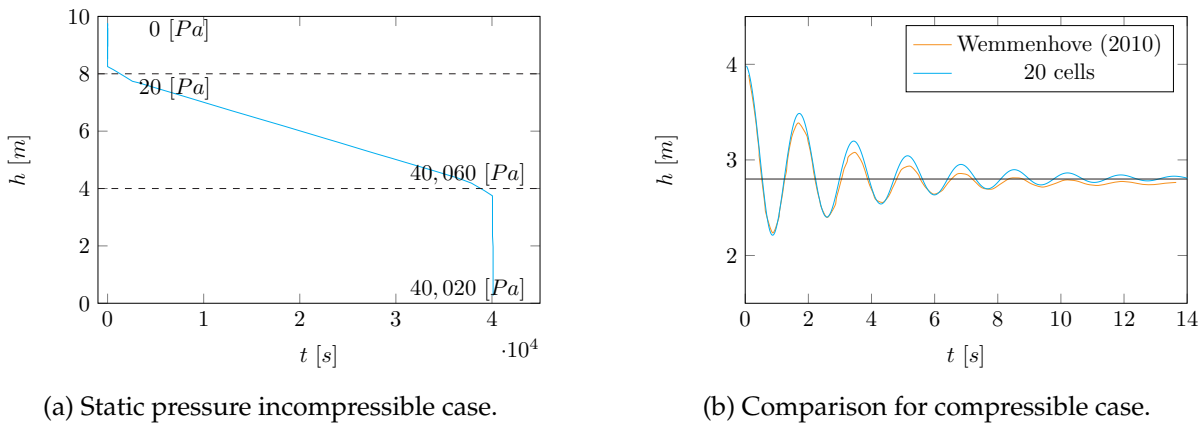


Figure 4.9: Results of incompressible and compressible air for the 1D water piston.

Looking to the oscillation of the water piston in fig. 4.9b, the steady position is indeed $\approx 2.86[m]$.

By increasing the amount of elements, a more accurate steady position is found due to the decrease of the artificial viscosity. This is illustrated in fig. 4.10a. For the small grid resolutions, the artificial viscosity is still dominant [149]. Comparing the results with Wemmenhove (2008), less damping is found. This can be caused by the difference in the upwind scheme. In the test of Wemmenhove (2008), a first-order upwind scheme is used instead of a second-order upwind scheme.

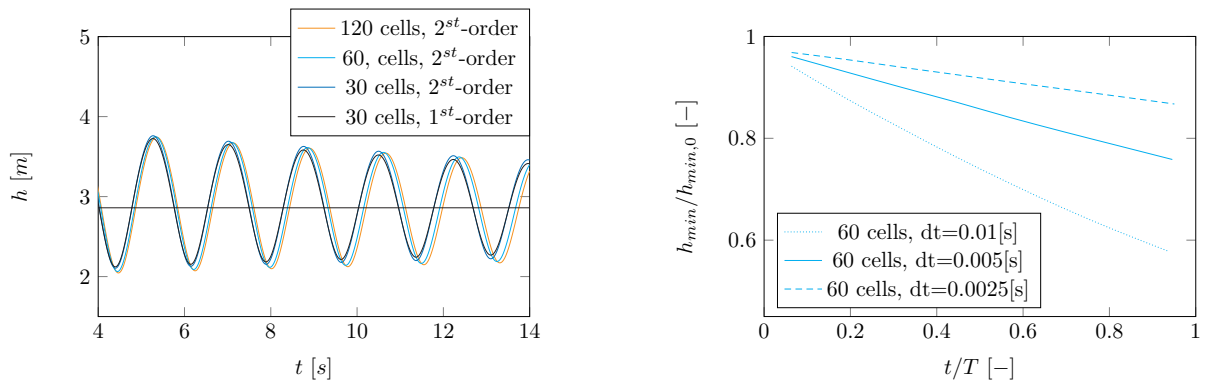
In fig. 4.10b is the convergence of the amplitude depicted for three different meshes and time steps. The parameter h indicates the height of air below the water. The rate of dissipation depends on the grid resolution. This rate decreases with an increased grid resolution. Note that the physical viscosity is neglected, which should result in a non-damping oscillation. Based on the height of the amplitude and the period of the oscillation, the results converges with $\mathcal{O}(dt^{0.95})$ and $\mathcal{O}(dx^{1.14})$. The time convergence corresponds with the first-order fractional step method, discussed in section 4.3.3.

The simulation for $dt=0.005[s]$ is also done for a first-order upwind scheme. It is shown in fig. 4.10 that the artificial viscosity significantly is increased. However, the order of convergence is almost the same: $\mathcal{O}(dx^{1.13})$. The second-order upwind scheme does not improve the order of convergence of this case. In section 3.3.3, it is discussed that the first-order free surface displacement method determines the overall accuracy. The difference in amplitude at 14[s] between the first-order and second-order upwind scheme is 1.1%.

It can be concluded that in fig. 4.10, the leading error is caused by time step instead of the grid resolution. The time step has more influence on the global error.

4.5.2 Standing gravity wave

To test the free surface displacement method, standing wave simulations can be performed [148] to assess the performance of the numerical method for free surface waves. All the important free surface dynamics are included [128]. It shows the capability of the model to simulate accurately the creation and propagation of free surface waves before the interaction with the structure [148].



(a) Results for different grid resolutions and upwind scheme.

(b) Time convergence of amplitude.

Figure 4.10: Convergence study for 1D water piston.

The first case simulated is a standing wave travelling between two cell centers. In this case the gravity consistent averaging method works, while the cell-weighted averaging method leads to spurious velocities, as discussed in section 4.3.8. When the cell-weighted averaging method is used for the densities at the cell edges for a hydrostatic case, the gravity is not balanced by the pressure. The effect on the standing wave is shown in fig. 4.14 for a wave amplitude of 0.001[m] and a wave period of ≈ 0.8 [s] in a flow domain of 1[m] by 1[m], 20 by 20 cells and fixed time step of 0.01[s]. It can be noticed that the wave is non-linear over time for the cell-weighted averaging method compared with the gravity-consistent averaging method. However, note that it is concluded in section 4.3.8 that the gravity-consistent method is in steep cases not necessarily better. For the steeper standing waves, the cell-weighted averaging method is still used.

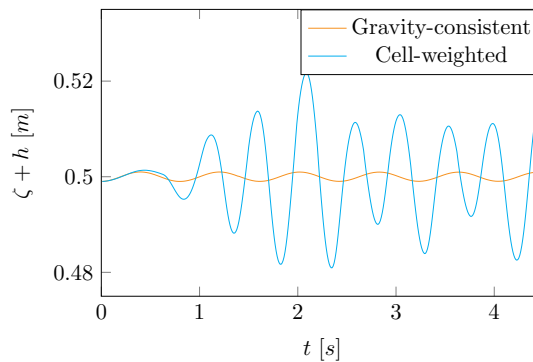


Figure 4.11: Standing wave comparison for cell-weighted and gravity-consistent averaging method at $x=0.5$ [m].

When for initial conditions a free surface is prescribed as a cosine function with a high amplitude, higher harmonics in the free surface elevations are generated leading to a nonlinear effect. An energy transfer takes place from a certain base mode towards higher harmonics. For small wave amplitudes, the non-linear effects are negligible and the wave can be seen as a linear wave as shown in fig. 4.14 for the gravity-consistent averaging method [148].

The next step is to model a standing gravity wave over a couple of cells in height to show that the method also can model the higher harmonics in the free surface elevation. It is known that

the exact solution for a linear wave is:

$$\zeta = \zeta_a \cos(kx - \omega t), \quad (4.51)$$

where the wave number $k = \frac{2\pi}{\lambda}$, the wave length $\lambda = 1[m]$, and the frequency $\omega = \frac{2\pi}{T}$. To find the frequency, the dispersion relation is used; $\omega^2 = kg \tanh(kh)$ where h will be equal to $0.5[m]$. For steeper waves, the wave length for a given frequency also depend on the wave height which is a non-linear effect [148]. The parameters are illustrated in fig. 4.12. Here at the top boundary the pressure is defined equal to the atmospheric pressure. A fixe time step of $2 \cdot 10^{-3}[s]$ is used.

The capability of the model to represent non-linear second-order waves, like observed by

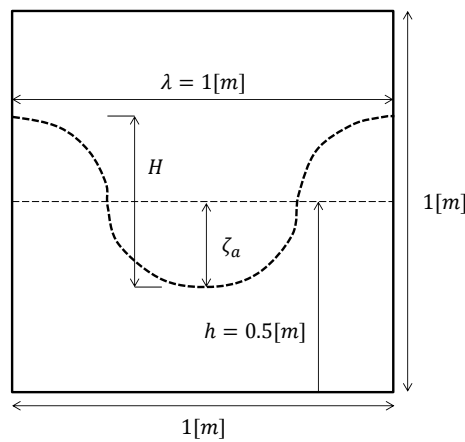


Figure 4.12: Standing wave simulation parameters.

Wellens (2012), is proven in fig. 4.13a. The steepness (H_0/L) used by Wellens (2012) is used for the simulation of the standing wave for different gridsizes. This is done to not experience breaking waves. In fig. 4.13b, the convergence is shown for two initial wave heights (H_0) for different gridsizes. It can be noticed that the dissipation rate is indeed dependent on the speed and so the steepness of the wave. However, the dissipation becomes smaller for an increase of the grid resolution. The order of convergence is not estimated due to the non-linear effect which becomes more dominant with the grid resolution.

As mentioned before, the model is robust. When using coarse grids in combination with an upwind discretization, the results are stable but the artificial viscosity has a greater share, which leads to energy dissipation in the system. Also, the free surface displacement algorithm (donor-acceptor method) uses an upwind discretization of the convective term in the transport equation, which also leads to wave-energy dissipation [148]. This is the reason why the wave amplitude becomes smaller over time. When the wave is steeper, the dissipation increases where also the velocity increases [149]. The dissipation is dependent on the velocity.

When the wave is steep enough, the flow becomes non-symmetrical in the flow domain. It starts to break in deep water when the steepness ratio H_0/L exceeds 0.14 [132]. This is illustrated in fig. 4.14 for a wave length (λ) of $1[m]$ and a wave height (H_0) of $0.6[m]$ on a grid of 30×30 . The black figures illustrate the free surface at the corresponding time. It can be noticed that after detaching a droplet at $2.7[s]$ from the free surface, no higher harmonics are experienced.

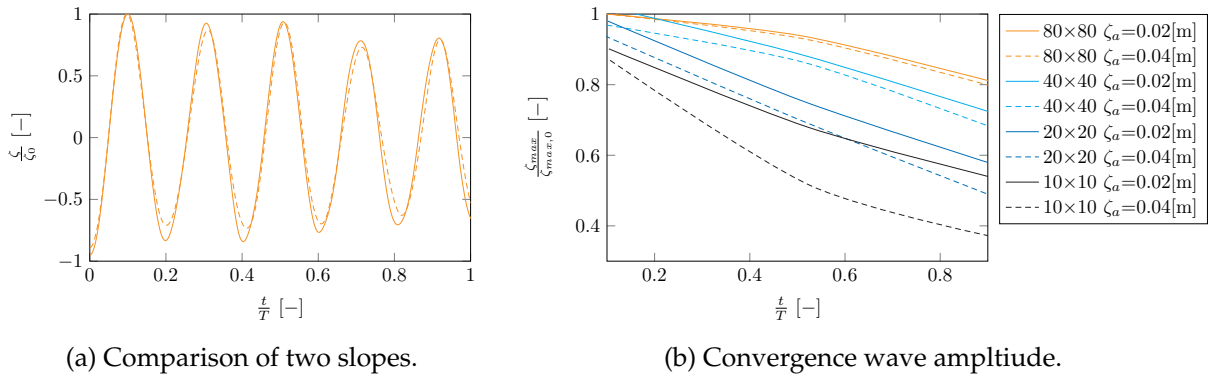


Figure 4.13: Standing wave simulation for $H_0=0.08[m]$ and $H_0=0.04[m]$ at $x=0.5[m]$.

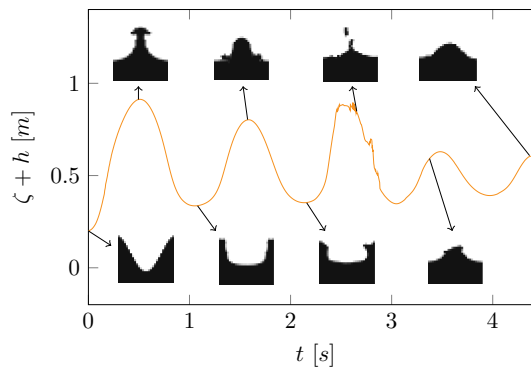


Figure 4.14: Standing wave simulation measured at $x=0.5[m]$, $\zeta_{a,0}=0.3[m]$.

4.5.3 2D oscillating planar rod

The next case is to model a 2D oscillating planar rod which starts initially as a squared bubble. With this case, it is shown that the model used to represent the surface tension in section 4.4.3 works. Further, the case can show that the numerical model can provide symmetrical results. The gravity is in this case neglected and for all boundaries the pressure as well as the velocity is prescribed as zero to maintain symmetrical conditions. According to Hua and Lou (2007), the effect of the boundary is negligible when the radial size of the domain is four times of the bubble diameter. The fluids are assumed incompressible. The results are compared with the results of ANSYS CFX [135].

The same setup is used [135]. A square with an area of $4 \cdot 10^{-4}[m^2]$ is used which should become, due to the surface tension, a circle with a diameter of $\approx 2.26 \cdot 10^{-2}[m]$. For the simulation, a surface tension of $\sigma=0.0236[N/m]$ is used. The equilibrium pressure in the bubble should be equal to $2\sigma/D$, where D is the diameter of $2.26 \cdot 10^{-2}[m]$. This is equal to a pressure of $\approx 2.09[Pa]$. The domain size is $0.04[m]$ by $0.04[m]$ with 40 cells in both directions equally spaced. The boundary conditions are enforced, which can result in an extra damping of the oscillation when a coarse grid is used. A fixed time step of $0.001[s]$ is used. The square consists of the liquid phase with a density of $\rho_l=790[kg/m^3]$ and the surrounding gas phase is $1.2[kg/m^3]$. The dynamic viscosity of the gas and liquid phase were both set to $0.001[Pa \cdot s]$.

According to Ham and Young (2003), in the inviscid limit the angular frequency of oscillation

for a 2D column can be given by the expression of Lamb (1932):

$$\omega^2 = (n)(n^2 - 1) \frac{8\sigma}{(\rho_l + \rho_a)D^3}, \quad (4.52)$$

where n is the mode of oscillation. This is equal to four for an initial square. This results in an oscillation period of $\approx 0.178[s]$.

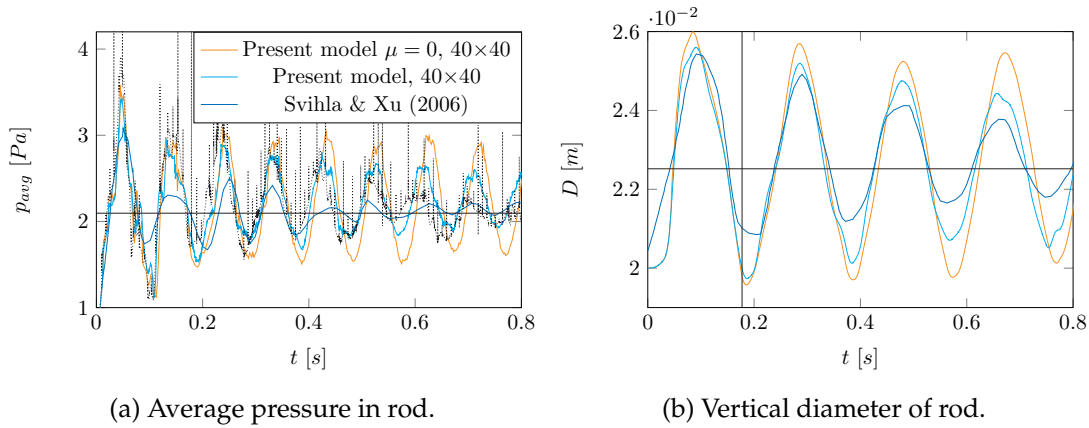


Figure 4.15: Pressure and diameter of the bubble over time compared with ANSYS; dotted line is method 1 for the diffusive term.

The results of the simulation are compared in figs. 4.15, 4.17 and 4.18 with the results of Svihla and Xu (2006), using 25,262 prism elements. It shows that the model represents the right period of oscillation, the pressure by equilibrium and the diameter of the bubble. An oscillation period of 0.182[s] and 0.185[s] for the inviscid and viscous case, respectively. Due to the artificial viscosity, the analytical oscillation period is lower than the period found. The decay and energy loss is caused by the numerical diffusion as well as the physical diffusion.

The stability criteria for the diffusive term in eq. (3.23) is not met during the entire simulation. This leads to mass losses (0.4%) and small asymmetric properties. However, this also reduces the computational costs due to the larger time step used. After one period of oscillation, it can be noticed that the total energy is increased. This may be caused by the criteria in eq. (4.46), which is not satisfied and no balance between the pressure gradient and the body force, leading to spurious velocities.

When adding viscosity, the fluctuating peaks in the pressure increases. The diffusive term becomes more important and discretized using the central difference scheme which can cause non-physical pressure oscillations [50]. Note that method 2 is used, where method 1 is plotted in fig. 4.15 by the black dotted lines. More pressure spikes are observed for method 1 than for method 2.

In fig. 4.16, the results for an air bubble in water are plotted. Using the same definition for the curvature, the pressure will be in opposite phase due to the different oriented normal vector (∇F). The surface tension is independent of the density. This entails that denser fluid elements experience the same acceleration as lighter fluid elements. This means that both cases should have the same period of oscillation. Further, the dynamic viscosity is the same for both fluids. This means that for the air rod more numerical damping is experienced.

A difference in water mass loss is found, 0.4% for the water rod case and 2.7% for the air rod case. It results in a lower steady-solution. The difference in mass loss can be explained by the next chapter in section 5.4.2 and not meeting the stability criteria. Note that the height function acts in a different direction for both cases. Further, the air rod case contains 4 times more water than the water bubble case. Together with the enforced boundary conditions, this might explain the extra damping.

The cell labeling is axi-symmetrical due to the machine accuracy which can result in non-symmetrical behavior. Furthermore, according to Lam (2009) the approach of the local height function is not symmetric. This is elaborated in section 5.4.2. This is also visible in fig. 4.16 where the last peak is increased for the liquid rod. The local height function depends on the labels.

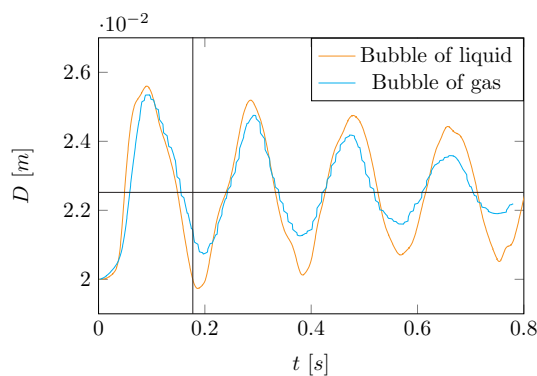


Figure 4.16: Diameter of the air rod over time compared with the water rod.

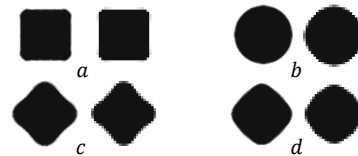


Figure 4.17: Volume fraction (right) against time compared with ANSYS CFX (left); (a) 0.01[s], (b) 0.05[s], (c) 0.09[s], (d) 0.13[s].

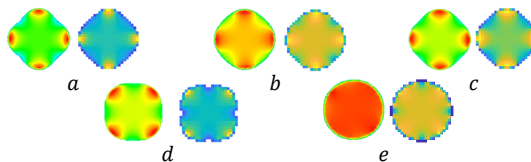


Figure 4.18: Pressure against time compared with ANSYS (left); (a) 0.49[s], (b) 0.51[s], (c) 0.67[s], (d) 0.75[s], (e) 0.79[s].

4.5.4 Standing capillary wave

Besides the case of the 2D oscillating rod, standing capillary waves are simulated to verify the CSF-model for free surface flows. The same setup is used as for the standing gravity waves, illustrated in fig. 4.12. The capillary waves are driven by the surface tension.

To simulate capillary waves, there is a time restriction for numerical stability. When surface tension is treated explicitly, the time step resolves the propagation of capillary waves [76]:

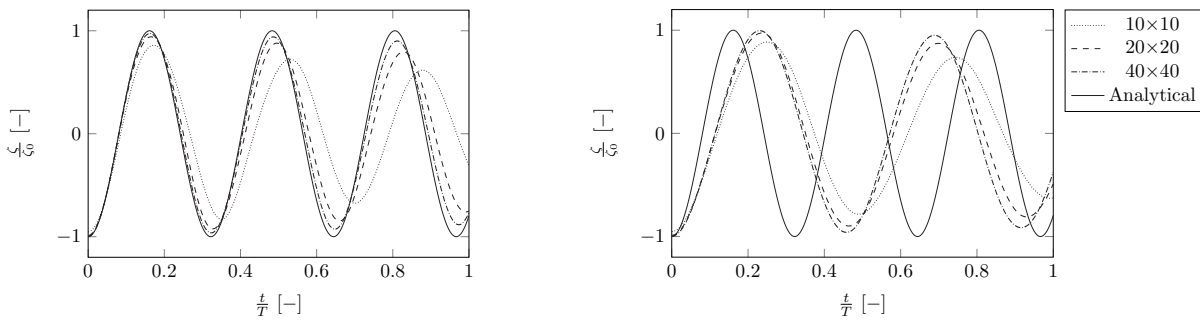
$$dt \leq \sqrt{\frac{\rho \delta x^3}{4\pi\sigma}}. \quad (4.53)$$

The effects of viscosity and gravity are neglected. The density of the water is $\rho_w = 997[\text{kg}/\text{m}^3]$, the density of the air is $\rho_a = 1[\text{kg}/\text{m}^3]$, and the wave number $k = 2\pi$. The dispersion relation for a capillary wave at zero gravity is given by [36]:

$$\omega^2 = \frac{\sigma}{\rho_w} |k^3|. \quad (4.54)$$

First, simulations are done of a standing wave over one cell height to show that the model converges. This is done for the averaging CSF-model of Baraldi et al. (2014) and the newly developed CSF-model. A fixed time step of $dt=0.01[\text{s}]$ and a wave amplitude of 40% of the cell height is used.

The normalized results, for $\sigma=1.5[\text{N}/\text{m}]$, are shown in fig. 4.19. Both models seem to converge in amplitude. However, the developed surface tension model converges to the linear analytical solution. The averaging CSF-model seems to converge to a wrong wave period. The next step



(a) New CSF-model in section 4.4.

(b) Averaging CSF-model [7].

Figure 4.19: Comparison of two CSF-models.

is to simulate standing waves over a couple of cell heights for different gridsizes. The wave amplitude is $\zeta_a=0.04[\text{m}]$ and a surface tension of $10[\text{N}/\text{m}]$ is used. The fixed time step is equal to $0.4\delta x$. This is done for the suggested CSF-model, to show that this method converges to the right solution as well as representing the second-order effect discussed in section 4.5.2. In fig. 4.20 the results are shown. During the simulations, the mass remains fully conserved using the suggested CSF-model.

In fig. 4.20b T_w represents the wave period in seconds. It is shown in fig. 4.20a that the model is slowly converging by increasing the grid resolution. Further, in fig. 4.20b the dotted lines show the eigen period and the double eigen period of the capillary wave. Two peaks are found by using the Fourier transform which are identical to the values T_0 and $2T_0$. Here the double wave period represents the second-order effect also found in section 4.5.2 for the standing gravity wave.

4.5.5 2D rising bubble

Shown that the SLIC-CSF-model produces reliable results for the 2D oscillating planar rod and standing capillary waves, the model is compared with the benchmark of the 2D rising bubble

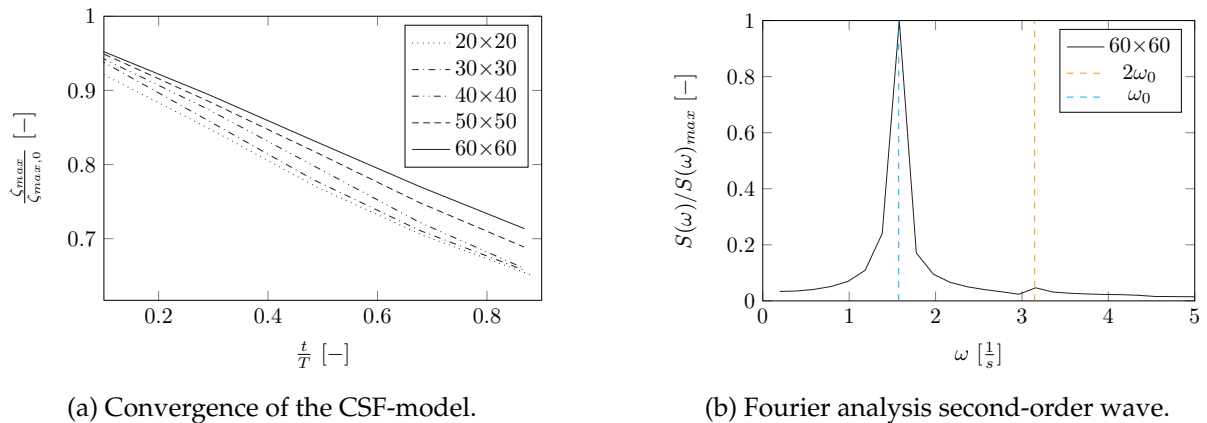


Figure 4.20: Properties of the CSF-model.

published by Hysing et al. [70]. This benchmark is made due the absence of analytic solutions and used for quantitative validation and comparison of incompressible interfacial flow codes. The initial fluid configuration of the 2D rising bubble test case is shown in fig. 4.21. All walls are non-penetrable and have the free-slip condition. At the top wall the pressure is prescribed as equal to the atmospheric pressure.

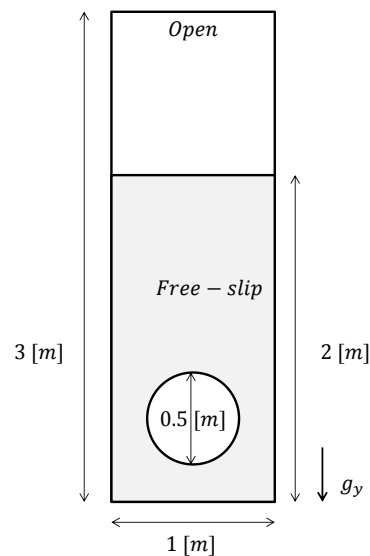


Figure 4.21: Flow domain for 2D rising bubble.

The values of the parameters are shown in table 4.3. Due to the relatively high viscosity, the stability criterion given in eq. (3.23) becomes significant. Besides comparing the results with the benchmark, the effect of the viscosity and the surface tension is investigated. As in Wemmenhove (2008), the incompressible multiphase model is used with a grid resolution of 40×120 and 80×240 . When using the compressible multiphase model the bubble starts to fragment and compress instantly. This can be seen in the results fig. 4.22a. The line of the compressible case oscillates around the line of the incompressible case. To prevent this, the surface tension needs to be a value far from realistic [149].

The Eötvös number ($E\ddot{o}$) is a dimensionless number, which indicates the importance of the gravitational forces compared to the surface tension forces. Further, the Reynolds number (Re), in this case also called Galilei number (Ga) [139], is a dimensionless number, which gives the

Test	D [m]	ρ_w [kg/m ³]	ρ_a [kg/m ³]	μ_w [kg/ms]	μ_a [kg/ms]	g [m/s ²]	σ [N/m]	Re	EO
Case 1	0.5	1,000	100	10	1	0.98	24.5	35	10
Incomp. 1	0.5	1,000	100	0.01	$1 \cdot 10^{-3}$	0.98	0	$35 \cdot 10^3$	∞
Incomp. 2	0.5	1,000	100	0.01	$1 \cdot 10^{-3}$	0.98	24.5	$35 \cdot 10^3$	10
Incomp. 3	0.5	1,000	100	10	1	0.98	24.5	35	10

Table 4.3: 2D rising bubble simulations and benchmark values.

ratio between the inertial and viscous forces. The formulas are found by [29]:

$$E\ddot{o} = \frac{\rho_w g D^2}{\sigma}, \quad (4.55)$$

$$Re = \frac{\rho_w \sqrt{g D D}}{\mu_w}.$$

To compare results with the benchmark given by Hysing et al. (2009), the mean velocity v_c of the bubble has to be calculated:

$$v_c = \frac{\int_{V_g} v dV}{\int_{V_g} dV}, \quad (4.56)$$

where V_g is the volume of the bubble region and v the vertical velocity. The mean velocity is plotted in fig. 4.22a for the different cases. Comparing to the 3D results of Wemmenhove (2008), it can be noticed that the rise time for the 3D case is shorter due to the higher buoyancy force. This is also found in the results of Chai et al. (2017). However, based on the results it can be concluded that the shape evolutions of the rising bubble in the 2D case and 3D case are in accordance with the benchmark. The bubble shapes are illustrated in fig. 4.24.

Looking to the graphs given in fig. 4.22a, it can be noticed that the bubble behaves quite differently when the viscosity is lower and/or the surface tension is zero. It can be seen that due to the surface tension, the bubble remains intact which leads to a more constant rise velocity and a higher peak velocity. This equilibrium velocity is found by the equilibrium of viscosity and buoyancy forces. The effect of viscosity seems to delay the rise velocity in time. It takes more time to reach the maximum rise velocity. Further, it can be noticed that increasing the grid resolution leads to better results. The result of increasing the grid resolution is given in fig. 4.22b.

In fig. 4.22b, the effect of decreasing the time step is negligible. It seems that the results are converged in time when using a CFL-number of 0.25. The resulting wiggles decrease by increasing the resolution. All these plots are simulated using the second-order upwind scheme for the convective term and the first model for the diffusive term, used by Wemmenhove (2008). It is remarkable that the first-order upwind scheme seems to better approach the benchmark. This means that the diffusive term could be underestimated using the second-order upwind scheme.

In case of using the second model for the diffusive term discussed in section 4.3.2, better results are obtained in fig. 4.23 than for the original method described by Wemmenhove (2008). Based on this result, the second model is used in further investigations. The maximum error is reduced from 3.0% to 0.4% when using the second model for the diffusive term. This means that the term $(\nabla \mathbf{u})^T$ cannot be neglected, when viscosity becomes more important, in the order of $Re=35$.

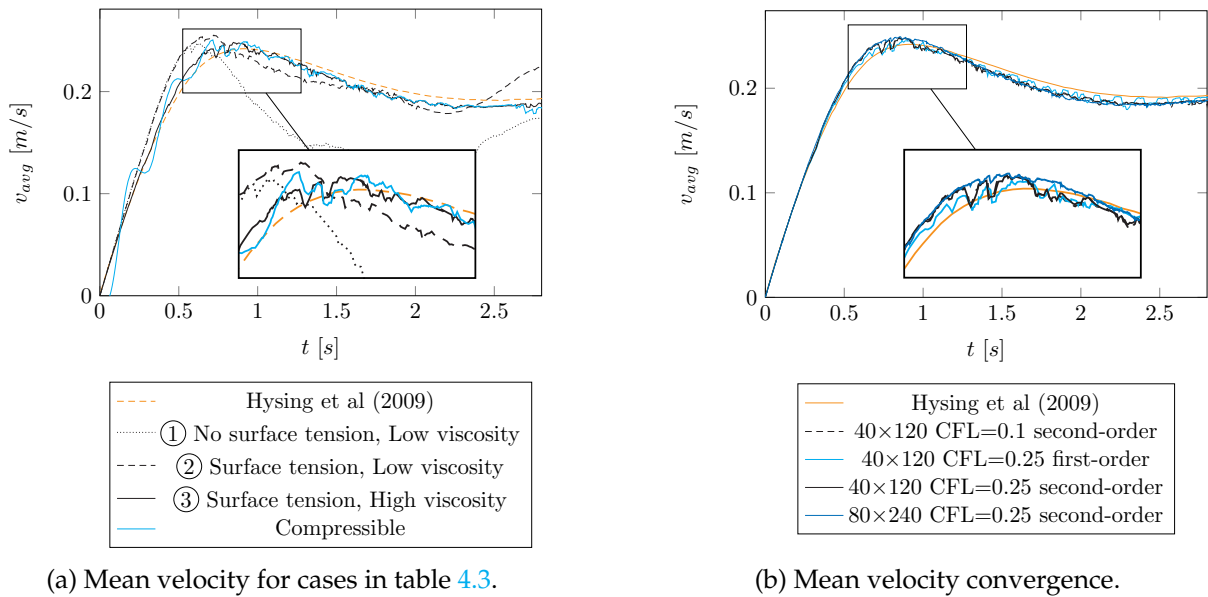


Figure 4.22: Rising bubble results for the original method.

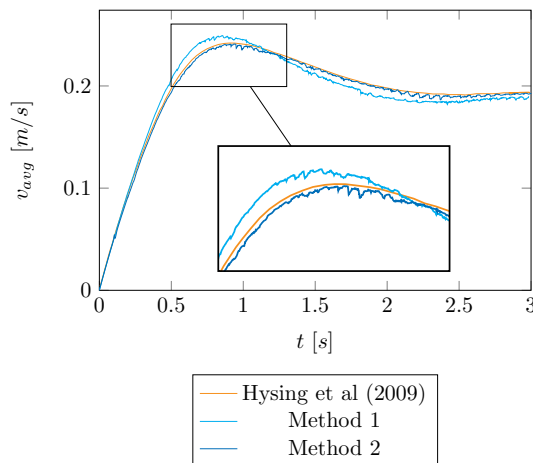


Figure 4.23: Mean velocity comparison of diffusive models for 80×240.

Bubble shape

According to Tripathi et al. (2015) and Clift et al. (2005) *case 1*, as well as *incompressible 3* should behave like an axisymmetric bubble. By increasing the Galilei number, like for *incompressible 2*, the characteristics of the rise velocity becomes less smooth. Further, a second maximum can be found in the characteristics which corresponds more with an offset break-up of the bubble and a skirted bubble. The rise time to find the maximum rise velocity becomes also shorter. Further, the shape shown in fig. 4.24 for *incompressible 1* seems to behave like a combination of central and peripheral breakup which corresponds with the results of Tripathi et al. (2015).

Besides the 2D rising bubble case, it need to be shown that the model is also capable of modelling the situation when the bubble reaches the free surface. The values for the density and viscosity used in section 4.5.6 are also used for this case. The surface tension has a value of 24.5[N/m]. The evolution is shown in fig. 4.25. The asymmetry is caused by the local height function. Due to the machine accuracy, the cell labeling becomes asymmetric.

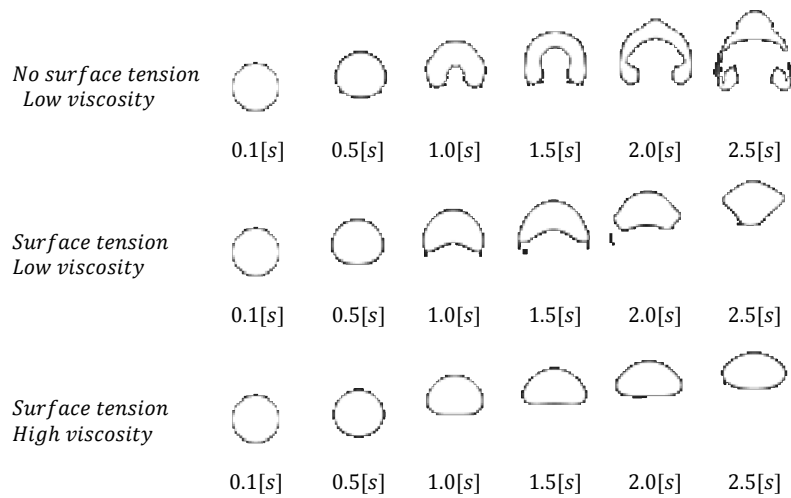


Figure 4.24: Snapshots of the 2D rising bubble in order of time for three different incompressible simulations.

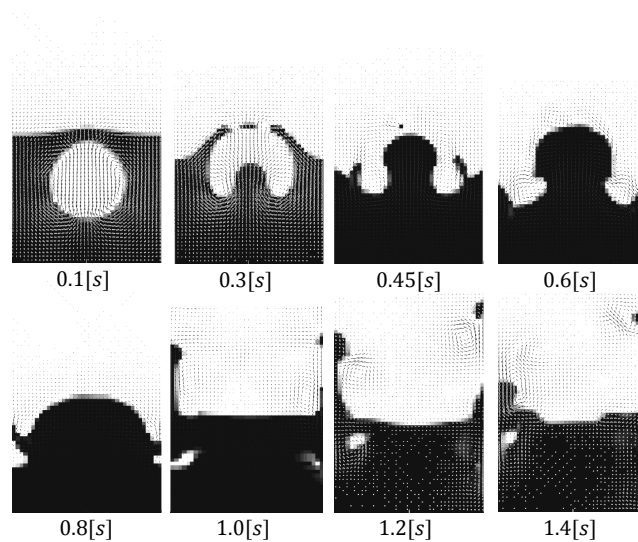


Figure 4.25: Snapshots of the 2D rising bubble through interface in order of time with surface tension $\sigma = 24.5[\text{N/m}]$.

4.5.6 Dam break case

After verifying that the model is capable to correctly simulate air pockets by looking to the oscillation frequency and pressure, the model is tested for the dam break case. The objective of this research is to look what the effect of aeration is on the impact, for example for a green water event. As explained in section 2.4, the dam break case is a simplified green water event. This case is often used for validation of two-phase flow model [75, 78, 149]. Before the effect of aeration is implemented in chapter 5, the dam break simulation is done for incompressible water to look which phenomenon can be experienced with the multiphase model, like [pocket oscillations](#). Validation needs to be done to show that the right equations are used and the numerical model is sufficient to predict the impact pressure for this case.

The first case discussed is to validate that the [Propagation of water](#) is well modelled by com-

paring the computational result with experimental results in section 4.5.6.

In the following case, the impact pressure caused by the water is measured during the simulation and compared with the experimental results of MARIN. Furthermore, [Impact comparison with COMFLOW](#) is done, using the computation results of Wemmenhove et al. (2010).

For these simulations, the [local height function is modified](#) as described in section 5.4.2 to have a fair comparison with the other results in the following chapter 5. Furthermore, based on section 4.3.3, the CFL criteria is set equal to 0.2.

Propagation of water

For the first simulation, the propagation of the wave front of the dam is analyzed. The setup in the report of Kees et al. (2011) is used and illustrated in fig. 4.27. A 3D level set formulation is used by Kees et al. (2011) where linear and quadratic finite elements were employed to compute the test case.

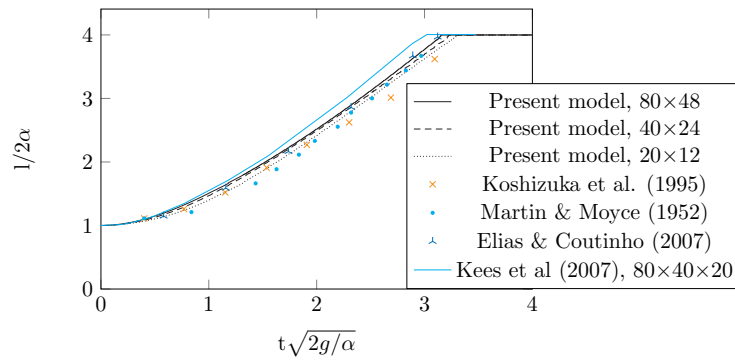
The size of the domain is $a=4\alpha$ by $b=2.4\alpha$ with $\alpha=0.146[m]$. The parameters for water and air are set to $\rho_w=1,000[kg/m^3]$, $\rho_a=1[kg/m^3]$, $\mu_w=1\cdot 10^{-3}[kg/ms]$, and $\mu_a=1\cdot 10^{-4}[kg/ms]$. The gravitational constant is set to $g=9.81[m/s^2]$ and the surface tension is neglected. The size of the dam is $c=\alpha$ by $d=2\alpha$. A 2D Cartesian mesh of 80×48 , 40×24 and 20×12 elements is used. Free-slip boundary conditions are imposed on all the walls and the atmospheric pressure is prescribed at the top boundary.

The results of the simulation are shown in fig. 4.26 and compared with different experimental results [45, 79, 98]. The change of the height and length, measured at the origin (O), over time is plotted. For fig. 4.26, non-dimensional numbers are used for the time (t), length (l) and height (h). The numerical results are in good agreement with the experimental data. Furthermore, the model converges in space. The time the wave front hits the wall is according to Elias and Coutinho (2007) at 0.38[s]. The error for grid resolution 80×48 is 0.07%. According to Kees et al. (2011), this can be caused by the free-slip conditions as well the 3D effects. The friction between the fluid and the wall may not be well represented [102].

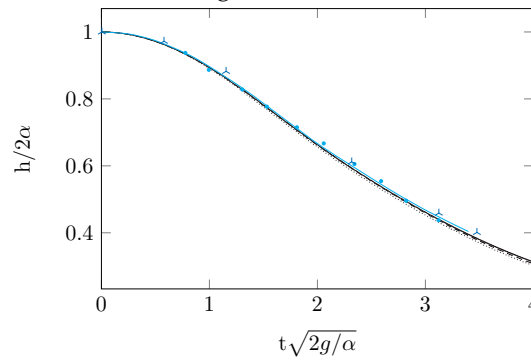
Impact comparison with COMFLOW

Besides the validation of the propagation of the water over time in 2D for the dam break simulation, the impact is also validated by comparing the pressures on the wall. These measurements are done by MARIN. The experimental setup for the dam break experiment consists of a tank with an open roof and a size of $a=3.22[m]$ by $b=1.0[m]$ by $1.0[m]$. A door is used to fill the column of water of $d=0.55[m]$ by $c=1.22[m]$. The setup is shown in fig. 4.27. The door is pulled up almost instantaneously by releasing a weight [78].

The height of the water is measured over time on the positions H_1 and H_2 , located at $0.58[m]$ and $2.72[m]$ from the origin, respectively. The measurements are done by using vertical wave probes. Further, the pressures by impact on the wall are measured, using pressure sensors, at P_1 and P_2 . The pressure sensors are positioned at a height of $0.03[m]$ and $0.41[m]$, respectively. The atmospheric pressure is subtracted from the measured pressure. This is done for three different gridsizes; 48×15 , 80×25 and 115×36 . The parameters for water and air are the same as in section 4.5.6. The dynamic viscosity for air is $\mu_a=1\cdot 10^{-5}[kg/ms]$. Further, the surface tension is equal to $\sigma=0.072[N/m]$.



(a) Length (l) in time (t).



(b) Height (h) in time (t).

Figure 4.26: Change and convergence of 2D dam over time in height (h) and length (l) using non-dimensional values.

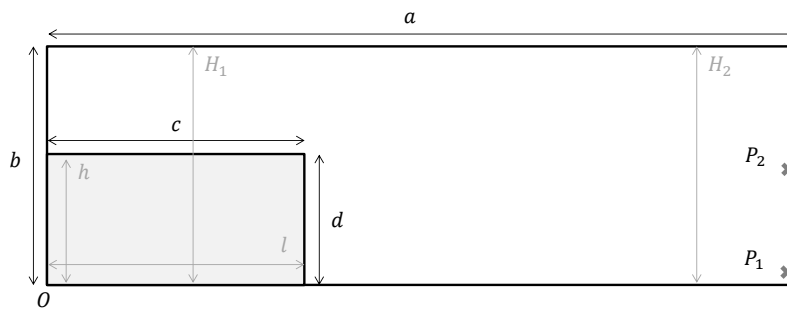


Figure 4.27: Setup 2D dam break case.

After pulling up the door, the water flows quickly towards the wall. When hitting the wall, a significant run-up is visible. After the run-up against the wall, the wave front starts moving back and forward. A gradual tendency towards a steady situation with a horizontal free surface is visible. Due to the flip-through impact, an air pocket is captured. It is important to note that the numerical model does not account for fragmentation due to the assumption of no-slip between fluids, see section 2.6. Further, the numerical simulations are done in a 2D domain, which restricts the motion of the water as well as the entrapped air pocket. As described in section 4.5.5, a lower buoyancy force is exerted on a 2D bubble than a 3D bubble.

Besides comparing the 2D simulation results with the 3D experimental data, the results are also compared with the 3D results found by Wemmenhove et al. (2010). The results are illustrated

in fig. 4.28. The results correspond to the three stages for green water loading discussed in section 2.4 [18].

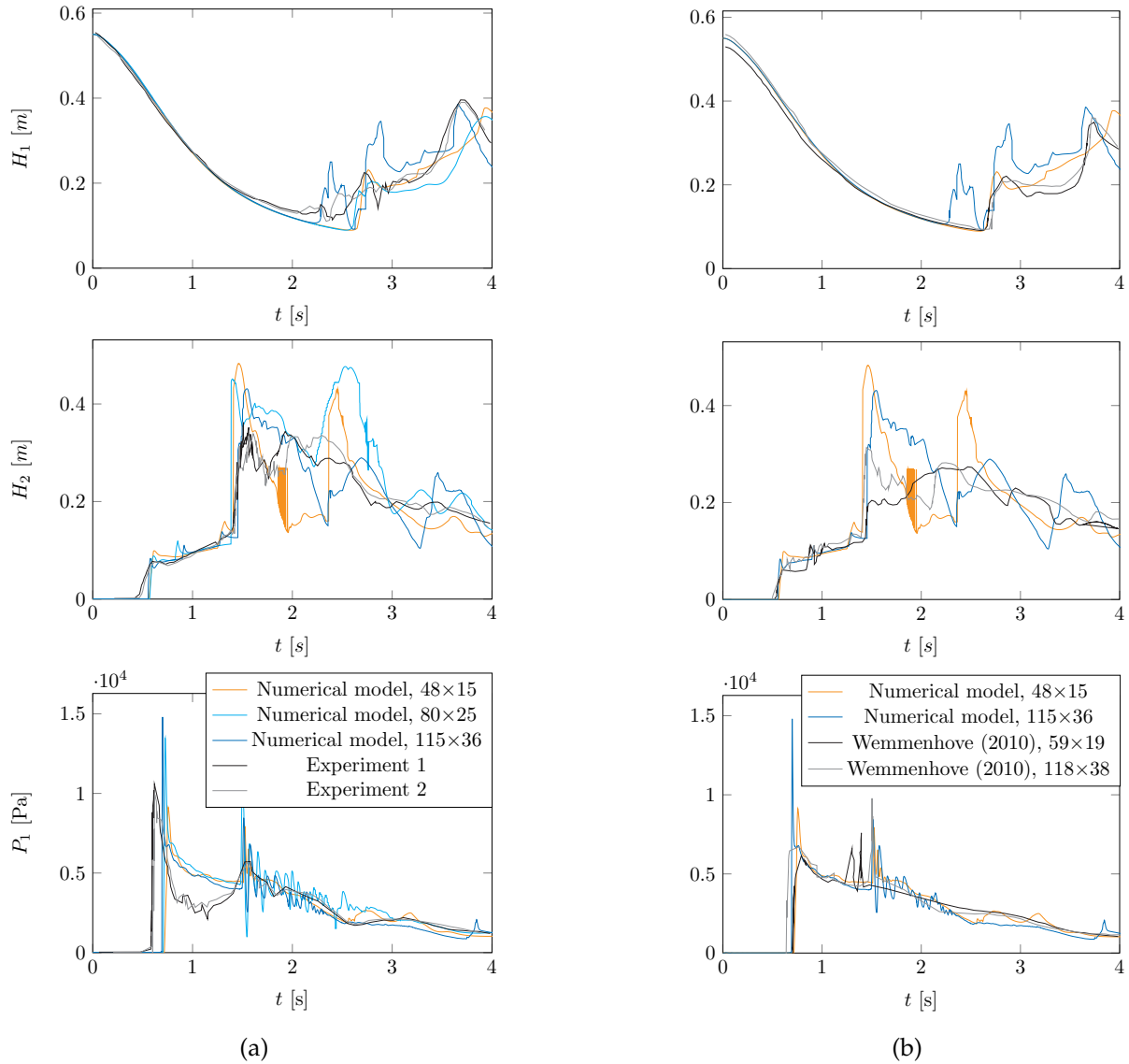


Figure 4.28: The results of the present model for the dam break case compared with experimental results of MARIN in the column (a) and numerical results of Wemmenhove et al. (2010) in the column (b).

In fig. 4.28 a time lag is visible between the experimental and simulation results. It is shown by Wemmenhove (2008) that the diffusion coefficient in the air increases by the artificial diffusion coefficient $k_d = \frac{|\mathbf{u}| \delta x}{2}$ for a first-order upwind scheme. This leads to an increase of the viscosity in the second phase to a value that may outnumber the physical viscosity of the air. The artificial viscosity seems to be more important on the deceleration of the dam break front than the physical air viscosity. This effect decreases with the second-order upwind scheme.

For the coarse grid, the magnitude of the pressure peak and the time scale of the second peak pressure are better predicted with the presented 2D model, compared with the 3D results of

Wemmenhove et al. (2010). However, note that the water for a 2D model is restricted in his movement which can lead to a higher impact pressure. The evolution of the pressure approaches the experimental results.

The results in fig. 4.28 shows that the global motion of the water is well captured. The higher peaks relative to the experimental results are caused again by the limitation of movement of the water. Furthermore, the straight peaks are caused by detached droplets propagating above the free surface.

The presented model seems to be more physical compared with the model of Wemmenhove et al. (2010), looking to the time period 2.0-2.8[s] of H_1 . The change of the water height for the presented model are less abrupt compared to the results of Wemmenhove et al. (2010). The results of COMFLOW look suspicious concerning pushing the fluid together or using the local height function in a non-conservative way. This is elaborated in section 5.4.2.

Further, it is remarkable that the dam break, in the results of Wemmenhove et al. (2010) for a coarse grid, propagates faster than the results of the presented model. This might be explained again by the 3D effects, like is experienced in section 4.5.6.

The grid refinement does not result in converging results. This can be caused by detaching bubbles propagating above the free surface. A grid convergence study cannot be done due to the limited computational power available for this research.

Oscillations

An air pocket is entrapped due to the flip-through impact. A sequence of fraction fields together with pressures in time are illustrated in appendix E.2, It can be noticed that the air pocket oscillates in time with a certain frequency. These oscillations are also found in fig. 4.28 after 1.5[s]. The pressure oscillations seem to be related to the pulsation of the air pocket which needs to be verified.

By doing a Fourier transform, the frequencies are found of the oscillation of the pressure as well as the pulsation of the air pocket. The average pressure of the air pocket is measured between 1.2[s] and 3.0[s]. Further, eq. (2.1) and eq. (2.2) can be used for a first approximation of the frequency of the pulsation. However, note that the first equation assumes a spherical bubble with an adiabatic pulsation and the second equation, proposed by Oumeraci et al. (1992), is simplified.

The radius R_0 is approximated by taking the average between the vertical and horizontal extent in steady state. The bubble does not have a spherical but a lens shape. The results of the Fourier transform are plotted in fig. 4.29 and summarized in table 4.4. The stepsize in frequency is 1[Hz]. The theoretical frequencies are not the same as the frequencies found by the simulation. However, the order of magnitude is the same, which means that the theoretical values might be related to the oscillation of the air pocket [118].

Besides the high frequency oscillation (>11 [Hz]) in the pressure in fig. 4.28, also a low frequency is observed. It is observed by Plumerault (2009) that this can be caused by the frequency of translation of the pocket. The motion of the air pocket is captured between 1.5[s] and 2.5[s] by taking the average translation of the total entrapped air. The frequency of the translation in vertical direction is plotted in fig. 4.29. From fig. 4.29, it can be noticed that the frequency peaks of the pressure oscillation at the foot of the wall corresponds with the frequency of the global motion and the pulsation of the air pocket.

	Value
R_0 [m]	0.10
f_0 high frequency (eq. (2.1)) [Hz]	29.57
f_0 high frequency (eq. (2.2)) [Hz]	24.09
Simulation high frequency pressure wall 1 [Hz]	13.04
Simulation high frequency pressure bubble 1 [Hz]	12.04
Simulation high frequency pressure wall 2 [Hz]	15.05
Simulation high frequency pressure bubble 2 [Hz]	15.05
Simulation low frequency pressure wall 1 [Hz]	1.00
Simulation low frequency motion bubble x 1 [Hz]	1.00
Simulation low frequency motion bubble y 1 [Hz]	1.00
Simulation low frequency pressure wall 2 [Hz]	3.01
Simulation low frequency motion bubble y 2 [Hz]	3.01

Table 4.4: High frequency and low frequency oscillations in pressure at the wall.

The higher frequency peaks observed in fig. 4.29 can be generated when the pocket is split-
ted in two parts [118] or due to higher harmonics. It can be concluded that the pressure oscillations after 1.5[s] in fig. 4.28 are caused by the pulsation and the global motion of the air pocket. Due to the assumption of no-slip between the fluids and the restricted movement of air pocket, these oscillation are less big in reality.

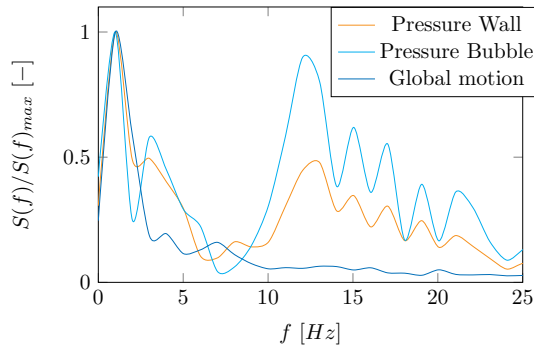


Figure 4.29: Fast Fourier transform of the entrapped air pocket.

4.6 Conclusion

In this chapter the extension from the one-phase model to the multiphase VoF model of Wemmenhove et al. (2010) is reproduced. Instead of a first-order upwind scheme for the convective term and the forward Euler time stepping scheme, the second-order upwind scheme in section 4.3.1 and the second-order Adams-Bashforth time stepping scheme in eq. (4.23) are used to reduce the artificial viscosity and maintain stability, given in table 4.1. Relative to the original method, a couple of improvements are done to improve the representation of the dynamics of an oscillating air pocket:

- Due to lack of documentation, a newly-developed CSF-model for SLIC is described in section 4.4. It is shown for the standing capillary wave in section 4.5.4 as well as the 2D oscillating planar rod in section 4.5.3 that the model can maintain a sharp interface in fig. 4.17, model the frequency of inviscid oscillation in fig. 4.15 with an error of 2%,

converges by increasing the grid resolution in fig. 4.20a, and free surface displacement can represent second-order effects in fig. 4.20b.

- Neglecting the transpose of the velocity gradient in the diffusive term in eq. (4.15) by assuming incompressibility cannot be neglected for the 2D rising bubble simulation in section 4.5.5 ($Re < 35$). The maximum error relative to the benchmark of Hysing et al. (2009) is decreased from 3.0% to 0.4%.
- The gravity-consistent averaging method of Wemmenhove et al. (2015) cannot be used for steep free surfaces represented by SLIC. This is illustrated in fig. 4.5 where after 3[s] of simulation, the spurious velocities is $\mathcal{O}(10^8)$ higher than for the cell-weighted averaging method.

Besides the improvement of the results of the 2D rising bubble, the modelling of the dam break case in section 4.5.6 seems to be improved. A good agreement is found with the experimental results for the propagation of the wave front in section 4.5.6 where the method converges in space.

Using a coarse grid, compared with the 3D original method of Wemmenhove (2008) the peak pressure as well as the timing of the second peak pressure and the time evolution of the pressure after the peak pressure are better predicted in section 4.5.6. The simulation results are in this aspect in better agreement with the 3D experimental results of MARIN. However, fragmentation and 3D effects are not accounted for. Furthermore, by increasing the grid resolution, the results are not very consistent compared with the original method. No grid convergence study for the 2D dam break case is done yet.

It is verified in fig. 4.29, that the presented model can simulate pressure waves caused by air pocket oscillations, corresponding with the pressure at the base of the wall.

In addition to the cases mentioned, the method is verified for the 1D water piston in section 4.5.1 and standing gravity waves in section 4.5.2. Both cases converges by increasing the grid resolution and match with the analytical solution in fig. 4.10 and fig. 4.13, respectively. For the 1D water piston it is observed that the convergence is $\mathcal{O}(dx^{1.14})$ and $\mathcal{O}(dt^{1.14})$ corresponding to the first-order free surface displacement method and fractional step method explained in section 3.3.3 and section 4.3.3, respectively.

The next step is to modify the multiphase model to a method that is capable of modelling the compressibility of a mixture of air and water. This is the last phenomenon in fig. 2.1 that has to be implemented in the model. This extended model is coded in MATLAB as well as FORTRAN, a compiled imperative programming language used by COMFLOW, to decrease the computational costs.

5 Double fraction VoF model

5.1 Introduction

After modelling the air pocket and the water in chapter 4, in fig. 2.1 a third phenomenon is illustrated: aeration. It is defined in chapter 2 that entrained air from numerical perspective is smaller than one grid cell. In section 2.3 it is described that aeration can increase the forces on a structure due to an increase in rise time of the impact pressure. Therefore a more accurate model is needed, which is capable to predict the pressure field in a dispersed-phase flow.

The multiphase VoF model of Wemmenhove (2008) is modified to model the compressibility of a dispersed flow. The multiphase model cannot represent the physical mixture speed of sound given in fig. 2.3, where the volume fraction β is in between 0 and 1. This is discussed in section 2.6.2.

The model proposed in this chapter is capable to model separated-phase as well as dispersed-phase flows. However, the mixing between these two layers is not taken into account. An additional volume fraction is added to the model; aeration indicated with volume fraction β . The model is implemented in the numerical computing environment MATLAB as well as in FORTRAN 90.

In section 5.2, the [Principle](#) of the extension of the multiphase model is given. The assumptions and limitations of the extension are highlighted. Furthermore, the governing equations are derived based on an extra volume fraction. Hereafter, a [Comparison with Multiphase model](#) is made in section 5.3. The extended model is compared with the multiphase model from numerical perspective.

In section 5.4, the extension of the [Numerical model](#), described in chapter 4, is derived. The governing equations are discretized for the extended model. This includes a new [Transport equation](#) in section 5.4.2 and a description of the limitations of the [Modified local height function](#) in section 5.4.2.

In section 5.5, the [1D Shock tube](#) is simulated for the extended model to show that the model is capable of representing the right speed of sound for a mixture in section 5.5.2 as well as for separated phases in section 5.5.1. It is also tested if the model is capable to model the reflection of shock waves at a wall in section 5.5.3.

The [2D Shock bubble interaction](#) for helium is described in section 5.6 and compared with experimental as well as numerical results. Hereafter, in section 5.7 the [Dam break](#) simulation is done to show the ability of the model to simulate a dispersed phase flow with a separated phase. The effect of aeration on the impact pressure is discussed in section 5.7.2 and the extended model is compared with the multiphase model in section 5.7.3. The chapter ends with a [Conclusion](#).

5.2 Principle

A distinction between multiple fluids is made in the extension of the multiphase model: the air above the free surface (ρ_a), the water (ρ_l) and the air within the water (ρ_g). In fig. 5.1, the hierarchy of the phase composition is shown. As derived in section 2.6, the governing equations for

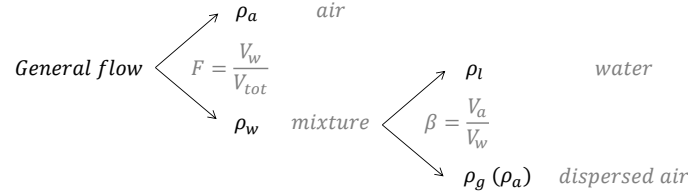


Figure 5.1: Extended model principle

a two-phase flow are given by eq. (2.21). When looking to section 2.6, based on the two-phase model of Baer and Nunziato (1986), the reduced 2-phase model is already derived by assuming no-slip and pressure equilibrium between the phases. The reduced model is strictly hyperbolic, but is not completely in the conservative form [73, 105]. These assumptions are also used for the "three fluids".

Looking to the size of the entrained air bubbles produced by whitecaps and wave breaking, experiments are done by producing wave-breaking in a large air-sea interaction simulating facility by blowing wind at 14[m/s] and generating waves [123]. An Eötvös number of around 0.03 was found which shows that the surface tension force is dominating. Using the Stokes solution, a terminal velocity of 0.1[m/s] is found, which is compared with the impact velocities negligible [134]. The assumption of no-slip between the entrained air and the water seems reasonable for violent free-surface flows, resulting in a homogeneous mixture.

Furthermore, the diameter of a bubble is smaller than a grid cell. When assuming a homogeneous mixture, the bubbles do not have to be tracked, leading to lower computational costs. An air mass fraction in fluid can be defined; $y = \frac{m_a}{m_w}$ [118].

This means that only one momentum equation has to be solved, like in eq. (2.21). The fluids l and g flow dispersedly while the fluids w and a flow separately. In this model no phase change is assumed and both fluids are assumed barotropic. Like for the multiphase model, there is no interest in the thermodynamic properties of the dispersed flow. Because of the "extra fluid", an additional continuity equation has to be satisfied:

$$\begin{aligned}
 \frac{\partial(F\beta\rho_g)}{\partial t} + \nabla \cdot (F\beta\rho_g\mathbf{u}) &= 0, \\
 \frac{\partial(F\rho_w)}{\partial t} + \nabla \cdot (F\rho_w\mathbf{u}) &= 0, \\
 \frac{\partial((1-F)\rho_a)}{\partial t} + \nabla \cdot ((1-F)\rho_a\mathbf{u}) &= 0, \\
 \frac{\partial(\rho\mathbf{u})}{\partial t} + \nabla \cdot (\rho\mathbf{u}\mathbf{u}) + \nabla p - \nabla \cdot (\mu(\nabla\mathbf{u} + (\nabla\mathbf{u})^T)) - \frac{2}{3}\mu\nabla \cdot \mathbf{u} - \rho\mathbf{F} &= 0, \\
 p_w &= p_a, \\
 p_l &= p_g,
 \end{aligned} \tag{5.1}$$

where the density is:

$$\begin{aligned}\rho_w &= \rho_l(1 - \beta) + \rho_g\beta, \\ \rho &= \rho_a(1 - F) + \rho_w F,\end{aligned}\tag{5.2}$$

which is also used for the dynamic viscosity. The first equation in eq. (5.1) represents mass conservation of the entrained air. The second equation represents mass conservation of the mixture and the last one represents conservation of the air above the free surface.

Besides the additional conservation equation for the entrained air, for this model it is assumed that the mass fraction remains constant and uniform ($\frac{D\beta}{Dt} = 0$) based on an initial value for β_0 . This results automatically in conservation of the entrained air when the mixture is conserved. The pressure equilibrium is used to derive the transport equation for the mixture F in section 5.4.2

The presented model is not fully conservative. The non-conservative momentum equation is still solved, leading to a momentum loss in a discontinuous velocity field due to a shock wave [149]. Furthermore, the fractional step method is used, leading to a splitting error as described in section 3.3.3.

One of the reasons to solve a non-conservative model is that fully conservative flow models have difficulties at the interfaces where unavoidable non-physical oscillations occur. This can happen due to non-physical pressure updates or negative volume fraction [2, 71, 72]. However, when solving the non-conservative form of the Navier-Stokes equations, underpredicted shock speeds and locations are often found due to momentum loss [49, 72]. For violent free-surface events, the interest in the prediction of the initial impact is greater than the propagation of shock waves. The combination of conservation laws with a non-conservative transport equation have proved competent and easier to implement in the past [72].

The objective of this method is to improve the modelling of violent free surface events and their impact on marine structures. As mentioned before in chapter 1, an impact happens in a short time period and to capture this a fine mesh is needed as well as a small time step. When using a non-conservative model, the mass losses due to compressible effects should decrease with an increasing gridsize. With a dense grid, even the compression wave is better modelled [49].

5.3 Comparison with Multiphase model

Comparing with the multiphase model, an additional mass conservation equation needs to be satisfied. The difference with the multiphase model of Wemmenhove (2008) is that the water is changed into a homogeneous mixture. In the multiphase model it is assumed that the liquid is incompressible and has a constant density. The divergence of the velocity in the fluid is equal to zero. In the extended model, the liquid is mixed with a compressible fluid. When looking to the continuity equation of the mixture, it can be rewritten in the following form:

$$\frac{DF}{Dt}\rho_w + \frac{D\rho_w}{Dt}F + F\rho_w\nabla \cdot \mathbf{u} = 0.\tag{5.3}$$

For the multiphase model this results in $\frac{DF}{Dt} = 0$ which is the transport equation used in eq. (3.5). In case of aeration, the equation cannot be simplified in this way. Namely, the assumption is made that the fluid w is a compressible homogeneous mixture which results in $\nabla \cdot \mathbf{u} \neq 0$. This means that the liquid needs to be compressible too as illustrated in fig. 5.2.

For example, in case of the 1D shock tube for separated phases in section 5.5.1, the domain

is completely closed while the interface is moving due to the shock wave. Both fluids in the mixture have the same velocity field, which means that the divergence of the velocity should not be equal to zero. As illustrated, this can lead to compression or expansion.

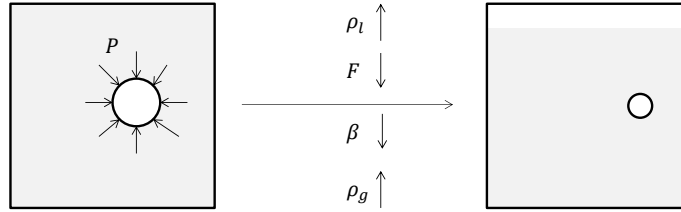


Figure 5.2: Illustration of the effect of pressure on mixture.

The relation $\mathbf{u} \cdot \nabla F = \nabla \cdot (\mathbf{u}F)$ does not hold anymore:

$$\frac{\partial F}{\partial t} + \nabla \cdot (\mathbf{u}F) - F \nabla \cdot \mathbf{u} = 0, \quad (5.4)$$

which is called the standard transport equation. The presented model is comparable to the model developed by Plumerault et al. (2012). However, instead of solving the volume fraction levels using the pressure equilibrium assumption, the transport equation is solved. Further, the presented model is more robust and does not make use of a Riemann solver for the fluxes. The reason to discretize the flux is to preserve the physics and to increase the simplicity of the model. The reduced two-phase model of Kapila et al. (2001) is solved, which results in a different transport equation than given in eq. (5.4). This is elaborated upon in section 5.4.2.

The solution method and the cell labeling do not change comparing with the multiphase model. This is discussed in section 5.4.6. For the temporal discretization, the second-order Adam-Bashforth timestepping scheme is still used. As solution method, the robust projection method (fractional step method) of Rannacher (1991) is used. For the interface representation, SLIC is used and is advanced by using the donor-acceptor method combined with the local height function.

5.4 Numerical model: *Extension*

The governing equations which need to be solved are given in eq. (5.1). This is again done on a fixed Cartesian grid where the variables are staggered. The Poisson equation remains almost the same:

$$dt \nabla \cdot \left(\frac{1}{\bar{C}} \nabla p^{n+1} \right) = \frac{1}{\rho^n} \frac{D\rho}{Dt} - \nabla \cdot \left(\frac{\mathbf{u}^n}{\rho^n} (\rho^{n+1} - \rho^n) \right) + \nabla \cdot \tilde{\mathbf{u}}^n, \quad (5.5)$$

where the striked term disappears for a non-conservative momentum equation. Note that the equation for total mass conservation is used, as also done for the multiphase model, to derive the Poisson equation. However, the fluids are not presented in every cell. In absence of shock waves:

- E-cell $F = 0$: The total mass conservation changes in just only conservation of mass of the air. In case of solving the momentum equation, every phase is conserved. An example is section 5.5.3.
- F-cell $F > 0, \beta \geq 0$: The total mass conservation changes into the conservation of the mixture. Knowing that the mass fraction of the aeration is constant, this equation results in the conservation of the liquid. An example is section 5.5.2.

- S-cell $F > 0$, $\beta \geq 0$: All attending fluids are present. Using the donor-acceptor method and a modified local height function should result in mass conservation. This is discussed in section 5.5.1.

Looking to the Poisson equation, the material derivative as explained before, changes due to the extension. Further, as described in section 5.3, the transport equation changes. The cases as in the order of section 4.3.4 to section 4.3.7 for the multiphase model are discussed.

5.4.1 Material derivative density

As mentioned before, the material derivative of the density derived in section 4.3.4 for the multiphase model is different for the extension. The mass derivative of the density is derived below:

$$\begin{aligned}
\frac{D\rho}{Dt} &= \frac{D(F\rho_w)}{Dt} + \frac{D((1-F)\rho_a)}{Dt} \\
&= \frac{D(F\beta\rho_g + F(1-\beta)\rho_l)}{Dt} + \frac{D((1-F)\rho_a)}{Dt}, \\
&= F \left(\frac{D(1-\beta)}{Dt} \rho_l + \frac{D\rho_l}{Dt} (1-\beta) + \frac{D\rho_g}{Dt} \beta + \frac{D\beta}{Dt} \rho_g \right) + (1-F) \frac{D\rho_a}{Dt} + \\
&\quad \frac{DF}{Dt} (\beta\rho_g + (1-\beta)\rho_l) + \frac{D(1-F)}{Dt} \rho_a, \\
&= F \left(\frac{D\beta}{Dt} (\rho_g - \rho_l) + \frac{D\rho_l}{Dt} (1-\beta) + \frac{D\rho_g}{Dt} \beta - \frac{D\rho_a}{Dt} \right) + \\
&\quad \frac{D\rho_a}{Dt} + \frac{DF}{Dt} (\beta\rho_g + (1-\beta)\rho_l - \rho_a).
\end{aligned} \tag{5.6}$$

The material derivative of F is for this model not equal to zero. The transport equation solved, is different than the standard transport equation given in eq. (5.4) [73]. This is discussed in the next section 5.4.2.

An additional air density ρ_g has appeared. When using the same adiabatic equation of state for both air densities, the Poisson equation can be simplified, using $\rho_g = \rho_a$. However, note that the pressure *cannot be corrected* anymore for the gas pressure as in section 4.3.7. The material derivative as well as the Poisson equation can be simplified. For this an additional volume fraction is made $A = F(1 - \beta)$, indicating the amount of liquid:

$$\begin{aligned}
\frac{D\rho}{Dt} &= \frac{D(F\rho_w)}{Dt} + \frac{D((1-F)\rho_a)}{Dt}, \\
&= \frac{D((F\beta + (1-F))\rho_a + F(1-\beta)\rho_l)}{Dt}, \\
&= \frac{D((1-A)\rho_a)}{Dt} + \frac{D(A\rho_l)}{Dt}.
\end{aligned} \tag{5.7}$$

5.4.2 Transport equation

The transport equation given in eq. (2.21) is a bit different than used in this section. The model used is a zero-order approximation of the model of Baer and Nunziato (1986) with stiff mechanical relaxation. It is important to have fraction values which are **positive** and represent a **sharp interface**. The reduced two-phase model is derived by Kapila et al. (2001). This model is capable to model partly dispersed shock waves, called compression waves.

General form of transport equation

The non-conservative transport equation is found by pressure equilibrium where the material derivative of the entropy is assumed zero [73]. This is called the isentropic constraint which is true for gas, except in shocks or in thin zones of velocity disequilibrium. The quasi-conservative form is given by [96]:

$$\frac{\partial A}{\partial t} + A \nabla \cdot \mathbf{u} + \mathbf{u} \cdot \nabla A = (A + A(1 - A)K) \nabla \cdot \mathbf{u}, \quad (5.8)$$

$$K = \frac{\rho_a c_a^2 - \rho_l c_l^2}{A \rho_a c_a^2 + (1 - A) \rho_l c_l^2},$$

where all parameters except the volume fractions A are on time level $n + 1$. This equation is derived from the pressure equilibrium assumption. The derivation of the transport equation is given in appendix G.1. The right hand side describes the exchange of energy between the two fluids. It ensures pressure equilibrium under compression and expansion by a change in volume fraction [80]. When the right hand side is neglected, the equation becomes a standard transport equation as given in eq. (5.4). This transport equation is not compatible with the isentropic constraint ($\frac{Ds}{Dt} = 0$) along material trajectories for each phase [105]. The transport equation is solved explicitly [118].

Extension COMFLOW

Comparing with COMFLOW, the transport equation solved for the multiphase model is based on the fraction F . To limit the effort to change the code, the same is done for the extended model. Because of a constant mass fraction of aeration and the no-slip condition, it does not matter if the complete mixture is transported or just only the liquid. Therefore, the transport equation in eq. (5.8) is rederived for the fraction F .

In this subsection, the transport equation as function of the fraction F is derived in the same way as in appendix G.1. First, the continuity equations for every fluid is needed:

$$\begin{aligned} \frac{D((1 - F)\rho_a)}{Dt} + (1 - F)\rho_a \nabla \cdot \mathbf{u} &= 0, \\ \frac{D(\beta F \rho_a)}{Dt} + \beta F \rho_a \nabla \cdot \mathbf{u} &= 0, \\ \frac{D(F(1 - \beta)\rho_l)}{Dt} + F(1 - \beta)\rho_l \nabla \cdot \mathbf{u} &= 0. \end{aligned} \quad (5.9)$$

The next step is combine all the equations of the fluids. To do this, it is assumed that the fluids flow isentropically, no heat transfer, leading to a material derivative of the entropy equal to zero. The relation in eq. (G.3) is used to substitute the material derivative of the pressure [80]:

$$\begin{aligned} \textcircled{1} \quad & \frac{(1 - F)}{\rho_a c_a^2} \frac{Dp}{Dt} - \frac{DF}{Dt} + (1 - F) \nabla \cdot \mathbf{u} = 0, \\ \textcircled{2} \quad & \frac{\beta F}{\rho_a c_a^2} \frac{Dp}{Dt} + \beta \frac{DF}{Dt} + F \frac{D\beta}{Dt} + \beta F \nabla \cdot \mathbf{u} = 0, \\ \textcircled{3} \quad & \frac{(1 - \beta)F}{\rho_l c_l^2} \frac{Dp}{Dt} + (1 - \beta) \frac{DF}{Dt} - F \frac{D\beta}{Dt} + (1 - \beta)F \nabla \cdot \mathbf{u} = 0, \end{aligned} \quad (5.10)$$

By summing these equations as is done to derive the equation of total mass conservation in eq. (5.2):

$$\frac{Dp}{Dt} = - \frac{1}{\frac{\beta F + (1 - F)}{\rho_a c_a^2} + \frac{(1 - \beta)F}{\rho_l c_l^2}} \nabla \cdot \mathbf{u}. \quad (5.11)$$

Substituting this in the equation of mass conservation for air in eq. (5.9), the transport equation for the extended model can be derived. The relation for the speed of sound of a mixture, see eq. (2.8) of Wood et al. (2000), is needed to derive the transport equation:

$$\frac{\partial F}{\partial t} + \nabla \cdot (\mathbf{u}F) = \frac{\beta F \rho_l c_l^2 + F(1 - \beta) \rho_a c_a^2}{(\beta F + (1 - F)) \rho_l c_l^2 + F(1 - \beta) \rho_a c_a^2} \nabla \cdot \mathbf{u}. \quad (5.12)$$

The term in the right hand side before the divergence operator is set equal to \hat{H} , see eq. (5.13). The transport equation is solved explicitly, where the fractions are on time level n and the density on time level $n + 1$. How to solve the density at time level $n + 1$ is discussed in section 5.4.4.

$$\begin{aligned} \hat{H}^{n+1} &= \frac{\beta^n F^n \rho_l^{n+1} (c_l^{n+1})^2 + F^n (1 - \beta^n) \rho_a^{n+1} (c_a^{n+1})^2}{(\beta^n F^n + (1 - F^n)) \rho_l^{n+1} (c_l^{n+1})^2 + F^n (1 - \beta^n) \rho_a^{n+1} (c_a^{n+1})^2}, \\ \hat{H}^{n+1} &= \frac{\beta^n F^n \rho_l^{n+1} (c_l^{n+1})^2 + A^n \rho_a^{n+1} (c_a^{n+1})^2}{(1 - A^n) \rho_l^{n+1} (c_l^{n+1})^2 + A^n \rho_a^{n+1} (c_a^{n+1})^2}. \end{aligned} \quad (5.13)$$

Note that the right hand side of the transport equation \hat{H} is almost similar to the right hand side of the transport equation for A in eq. (5.8), called K , and is derived in the same way. The discretization can be splitted in fluxes per cell face using the notation in fig. 3.1:

$$\begin{aligned} \delta F_n &= v_n^{n+1} \delta x_c dt (\hat{H}_c^{n+1} - F_n^n), \\ \delta F_s &= -v_s^{n+1} \delta x_c dt (\hat{H}_c^{n+1} - F_s^n), \\ \delta F_e &= u_e^{n+1} \delta y_c dt (\hat{H}_c^{n+1} - F_e^n), \\ \delta F_w &= -u_w^{n+1} \delta y_c dt (\hat{H}_c^{n+1} - F_w^n), \end{aligned} \quad (5.14)$$

where volume fractions at n , s , e and w are the fractions at the cell faces. Note that these fluxes look like the fluxes of the donor-acceptor method used in eq. (3.37). This indicates that the donor-acceptor may be re-used for the presented model using downwinding or upwinding.

Advancing F in time

The scheme illustrated in eq. (3.39) can also be used for the double fraction model. The transport equation in eq. (5.12) shows similarities. The difference is that an extra term needs to be taken into account; $\hat{H} \nabla \cdot \mathbf{u}$.

Looking to the transport equation, the right hand side shows in areas where $F = 1$ and $\beta = 0$, the transport equation becomes the standard transport equation. This is the case for the fluid l . Further, in areas where $F = 0$ in the air, the total transport equation is zero while $\nabla \cdot \mathbf{u} \neq 0$. This means that the right hand side only has a value where a mixture is present and $\beta \neq 0$.

For the transport equation a similar scheme can be used as the donor-acceptor method. The second term of eq. (5.12) contains the advection term. For this term, the donor-acceptor method is still used. For the explicit scheme, due to the MIN-function the donor cell cannot transport more fluid than it contains on time step n . When looking to eq. (5.4), the third term is a divergence of the velocity, which causes an extra flux. This flux needs to be added to the scheme, in

horizontal direction:

$$\delta F_{adv,f} = \pm \delta S_f \text{MIN} (F_{AD} |u_f \delta t| + AF, F_D \delta x_D). \quad (5.15)$$

When $F_{AD} = F_D$ and $u_f > 0$, the value of $F_D = F_f^L$. However, when $F_{AD} = F_A$ and $u_f > 0$, the value of $F_A = F_f^R$. The value of F_f^R and F_f^L in eq. (D.1) depends on the flux limiter used. How a fluxlimiter works is discussed in appendix D.3. The meaning of superscript "L" and "R" is also given in this section. The term AF is calculated in the same way as in eq. (3.40).

Note that the flux caused by the divergence term is not taken into account in the MIN function, because the divergence term in eq. (5.12) represents the compression of the fluid in cell c . Compression is not part of advection of the fraction at time level n in eq. (5.15) and only depends on the fraction F_c . Because the transport equation is solved explicitly, the advective term and the compressive term can be solved separately.

Additionally, the eq. (3.38) has to be corrected for the compressive term:

$$F_c^{n+1} = F_c^n - \frac{1}{\delta x_c \delta y_c} \left(\sum_{f=n,w,s,e} \delta F_{adv,f} + \sum_{f=n,w,s,e} \delta F_{div,f} \right), \quad (5.16)$$

where:

$$\delta F_{div,f} = \pm \delta S_f \text{MIN}(\hat{H}_c |u_f \delta t|, \hat{H}_c \delta x_c),$$

and \hat{H}_c^{n+1} is equal to F_c^n in case of solving the standard transport equation. To solve for the local height function the equation for F_c^{n+1} can be written as:

$$F_c^{n+1} = F_c^n - \frac{1}{\delta x_c \delta y_c} \left(\sum_{f=n,w,s,e} \delta F_{adv,f} + \delta F_{div,c} \right). \quad (5.17)$$

For the height function of cell (i,j) with a horizontal orientation:

$$H_c^{n+1} = H_c^n - \frac{\sum_{f=n,w,s} \delta F_{f,s} + \sum_{f=n,s} \delta F_{f,c} + \sum_{f=n,s,e} \delta F_{f,n} - \sum_{g=s,c,n} \delta F_{div,g}}{\delta y_c}. \quad (5.18)$$

By assuming pressure equilibrium between the fluids, a closed system is found [96, 118]. The material derivative of the terms F and β , needed for the material derivative of the total density ρ in eq. (5.6), can be derived:

$$\frac{DF}{Dt} = (1-F)(1-\beta)F \frac{\rho_a c_a^2 - \rho_l c_l^2}{(\beta F + (1-F))\rho_l c_l^2 + (1-\beta)F\rho_a c_a^2} \nabla \cdot \mathbf{u}, \quad (5.19)$$

$$\frac{D\beta}{Dt} = (1-\beta)\beta \frac{\rho_l c_l^2 - \rho_a c_a^2}{(\beta F + (1-F))\rho_l c_l^2 + (1-\beta)F\rho_a c_a^2} \nabla \cdot \mathbf{u}. \quad (5.20)$$

The material derivative of the total density ρ can be simplified to:

$$\begin{aligned} \frac{D\rho}{Dt} &= -(1-\beta)F \left(\beta K \nabla \cdot \mathbf{u} (\rho_a - \rho_l) + \frac{D\rho_a}{Dt} - \frac{D\rho_l}{Dt} \right) + \frac{D\rho_a}{Dt} \\ &\quad + (\rho_l - \rho_a)(1-F)(1-\beta)^2 F K \nabla \cdot \mathbf{u}, \\ &= A \frac{D\rho_l}{Dt} + (1-A) \frac{D\rho_a}{Dt} + A(1-A)(\rho_l - \rho_a) K \nabla \cdot \mathbf{u} \end{aligned} \quad (5.21)$$

Comparing to the multiphase model, the extra term is $A(1 - A)(\rho_l - \rho_a)K\nabla \cdot \mathbf{u}$ appears. Using eq. (4.2) for deriving the Poisson equation and defining $\tilde{C} = (\rho^n + (\rho_l^n - \rho_a^n)A^n(1 - A^n)K^{n+1})$ by substituting eq. (5.21), the Poisson equation can be obtained in a similar way as in section 4.3.3:

$$dt\nabla \cdot \left(\frac{1}{\rho^n} \nabla p^{n+1} \right) = \frac{1}{\tilde{C}} \left((1 - A^n) \left(\frac{\rho_a^{n+1} - \rho_a^n}{dt} + \mathbf{u}^n \cdot \nabla \rho_a^n \right) + A^n \left(\frac{\rho_l^{n+1} - \rho_l^n}{dt} + \mathbf{u}^n \cdot \nabla \rho_l^n \right) \right) - \nabla \cdot \left(\frac{\mathbf{u}^n}{\rho^n} (\rho^{n+1} - \rho^n) \right) + \nabla \cdot \tilde{\mathbf{u}}^n. \quad (5.22)$$

Modified local height function

Compared with the multiphase model, for the extended model the local height function is changed. It is shown by Kleefsman et al. (2005) that the use of the local height function for the dam break case reduces the mass loss from 7% to 0.02% in 6[s]. With the presented one-phase model it is tested for the standing wave cases where the result in fig. 3.6 shows that the mass losses are also reduced. In the reports of Kleefsman et al. (2005) and Gerrits (2001) it is mentioned that the local height function is used for every S-cell and is strictly mass conserving when meeting the CFL-criteria. However, the question is if the local height function, consisting of 3×1 cells, is mass conserving in every situation. As illustrated in fig. 3.5, these functions can overlap. Further, the effect of redistributing compressible fluids need to be discussed.

To update the height function, eq. (5.18) is used. Note that these fluxes are based on the old time level of the fraction field, resulting in a height value at the new time level. This means there is no intermediate time step for updating the fraction field. In case of overlapping due applying the local height function on every S-cell, this can lead to contradicting height values at the new time step. A couple of these situations are illustrated in appendix D.2 for incompressible fluids ($\delta F_{div} = 0$). A solution for this is to look to the labels of the neighbouring cells. The update of the fraction field is based on the surrounding cells, a domain of 3×3 cells. The local height function can be applied when it meets the following points:

- When the local height function overlaps with another height function, the local height function which contains the most S-cells is applied to limit the amount of jetsam and flotsam. For the other, no local height function is applied.
- When an empty cell is placed in the negative direction of the normal vector of the free surface, no local height function can be applied to prevent non-physical displacement.

An empty cell in the positive normal direction of the free surface is preferred. Further, for a droplet consisting of two S-cells with opposite orientation, the droplet gets a non-physical velocity using the height function for one of those two S-cells.

In case of using a local height function to redistribute the compressible fluids, the fluxes are based on the already calculated velocity and pressure field. Updating the height value instead of the cells individually, can lead to a change in mass of the compressible fluid. When the fluids are redistributed, based on the updated height value, the fluids pushed into cells where the pressure can be different. This results in a different density value and a change in mass. Due to this effect, the local height function cannot be considered as a physical application.

To reduce this effect, the local height function can only be used when it consists of the labels F , S , and E . In this case the local height function is not used anymore as a function which

pushes the water to the free surface. However, this is not applied on the extended model because this cannot lead to a less sharp distinction between the fluids. This is not beneficial for the transport equation, discussed in section 5.4.2.

Due to using the local height function for the curvature, it can have asymmetrical properties when the fraction field is updated. In the original method the free surface displacement is calculated using a for loop over the grid. To solve this problem, the displacement algorithm *VFLUP* can be used. The free surface is advected first before the internal cells are advected [83].

In case of the extended model, the height function is used in a way as discussed above. Using these restrictions, the mass of water is conserved in chapter 3 and chapter 4. However, due this decrease in application, the question arises if the local height function, in combination with SLIC, still can maintain the sharp interface needed for the transport equation [73].

Droplets

A cell is labelled as flotsam when the cell contains liquid while the surrounding cells are empty. Using the free surface displacement algorithm of Hirt and Nichols (1981), the bubbles, smaller than a cell size, are not transported anymore. To solve this, an additional transport equation can be solved as is done by Wemmenhove (2008) for air bubbles. However, it need to be prevented that the bubbles are tracked to reduce the computational costs. The drag effects and deviations of the bubble are not included in the model. This is allowed when the macroscopic behavior is of major interest. Another solution could be to redistribute the bubble so that it contains an F-cell and exists of multiple cells. However, the treatment of droplets is left out of scope.

5.4.3 Convective density term

Besides the material derivative of the density, also the convective density term in the Poisson equation changes in the same way as in the multiphase model. The difference is that also the density of the water is compressible and can change in time. Note that this is only done when the conservative momentum equation is solved, discussed in section 4.3.3:

$$\nabla \cdot \left(\frac{\mathbf{u}^n}{\rho^n} (\rho^{n+1} - \rho^n) \right) = \nabla \cdot \left(\frac{\mathbf{u}^n}{\rho^n} \left((1 - A^n) (\rho_a^{n+1} - \rho_a^n) + A^n (\rho_l^{n+1} - \rho_l^n) \right) \right). \quad (5.23)$$

Substituting this equation in eq. (5.22), results in an updated Poisson equation using the non-conservative momentum equation:

$$\begin{aligned} dt \nabla \cdot \left(\frac{1}{\rho^n} \nabla p^{n+1} \right) = \\ \frac{1}{\bar{C}} \left((1 - A^n) \left(\frac{\rho_a^{n+1} - \rho_a^n}{dt} + \mathbf{u}^n \cdot \nabla \rho_a^n \right) + A^n \left(\frac{\rho_l^{n+1} - \rho_l^n}{dt} + \mathbf{u}^n \cdot \nabla \rho_l^n \right) \right) \\ - \nabla \cdot \left(\frac{\mathbf{u}^n}{\rho^n} \left((1 - A^n) (\rho_a^{n+1} - \rho_a^n) + A^n (\rho_l^{n+1} - \rho_l^n) \right) \right) + \nabla \cdot \tilde{\mathbf{u}}^n. \end{aligned} \quad (5.24)$$

5.4.4 Equation of state

To find the densities for the next time step, an equation of state is used. While for the gas eq. (4.34) is used, the adiabatic version of the stiffened equation of state can be used for the

liquid. This equation is called Cole equation of state [30]:

$$\rho_l = \rho_{l,0} \left(\frac{\gamma_l p_l + p_c}{\gamma_l p_{atm} + p_c} \right)^{\frac{1}{\eta}}. \quad (5.25)$$

Note that this equation mispredicts the heat capacity of water. When using this equation for the air density, the value of p_c is equal to zero and $\gamma=1.4$. For water the value for p_c is $23 \cdot 10^8 [Pa]$ and γ is 7.0 [30].

Besides the Cole equation of state, the choice can also be made to use a linear relation between the density and pressure in water by using a constant sound propagation [118]. Here the speed of sound for water is assumed constant:

$$\rho_l = \rho_{l,0} + \frac{p_l - p_{atm}}{c_{l,0}^2}. \quad (5.26)$$

Note that the derivative $\frac{d\rho_l}{dp}$, needed for the Newton approximation in eq. (4.30), becomes easier than the Cole equation of state. Further, no extra step to calculate the speed of sound for the liquid is needed. When using water, assuming a constant speed of sound is reliable [118], see eq. (2.4). The Poisson equation can be filled in again:

$$\begin{aligned} dt \nabla \cdot \left(\frac{1}{\rho^n} \nabla p^{n+1} \right) = & \\ & \frac{1}{\bar{C}} \left((1 - A^n) \left(\frac{1}{dt} \left((p^{n+1} - p^*) \frac{\rho_a^* p^*}{\gamma_a + p_{c,a}} + \rho_a^* - \rho_a^n \right) + \mathbf{u}^n \cdot \nabla \rho_a^n \right) \right. \\ & + A^n \left(\frac{1}{dt} \left((p^{n+1} - p^*) \frac{\rho_l^* p^*}{\gamma_l + p_{c,l}} + \rho_l^* - \rho_l^n \right) + \mathbf{u}^n \cdot \nabla \rho_l^n \right) \\ & \left. - \nabla \cdot \left(\frac{\mathbf{u}^n}{\rho^n} \left((1 - A^n) (\rho_a^* - \rho_a^n) + A^n (\rho_l^* - \rho_l^n) \right) \right) + \nabla \cdot \tilde{\mathbf{u}}^n. \end{aligned} \quad (5.27)$$

After solving the new pressure and velocity by iterating, the transport equation is solved. Note that the velocities are defined at the cell faces (staggered grid). The discretization is based on fig. 3.1. When using eq. (5.25) for calculating the speed of sound:

$$\begin{aligned} \frac{\partial \rho}{\partial p} &= \frac{1}{c^2}, \\ \frac{1}{c^{n+1}} &= \sqrt{\frac{\rho_0}{(\gamma p_{atm} + p_c)^{\frac{1}{\gamma}} (\gamma p^{n+1} + p_c)^{\frac{1}{\gamma} - 1}}}. \end{aligned} \quad (5.28)$$

5.4.5 Constant mass fraction

When the mass fraction is assumed constant, the fraction β can be found for every cell:

$$\begin{aligned} y &= \frac{m_a}{m_w}, \\ y &= \frac{\rho_a V_a}{\rho_w V_w}, \\ \rho_w V_w y &= \rho_a V_a, \\ F \delta x \delta y \rho_w y &= \rho_a F \beta \delta x \delta y, \\ y \rho_w &= \beta \rho_a \\ \beta &= \frac{y \rho_l}{(1 - y) \rho_a + y \rho_l}, \end{aligned} \quad (5.29)$$

where the densities are found by using the equation of state in section 5.4.4. Note that the change of $(1 - F)$ to β is not possible. This leads to a non-uniform mass fraction (y) field and $\frac{Dy}{Dt} \neq 0$. The mass fraction can be found at the beginning of the simulation by the input of initial aeration level β_0 :

$$y = \frac{\beta_0 \rho_{a,0}}{(1 - \beta_0) \rho_{l,0} + \beta_0 \rho_{a,0}}. \quad (5.30)$$

5.4.6 Sequence of calculation

For the solution method, exactly the same method is used as for the multiphase model given in section 4.3.3. The fractional step method is used, combined with the second-order Adams-Bashforth time scheme and the second-order upwind scheme for the convection term.

However, the cyclus of the calculation of the next time step is increased with respect to the multiphase model. During each time step, the variables A and β also need to be calculated. This is illustrated in fig. 5.3.

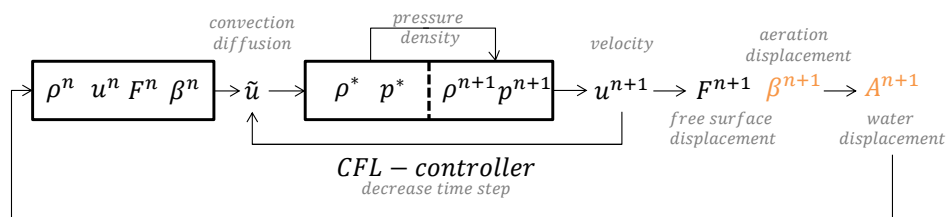


Figure 5.3: Calculation sequence of the variables for compressible double fraction model during a time step.

Additionally, a CFL-controller is implemented, which decreases the timestep when the CFL-criteria is not met. The pseudo code of this controller is given in appendix G.2.

Before starting the simulation, an iteration needs to be done for the initial conditions, resulting in a fraction field β of values between 1 and 0. The pressure is solved by a self-implemented Successive Over Relaxation code by solving the Gauss-Seidel method and the equation $x^{(\omega)} = (1 - \omega)x^{old} + \omega x^{new}$, where x^{new} is the result of an iteration step using the Gauss-Seidel scheme. The extended model is completely coded in FORTRAN 90. In appendix G.3 it is analytically proven that the model should represent the acoustics of the mixture, based on the derivation of Plumerault (2009).

5.5 1D Shock tube

The shock tube problem is a case which is often used for the validation of a compressible model [37, 80, 96, 100, 118]. With this case it is possible to show that the model is capable to reproduce the speed of sound of a dispersed flow as well as a separated flow. It is mentioned in section 2.3 that the speed of sound is related with the compressibility of a mixture. Note that the multiphase model in chapter 4 is not capable to reproduce shock waves in water, because it does not take into account the compressibility of the liquid. Further, it is known that the presented model is not capable to model shock waves. A shock wave represents a discontinuity in the pressure while the double fraction model smears out the discontinuity over a couple of cells.

This is called a compression wave instead of a shock wave.

A shock tube consists of two tubes with the same cross section separated by a diaphragm. In one tube, high pressure (p_4) can be found, called the driver. The other tube contains low pressure (p_1): the driven section. By removing the diaphragm, a rarefracting wave is generated which propagates into the driver section. At the same time, a contact surface is generated which propagates behind the shock front into the driver section. In fig. 5.4 the different stages in pressure with reflection at the wall are indicated.

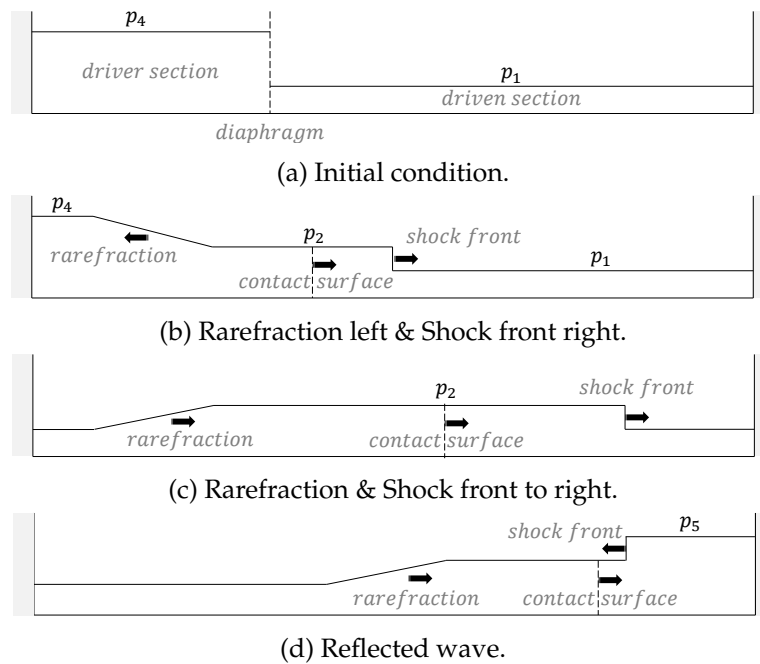


Figure 5.4: Different stages by shock tube for same liquid [38].

The pressures p_4 and p_1 are defined as initial condition. This will result in a pressure p_2 which depends on the ratio of the specific heat at constant pressure and at constant volume of the driven gas (γ), pressure p_1 and the Mach number of the advancing shock wave [38].

The compressible model will be validated for several cases to demonstrate the ability to resolve rarefaction waves and contact discontinuities. Shock waves are likely to happen around the wave impact zone [114]. The first case will be a shock wave between two **Seperated fluids** fluids divided by a membrane in section 5.5.1 [100]. In the second case a shock wave is produced in a **Mixture** in section 5.5.2; water containing air [96, 118]. At the end, the model is tested to reproduce **Reflection** of a wave in air at a wall in section 5.5.3 [38]. In all cases, the simulation is 1D and the domain has a length of 1[m].

5.5.1 Seperated fluids

In the first case, a shock wave between two liquids is modelled as a seperated flow. It is similar to the 1D Sod shock tube problem but than with two phases [131]. The equation of state, as

described in section 5.4.4, is different for this case. The equations are given:

$$\begin{aligned} \rho_l &= p & \frac{1}{c_l^2} &= 1 \\ \rho_a &= \left(\frac{p}{1.34543}\right)^{\frac{1}{\gamma_a}} & \frac{1}{c_a^2} &= \frac{1}{1.34543\gamma_a} \left(\frac{p}{1.34543}\right)^{\frac{1-\gamma_a}{\gamma_a}} \quad \gamma_a = 1.25. \end{aligned} \quad (5.31)$$

These equations correspond with the case done by Miller et al. (2013). The final time of the simulation is $t=0.25[s]$. This is before the rarefaction and the shock front reaches the boundary. Further, the viscous and gravity terms are neglected. No-penetration boundary conditions are applied and the pressure is described at $x=0$. The initial conditions are specified as:

$$F = \begin{cases} 1, & x < 0.5 \\ 0, & x > 0.5 \end{cases}, \quad u = 0, \quad p = \begin{cases} 1.0, & x < 0.5 \\ 0.1, & x > 0.5 \end{cases}, \quad \rho = \begin{cases} 1.0, & x < 0.5 \\ 0.125, & x > 0.5 \end{cases}$$

The simulation is done for a couple of different meshes; 100, 200, 400, and 800 cells. Besides the different meshes, also different fixed time steps are used; $3.13 \cdot 10^{-4}$, $6.25 \cdot 10^{-4}$, $12.5 \cdot 10^{-4}$, $25 \cdot 10^{-4}$ [s]. This is done to find the order of convergence by looking to the "water" mass loss. The Richardson extrapolation is used which showed that due to decreasing the timestep as well as increasing the amount of cells results in monotonic converging [42].

By decreasing the time step, a convergence of $\mathcal{O}(dt^{0.91})$ up to $\mathcal{O}(dt^{1.05})$ is found. This corresponds with the explanation given in section 4.3.3 for the fractional step method.

For the convergence in spatial dimensions and fixed time step of $3.13 \cdot 10^{-4}[s]$, an order of $\mathcal{O}(dx^{1.11})$ up to $\mathcal{O}(dx^{1.34})$ is reached for the liquid mass. The same order found as in section 4.5.1. However, for the convergence of the total mass, values of $\mathcal{O}(dt^{0.89})$ up to $\mathcal{O}(dt^{1.10})$ are found.

The gas-mass value is not converging to the initial value and reaches sometimes even values above the initial conditions. The total mass loss, like the displacement of the wave front, is linear in time.

The mass loss can be explained by the non-conservative transport equation. The mass loss of "water" and total mass is 0.08% and 0.9%, respectively. However, the loss in "air" was up to 7% for 800 cells and a fixed timestep of $10^{-4}[s]$. Looking to the initial conditions, the total mass of "air" is eight times smaller than the "water" which means that a small mass loss in "air" is easier to notice.

According to Miller et al. (2013), due to strongly enforcing the equations of state instead of solving the energy conservation done by Sod (1978), energy losses can be transformed into mass losses. However, this is not proven. With the fractional step method, total mass conservation is enforced, discussed in section 3.3.3 [26].

Besides looking to the convergence of the mass loss, the results are compared with the results of Miller et al. (2013). The model of Miller et al. (2013) is a pressure-based, compressible, two-phase flow finite volume method which is quite similar to the model used in this report. However, for the extended model it is not possible to simulate air-water mixtures and makes use of an implicit method due to the transport equation in section 5.4.2.

Similar results as the non-conservative model of Miller et al. (2013) are found. The results are compared with the analytical solution shown in fig. 5.5. Note that the illustrated results are found by using a Van Leer limiter and the local height function, to show that the flux limiter works. In the results it can be noticed that the velocity u is overestimated, causing a front which

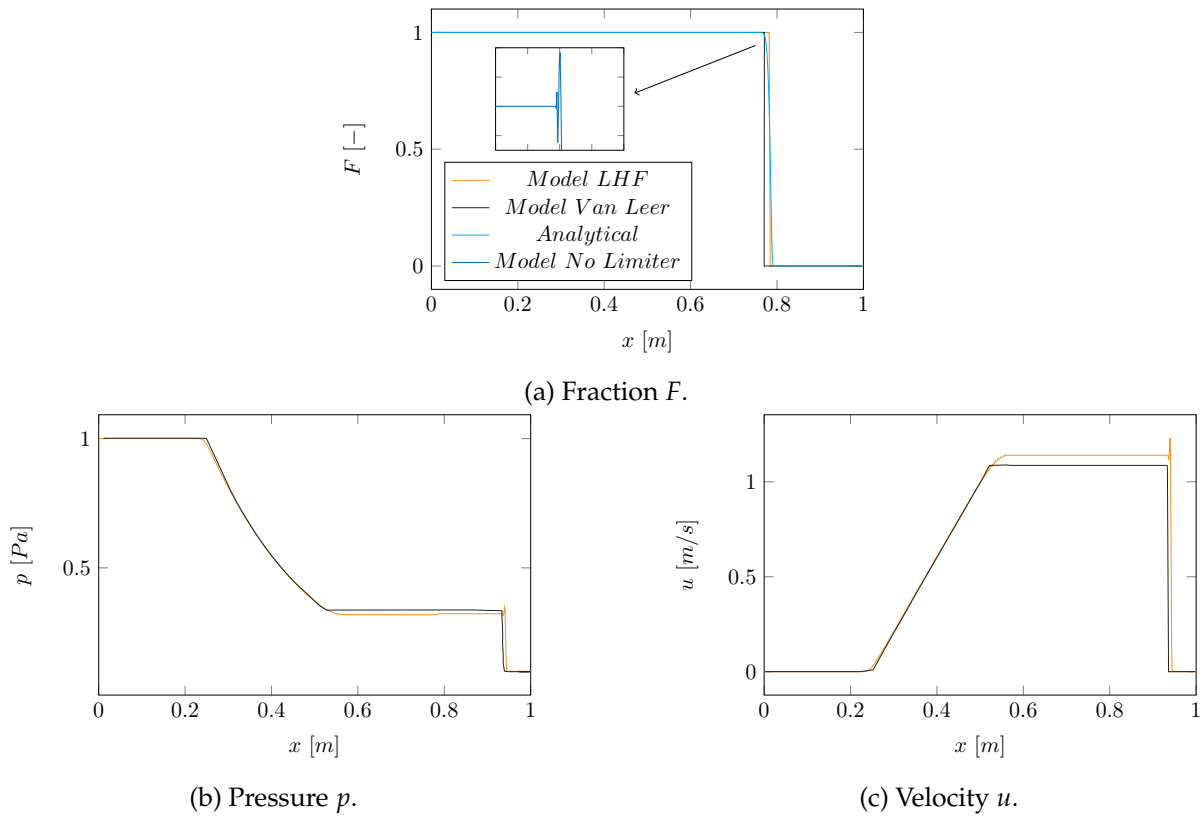


Figure 5.5: The effect of flux limiter and results of shock tube in separated fluids on $t=0.25[s]$ for $dt=1 \cdot 10^{-4}[s]$ and $N=800$.

is further displaced than the analytical solution. The pressure p_2 is almost 5% lower than the analytical solution described by Miller et al. (2013). The difference in pressure can partly be explained by the loss in mass.

The difference in pressure area where the "water" is present, is in the order of 0.1%, like the mass loss of water. If the same is done for the air, by taking into account the equation of state used, a mass loss in the order of 6.7% is found. When the model is solved no splitting error for the momentum, as discussed in section 3.3.3, is experienced.

A non-conservative momentum equation is solved which can contribute to the error, discussed in section 5.2. The difference in pressure causes a change in the speed of sound in eq. (5.28) which affect the Mach number and the velocity.

5.5.2 Mixture

For the second case, the analytical model presented by Franquet (2006) for a mixture shock tube is used. In this analytical model also stiffened gas equations of state are used. However, in the model represented by this report, no energy conservation equation is solved. The initial parameters for a computational domain with a length of $1[m]$ and $F = 1$. This means that for this case no transport equation has to be solved. The equation of states described in section 5.4.4, are used for air and water:

$$\beta = \begin{cases} 0.00194716, & x < 0.5 \\ 0.01, & x > 0.5 \end{cases}, \quad u = 0, \quad p = \begin{cases} 10^6, & x < 0.5 \\ 10^5, & x > 0.5 \end{cases}$$

$$\rho_a = \begin{cases} 6.908, & x < 0.5 \\ 1.33, & x > 0.5 \end{cases}, \quad \rho_l = \begin{cases} 1027.4, & x < 0.5 \\ 1027, & x > 0.5 \end{cases}$$

The initial air mass fraction in both parts of the tube is $y=1.311810 \cdot 10^{-5}$. The final time of the simulation is $t=5.5137 \cdot 10^{-4}$ [s] and the amount of computational cells is 800. The fixed time step is $dt=1.66 \cdot 10^{-7}$ [s].

For this case, the total mass is nearly conserved. One percent in air mass is gained, which might be caused by numerical errors gained due to solving the density and the velocity in a different step (fractional step method), discussed in section 3.3.3 [26]. The ratio between the density of water and air is ≈ 1000 . This means the air is more sensitive to errors.

Looking at the results in fig. 5.6, the pressure p_2 is well presented. As explained before this pressure depends on the Mach number of the advancing shock wave, the pressure p_1 and the specific heat constant [38]. The Mach number depends on the speed of sound which means that the extended model well presents the speed of sound of the dispersed flow. The maximum error is 0.4%.

The observed pressure oscillations can be caused by the discontinuity in the solution. By the Gauss' divergence theorem, the assumption is made that the function is continuous. Further, in section 4.3, it is discussed that the non-conservative momentum equation only can solve continuous velocity fields. It is shown in section 5.5.3 that these oscillation decreases when the amount of cells increases. This corresponds with the experiences of Lamnaouer (2010) who also found that the oscillations decrease with increasing the grid resolution. When using a finite volume discretization, a stable solution without unphysical numerical oscillations and nonlinear instabilities is not possible without introducing a numerical dissipation or increasing the mesh resolution at the position of the shock [86].

The step in the analytical results at $0.5 < x < 0.6$ is caused due to the temperature change. This is not solved by the presented model.

5.5.3 Reflection

Besides calculating the convergence, also a simulation to reflect the compression wave is done. Note that the boundary conditions need to be changed. The pressure boundary condition has to be changed from a Dirichlet boundary condition to a Neumann boundary condition to reflect the shock wave. At both sides, the pressure gradient at the wall needs to be zero. There are two propagating fronts; the shock front and the rarefaction [38]. Note that in this case the pressure needs to be calibrated. For this case, the non-conservative transport equation is not solved.

To validate the reflecting shock front, pressure p_5 of fig. 5.4 has to be known. This pressure depends on the ratio p_2/p_1 and the specific heat ratio γ . The initial parameters for a computational domain with a length of 1[m], 400 cells and $F=0$:

$$p = \begin{cases} 10^6, & x < 0.5 \\ 10^5, & x > 0.5 \end{cases}, \quad u = 0, \quad \rho_a = \begin{cases} 6.908, & x < 0.5 \\ 1.33, & x > 0.5 \end{cases}$$

The fixed time step is $dt=3.33 \cdot 10^{-7}$ [s]. The resulted pressure p_2 is equal to 324[kPa]. Further, the speed of the shock front is around 550[m/s]. Using the equation of state in eq. (5.28), based on the properties of the driven section, a speed of sound is found of 324.44[m/s] is found which

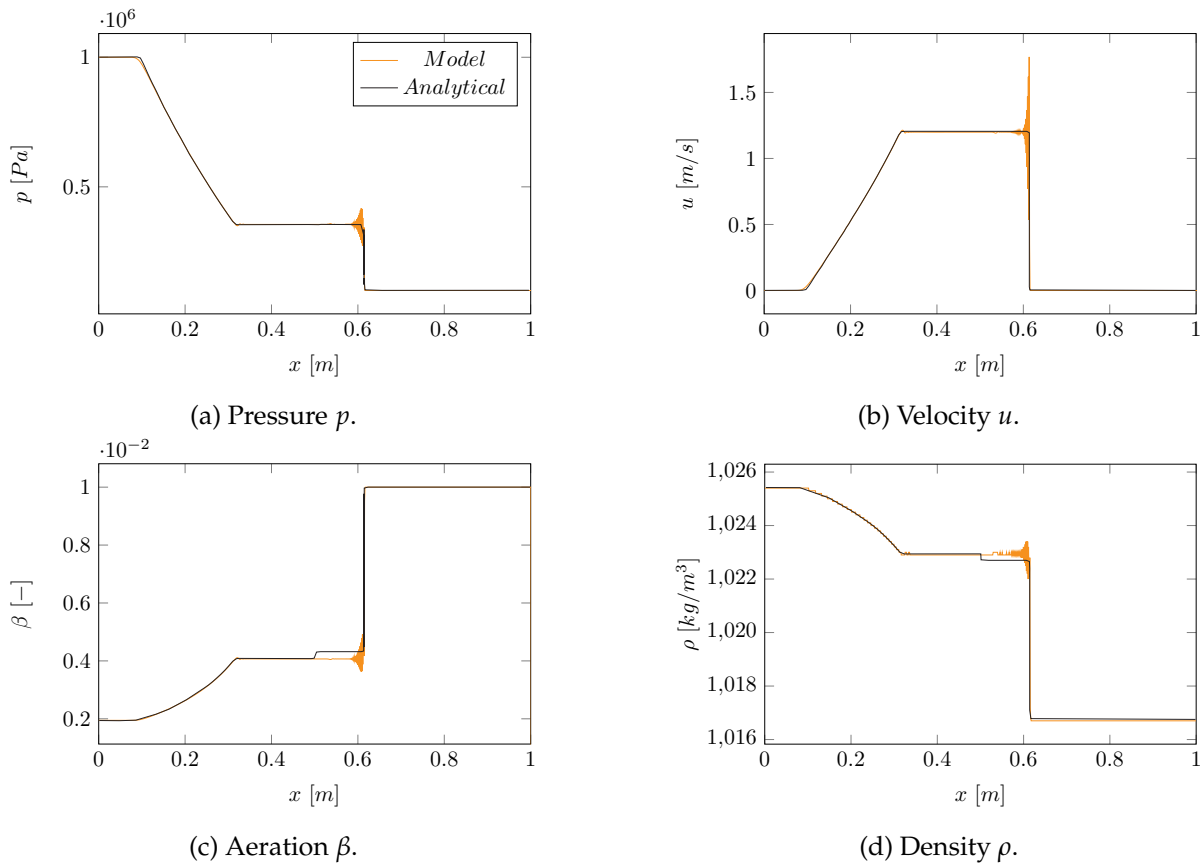


Figure 5.6: Shock in fluid mixture at $t = 55.137 \cdot 10^{-5}$ [s].

results in a Mach number of 1.705. The equation for p_2 according to Downes et al. (2014) is:

$$p_2 = p_1 \left(1 + \frac{2\gamma_1}{\gamma_1 + 1} (Ma^2 - 1) \right). \quad (5.32)$$

This results in $Ma=1.708$ which verifies eq. (5.32). Knowing that for air the specific ratio is $\gamma=1.4$, the pressure p_5 can be calculated [38]:

$$p_5 = p_2 \left(\frac{8 \cdot 10^{-5} p_2 - 1}{10^{-5} p_2 + 6} \right). \quad (5.33)$$

This results in p_5 equal to $875[kPa]$. When doing the simulation, a pressure of $p_5=915[kPa]$ is found. The difference may be caused by the loss of air of ≈ 1 percent.

The numerical oscillations found after reflection may be caused by the imposed boundary conditions. This could be solved by using characteristic boundary conditions for the acoustic waves [119].

Using more elements, $N=600$ with fixed timestep of $dt=3.33 \cdot 10^{-7}$ [s], a pressure of $p_2=324.5[kPa]$ and $p_5=908.7[kPa]$ is found. According to eq. (5.33), the pressure p_5 should be equal to $878[kPa]$. It can be concluded that the error seems to decrease with the amount of elements. Further, it is important to note that the height and range of the wiggles decreases with the amount of elements. The results are plotted in fig. 5.7. The numbers indicate the order in time. In the results pressure oscillations are found which may be caused by the discontinuity, explained in

section 5.5.2.

Comparing the wiggles occurring by p_5 , for grid resolution 100 the peak value is $1.75 \cdot 10^3 [kPa]$, for grid resolution 200 the peak value is $1.17 \cdot 10^3 [kPa]$, for grid resolution 300 the peak value is $1.05 \cdot 10^3 [kPa]$, for grid resolution 400 the peak value is $1.01 \cdot 10^3 [kPa]$ and for gridsize 600 the peak value is $0.98 \cdot 10^3 [kPa]$. This means that the maximum of the pressure oscillation after reflection is converging with $\mathcal{O}(dx^{2.3})$.

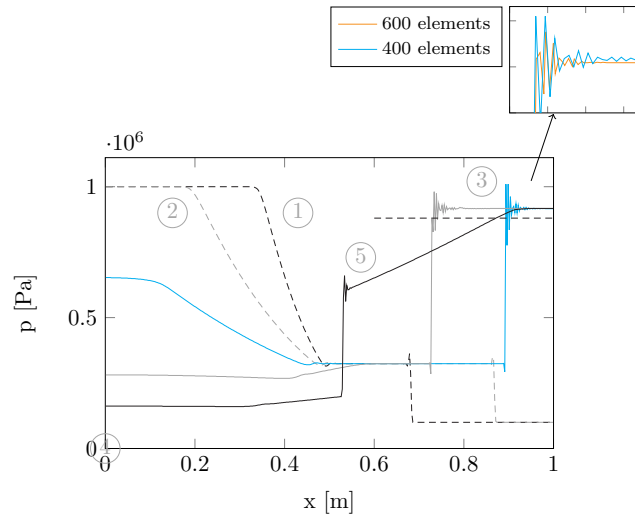


Figure 5.7: Reflected shock front in order of time for 400 elements.

5.6 2D Shock bubble interaction

The shock bubble interaction experiments are well documented by Haas and Sturtevant (1987). Besides modelling a shock between two fluids and through mixture, with this case it is shown that the presented model is capable to reproduce compression waves through a 2D bubble. During a green water event, an air pocket can be entrapped generating pressure waves affecting other pockets.

The experimental results can be used as benchmark for evaluating physical models and computational methods for compressible two-fluid flows [80, 120]. The experiment is done for a spherical and cylindrical bubble. Because the present model is described in 2D, the results of the cylindrical bubble, made of *helium*, are used as verification. The setup for the simulation is shown in fig. 5.8 for a grid resolution of 400×50 for the half of the cylinder, resulting in a grid spacing of $0.89 [mm]$. The boundary conditions are free-slip and no penetration on all walls. This means that the domain is closed. The pressure is prescribed at the right boundary. Further, the initial conditions for the setup are described in table 5.1. Note again that the model only is capable to model compression waves. The same notation for the pressures as in fig. 5.4 is used.

The generated shock wave has a high velocity comparing with the size of the bubble. In the experiment it is observed that the shock passes the bubble in about $10^{-4} [s]$. The deformation of the cylindrical bubble strongly depends on the kind of gas inside the bubble. Before the simulation results are shown, the pressure waves which can occur during the simulation are

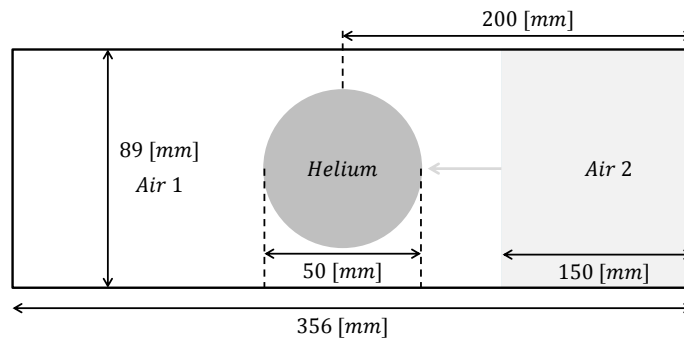


Figure 5.8: Shock bubble interaction setup.

	γ [—]	ρ [kg/m ³]	p [kg/ms ²]	F [—]	β [—]
Air 1	1.4	1.4	$1.0 \cdot 10^5$	1.0	0
Air 2	1.4	2.616	$2.40 \cdot 10^5$	1.0	0
Helium	1.67	0.25463	$1.0 \cdot 10^5$	0	0

Table 5.1: Initial conditions and gas properties for the shock bubble interaction simulation.

discussed. The different waves are illustrated in fig. 5.9 [80].

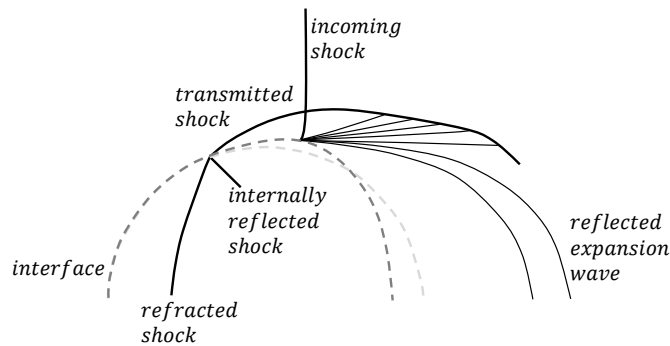


Figure 5.9: Illustration of different pressure waves at the interface of the cylinder.

The bubble exists of helium. This gas has a lower density and higher ratio of specific heat than air. This results in a higher speed of sound for the gas. Due to the higher speed of sound, the refracted shock in the Helium bubble runs ahead of the incoming shock outside the bubble. The reflected wave, occurring at the beginning of the bubble, is an expansion wave. The refraction appears to be irregular because the refracted wave intersects the interface ahead of the other waves. This results in a transmitted wave on the place where the refracted wave hits the interface of the bubble. The transmitted wave will partly deflect the incoming shock between the transmitted wave and the interface of the bubble. The incoming shock and transmitted shock wave together form a shock called λ [80].

The pressure of the shock (p_2) at Air 2, in the results of Nourgaliev et al. (2006) and Kreeft and Koren (2010) is equal to $1.57 \cdot 10^5$ [Pa]. To achieve this pressure value in a closed domain, the

pressure p_4 has to be equal to [4]:

$$p_4 = p_2 \left(1 - \frac{(\gamma - 1) \frac{c_1}{c_4} \left(\frac{p_2}{p_1} - 1 \right)}{\sqrt{2\gamma (2\gamma + (\gamma + 1) \left(\frac{p_2}{p_1} - 1 \right))}} \right)^{\frac{-2\gamma}{\gamma - 1}}. \quad (5.34)$$

By doing an iteration for the equation above, a pressure for $p_4=2.40 \cdot 10^5 [Pa]$ is found, where $\rho_{a,0}=1.4 [kg/m^3]$ and $p_0=10^5 [Pa]$. When looking to the 1D shock tube case in section 5.5.1, it is known that the pressure level of p_2 is underpredicted by the model. The resulting value for p_2 found in the simulation is $1.544 \cdot 10^5 [Pa]$ and the density $\rho_2=1.91 [kg/m^3]$ which slightly underpredicts (1.5% and 0.9 respectively) the values used by Kreeft and Koren (2010).

For the air gas and the helium gas, still the adiabatic equation of state is used. However, it is known that a small difference in density is found compared with Kreeft and Koren (2010) and Quirk and Karni (1996).

The method of Quirk and Karni (1996) make use of two-component compressible Euler equations. In this method five equations are solved, including the energy equation, and a non-conservative shock-capturing scheme is used. Making use of a grid refinement algorithm, the effective grid resolution is equivalent to a uniform mesh of $16,000 \times 800$ with a spatial resolution of $0.056 [mm]$.

The method used by Kreeft and Koren (2010) is based on Kapila's five equation model [73] for an inviscid compressible two-fluid flow. This means that a similar non-conservative transport equation is used. However, the method solves also the energy equation and makes use of Osher's Riemann solver for the flux evaluation. The system is solved with a third-order accurate, three-stage explicit TVD Runge-Kutta scheme which should make the model more advanced than the presented model. The domain contained 800×200 cells which leads to a cellsize of $0.22 [mm]$, four times smaller than the case discussed in this section.

During the simulation a couple of velocities are measured and compared with the experimental results of Haas and Sturtevant (1987), the computational results of Kreeft and Koren (2010) and Quirk and Karni (1996). The notation of the velocities is illustrated in fig. 5.10a. The measuring time starts when the shock front hits the right interface of the helium bubble. The results of the present model are compared in fig. 5.10b with the results of the model used by Quirk and Karni (1996). It can be noticed that similar results are obtained with the presented model. It is visible that the downstream interface moves later than the upstream interface. Further, the shock front in the helium bubble has a different speed than the resulting shock front in the air.

When zooming in on the results, it can be noticed that every speed of the compression wave is underpredicted in location. This is because the non-conservative form of the Navier-Stokes equations is solved which can lead to the underprediction of the location of shock waves [49, 72].

The resulting values for the velocities of the waves are illustrated in table 5.2. The first four speeds (v_s, v_r, v_t and v_{ui}) are measured until $t=2.67 \cdot 10^{-4} [s]$. Further, v_{di} is based on the whole simulation until $6.7 \cdot 10^{-4} [s]$. The jet velocity v_j is measured after v_{ui} . Instead of one value, ranges are found due to not accurately knowing where the compression wave is in the cell. It can be concluded that the robust model, even with a non-conservative method and greater cell size, can obtain similar result. The computed speeds show a good similarity with the other

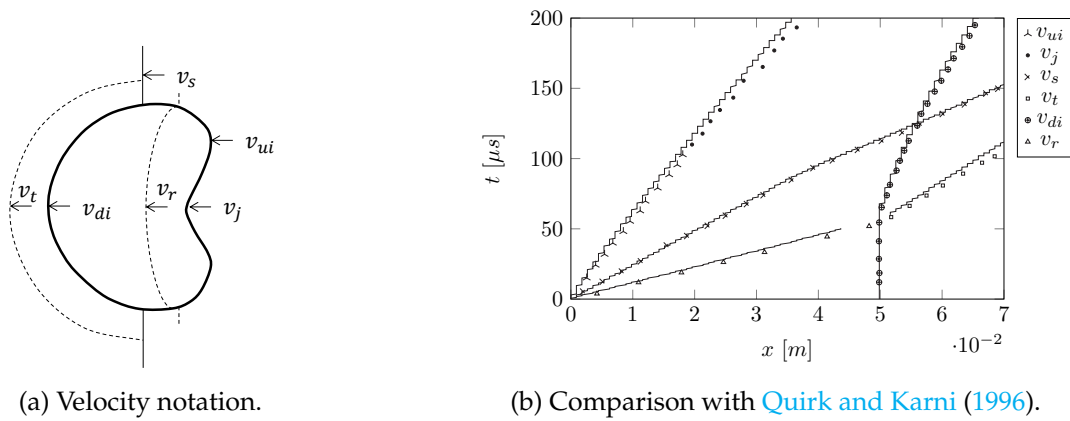


Figure 5.10: Velocity notation shock cylinder; continuous lines: present model, figures: model of Quirk and Karni (1996)

	v_s	v_r	v_t	v_{ui}	v_{di}	v_j
Haas and Sturtevant (1987)	410	900	393	170	145	230
Quirk and Karni (1996)	422	943	377	178	146	227
Kreeft and Koren (2010)	419	956	-	176	-	-
Present model	423-425	890-952	360-368	177-184	130-136	196-210

Table 5.2: Resulting velocities in [m/s] for 2D helium cylinder.

speeds given in table 5.2, especially with the results of Quirk and Karni (1996).

In fig. 5.12 the resulting images of the simulation are illustrated. These are plotted for two different colormaps and compared with the experimental results of Haas and Sturtevant (1987) and computational results of Quirk and Karni (1996). The white line indicates the initial bubble.

All the features of the interaction process seem to be reproduced. Starting with fig. 5.12(a), a curved refracted shock is visible in the helium bubble (v_r) propagating faster than the incident shock (v_s). The refracted shock interacts with the transmitted wave (v_t) which leads to a deflected interface. This transmitted wave arises where the refracted wave hits the interface. Besides the transmitted shock, the refracted shock also causes an internal reflected shock. This one is weakly visible in fig. 5.12(c). A schematic drawing of this process is made by Kreeft and Koren (2010), illustrated in fig. 5.11.

The refracted shock leaves the bubble and continues in the air as a circular transmitted wave with a different speed. When the internally reflected waves cross each other, a loop expanding to the interface appears. This is illustrated in fig. 5.12(e).

In fig. 5.12(f), the waves completely cross the interface and are propagating further as a compression wave. A jet is penetrating the bubble at the upwind interface and rolls up the bubble. Hereafter, in fig. 5.12(c) the bubble starts to move when the refracted wave hits the downwind interface.

The pressure in the bubble and the volume fraction over time are illustrated in appendix G.4. At the end, a loss of total mass of 2% is found. The loss of mass was nearly linear in time as in the case of section 5.5.1. It is found in section 5.5 that the mass loss decreases by decreasing the timestep and increasing the resolution.

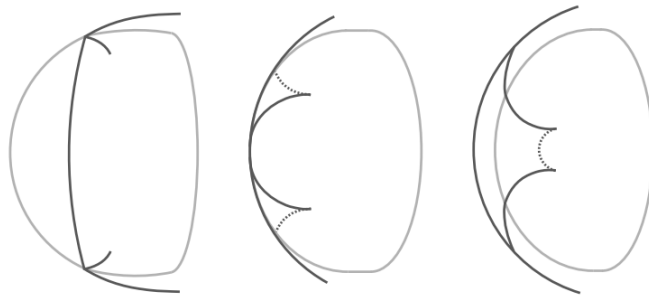


Figure 5.11: Schematic drawing of the waves inside the Helium bubble corresponding with fig. 5.12(b)-(d) [80]; dotted line is relatively weak pressure waves, dark line is strong pressure waves.

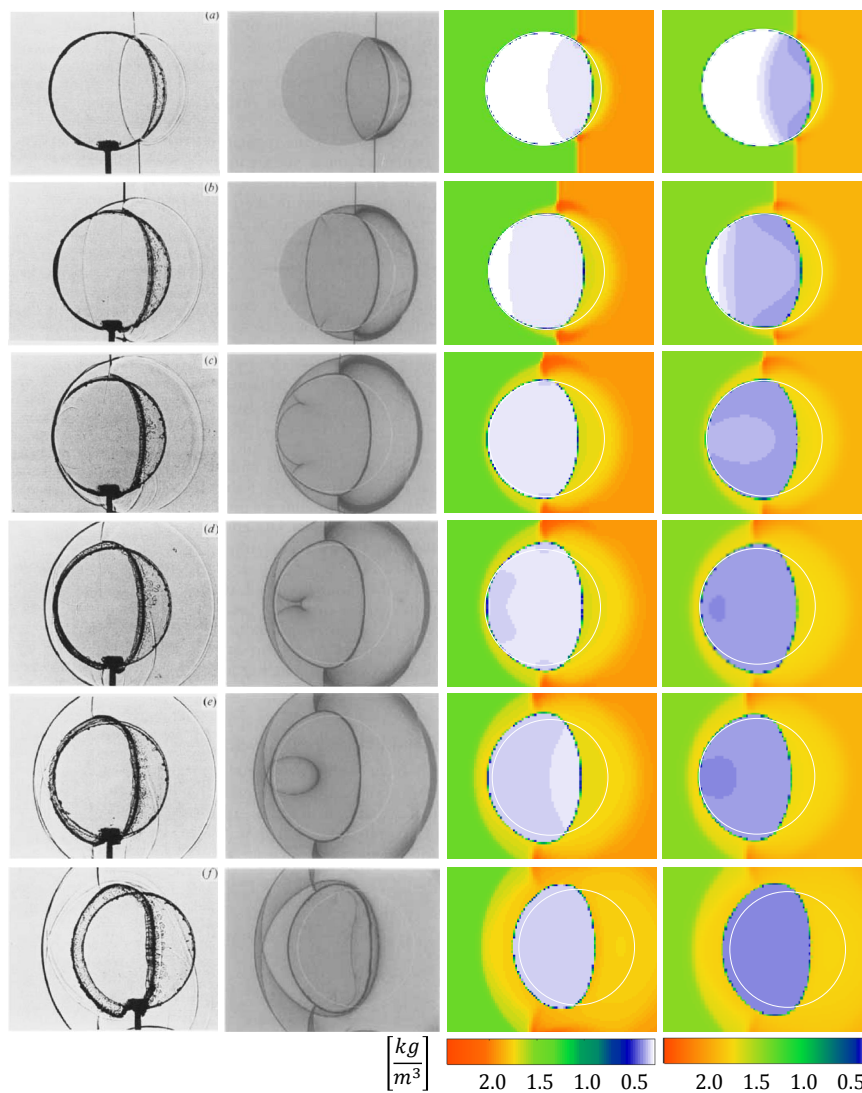


Figure 5.12: Sequence of images of the density in $[kg/m^3]$ from (a) $32[\mu s]$, (b) $52[\mu s]$, (c) $62[\mu s]$, (d) $72[\mu s]$, (e) $82[\mu s]$ till (f) $102[\mu s]$ for from left to right; Haas and Sturtevant (1987), Quirk and Karni (1996), and the present model.

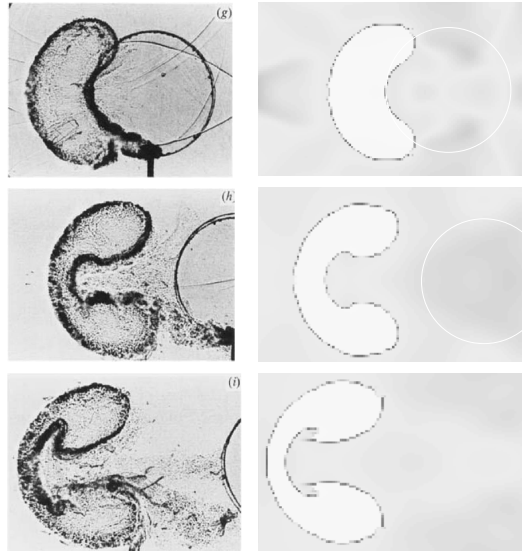


Figure 5.13: Sequence of images of the density in $[kg/m^3]$ from (g) 245 $[\mu s]$, (h) 427 $[\mu s]$ till (i) $\approx 600[\mu s]$ computational / 674 $[\mu s]$ experimental for from left to right; Haas and Sturtevant (1987) and the present model.

5.7 Dam break case

The next step is to model a green water event with the last phenomenon of fig. 2.1: *aeration*.

By doing the 2D dam break simulation with the setup illustrated in fig. 4.27, the propagation speed of the water front is not depending on the density of the fluid by neglecting the viscosity. As described in section 2.4, the shallow water flow assumptions can be applied. These assumptions can be applied when the horizontal length scale is much greater than the vertical length scale. Further, the assumption can be made that the change in density is small which makes the non-conservative form of the shallow water equations independent of the density. Using the dispersion relation for shallow water, where the wave length λ is much larger than the waterdepth H :

$$\begin{aligned}\omega^2 &= \frac{2\pi g}{\lambda} \tanh \frac{2\pi H}{\lambda}, \\ &\approx \frac{4\pi^2}{\lambda^2} gH.\end{aligned}\tag{5.35}$$

Knowing that the phase velocity c_p is equal to $\frac{\omega\lambda}{2\pi}$, the phase velocity is equal to \sqrt{gH} . The water front velocity is equal to $u=2c_p$, which shows that the velocity of the wave front is independent of the density. This is also shown in eq. (2.14) in section 2.4.

Further, in eq. (2.13) it is shown that the change in height of the dam is independent of the density. However, the force and moment depend on the density, see eq. (2.15).

In this section, the [Propagation of the water](#) is again verified in section 5.7.1 for different levels of aeration. The same results for the free surface dynamics should be obtained due to the independency of density. For the same case (at model scale), eq. (2.15) is compared with the measured forces on the wall.

Hereafter, the [Dam break at real scale](#) is tested in section 5.7.2. The effect of aeration should stand out. Finally, the multiphase model is compared with the compressible double fraction model at model scale in section 5.7.3.

5.7.1 Propagation of the water

The case, described in section 4.5.6 for the propagation speed of the water, is used to test the effect of aeration on the free surface dynamics. The test is done at model scale, which should result in no compressible effects ($Ma < 0.3$), as discussed in section 2.5. The same slope of water displacement, independent of the aeration level, should be expected.

The simulations done are shown in table 5.3. For every simulation the values of μ_l and μ_a are equal to $1 \cdot 10^{-3} [kg/ms]$ and $1 \cdot 10^{-4} [kg/ms]$, respectively.

Test	β_0 [%]	P_1 3.65[mm] [%]	P_2 5.48[mm] [%]	c [m/s]	ρ_w [kg/m ³]	$P_1/\rho gh$ [-]
Incompressible	0	98.5	100.2	1,500	1000	11.45
Compressible	0	100.0	100.0	1,500	1000	11.62
Compressible	0.1	99.96	99.84	365.5	999	11.63
Compressible	1	99.1	98.8	119.3	990	11.63
Compressible	5	95.7	95.5	54.6	950.1	11.70
Compressible	10	91.9	90.4	39.7	900.1	11.86
Compressible	20	82.3	80.2	29.8	800.2	11.96
Compressible	30	72.1	70.3	26.0	700.3	11.96
Compressible	50	51.4	50.6	23.8	500.5	11.94

Table 5.3: Dam break simulations at model scale with different amount of aeration.

Besides measuring the displacement of the front of the dam, also the pressure on the wall is measured on the heights of 3.65[mm] and 5.48[mm]. The propagation of the wave over time is illustrated in fig. 5.14b, compared again with the results of Martin et al. (1952).

It can be noticed that the change of propagation of the wavefront in time is negligible which proves eq. (2.14). However, there is a change visible in pressure. The change is noted in table 5.3. It can be noticed that the pressure is nearly linear dependent on the initial amount of aeration. Looking to eq. (2.15), the force and so the pressure is linear dependent on the density assuming a constant drag coefficient. It is known that $\rho = (1 - \beta)\rho_l + \beta\rho_a$, which shows that the percentage of the pressure given in table 5.3 is comparable with the decrease of the density value of the mixture. Note that the maximum Mach number (0.18) of the flow is not higher than 0.3 to result in compressible effects, discussed in section 2.5. This explains why eq. (2.15) still is valid.

5.7.2 Dam break at real scale

The results at model scale show that it is difficult to achieve compressible effects due to the scale effect, discussed in section 2.3.4. For this reason, the domain size of the case in section 4.5.6 is multiplied by a factor of 10. As discussed in section 2.4, corresponding to a freeboard exceedance higher than 5.5[m], this situation is likely to occur. A grid resolution of 115×36 is used. The simulations done are shown in table 5.4.

All the simulated cases achieve a Mach number in the order of 0.3. For the filling flow model in appendix B.3, a relation is derived for the maximum pressure depending on the violence (ϵ) and the aeration of the flow. This equation is suitable to use for flip-through impacts, like this

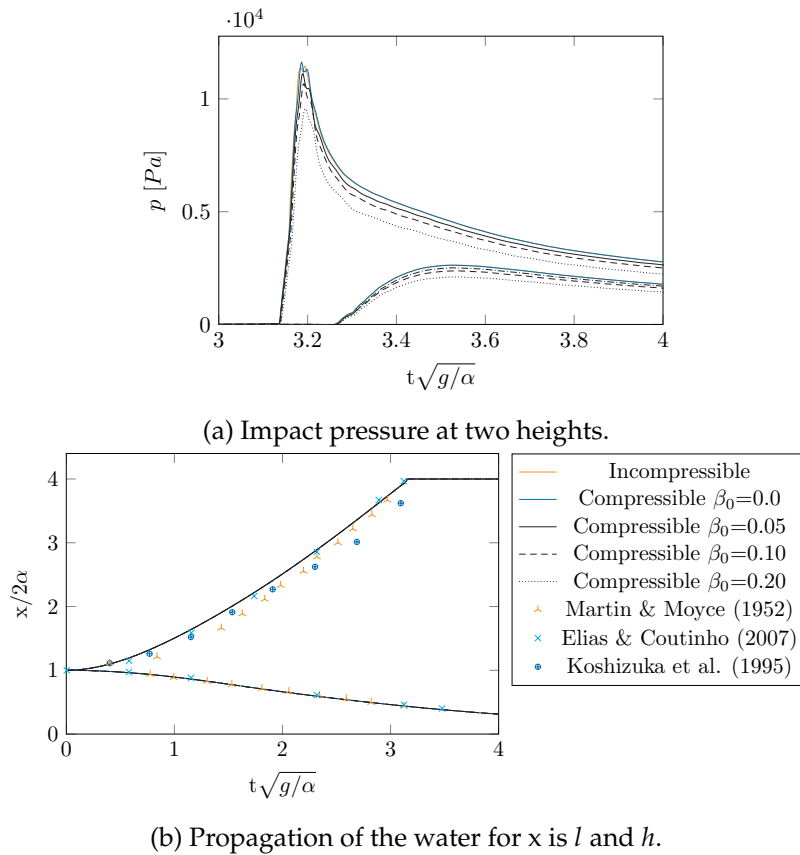


Figure 5.14: Pressure and propagation of the water with aeration.

Test	β_0 [%]	P_1 36.5[mm] [%]	Ma	f_0 [Hz]	c [m/s]	t_{ris} $\cdot 10^{-2}$ [s]
Compressible	1	100.0	0.12	-	119.3	1.48
Compressible	5	82.0	0.27	-	54.6	1.63
Compressible	10	73.4	0.37	18.2	39.7	1.78
Compressible	15	64.3	0.44	13.7	33.3	1.89
Compressible	20	61.7	0.49	11.4	29.8	1.96

Table 5.4: Dam break simulations at real scale with different amount of aeration.

case [15, 113]. The eq. (B.10) can be rewritten in the non-dimensional form [15]:

$$\frac{p_{max} - p_0}{\rho_w g h} = \tilde{K} \frac{1}{(1 - \beta_0)} \frac{1}{(1 + \frac{\beta_0}{\epsilon})^2} \quad (5.36)$$

were constant \tilde{K} and ϵ are found by the best-fit. This fit is illustrated in fig. 5.15a. Further, the pressure at the foot of the wall is plotted in fig. 5.15b.

It can be noticed that, besides the decrease in impact pressure by increasing β_0 , increasing β_0 lead to a pressure oscillation due to the initial impact. The oscillations are found for $\beta_0 \geq 0.05$, which lead to a diffusing compression wave propagating in the opposite direction of the fluid. This wave is observed until the half of the domain. The speed of the compression wave is in the order of the speed of sound of the mixture.

According to Bullock et al. (2007), the damped oscillations in the pressure are compatible with the alternate expansion and compression of the air following the time of peak pressure. Note that the uniform grid used have a cell size of $277.8[mm]$, leading to a compression wave which was not be fully captured. The frequencies are given in table 5.4. Besides the increasing intensity of the oscillation, the frequency is decreasing due increasing of β_0 . This is also observed by Plumerault (2009). The results correspond with the observation of Bredmose et al. [15] where the maximum pressure and the maximum force decrease with β_0 and the rise time of the pressure (t_{ris}) increases with β_0 .

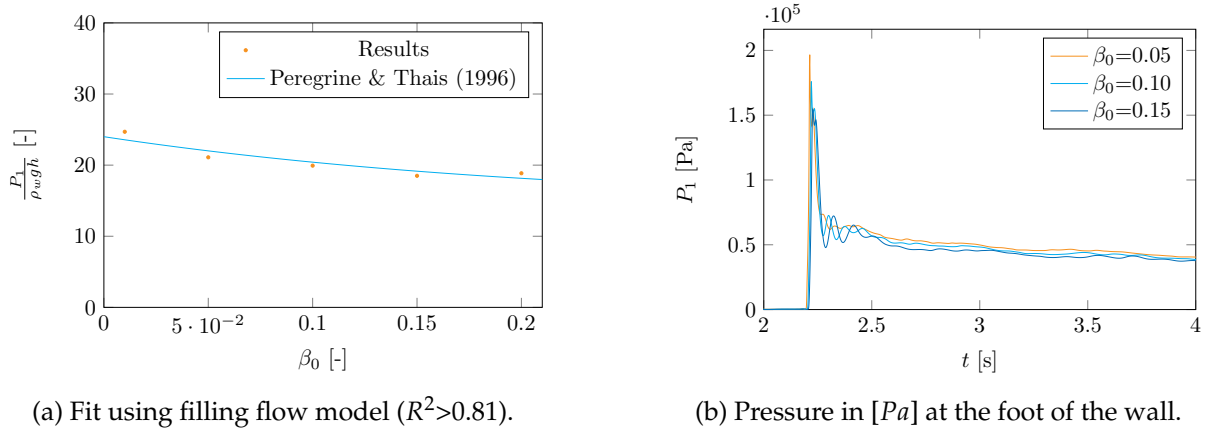


Figure 5.15: Impact pressure for aerated water in dam break case at real scale.

5.7.3 Compressible versus Incompressible

Besides the case for the propagation of the water, the compressible double fraction model is also tested for the case discussed in section 4.5.6. This is done for a grid resolution of 115×36 . The same values for the parameters as in section 4.5.6 are used. The simulation is done for the standard transport equation in eq. (5.4) as well as the transport equation obtained in eq. (5.12). Note that the standard transport equation is not compatible with the isentropic constraint along material trajectories for each phase, discussed in section 5.4.2 [105].

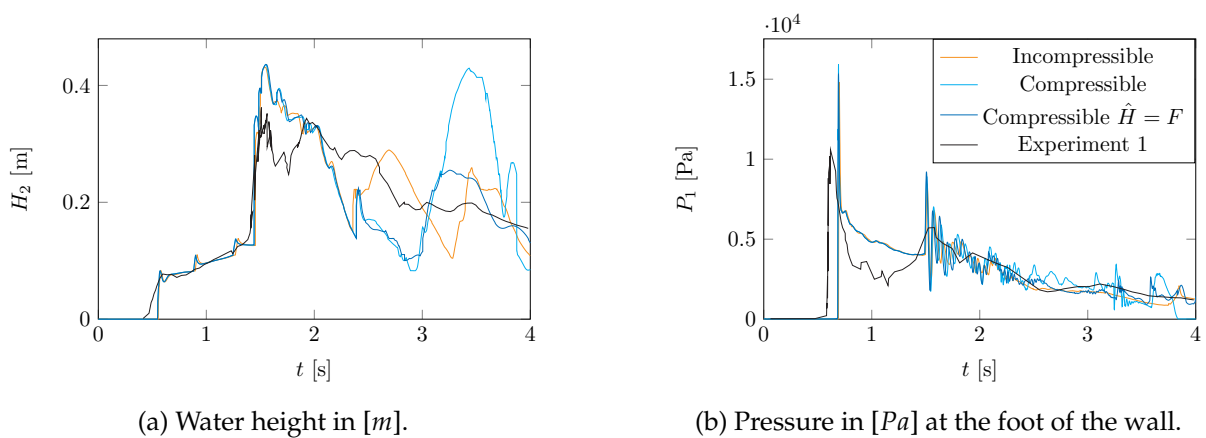


Figure 5.16: Compressible model compared with incompressible multiphase model for dam break case.

The results are plotted in fig. 5.16. The same results are obtained as the incompressible model

until $\approx 1.5[s]$, which is the moment that an air pocket becomes entrapped due to the returning wave.

For both compressible cases, the oscillations seems to be more intensive compared to the incompressible case. The pulsation of the bubble seems to be less damped than for the incompressible case. The reason for this is that the transport equation used is different. This resulted in a bubble which remained longer in time. For an infinite amount of elements, the results should converge to the same solution. This cannot be proven due to the limited computational power. No compressible effects should be involved due to the obtained Mach number of $3 \cdot 10^{-3}$.

The impact pressure for the compressible model is 3.2% higher than for the incompressible case. Similar frequencies are obtained comparing with the incompressible case. The frequencies are given in table 5.5.

	Incompressible	Compressible
Simulation high frequency pressure wall 1 [Hz]	13.04	14.04
Simulation high frequency pressure bubble 1 [Hz]	12.04	14.04
Simulation high frequency pressure wall 2 [Hz]	15.05	17.05
Simulation high frequency pressure bubble 2 [Hz]	15.05	17.05
Simulation low frequency pressure wall 1 [Hz]	1.00	1.00
Simulation low frequency motion bubble y 1 [Hz]	1.00	1.00
Simulation low frequency pressure wall 2 [Hz]	3.01	4.01
Simulation low frequency motion bubble y 2 [Hz]	3.01	4.01

Table 5.5: High frequency and low frequency oscillations in pressure at the wall; step size of 1[Hz].

Besides the comparison between the incompressible and the compressible case, the effect of the transport equation on the results fig. 5.16 need to be evaluated.

For the use of the transport equation in eq. (5.12), it is important to maintain a *sharp* interface. Looking to the fraction values F far from the free surface, values are obtained of 0.90 before the returning wave. This is caused by the change of an S- or E-cell to an F-cell. This would indicate that the aeration level is increased with 10%, which affects the transport equation. Due to the diffused interface, momentum losses can occur as experience by Plumerault (2009) for a breaking Stokes wave. When the standard transport equation is solved, the results are in better agreement with the incompressible results.

Note that the right hand side of eq. (5.12) is non zero for an S-cell. The value \hat{H} becomes equal to:

$$\hat{H} = \frac{F\rho_a c_a^2}{(1-F)\rho_l c_l^2 + F\rho_a c_a^2} \quad (5.37)$$

When $F=1$ the transport equation becomes the same as for the multiphase model. The difference is made at the interface where the transport equation for the compressible double fraction model enforces pressure equilibrium between the water and air, and satisfy the constraint of no mechanical energy transfer ($\frac{D_s}{Dt}$).

A higher-order reconstruction method of the free surface might need to be implemented to look if this improve the results. The model cannot fully obtain the limit of incompressibility yet.

5.8 Conclusion

In this chapter, a finite volume formulation is described that improves the multiphase model in chapter 4 with the representation of the dynamics of air entrainment for a compressible two-phase flow.

A [new transport equation](#) is derived in section 5.4.2, based on the pressure equilibrium under expansion and compression by a change in air volume fraction, with the restrictions that the interface need to be *sharp* and the volume fractions *positive*.

For the extension, only two extra equations are solved: to update the aeration field for a constant mass fraction with eq. (5.30) and the extra equation of state for the liquid in eq. (5.26).

For the dam break simulation in section 5.7, the following results are observed:

- In table 5.3, for $Ma < 0.20$ the pressure decreases linearly with the density as the force in eq. (2.15), up to a maximum error of 4.1% based on table 5.3.
- In fig. 5.16a, the free surface displacement is affected by the aeration up to a value of $3 \cdot 10^{-4}$.
- In table 5.4, for $Ma \geq 0.27$ compressible effects are experienced. The pressure is non-linear dependent on the aeration. It corresponds with eq. (5.36) with $R^2 > 0.81$.
- For $Ma \geq 0.27$, the intensity of pressure oscillation and rise time in fig. 5.15b increases with β_0 , while the pressure decreases due to the cushioning effect.
- In fig. 5.15b, the oscillation frequency decreases with β_0 due to increased compressibility.
- In section 5.7.1 where $Ma < 0.20$, the difference in peak pressure between the compressible (β_0) and incompressible case in fig. 5.14a is 1.5% at $y = 3.65[mm]$ and 0.2% at $y = 5.48[mm]$.

Furthermore, the [local height function](#) used by Wemmenhove et al. (2015) is [not strictly mass conserving](#). This is shown in appendix D.2. It is modified in section 5.4.2, resulting in a more mass conserving method. Furthermore, it is shown that the local height function is *not physical*.

Besides the dam break simulation, for the [1D shock tube](#) in section 5.5.1 a first-order convergence in time and space is found based on the liquid mass conservation. The shock tube with separated phases, an error of 5% is found on the pressure for 800 elements. The case in section 5.5.2 with a mixture, an error of 0.04% is found for 800 elements. One speed of sound is verified for a mixture. However, more shock tube tests are needed to verify fig. 2.3.

For the [2D shock helium bubble](#) in section 5.6 quite good results are obtained compared with the numerical model of Quirk and Karni (1996). A maximum error of 4% on the position of the jet wave in fig. 5.10b is found. Furthermore, all waves in fig. 5.10a are observed and measured.

In section 5.7.3, it is recommended to look what the effect is of a higher-order interface tracking method than SLIC on the dam break results. Further, it is suggested to do a grid convergence study. In fig. 5.16, it is shown that the results of the compressible double fraction method are not in agreement with the results of the multiphase model due to the difference of the transport equation for $F < 1$, represented by eq. (5.37).

6 | Dam break simulations

6.1 Introduction

In this chapter the extended model, derived in chapter 5, is used to simulate the dam break problem at real scale. As explained before, the dam break case is often used as validation for free surface flow solvers. As described in section 2.4, the results of a simulation of the dam break can give an impression of the forces due to green water acting on a superstructure positioned on deck. This superstructure can stand in front of e.g. a deckhouse. The setup is simple where no special in- or outlet conditions are used. The dam break problem is modelled for a couple of aerated-water flows and an one-phase flow, to compare the behavior and the [influence of aeration](#).

In section 6.2, the [Numerical setup](#) of the dam break problem is discussed. All the simulations of this chapter are summed in section 6.4.2 with the corresponding initial conditions.

Hereafter, in section 6.3 the double fraction model is compared with the one-phase model, as discussed in chapter 3 and with the experimental results of MARIN [108].

In section 6.4 the [effect of aeration](#) is discussed for a domain four times larger than the experimental setup of MARIN. The differences in water heights and pressures are elaborated and oscillations of air pockets and corresponding pressure waves are highlighted. The [Conclusion](#) of section 6.4 can be found in chapter 7. The results of this chapter are closely connected with the aim of this report, described in chapter 1.

6.2 Numerical setup

Experiments have been performed at MARIN for breaking dam flows. As mentioned in section 4.5.6, this is done in a large tank of $3.22 \times 1 \times 1 [m]$. The only difference is that for this case an obstacle is added to the setup. The roof of the tank is open which means the pressure at the top is equal to the atmospheric pressure. The size of the water block is $c=1.22\alpha[m]$ by $d=0.55\alpha[m]$. The obstacle is positioned at $2.67\alpha[m]$ till $2.83\alpha[m]$ and has a height of $0.161\alpha[m]$. The setup is illustrated in 2D in fig. 6.1. Note that the simulations discussed are modelled in a 2D-domain while the experiment is 3D. The limitations of 2D modelling for the dam break problem are discussed in section 4.5.6.

The pressure is measured at six positions (P_1 - P_6) on the obstacle: at all corners. The pressure at the wall is also measured on the heights $0.03\alpha[m]$ (P_7) and $0.41\alpha[m]$ (P_8). The atmospheric pressure is subtracted from the measured pressure.

The water heights are measured at $H_1=0.58\alpha[m]$, $H_2=1.73\alpha[m]$, $H_3=2.23\alpha[m]$, and $H_4=2.72\alpha[m]$ relative to the origin (O). Furthermore, the water heights above the obstacle (H_o) and the jet

along the wall (H_{jet}) are measured in time.

The force per unit width, acting on the obstacle, is measured in horizontal direction ($F_{o,h}$) as well as in vertical direction ($F_{o,v}$). At the wall, the force (F_w) and the moment (M_w) around the foot of the wall are measured. The forces are calculated based on the gauge pressure distribution.

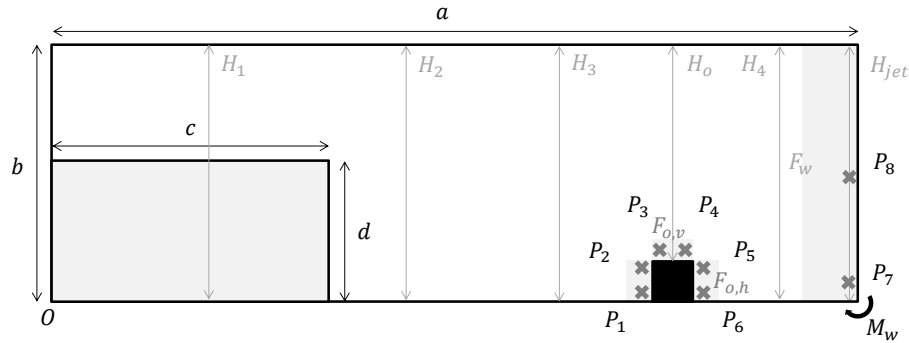


Figure 6.1: Setup dam break case of MARIN 3D experiment; cross sign: measure point pressure, grey area: measure acting force, arrow: measure water height.

The different cases that are modelled, are noted in section 6.4.2. The amount of initial aeration β_0 is based on the values used by Plumerault (2009) and discussed in section 2.3.3. Using the shallow water equations in eq. (5.35), a Mach number is obtained. No compressible effects are expected during the simulations.

For the first two simulations in section 6.3, the domain of the experimental setup of MARIN is used ($\alpha = 1$). Furthermore, the simulation time is 6[s].

For the simulations in section 6.4, containing aeration, the domain is increased with $\alpha=4$ to have a significant Mach numbers. Resonance effects for oscillating air pockets are not easily predicted by small-scale model tests, as the phenomenon depends on the scale as well as aeration, as discussed in section 2.3.4 [15]. The grid resolution remains the same: 115×38 . The

Case	Compressible Water	β_0 [-]	c_w [m/s]	Ma [-]
One-phase	No	-	-	-
Two-phase	Yes	0	1,500	$3 \cdot 10^{-3}$
Two-phase	Yes	0.001	365.49	0.03
Two-phase	Yes	0.01	119.43	0.08
Two-phase	Yes	0.05	54.61	0.17

Table 6.1: Simulations dam break case with obstacle

parameters for water and air are set to $\rho_w=1,000[\text{kg}/\text{m}^3]$, $\rho_a=1[\text{kg}/\text{m}^3]$, $\mu_w=1 \cdot 10^{-3}[\text{kg}/\text{ms}]$, and $\mu_a=1 \cdot 10^{-5}[\text{kg}/\text{ms}]$. The gravitational constant is set to $g=9.81[\text{m}/\text{s}^2]$ and the surface tension is $\sigma=0.072[\text{N}/\text{m}]$. Free-slip conditions are imposed on all walls.

6.3 Comparison of models

The comparison between the multiphase model and the one-phase model is already done by Wemmenhove (2008). As mentioned before in section 5.7.3, it is expected that the fully compressible flow model should have the same behavior as the multiphase model due to the absence of compressible effects. Further, the results are also compared with the 3D experimental results. The results are illustrated in fig. 6.6.

Like for the multiphase model, a slower movement of the wave front is observed for the compressible flow model compared with the one-phase model. This is related to the presence of air around the front. The air is more viscous than the vacuum in the one-phase model [149].

In case of the impact pressure P_1 , for the one-phase model more pressure spikes and even negative value are observed. This is caused by the change in cell labeling. For the one-phase model, no mass conservation is required for Surface and Empty cells. Due to the change in labeling from S and E to F, a new Fluid cell is created where mass conservation is required. This results in a spike in the pressure signal while for the multiphase model in all cells mass conservation is required [149].

The pressure oscillation observed by the compressible flow model is caused by the presence of air in the entrapped pocket. The one-phase model cannot model these oscillations due to treating the air as void. This pocket acts like a spring. The impact pressure for the one-phase flow is lower than the impact pressure for the compressible flow. This can be caused by the difference in the method and grid resolution. However, it is expected that the impact for the compressible double fraction model is lower due to the cushioning effect of the air.

The difference in water height may be caused by the presence of air which has a damping effect on the motion of the water. This results in a better prediction of the water height of the returning wave at $\approx 2.5[s]$ for H_1 and at $\approx 4.7[s]$ for H_2 . The two straight peaks for the compressible model at $t=2.5[s]$ for H_2 are caused by droplets propagating above the free surface.

Comparing with the experimental results, the difference in pressure peak as well as the abrupt changes in water height is caused by the restricted movement of the water, as discussed in section 4.5.6. For the 3D experiment, the obstacle does not extend to the full width of the domain. Further, it is important to note that fragmentation is not taken into account so the damping is not as strong as in the experiment. *These restrictions are also important to note when looking at the results of the real scale in the next section.*

6.4 Comparison of Results

In this section, the results of the fully compressible model are compared for aeration levels 0.1%, 1% and 5%. The dam has a height of $2.2[m]$ that corresponds with a freeboard exceedance higher than the dam height. As mentioned in section 2.5, this is realistic to happen. According to the shallow water theory in eq. (2.14), this leads to a propagating speed of $11.8[m/s]$. A uniform cell size of $111[mm]$ is used. The simulation time is $7[s]$ to capture the initial impact and the behavior of the mixture after this impact.

In section 6.4.1, all the measured Pressures and the impulse, as discussed in section 6.2, are compared. Hereafter, the observed Oscillations are evaluated in section 6.4.2. In section 6.4.3, the Forces on the obstacle and the left wall are compared. Furthermore, the Moment on the wall is analyzed for the different aeration level. In the end, the Free surface dynamics in section 6.4.4 is compared by evaluating the water heights and the entrapped air pocket.

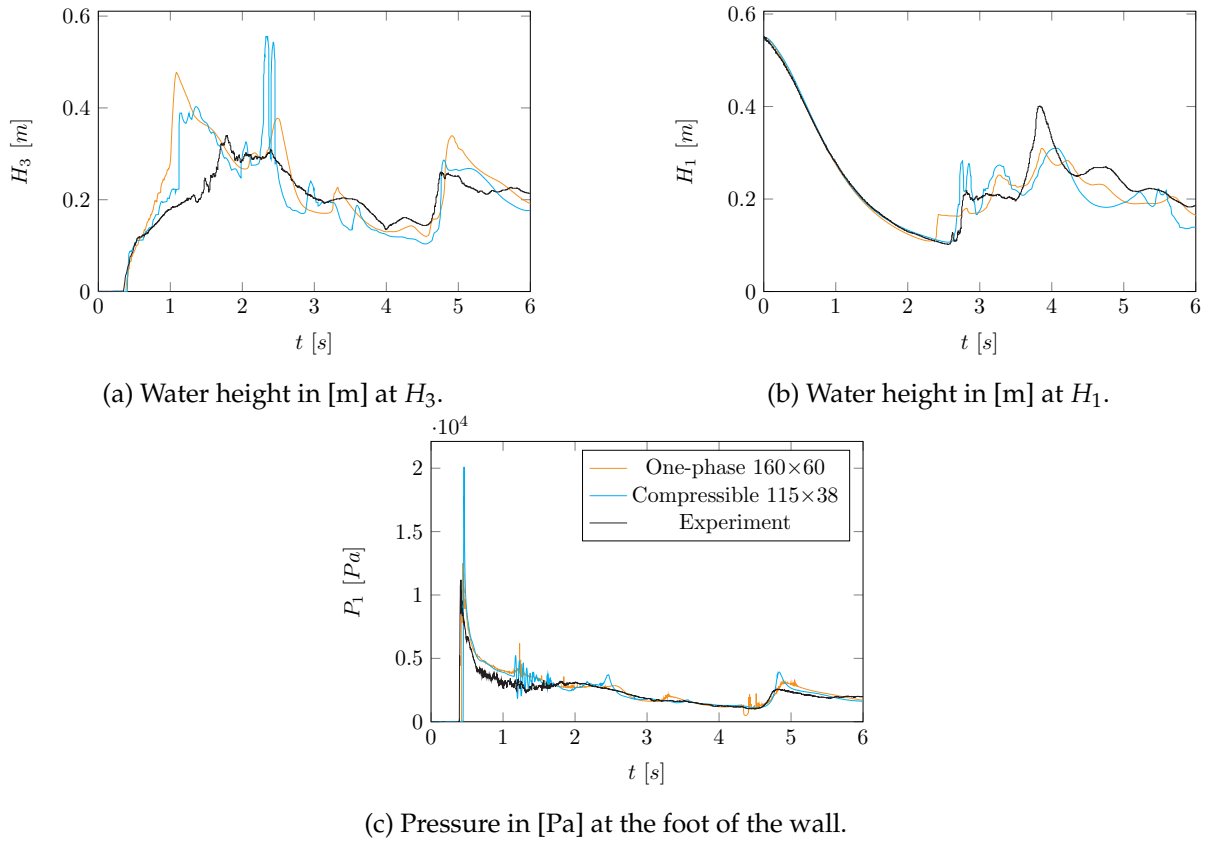


Figure 6.2: The comparison of the one-phase model and the fully compressible model for the dam break case with obstacle.

6.4.1 Pressures

In this subsection, the effect of aeration on the pressure is discussed. Based on the documentation in section 2.7, it is expected that the aeration has a cushioning effect on the impact pressure.

The pressures in altitude and time are illustrated in fig. 6.3 for the obstacle and the wall. Furthermore, the difference in pressures measured for all β_0 values are illustrated in fig. 6.4a. The pressures at the foot of the obstacle and the wall are illustrated in fig. 6.4c-6.4d, respectively.

Pressure at the block

The pressure at the block is measured at six positions (P_1 - P_6) where for P_1 the largest impact pressure is found. For this pressure, no compressible effects are expected ($Ma < 0.3$). Therefore, as discussed in section 5.7.1, the decrease in maximum pressure for P_1 is caused by the difference in density as for eq. (2.15). A relative decrease of 1.7% and 3.2% in pressure is obtained relative to $\beta_0=0.001$, for $\beta_0=0.01$ and $\beta_0=0.05$. The time of impact differs $1 \cdot 10^{-4}$ [s]. This corresponds to the results of section 5.7.1.

After the impact on the obstacle at 0.89[s], a small vibration is found for $\beta_0=0.05$. This is hardly visible in fig. 6.4c but is increasing with β_0 . It is discussed in section 5.7.2 that the amplitude of oscillation increases with the Mach number.

When the wave front overtakes the obstacle, an air pocket is entrapped after 2.35[s]. This pocket starts to pulsate, like in section 4.5.6 due to the flip-through. A difference in initial impact is

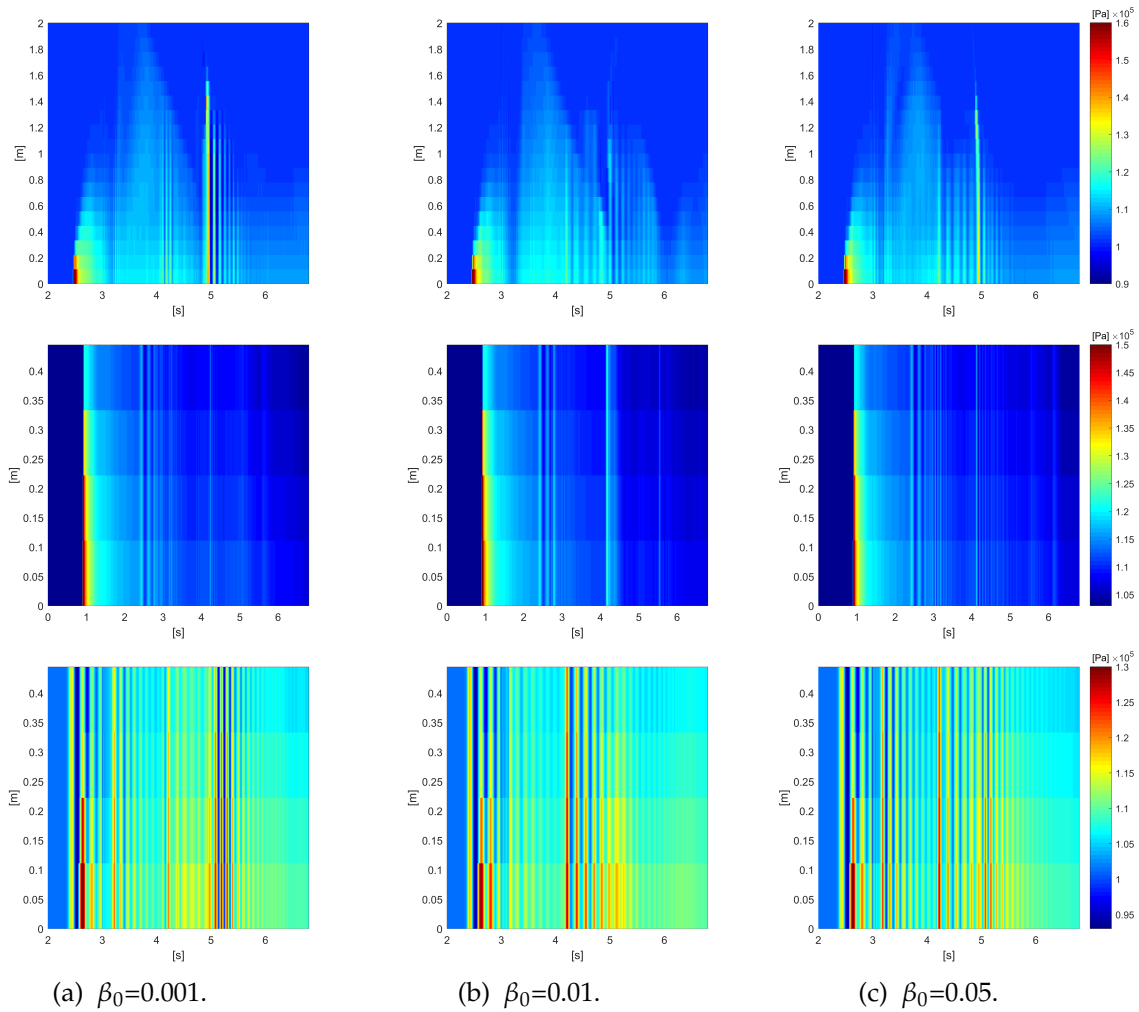


Figure 6.3: The evolution of the distribution of pressure for all β values; the first row represents the pressure on the wall, the second row at the front of the obstacle, and the third row at the back of the obstacle.

found for P_6 in fig. 6.4b. The impact changed the free surface dynamics leading to a different volume of the entrapped air pocket, given in table 6.6. The initial impact increases with the volume. The pulsation of this entrapped air pocket is also experienced by the pressure P_1 . Note that sub-atmospheric pressures are obtained for P_6 , independent of the aeration level, which can lead to destabilizing forces on the obstacle [14].

After 2.57[s], the water hits the bottom, generating a returning wave which hits the obstacle at P_6 . The time difference between $\beta_0=0.01$ and $\beta_0=0.001$ is 0.01[s] with first $\beta_0=0.01$. The event in time seems to happen earlier in time for a larger air pocket where the larger air pocket corresponds with a larger horizontal velocity. The impact for $\beta_0=0.001$ is higher but damps faster. The double peak maximum for P_6 is also found by Schmidt et al. (1993) for a breaking wave impact. However, they relate the first peak pressure with the impact of the wave crest and the second to the compression of the air pocket while in this case it is conversely. The jump in between the two peaks seems to increase with a decreasing volume of an air pocket. This corresponds with the result of ? (?) who found that a small air pocket gives the highest impact pressure.

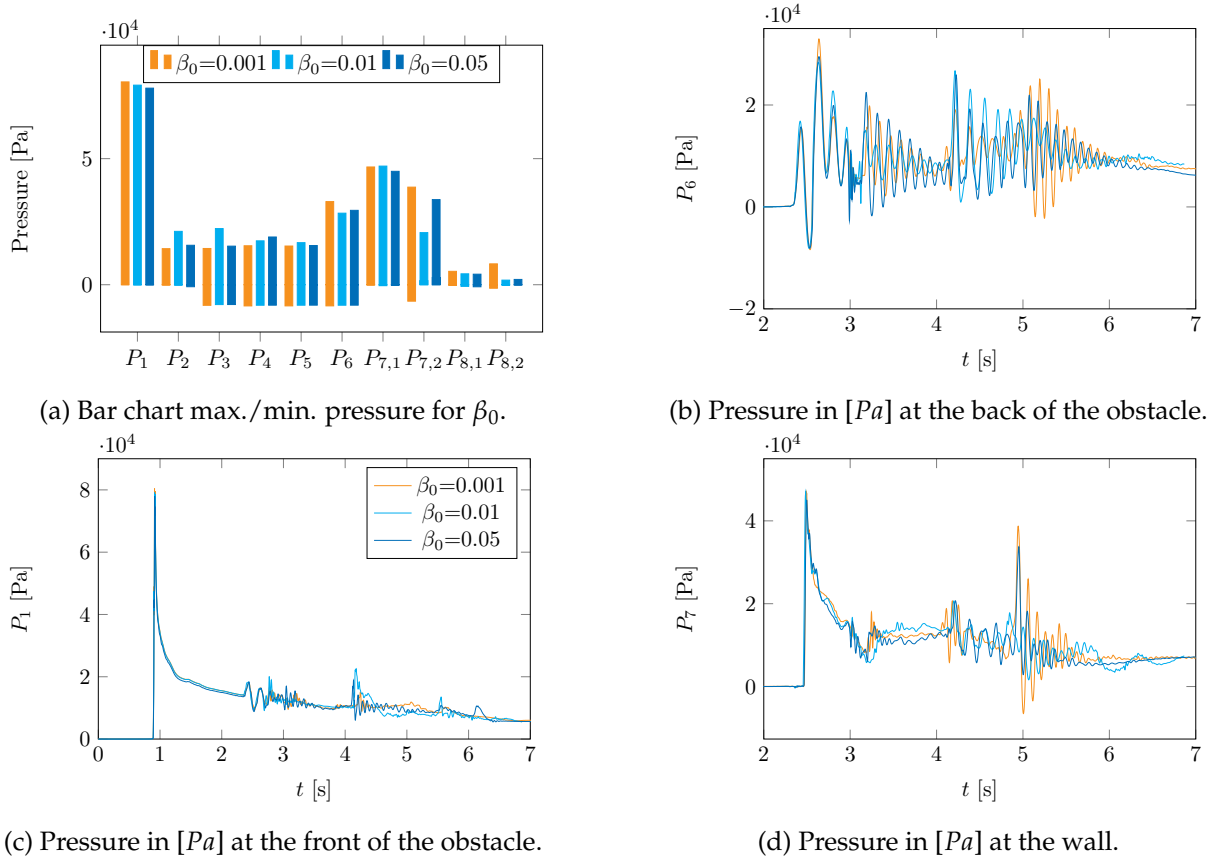


Figure 6.4: Pressures measured during the simulation in time; subscripts ",1" and ",2" represent time periods given in table 6.5.

At around 3[s], the air pocket starts to fragment, leading to a higher frequency oscillation, visible in fig. 6.4b-6.4d. This is also observed by Plumerault (2009). A new air pocket with a different size, depending on β_0 is obtained. The pulsation of the fragmented air pocket will have a higher frequency due to the smaller diameter.

After 4.2[s], the returning wave of the flip-through impact hits the free surface. This event depends in time on the aeration level. The magnitude of the pressure is for high aeration level larger than for a low aeration level due to a higher returning wave. Furthermore, the intensity of the pressure oscillation is larger for $\beta_0=0.01$ than for $\beta_0=0.001$ up to 40%. Note that this pressure is $3.5\times$ smaller than the maximum pressure of P_1 .

Looking to fig. 6.4b, after the impact, the frequency of oscillation decreases with the aeration level. This is also observed in section 5.7.2 due to decreasing of the speed of sound.

At around 5[s], large droplets ($0.07\sim 0.10[m^2]$) evolved from the jet due to the flip-through impact hit the free surface. For the case with $\beta_0=0.001$, this lead to extreme oscillations in P_6 . The oscillations are also visible in fig. 6.3. These oscillations are not experienced by P_1 which makes it a local effect.

Note again that this maximum of this oscillation is $3.5\times$ smaller than the maximum pressure of P_1 . The pressure difference between $\beta_0=0.001$ and $\beta_0=0.01$ is up to 32%.

The oscillation frequency is elaborated upon in section 6.4.2. The change in free surface

dynamics by impact with the obstacle is discussed in section 6.4.4.

Pressure at the wall

The initial impact at P_7 is at $\approx 2.45[s]$. The time of the impact for the aeration levels; 0.1% at 2.467[s], 1% at 2.456[s] and 5% at 2.466[s]. It is remarkable to see that the maximum impact pressure is found by $\beta_0=0.01$. Due to the change in free surface dynamics, looking to fig. 6.4a, the initial impact pressure of $\beta_0=0.01$ is the largest for P_7 but the smallest for P_1 . The reverse applies for $\beta_0=0.01$, while $\beta_0=0.05$ is in between. It seems again that the time and the pressure on the wall depends on the volume of entrapped air pocket. The larger the air pocket, the larger the initial impact at P_1 and the smaller the water impact at P_6 .

After 2.45[s], the same events experienced by P_6 are also experienced by P_7 . The pressure peak at 5[s] ($P_{7,2}$ & $P_{8,2}$ in fig. 6.4a) depends on the height of the jet (H_{jet}), which is discussed in section 6.4.4.

As mentioned before, at around 5[s], a droplet hits at a height of $\approx 1.4[m]$ the free surface. This is illustrated in the first row of fig. 6.3 by the pressure increase. This impact leads to a compression wave in the direction of the base of the wall. This results in high pressure values as well as sub-atmospheric values for P_7 and P_8 . The maximum pressure difference between $\beta_0=0.001$ relative to $\beta_0=0.01$ is 118%, where the pressure is $2\times$ smaller than the maximum pressure of P_1 . Similar conditions are obtained by other investigations for a breaking wave [14, 22, 118].

A similar jet is found for $\beta_0=0.01$ and $\beta_0=0.05$, as discussed in section 6.4.4. However, the extremity of the pulsation of this air pocket seems to decrease for a higher aeration level [118].

It is concluded, using fig. 6.4a, that the larger the magnitude of the initial impact pressure, the lesser the effect of the aeration level. This is also experienced by other investigations [22, 118]. For P_1 the maximum difference in initial impact pressure is 3.2%, for P_7 it is 4.4%, for P_6 it is 8.0% and for P_8 it is 21%.

Besides the comparison of the pressure magnitude, the pressure impulses caused by P_1 , P_6 , and P_7 are given in table 6.2. The impulse can be found by integrating the area of the pressure over time. For the impulse values in the time period of 0.0-3.0[s], where fragmentation did yet not happen, it is found that the pressure impulse decreases with β_0 due to the cushioning effect of aerated water [15].

Taking into account the oscillations of the air pockets, the impulse can increase due to the increase in spatial and temporal extent of the impact [15]. However, this is based on a breaking wave entrapping an air pocket and not for a flip-through impact. Except for I_6 , the impulse of the pressure decreases with β_0 .

Time [s]	Impulse	$\beta_0=0.001$	$\beta_0=0.01$	$\beta_0=0.05$
0.0-3.0	I_1 [kPa·s]	12.0	12.0	11.4
0.0-3.0	I_6 [kPa·s]	39.1	38.9	37.7
0.0-3.0	I_7 [kPa·s]	7.1	7.2	6.5
0.0-7.0	I_1 [kPa·s]	52.9	49.2	48.3
0.0-7.0	I_6 [kPa·s]	77.9	74.2	74.4
0.0-7.0	I_7 [kPa·s]	47.3	45.4	42.8

Table 6.2: Pressure impulse acting on the obstacle and the wall.

6.4.2 Oscillations

It has been mentioned that the first air pocket is entrapped after 2.35[s]. The area of this entrapped air pocket is given in section 6.4.2. It seems that a larger air pocket results in a larger pulsation and pressure for P_6 . The difference in initial impact between $\beta_0=0.01$ and $\beta_0=0.001$ is 7.9%. Furthermore, the difference in volume of the initial air pocket is 7.8%.

The frequency of the pulsation of the air pocket ($f_{p,p}$) and P_6 ($f_{P_6,2}$) are predicted with an accuracy of 1.25[Hz] for the time period 2.2-3.0[s]. The double frequency of the pulsation in pressure of the air pocket is also observed in the resulting pressure P_6 . The Fourier transforms are illustrated in fig. 6.5a. The low frequency of P_6 ($f_{P_6,1}$) in this time period seems to correspond with the frequency of horizontal translation of the pocket ($f_{p,x}$). Due to the accuracy, it cannot be shown that the low frequency depends on the shape of the air pocket and the high frequency also depends on the aeration level [118]. Using eq. (2.1) and eq. (2.2), the natural frequency of the air pocket $f_{0,1}$ and $f_{0,2}$ are obtained, respectively. Note that for these theoretical frequencies, a couple of assumptions are made. This is discussed in section 2.2.2. The same order of magnitudes are obtained as for the dominant frequencies found in section 6.4.2.

β_0	A_p [m ²]	$f_{0,1}$ [Hz]	$f_{0,2}$ [Hz]	$f_{p,p}$ [Hz]	$f_{p,x}$ [Hz]	$f_{P_6,1}$ [Hz]	$f_{P_6,2}$ [Hz]
0.001	0.59	10.72	8.73	5.03	1.26	1.26	5.02
0.01	0.64	10.34	8.38	5.02	1.26	1.26	5.02
0.05	0.61	10.81	8.59	5.02	1.26	1.26	5.03

Table 6.3: Dominant frequency oscillations for t=2.2-3.0[s].

Besides the entrapment of the first air pocket, it is observed that the oscillation of P_6 after 5.0[s], in fig. 6.4b, is amplified. Around the same time, for P_7 also an oscillation is observed due to the large droplets from the jet hitting the free surface. The impact of these large droplets generates a pressure wave in the direction of the base of the wall and the obstacle. At the wall the pressure wave is reflected in the direction of the obstacle. At this moment beneath the free surface no air pockets are found, except for $\beta_0=0.01$.

Due to the violence, mixing of air and water occurs. This results in an air volume fraction up to 25%, resulting in a speed of sound in the order of 30[m/s]. This means that for $\beta_0=0.001$ and $\beta_0=0.05$, the fluid between the obstacle and the wall can be seen as a homogeneous mixture. Using eq. (2.3), this results in a domain frequency between the obstacle and the wall of $f_l \approx 9.6$ [Hz] and $f_t \approx 13.6$ [Hz].

In case of $\beta_0=0.01$, the domain frequency is difficult to calculate due to persisted air pockets. The amplification in P_6 can hardly be observed due to the air pockets and the smaller returning jet, discussed in section 6.4.4. More frequencies are found due to the presence of air pockets.

The mixture starts to oscillate due to the impact as found in section 5.7.2. This means that compressible effects for the mixture are obtained. The amplification of the pressure P_6 is caused by the reflecting pressure waves and the domain frequency (f_l).

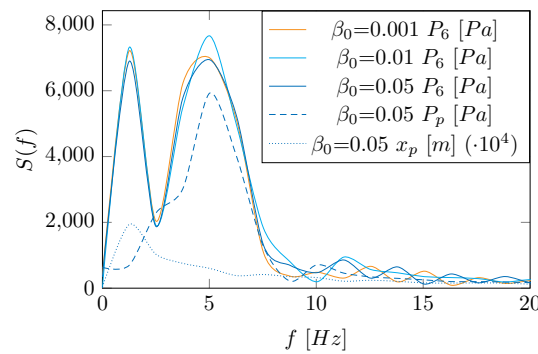
The frequency of the pressure oscillation observed by P_6 and P_7 are given in section 6.4.2 for a time period 4.8-6.0[s] and an accuracy of 0.84[Hz]. The low frequency is given by $f_{P_6,1}$ and $f_{P_7,1}$. Further, the high frequency is given by $f_{P_6,2}$ and $f_{P_7,2}$. The Fourier transforms are plotted in

fig. 6.5b. Further, in fig. 6.5c the pressures P_6 and P_7 are illustrated for the time period 4.8-6.0[s].

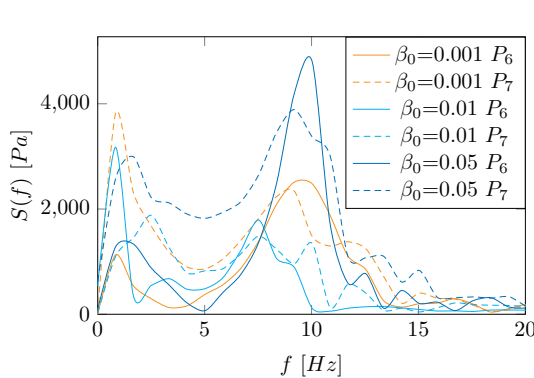
β_0	$\beta/(1-F)$ [%]	$f_{P_6,1}$ [Hz]	$f_{P_6,2}$ [Hz]	$f_{P_7,1}$ [Hz]	$f_{P_7,2}$ [Hz]
0.001	≈ 25	1.67	10.03	1.67	9.20
0.01	≈ 10	3.34	7.53	2.50	7.53
0.05	≈ 25	0.84	9.19	0.84	9.19

Table 6.4: Dominant frequency oscillations for $t=4.8-6.0$ [s].

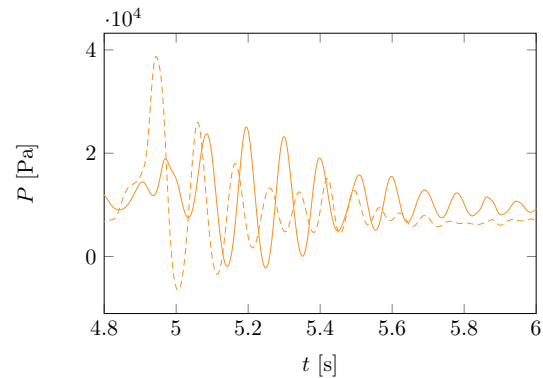
The dominant frequency found for the pressure oscillations is similar to the value found for f_1 . This lead to a forced vibration of the mixture. In fig. 6.5b, relatively small maxima are found for $f > 11$ [Hz]. These may be caused by the domain frequency f_t .



(a) Fourier transform of P_6 and pocket for 2.2-3.0[s].



(b) Fourier transform of P_6 and P_7 for 4.8-6.0[s].



(c) Pressures P_6 and P_7 $\beta_0=0.001$.

Figure 6.5: The initial entrapped air pocket and the effect of the returning jet on P_6 and P_7 .

6.4.3 Forces & Moments

Besides the pressures, the forces on the obstacle ($F_{o,h}$ & $F_{o,v}$) and the wall (F_w) are measured. Furthermore, the moment acting on the base of the wall (M_w) is measured. The maximum and minimum forces and moments are illustrated in the bar chart in fig. 6.6a and fig. 6.6b, respectively. The maximum and minimum values are summarized in table 6.5.

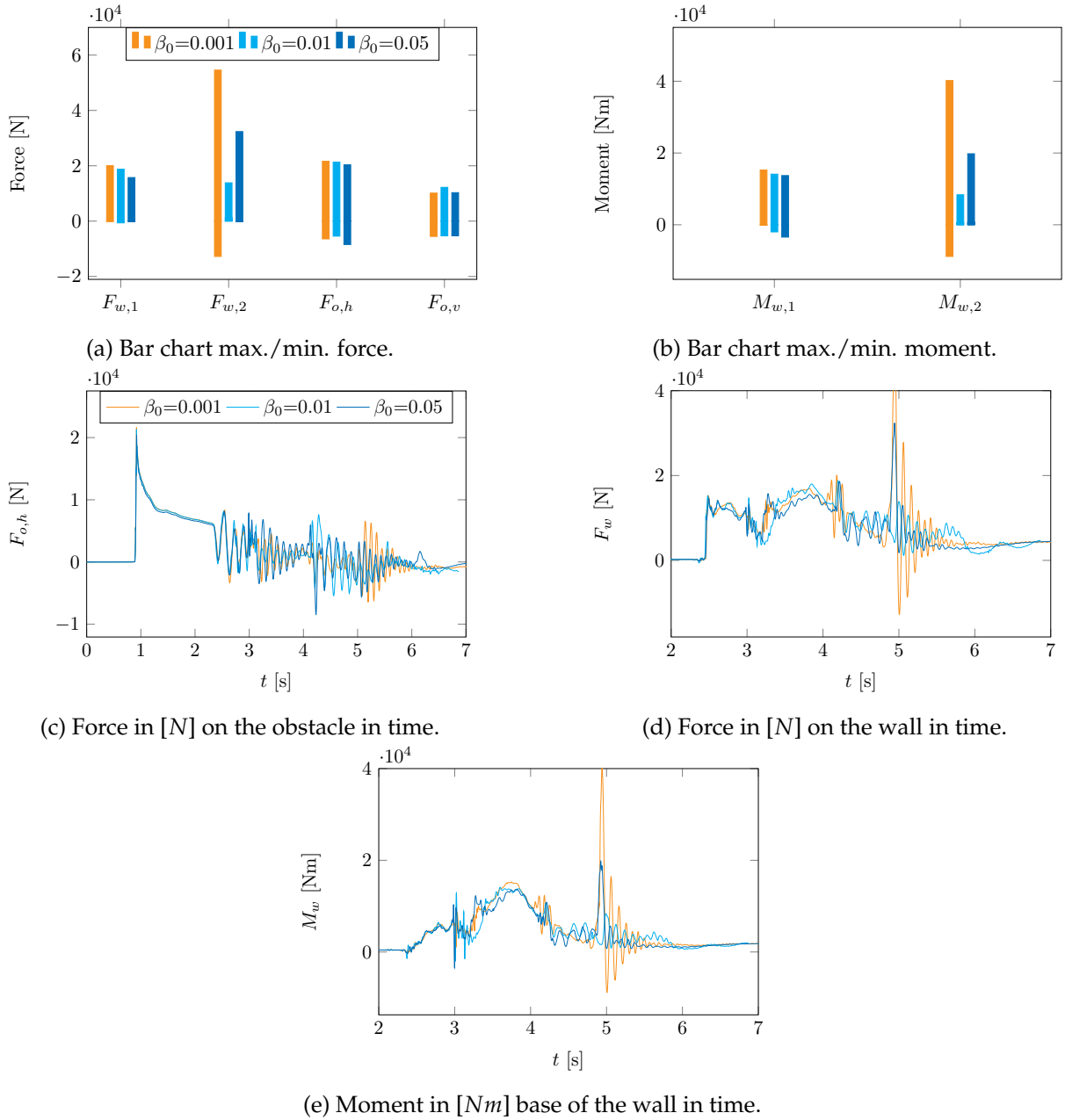


Figure 6.6: The forces and moment measured during the simulation for β_0 in time; subscripts "1" and "2" represent time periods given in table 6.5.

For the force on the wall in time period of 2.0-4.2[s] ($F_{w,1}$), the maximum force decreases with β_0 . The same is true for the maximum horizontal force (directed to the right) on the obstacle ($F_{o,h}$). The magnitude of the force $F_{w,1}$ decreases non-linear up to 21.5%. This is caused by the cushioning effect due to the softer fluid and agrees with similar results of others [14, 15, 118].

The force $F_{o,h}$ decreases with 6% and 1.5% for $\beta_0=0.05$ and $\beta_0=0.01$ relative to $\beta_0=0.001$. This is mainly caused by the density change, based on eq. (2.15). The maximum force $F_{o,h}$ on the obstacle, illustrated in fig. 6.6c, is observed at the same instant as the maximum pressure for P_1 while for the maximum force F_w on the wall, illustrated in fig. 6.6d, a different time is found compared to P_7 .

The vertical force on the obstacle ($F_{o,v}$) is negative for every β_0 due to the sub-atmospheric pressure caused by the pocket oscillations. This results in a lifting force. The maximum vertical force is caused by the pulsation of the air pocket and the returning wave. The magnitude depends on the size of the air pocket. Similar results are obtained by Bredmose et al. (2009) and Plumerault (2009) who found that the lifting force decreases with the aeration level. The obstacle needs to have a density of $1,365[kg/m^2]$ to prevent a translation in vertical direction.

When looking to the time period of 4.8-6.0[s], the most severe forces are found. Due to the returning large droplet evolved from the jet, especially the force on the wall is affected. It is remarkable that the mutual difference in $F_{o,h}$ for β_0 is relatively small compared with $F_{w,2}$. For $\beta_0=0.001$, even negative forces are obtained due to the sub-atmospheric pressure found in the first row of fig. 6.3. The maximum force for $\beta_0=0.001$ of $F_{w,2}$ relative to $F_{o,h}$ is $2.5\times$ higher while for $\beta_0=0.01$ it is $0.65\times$. This shows that not only the initial impact is of importance and the force on the deckhouse can even be bigger due to a superstructure.

It is not observed that the minimum forces increases with β_0 , as found by Plumerault (2009) for a breaking wave. Further, Bullock et al. (2007) found that the forces for a high aeration level can be larger due to the less spatially localised pressure. This is not observed for the flip-through impact due to the relatively small obstacle.

Besides the forces, the moment $M_{w,2}$ can also be negative. By comparing the magnitude of the moment with the force, it can be observed that the height position of the acting force is nearby the base of the wall. For the maximum of the moment $M_{w,1}$, the point of engagement of the acting force is for $\beta_0=0.05$ higher than for $\beta_0=0.001$.

Looking at fig. 6.6b and table 6.5, increasing the aeration level seems to move the moment $M_{w,1}$ downwards while the range slightly increases up to 12%. The negative moment is caused by the fragmentation of the entrapped air pocket at 3[s], illustrated in fig. 6.6e, leading to a sub-atmospheric pressure up to a height of 4[m], corresponding with the height of the jet along the wall in fig. 6.3.

Time [s]	Force Moment	$\beta_0=0.001$		$\beta_0=0.01$		$\beta_0=0.05$	
		Max.	Min.	Max.	Min.	Max.	Min.
2.0-4.2	$F_{w,1}$ [kN]	20.06	-0.07	18.76	-0.635	15.75	-0.21
4.8-6.0	$F_{w,2}$ [kN]	54.58	-12.77	13.85	1.16	32.36	1.78
2.0-4.2	$M_{w,1}$ [kNm]	15.26	-0.09	14.11	-1.99	13.71	-3.44
4.8-6.0	$M_{w,2}$ [kNm]	40.20	-8.83	8.37	0.60	19.79	0.75
-	$F_{o,h}$ [kN]	21.64	-6.43	21.33	-5.44	20.35	-8.45
-	$F_{o,v}$ [kN]	10.14	-5.54	11.01	-5.33	10.29	-5.32

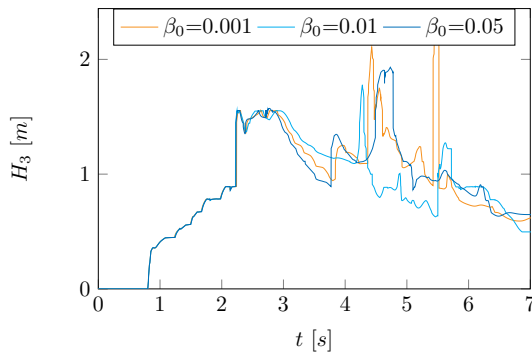
Table 6.5: Maximum and minimum forces and moments.

6.4.4 Free surface dynamics

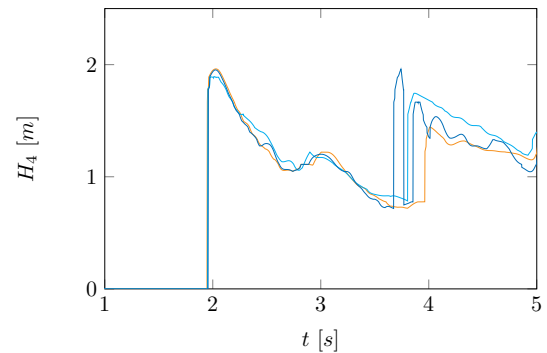
The water heights H_3 and H_4 in time are plotted in fig. 6.7a and fig. 6.7b, respectively. It can be observed that the free surface dynamics for every β_0 remains the same until a reflecting wave is observed, affected by the impact. This is in agreement with the results of Plumerault (2009). However, the entrapped air pocket volume, given in section 6.4.2 does not decrease with β_0 . A maximum difference of 7.8% is found.

After 3.8[s], in fig. 6.7b, due to the impact with the wall, the returning wave is observed. The height of this wave is dependent on β_0 . Furthermore, after 3[s] in fig. 6.7a, due to the impact with the object, the returning wave is also dependent on β_0 . An illustration of the fragmentation of the air pocket is given in fig. 6.7c at around 3[s].

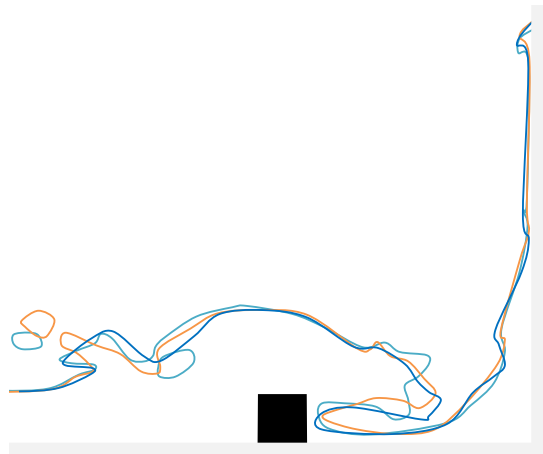
In table 6.6, the maximum water height above the obstacle and along the wall are given. The height above the obstacle seems to be independent on β_0 , which is in contrast with the results of Plumerault (2009) for a breaking wave against a vertical wall. The maximum difference is 1.2%. This may be caused by the small height of the obstacle. The maximum height of the jet along the wall for $\beta_0=0.01$ is lower but the pressure at the base of the wall at 2.45[s] is slightly higher than for $\beta_0=0.001$. Due to the higher impact and the lower jet for $\beta_0=0.01$ at 2.45[s], a larger returning wave is found. This is also observed in fig. 6.7b (the earlier peak for $\beta_0=0.05$ is caused by a droplet).



(a) Mixture height in [m] at H_3



(b) Mixture height in [m] at H_4 .



(c) Free surface at 3.12[s] fragmentation.

Figure 6.7: Behavior of the mixture in time.

The local height function can affect the free surface dynamics due to the coarse grid. Furthermore, droplets with an area of $0.10[m^2]$ do not seem realistic. These droplets significantly affect the pressure and the free surface dynamics after 5[s], illustrated in fig. 6.7a. For this reason, a grid refinement needs to be done to look if similar results can be obtained.

Besides the grid refinement, the effect of implementing a more accurate interface tracking method needs to be investigated. For air volume fraction $\beta_0=0.001$ and $\beta_0=0.05$, values up

to 25% of aeration are found in the fluid due to mixing and fragmentation, as explained in section 5.7.3. For $\beta_0=0.01$, still air pockets were observed with a surrounding mixture containing less aeration.

	$\beta_0=0.001$	$\beta_0=0.01$	$\beta_0=0.05$
$H_{jet} [m]$	5.94	5.62	5.98
$t_{jet} [s]$	3.74	3.67	3.79
$H_o [m]$	3.09	3.10	3.06
$t_o [s]$	1.60	1.61	1.60

Table 6.6: Maximum water height at wall and obstacle.

7 Conclusion

The aim of the graduation project was to evaluate the effect of a homogeneous mixture of water and air on the wave impact, specifically for a green water event.

To evaluate the effect, the numerical method COMFLOW is in chapter 5 extended to a model which is capable of modelling the effect of aeration as a compressible homogeneous mixture by assuming the inertial effects as dominant and mass fraction of air constant. Using this model to simulate a simplified green water event for aeration levels of 0.1, 1 and 5%, the following observations are made based on the results in chapter 6 and section 5.7.2. Considering the effect of aeration on the impact:

- In section 6.4.4 and fig. 5.14b, it is observed that the water height is not affected *before* the impact by the aeration level, neither the density. This corresponds to the shallow water equations in eq. (2.13) and eq. (2.14). An maximum error of $3 \cdot 10^{-4}[m]$ in water height is observed.
- In section 6.4.3 for a flip-through impact, the initial impact force and pressure for $Ma < 0.20$ decreases *linearly* with the density. This corresponds to eq. (2.15) up to a maximum error of 1.0%.
- In section 5.7.2, for $Ma > 0.27$ the initial impact pressure decreases non-linear with the air content in the order of 5%. Using eq. (5.36), a fit accuracy of $R^2 > 0.81$ is found.
- In fig. 6.4a, the increase of violence decreases the effect of the cushioning effect on the initial impact pressure. For an impact pressure $15 \times$ higher, the cushioning effect decreases with $6.6 \times$.
- In fig. 5.15, for a freeboard exceedance higher than $5.5[m]$ the rise time of the pressure increases in the order of $0.01[s]$ non-linear with the air content.
- In table 6.2, for a flip-through impact the impulse of the initial impact pressure decreases with the air content up to 5%.
- In fig. 5.15b, the oscillation frequency after impact decreases with β_0 in the order of $1[Hz]$ due to the increased compressibility. In fig. 5.16, the intensity of the pressure oscillation increases with β_0 .
- In fig. 6.4a, sub-atmospheric pressures are found due to oscillations of an entrapped air pockets, resulting in lifting forces acting on the obstacle in fig. 6.6a. These forces are 25% of the initial impact force on the obstacle.
- In fig. 6.5b for $Ma = \mathcal{O}(0.10)$, values up to $\beta = 0.25$ are found. The longitudinal acoustic mode (f_l) between the obstacle and the wall, eq. (2.3), interacts with the pressure wave caused by an impact of a returning jet, resulting in a pressure increase up to 32%. This depends on the case and the air content.

- In fig. 6.6a, higher forces are observed on the secondary structure than on the obstacle, up to $2.5\times$, caused by an impact of the returning jet. A pressure wave propagates to the base of the wall. This is illustrated in the first row of fig. 6.3. This depends on the case and the air content.

In fig. 6.6a, the most dominant forces are caused by the impact of the returning jet of the flip-through impact along the wall. Based on these observations, the effect of aeration after the initial impact is most relevant where the forces in table 6.5 are case and aeration level dependent.

During the process of implementation of the numerical method COMFLOW in FORTRAN and MATLAB, based on chapter 4, the steps to implement the method were reviewed again and improved when necessary. Based on all the simulation results, an improvement of the original method COMFLOW is achieved:

- In section 3.4.1, the implementation of the orientation of a wave front along a wall is in detail explained to achieve an interface perpendicular to the wall by modifying the fraction values in the ghost cells, illustrated in fig. 3.3.
- In section 4.3.8, it is shown that the gravity-consistent averaging method of Wemmenhove (2008) is worse than the cell-weighted averaging method for steep interfaces. This is illustrated in fig. 4.5 where after 3[s] of simulation, the spurious velocities is $\mathcal{O}(10^8)$ higher than for the cell-weighted averaging method.
- In section 4.4.3, a new-developed CSF-model for SLIC is derived due to lack of documentation for the multiphase model of COMFLOW. It is shown in fig. 4.15 for the oscillating 2D planar rod and fig. 4.20 for standing capillary wave that the capillary forces are well modelled and converges, preserves the free surface in fig. 4.15, the free surface displacement can represent second-order effects in fig. 4.20b, and model the frequency of inviscid oscillation in fig. 4.15 with an error of 2%.
- In section 4.3.1, another way to discretize the diffusive term is discussed than used by Wemmenhove (2008). It is shown in fig. 4.23 for the 2D rising bubble case ($Re < 35$) that the transpose of the velocity gradient cannot be neglected and a good agreement is found with the benchmark of Hysing et al. (2009). The maximum error relative to the benchmark of Hysing et al. (2009) is decreased from 3.0% to 0.4%.
- The local height function is improved in section 5.4.2. According to Kleefsman et al. (2005) the local height function can be used for every free surface cell and is strictly mass conserving. However, it is proven in appendix D.2 that the non-physical method is not mass conserving in case of overlapping and therefore modified to reduce the mass loss versus still preserving the interface.

The physics behind the oscillations of air pockets and the compressibility of aerated water are described in chapter 2. In section 2.3, it is discussed that the compressibility of a mixture is larger when the aeration level is around 0.01% while values up to 14% at atmospheric conditions are measured at real scale. Using eq. (2.5), this can result in a compressibility which is an order higher than for air.

In section 2.3.4, it is discussed that the effect of aeration can be experienced on real scale and is a subject to scale effect. This makes it hard to achieve compressible effects at model scale. For this reason, the interest in well validated numerical methods is increasing.

8 Recommendations

With the extension made in chapter 5 for the multiphase flow model, the effect of entrained air on the initial impact and the following free surface dynamics can be modelled. For this extension, a transport equation is derived in section 5.4.2, eq. (5.12), which ensures pressure equilibrium under compression and expansion by a change in volume fraction.

To obtain accurate results, it is necessary to have a clear distinction between the air and the water at the free surface. However, during the simulation of the dam break case in section 5.7.3 and chapter 6, violent free surface dynamics are observed leading to fraction values $F < 1$ beneath the interface. This results in a non-zero right hand side as illustrated in eq. (5.37) and difference in fig. 5.16 between the compressible double fraction model and the multiphase model.

Due to the obtained restrictions for the local height function in section 5.4.2, in combination with a piecewise constant representation of the interface, the free surface is less "sharp" than it has to be. This results in fraction values significantly below one, leading to a greater amount of aeration. When the aeration increases, it cannot be assumed that the mass fraction of aeration is constant. Due to the diffused interface, momentum losses occur which can lead to underestimated pressure maxima [118].

It is recommended to investigate other Volume-of-Fluid reconstruction methods, like PLIC, SVOF and WLIC [41, 97, 156].

Besides the reconstruction methods, a convergence study of the dam break case in section 4.5.6 and chapter 6 need to be done to compare the observations. Furthermore, the speed of sound of the mixture needs to be verified for different aeration level with the analytical equation of Wood (1941), illustrated in fig. 2.3, for strenghtening the accuracy of the numerical method.

A | Impact types

The impact pressure depends on a lot of parameters. These parameters can be represented in groups; the geometrical, stiffness, incoming wave and water factors [69]. For example, the shape of the structure and position related to the waves are geometrical factors. With stiffness the compressibility of the water and the elasticity of the structure is meant. Further, the wave height, wave period, angle of attack, salinity of the water and current affect the pressure.

Before discussing the types of wave impacts, the term pressure impulse is defined. In fig. 2.2 it is shown that the pressure history can be seen as a cathedral shape [118]. The first step is that the pressure rises in time until it reaches the peak pressure. After that, the pressure decreases to a local minimum and makes a hump to the reflective pressure. Finally, it decreases to the end of the impact duration. The peak pressure and the impact duration is different and depends on the situation. However, Bagnold (1939) found experimentally that the integrated pressure over the total impact duration remains approximately constant. When this integration of the pressure over time is done, the pressure impulse is found. In confined spaces, like cracks, the pressure impulse is higher [33]. Besides the couple of impact types discussed in this section, analytic models are presented in appendix B.2, which can predict the impact pressure.

A distinction between two categories or pressures due to wave action is made by Allsop et al. (1996). The first one is quasi-static loads. These are caused by for example hydrostatic loadings, wind waves, and tides. The pressure has the same period as the wave period. The other kind of loading is dynamical impact wave loads. This happens when a wave breaks onto the structure and causes an impact loading. Impact pressure of shorter duration and greater intensity than quasi-static loads can be found. Here the magnitude of the force depends on the type of wave breaking onto the structure. In this report, the focus is on dynamic impact loadings.

There are three cases where wave breaking can happen [118]. The first case is when a wave approaches the coast, the height and steepness of the wave increases as the water depth decreases. This leads to an instability when the wavelength reaches a limiting value. The wave will start with breaking which is called bathymetric breaking. In this case, energy will be dissipated. The second case is when instability happens due to multiple waves, current or wind. The last case is wave breaking on a structure. This can happen when a wave propagates along, for example, a complex geometry or over a bathymetry variation.

When a wave breaks, several zones can be distinguished [118]. The zone where breaking is the dominant hydrodynamic process is called the surf zone. This is the range between the seaward outermost breaking wave to the swash zone. The swash zone is part of a sloped structure that is covered by the action of waves. The size of and when a wave breaks depends on the ratio between the wave height and the water depth.

There is a difference between sloped wall impacts and vertical wall impacts. The criterion for

sloped walls is described by Vink (1997). Further, also the different impact types are described. In this report, the focus is on the vertical wall impacts. Schmidt et al. (1993) made a distinction between seven types of impacts by doing large scale flume wave experiments. The way of breaking decides which kind of impact it is. A distinction is made between the type of breaking (plunging or spilling) and the relative position of the breaker relative to the wall. However, from experiments Oumeraci et al. (1992) distinguished four types of impact. The four types are illustrated in fig. A.1. These types depend on the relative distance between the wall and the wave which starts to break:

- Turbulent bore with foamy front: the wave is already broken before reaching the structure.
- Plunging breaker entrapping a large air pocket: can give pressure oscillation with high frequencies.
- Plunging breaking entrapping small amount of air: gives a single sharp peaked pressure.
- Flip-through: non-breaking wave without air entrapment

The highest pressure impacts are reached when entrapping a small air pocket. Hereafter, the plunging breaker entrapping a large air pocket gives the highest impact pressure. The weakest impact pressure is caused by the turbulent bore. The larger the amount of entrapped air, the lower the pressure magnitude and the longer the rise time of the impact force will be [60].

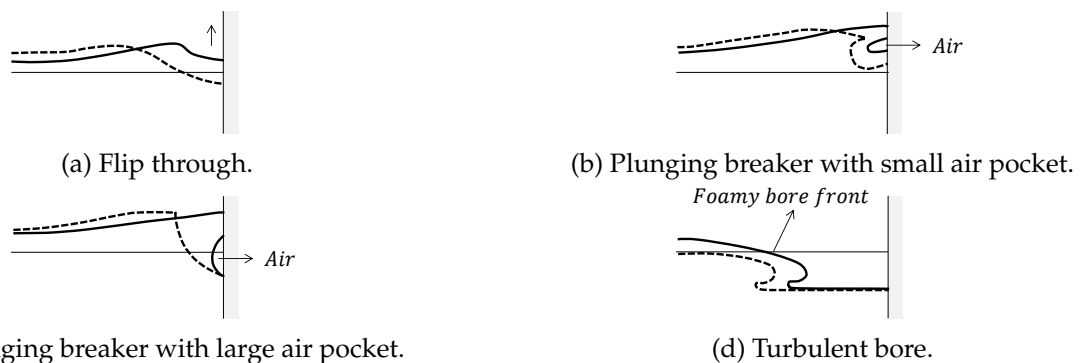


Figure A.1: Classification of breaking wave impact type according to Oumeraci et al. (1992).

For the flip-through impact, the wave is deflected upward where the waterline at the wall rises very rapidly. This happens earlier than the overturning wave crest hitting the wall. When the water rapidly accelerates upward along the wall, a jet is formed [32]. The air which is entrapped has to be expelled in an upward direction. Lugni et al. (2005) showed with experiments in a 0.1[m] wide channel that the jet can be accelerated up to 1500g. Further, it could reach a speed ten times the inflow velocity. A distinction can be made between several types of flip-through impact:

- Flip-through without air entrapment
- Flip-through which entraps a single small air cavity where no phase mixing happens
- Flip-through where a large number of minute bubbles are entrapped. Phase mixing will happen.

For the last case, the wave needs to be air entrained and have a turbulent front.

Kirkgöz (1995) also proposed a classification of wave breaking. A distinction is made between three types of impact:

- Early breaking wave: the wave crest has already started overturning and is not vertical anymore when impacting the wall. Air can escape out of the water or is entrapped.
- Perfect breaking wave: the wave reaches the wall when wavefront is perfectly vertical.
- Late breaking wave: the wave is not yet vertical when reaching the wall.

Further, by Vink (1997) a distinction is made between no air entrapment which is called Wagner type wave impact and with air entrapment which is called Bagnold type wave impacts. Between those two cases, a transition region can be found, called transition type wave impacts. This is when small air bubbles are entrapped and the highest impact pressure can be found [60]. Also, forces can be exerted on the seabed. Due to strong pressures propagating away from the impact zone along the wall to the seabed, significant forces can be observed. Three different types can cause these significant forces [104]. The first type is caused by impact-induced pressures which propagate away from the wall immediately after impact. The second type is due to oscillations of the air pocket which can generate pressure waves. The third type is caused by water droplets falling down after the jet. This can generate small pressure oscillations where pressure waves propagate to the seabed.

Hull and Müller (2002) did experiments to visualize the shape of breaking waves as a function of the offshore wave height. They could not observe the flip-through with a vertical jet and the existence of a parallel wavefront could not be confirmed. A contradiction was found that the plunging breaker with entrapment of a large air pocket gives the maximum pressure.

The case of perfect breaking is an ideal case because the wavefront is never totally flat. It is not proven that there is a difference between flip-through and perfect breaking. This proves that the kinematics of wave breaking on structures is still unclear [68, 118]. Further, multiple reports use different types of wave breaking, which makes the difference unclear. In this report, the focus is on the flip-through impact happening during green water events.

B Models

In this appendix, a very short overview of numerical models is given in appendix [B.1](#). Further, a list of simple analytic estimation of the impact pressure is given in appendix [B.2](#) and a short summary of the filling flow model of Peregrine and Kalliadasis (1996) is given in appendix [B.3](#).

B.1 Overview Numerical models

In this chapter a very short overview of numerical models is given. The first distinction which is made is between the Eulerian and the Lagrangian representation. Most approaches are based on the Eulerian representation of the flow. However, there are attempts to use the Lagrangian approach. Making use of the Smoothed Particle Hydrodynamics (SPH) method a set of particles move due to mutual interaction. Every particle has its own properties and moves according to the governing equations. The advantage of this method is that it can handle problems with large deformations. However, the computational costs are high because of solving the governing equations for every particle. The method is meshfree and was first proposed in the field of astrophysical problems [93]. The method is used among others by Yang and Tryggvason (1998) for simulating breaking waves.

The two different approaches, Eulerian and Lagrangian, can also be combined. An example of this combination is the Trackers method. The velocity and pressure fields are calculated on a fixed grid solving a two-phase Navier-Stokes model while the interface is localized by Lagrangian particles. Using this, the deformation of the interface at the subgrid level can be calculated over time. This method is among others used by Lee and Heo (2005) for simulating breaking waves.

Concerning Eulerian methods, several approaches can be found in the literature. Examples are the Boussinesq model of Bredmose et al. (2003) used for steep-wave sloshing in a tank to compare with experimental results, a VOF/Boundary element method used by Biauxser et al. (2004) studying breaking waves. Further, the multiphase model of Wemmenhove (2008) who extended the one fluid VOF method of Kleefsman et al. (2005). Two test cases with this model for hydrodynamic loading are done, including the dam break simulation, which gave good accuracy compared with the experimental results.

Besides making a distinction between the approaches of representation of the flow, also a distinction between the governing equations used can be made. For the simulation of free-surface flows also non-Navier-Stokes models have been used. However, these models are beyond the scope. A summary of these models is given by Duval (2007).

Using an incompressible one-phase Navier-Stokes model is the most common approach for modeling a free-surface model. The model is based on the Navier-Stokes equations in each phase and on stress and momentum continuity conditions at the interface [118]. Assuming

no slip between phases, no description of dynamics at a subgrid level and no mass transfer between phases at the interface, a set of incompressible Navier-Stokes equations usable in the entire domain can be found [39]. This procedure is also often used for the multifluid model. To track the interface, a choice can be made between the Lagrangian and Eulerian perspective. Using the Lagrangian perspective can lead to severe difficulties when the topology of the interface becomes complex [118]. The Volume of Fluid (VOF) method, from the Eulerian perspective and developed by Hirt and Nichols (1981), is a tracking method using a transport function of the fraction of liquid. This method is widely used and is explained in section 3.4.1. When the grid is not dense enough, the jump in the fraction value at an interface can thicken due to numerical diffusion. This makes it more difficult to localize the interface.

Another tracking method is the Level-Set method, for example, the tracking method used by Osher and Sethian (1988). With a Level-Set method, the distance to the interface is measured. However, this method can give losses of mass and the description of the distance field is complex.

An one fluid incompressible Navier-Stokes model is used by Kleefsman et al. (2005) for simulating wave impact problems. This model is partly described in chapter 3. The equations in this model are only solved for the cells containing fluid. The domain is limited to the interface. With this model, tests cases were run for the dam break, water entry, and wedge which gave good accuracy compared to the experimental results.

Not only direct numerical simulation models were used for modeling free-surface flows. Also, Reynolds Averaged Navier-Stokes (RANS) equations were used to solve wave breaking. Lin and Liu (1998) studied wave breaking in the surf zone using the turbulence model $k-\epsilon$. The results gave satisfactory results compared with the experimental data. Further, RANS results were also compared with Large Eddy Simulations (LES) by Losada et al. (2005) for wave breaking at a breakwater. With these models, turbulence can be described as accurate by fluid-structure interaction.

Besides incompressible one-fluid models, also compressible multifluid models are used for prediction of wave impacts. It is shown before by wave impact, compressible effects by entrapping air can be found. Therefore the compressibility should be taken into account by prediction of the wave impact to get more accurate results.

Models based on the Euler equations in each pure phase, non-viscous fluid, is proposed by Karni (1994). In this model, a transport equation for the mass fraction is used. However, for the application on breaking waves and wave impact, assuming inviscid flows is not suitable [118].

When not neglecting the viscosity of a fluid, the multiphase Navier-Stokes equations are solved. Using the averaging approach of Drew (1983), a multifluid model is developed by Saurel and Abgrall (1999) which solves the same governing equations in the whole domain for both fluids. When dealing with two phases, seven equations need to be solved; two mass conservation, two momentum, two energy and one transport equation. Using general equations as an equation of state, the equations can be solved. A multifluid model is also used in the software program COMFLOW and is explained in the next section. Multifluid models can be used for shock waves in compressible mixtures or to give interfaces Saurel and Lemetayer (2001) came even with a model for n amount of phases [118].

Bredmose et al. (2009) developed a compressible model based on the same seven equations solved in a finite volume framework assuming inviscid flow. No assumption of a smooth flow is made and an exact Riemann solver for the model equation is used. The gas phase was assumed compressible and the liquid phase incompressible. This model is used for breaking waves against a vertical wall and the results show that the compressible model successfully reproduces the main characteristics of violent breaking-wave impacts. This model also deals

with an initial aeration level to make the water compressible.

Also a compressible multiphase flow model that improves the representation of the flow physics for violent wave impact problems involving aeration is presented by Ma et al. (2014). An HLLC approximate Riemann solver is used for the compressible water-air mixture to discretize the integral form of the governing equations. The results showed clearly the advantages over other single-fluid and two-fluid incompressible flow models used for wave impact.

B.2 Analytic estimation of impact pressure

Before doing a numerical simulation, first an estimation of the impact pressure can be found using a simple analytical equation. These equations can be used to get more insight into the phenomena which may occur when waves break onto a structure.

B.2.1 Shock wave model

When this model is used, it is assumed that a homogeneous fluid approaches the wall perpendicularly and cannot escape. This will result in compression of the water which gives a shock wave moving away from the wall [69]:

$$\Delta p = p_{max} - p_0 = \rho_w c_w u_0, \quad (\text{B.1})$$

where u_0 is the velocity of the approaching front of the water. With this model, an absolute upper limit is given for the wave impact pressure. It is unlikely that the wave front is completely flat as discussed in the previous paragraph.

When the water contains air, the speed of sound of the mixture c_w can be replaced by eq. (2.8). This results in the following relation:

$$\Delta p = u_0 \sqrt{\frac{\gamma p_0 (1 - \beta) \rho_l}{\beta}}. \quad (\text{B.2})$$

The vertical wall experiencing the impact pressure can be compressible. When this is the case, also a compression wave is created in the wall. This effects the velocity of the water to $(1 - \epsilon)u_0$ where ϵ is the fraction of the inflow velocity that the wall moves. The pressure, in this case, will be equal to [69]:

$$\Delta p = \rho_w c_w u_0 \frac{1}{1 + \frac{\rho_w c_w}{\sqrt{\rho_s E_s}}}, \quad (\text{B.3})$$

where underscore s the values are for the structure and E is the elasticity modulus. When the structure does not compress but sag, the equation is not valid.

B.2.2 Models for Wagner type pressure

Wave impacts which cause Wagner type pressures are also called ventilated shocks [145]. These impacts can be described by the simple flow pressure model. The assumptions made in this model are based on no entrapped air and compression. The maximum pressure can be found using a coefficient k ; $p_{max} - p_0 = k(\frac{1}{2}\rho_w u_0^2)$. This coefficient can be seen as the slamming coefficient and is dependent on the angle between the front of the water and the structure which determines the added mass. For a circular cylinder, this coefficient varies between two and six depending on the geometry of the cylinder [145]. With this model probably the lowest impact pressure can be found using analytical models. The pressure of the model is lower than the observed impact pressures [99]. It is not applicable when both water and the object are

moving. An extension is made by Takahashi et al. (1993) using the attack angle of the wave front (θ). This is illustrated in fig. B.1. This model is applicable for all types of wave impact [145]. Wagner type impact happens when $\xi \leq \theta$. Here θ is the attack angle of the wave front and ξ the curvature of the wave front surface. According to Takhashi et al. (1993), the transition between Wagner type pressure and the transition pressure happens at $\theta \approx 20$ deg. The peak pressure is equal to:

$$p_{max} = \frac{1}{2} \rho_w u_0^2 \kappa_m^2 \left(\frac{\pi^2}{4} \cot^2 \theta + 1 \right), \quad (\text{B.4})$$

where κ_m is the added mass correction factor and part of the slamming coefficient. The average pressure is $0.25 \rho_w \pi^2 u_0^2 \kappa_m^2 \cot \theta$. The only difference with the flow pressure model is that the slamming coefficient is replaced by different coefficient and the atmospheric pressure is not added [145].

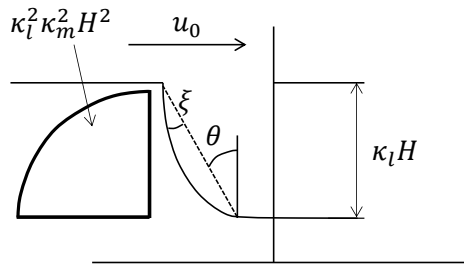


Figure B.1: Collision of a wave on a vertical wall [145].

B.2.3 Models for transition type pressure

According to Takhashi et al. (1993) when the attack angle of the wave front (θ) is smaller than the curvature of the wave front surface (ξ), the impact can be modeled as a Wagner type pressure. The peak pressure decreases and the duration time increases by the existence of air. This effect can be taken into account using the equivalent angle θ^* :

$$\theta^* = \theta_0 + \frac{\xi - \theta_0}{\xi} \theta \quad (\text{B.5})$$

$$\theta_0 = \tan \left(\frac{2}{\pi \kappa_m^2} \left(\frac{p_{max}}{\frac{1}{2} \rho_w u_0^2} \right)_{\theta=0} \right). \quad (\text{B.6})$$

This model is used for the transition type pressure [145].

B.2.4 Models for Bagnold type pressure

For a Bagnold type wave impact, air is entrapped. For this, the air compression model is used. With this model not only the maximum pressure can be calculated, also an approximation of the oscillation frequency of the air pocket can be found. The model is not valid when the wave surface hits the structure before the wave top. Bagnold (1939) formulated the problem of the compression of the air as a piston model where the water mass is the piston and the spring element the trapped air. The stiffness is assumed constant which is only applicable when the compression is not too big. Using an adiabatic polytropic relation between pressure and density, the following equation is found:

$$p - p_0 = u_0 \sqrt{\frac{\gamma p_0 \rho_w L}{D}} \sin \left(\sqrt{\frac{\gamma p_0}{\rho_w D L}} t \right), \quad (\text{B.7})$$

where L gives the size of the added water mass and D the size of the air pocket. The maximum pressure is equal to $p_0 + u_0 \sqrt{\frac{\gamma p_0 \rho L}{D}}$ and the period of the oscillation $T = 2\pi \sqrt{\frac{D \rho_w L}{\gamma p_0}}$. Good similarity by doing measurements with Bagnold's theory are found [121]. Note that the oscillation is not damped and that this model is equal to the linear shock wave model when $(1 - \beta)/\beta = L/D$. However, the air pockets is often bigger than the air content in the water which results in a lower pressure for the air compression model [121].

For the model of Takahashi et al. (1993) air is trapped when $\theta \leq 0$. Using the Bagnold number $\frac{\rho_w L u_0^2}{p_0 D}$ and assuming the impact pressure as a sinusoidal oscillation with relatively high damping, the following equations can be found for the oscillation period and the maximum average pressure:

$$p_{max,avg} = 1.6 \left(\frac{\rho_w L u_0^2}{D p_0} \right) p_0 \quad (\text{B.8})$$

$$T = 2\pi \sqrt{\frac{\pi \rho_w \kappa_m^2 \kappa_l^2 \kappa_a H^2}{4\gamma p_0}}, \quad (\text{B.9})$$

where κ_a is the air thickness coefficient, H is the wave height and κ_l the impact height function. For this equations a good agreement is found [145]. Note that air leakage is not accounted for.

B.3 Filling flow model

Peregrine and Kalliadasis (1996) introduced the *filling flow* model. This approach can be used to estimate the pressure at the surface of a confined space where jets can occur, as illustrated in fig. B.2. With this study it can be estimated whether the filling flow pressure is great enough to lift a structure. In fig. B.2 the velocity V_1 of the flow with a depth of h hits the dead end of the slot. The impacted wall is the top boundary. When the velocity is high enough, a jet along the top boundary with velocity V_2 and depth d can be generated. This is similar to the jet rising from the impact region of the flip through impact case [118]. Such a flow is considered steady, incompressible, inviscid and the model does not account for air entrainment and the jet breaking into droplets or entrapping air pockets.

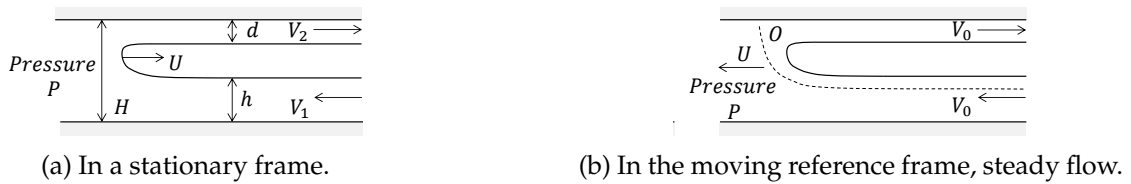


Figure B.2: Illustration of idealized configuration of the filling flow [113].

Peregrine and Thais (1996) developed an analytic method to estimate the cushioning effect of air in violent free-surface flows. This is done by extending the model for the filling flow. The extension was designed for the modelling of the flip-through, see appendix A. In this case the filling liquid is an air-water mixture and so air was already entrapped due previous impacts. To find this analytic model based on the Bernoulli equation, a couple of assumptions are made. It is assumed there is no slip between the two phases water and air. This results in the same velocity for both phases and a constant mass flux of gas in the mixture. Further, there is no dissipation caused by the relative motion between the liquid and the bubbles. The surface tension by the equation of state can be neglected. Namely, high pressures are caused due to the violent impact compared with the Laplace pressure. Due to dominance of inertial effects,

neglecting surface tension is realistic. This means that the pressure in the bubble is equal to the pressure in the liquid. The bubbles are dispersed homogeneously. The effect of gravity is also neglected which is appropriate for Froude numbers of order or larger than one.

The gas density is negligible compared to the density of the liquid for pressures up to ten bar. This means that the density of the mixture $\rho_w \approx (1 - \beta)\rho_l$. Assuming the liquid phase as incompressible, for the compressible gas phase an equation of state is needed. Assuming that the gas changes volume according to the polytropic law $p_g \rho_g^{-\gamma} = c$, the steady inviscid Bernoulli's equation can be filled in. The sensitivity of the choice between an isothermal and an adiabatic flow is small. In high pressure regions the flow becomes isothermal. However, the bubbles do not have significant inertia other than their added mass. They have a very strong response to pressure gradients which lead to fewer bubbles in the region of high pressures.

When neglecting second order terms, this results in first order equations for the filling and maximum pressure:

$$p - p_0 = \frac{2}{\epsilon + \beta} \quad \text{and} \quad p_{max} - p_0 = \frac{1}{(\epsilon + \beta)^2}, \quad (\text{B.10})$$

where $\epsilon = 1 - \frac{h}{H}$ indicating the violence of the impact. With this first order approximation the cushioning effect can be predicted. The compressibility of the mixture can give substantial changes of the pressure. The maximum pressure is reduced as the square of the background pressure. The background pressure is comparable to the pressure with the impact region in the flip through.

Due to the influence of the air content on the speed of sound, this affects the pressure. For an adiabatic behavior, the pressure in gas can be related to the air content [14, 113, 141]:

$$c_w^2 = \frac{\gamma p_g}{\rho_l \beta (1 - \beta)}, \quad (\text{B.11})$$

where p_g is the pressure in gas. It shows that indeed air content can have a cushioning effect and reduce the pressure in the gas. According eq. (B.10) the cushioning effect of the air increases with the violence of the flow.

When the air content is high enough the jet along the wall may be supersonic. However, it is assumed that the flow is steady while it is unsteady. The stagnation point O where inflow's free surface and outflow's free surface are connected, moves towards the entrance of the slot as it is filled. The velocity of this filling is influenced by the incoming air content. When the air content increases, the filling velocity will decrease. A volume reduction due to compression by high pressure reduces the effective filled volume. This is relevant for the flip through impact [118].

Normally compressible effects are visible for a Mach number higher than 0.3. However, when the impact is violent, the velocity varies which means that for lower Mach numbers of the inflow velocity, compressible effects can be observed.

Peregrine and Thais (1996) concluded that there is good agreement between the approximated solution and the exact numerical solution. For practical applications the model can give an estimation of the volume fraction of entrained air. Further, they explicitly mentioned that the problem of ship slamming seems particularly pertinent to take into account aeration.

C | Green water loading

In this appendix, the green water effect is in more detail explained than in section 2.4. In appendix C.1, the relation between green water, ship motions and environmental conditions is discussed. Hereafter, two Numerical simulations of green water events are discussed in appendix C.2. Besides the transverse force exerted by green water, also a Longitudinal force can be experienced. This is discussed in appendix C.3. The appendix ends with the Limiting range of dam break.

C.1 Effect of ship motions & environment

Green water can have a significant effect on the ship motions. In short waves, green water can generate great turning moments. Buchner (2002) noticed that the wind does not affect the green water. Further, it is incorrect to directly assume that the flow of the green water onto the deck can be seen as a breaking wave. The difference between slamming and green water impact is that with slamming a solid impact occurs while with green water impact loading only an impinging jet can be observed, similar to the flip-through effect.

Buchner et al. (1995) did model tests with a fixed foredeck of an FPSO to gain insight into the green water effect. He concluded that loadings due to green water depend strongly on the wave period, wave height and the current of the water. The current can increase the ship motions as well as affect the water flow around the bow. The wavelength increases with the current depending on the wave period. When the wavelength increases, higher wave exciting forces are expected, which lead to greater motions of the ship. Combining the increase of the motions with the current speed around the bow, the occurrence of green water events increases.

Another conclusion made by him is that the position of a structure in longitudinal direction does not affect the loading. Further, the pressure on the superstructure caused by green water is more or less dependent on the cube of the wave height. Small differences in the wave height significantly affect the green water loading, which makes it not very accurate to couple the loadings with linear ship motion predictions. When looking to the wave period, short waves resulted in the largest peak impact pressures due to the increased relative motions. The pattern of the flow is dependent on the wave period. The flow is more concentrated on the deck in short waves and there is a larger variation in the velocity of the flow.

C.2 Numerical simulations

By Fekken et al. (1999) numerical simulations are done on the fixed fore deck of a ship at model scale used in the experiments of Buchner et al. (1995). The numerical method solves the Navier-Stokes equation using the Volume-of-Fluid method of Hirt and Nichols (1981). The

global physical behavior of the water on the deck was described well. Further, the numerical results showed that the computed forces and pressure were similar to the experimental results.

In CFD simulations for high-speed container ships, Pham and Varyani (2005) concluded that the dam break case fails to represent the green water effect for ships with forward speed. A model based on dam break with an initial velocity would be more suitable. For horizontal loading, the behavior, the peak load and the rise time during the water-structure interaction can be predicted well with this model. For vertical deck pressure, the trend of the pressure curve, peak pressure and the rise time of the pressure can be predicted well. The acceleration of the deck is not taken into account.

C.3 Longitudinal force

When water comes onto the deck from the side of the ship, not only a transverse flow can be observed but also a velocity in the longitudinal direction (v). The velocity in longitudinal direction is dependent on the wave period (T_w); $v = \frac{2\pi(h+freeboard)}{T_w}$. Rewriting eq. (2.15) as function of u , the parameter u can be replaced by v to get the force and momentum generated by the velocity in the longitudinal direction. Note that the direction of the force is different as for the force generated by the transverse flow. The equations can only be used for slender structures. The loadings on larger structures are a result of the momentum in the green water which is completely deflected by the structure [16].

C.4 Limiting range of dam break

Besides the dam break problem, an almost breaking wave can also hit the deck or the superstructure directly. These two scenarios give the limiting range [55]. The plunging breaker starts hitting the deck in a small timescale. This causes a cavity which breaks into bubbles. After this rapid phase, it develops into a dam breaking type as shown in fig. 2.4. This case is not affected by the initial plunging phase.

Another scenario which can happen is the form of a hammer fist hitting the deck bluntly. This happens due to a steep incoming wave which is far from breaking. Further, also flip-through impact can happen [56].

D | Free surface displacement

In this appendix the different cases possible for the donor-acceptor method are discussed in appendix [D.1](#). After this, the limitations of the local height functions are highlighted by a couple of situations illustrated in appendix [D.2](#). Furthermore, the operation of a flux limiter is in short discussed.

D.1 Donor-Acceptor method

In this section, the different cases able for the donor-acceptor method are illustrated in fig. [D.1](#). It shows how much fluid is transported in one timestep. For this the CFL-restriction is needed. The orange dotted line represents $|V|$ which is equal to the transported volume $|u_f dt|$ through cell face f . The left cell is in every case the donor cell. The orange area represents the amount of fluid F which is transported using the donor-acceptor method.

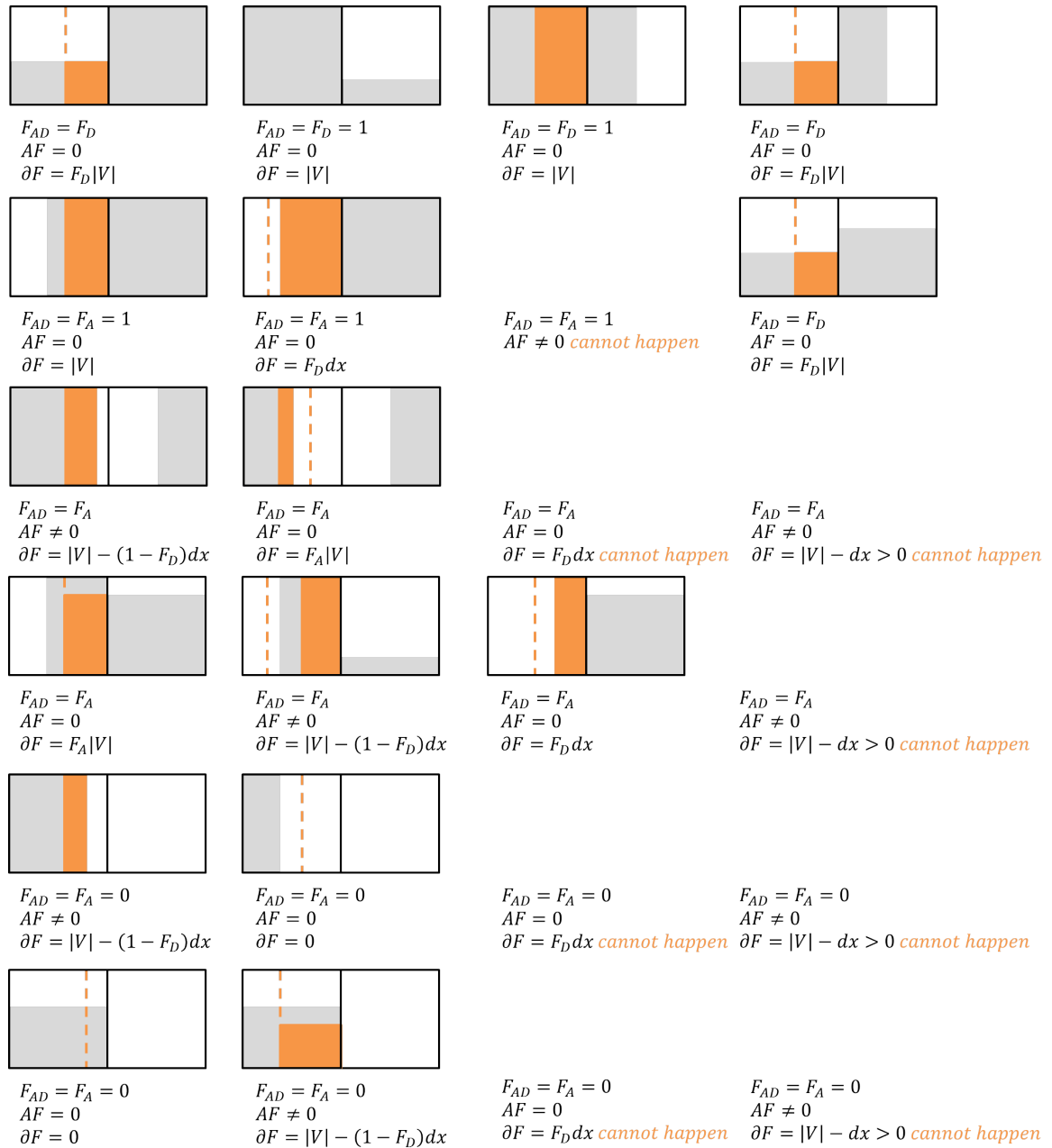
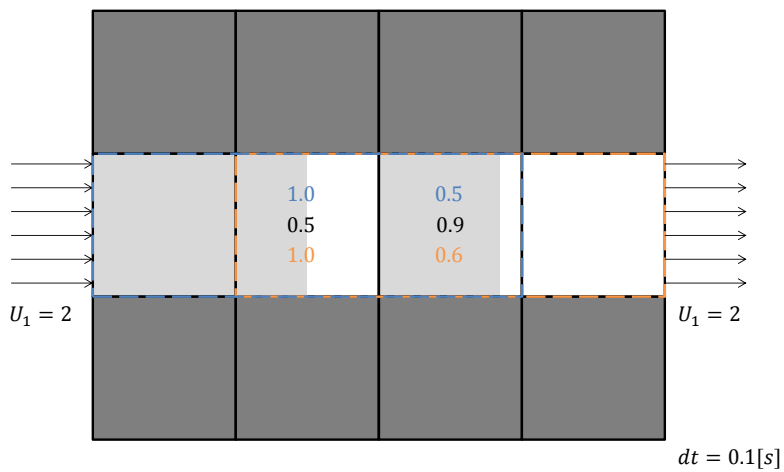
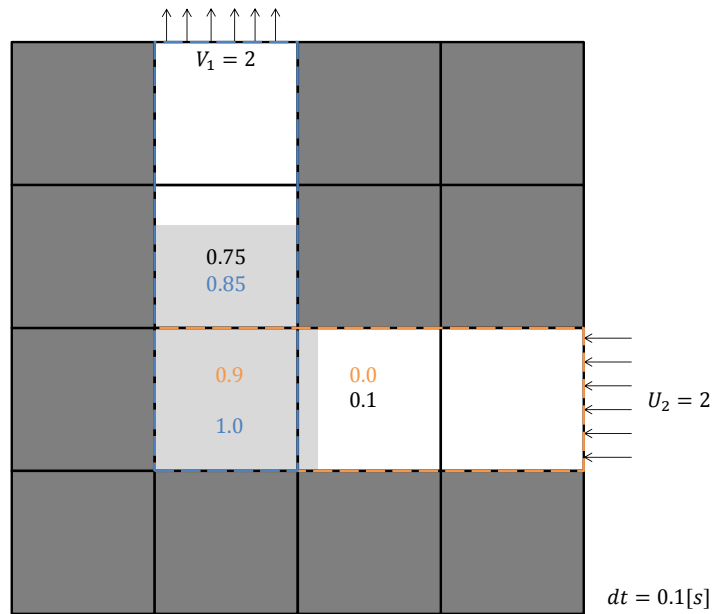


Figure D.1: Most common situations during a simulation of a free surface flow.

D.2 Local height function

In this section examples of contradicting height values due to overlapping of height functions are given in appendix D.2. Both fluids, air and water, are assumed as incompressible. The coloured values in the cells indicates the fraction of the next timestep.



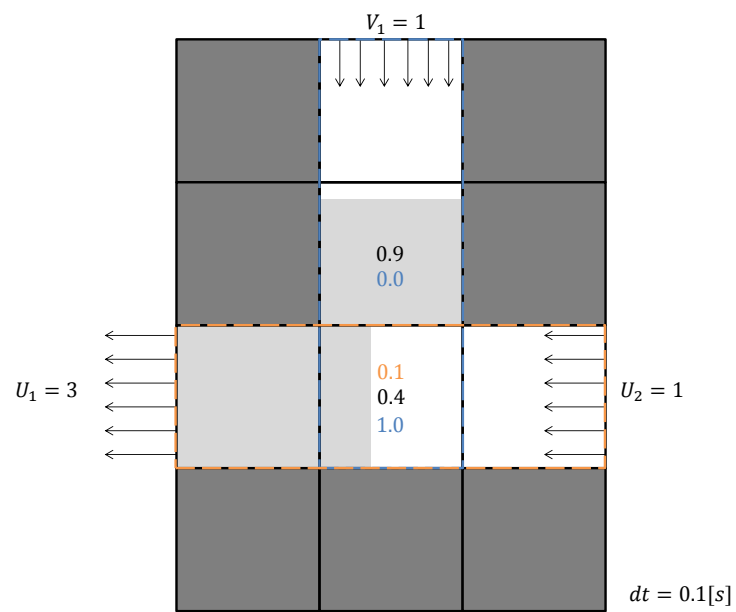
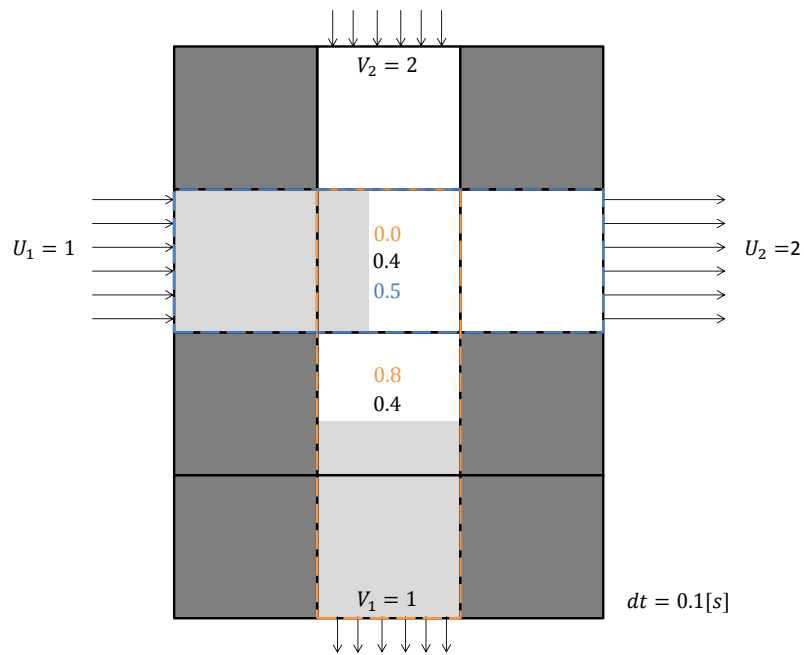


Figure D.3: Four examples of mass loss due to overlapping of local height functions.

D.3 Flux limiter

For the values of the volume fraction at the cell faces, a flux limiter is used to prevent wiggles in the volume fraction [100]. The volume fraction at the cell face can be estimated in many ways. This is illustrated in fig. D.4 where the difference is shown between the second-order upwind and first-order upwind estimation of the flux at the cell face. It is known that the donor-acceptor scheme makes use of upwinding and downwinding. The values can be estimated by using the

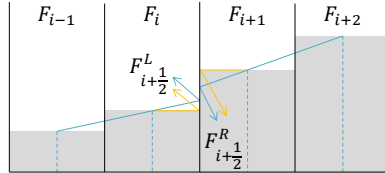


Figure D.4: Calculation of fraction at the cell face; blue: second-order upwind, orange: first-order upwind.

following equation:

$$\begin{aligned} F_{i+\frac{1}{2},j}^L &= F_{i,j} + \frac{1}{2}\Psi(r^L)(F_{i,j} - F_{i-1,j}), \\ F_{i+\frac{1}{2},j}^R &= F_{i+1,j} - \frac{1}{2}\Psi(r^R)(F_{i+1,j} - F_{i,j}), \end{aligned} \quad (\text{D.1})$$

where:

$$\begin{aligned} r^L &= \frac{F_{i+1,j} - F_{i,j}}{F_{i,j} - F_{i-1,j}}, \\ r^R &= \frac{F_{i+2,j} - F_{i+1,j}}{F_{i+1,j} - F_{i,j}}. \end{aligned}$$

For the function $\Psi(r)$, multiple limiters can be used. For example the Van Leer limiter which has an overall accuracy of second order in space:

$$\Psi(r) = \frac{r + |r|}{1 + r}. \quad (\text{D.2})$$

The difference between using the central differencing scheme and the Van Leer limiter, without height function, is shown in fig. 5.5. It results in a much smoother distribution of the volume fraction and hardly exceedance of a fraction of one. Using this scheme leads to fluxes only around the surface cells when the value of β is equal to zero. When $\Psi(r)$ is equal to zero, a first order estimation is found by upwinding. Besides the Van Leer and upwind scheme, also the Minmod, Superbee and MUSCL limiter is implemented.

E Dam break results

In this appendix, results of the one-phase model are given in appendix E.1. Furthermore, air pocket oscillations are illustrated for the multiphase model in appendix E.2.

E.1 Original VOF model

For the one-phase model, dam break simulations without an obstacle are done. The results are compared with the experimental results of Lobovsky et al. (2014).

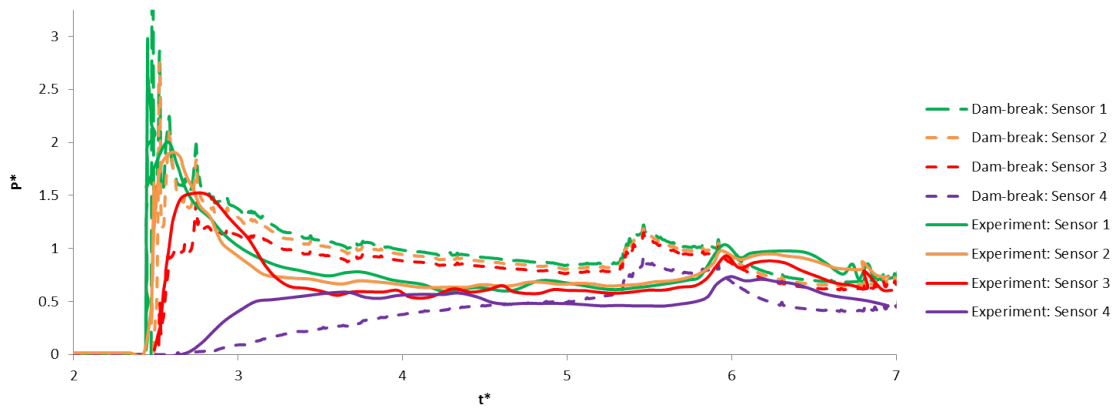


Figure E.1: Continuous lines are experimental results of [90], dotted lines are simulation results $H = 0.3[m]$.

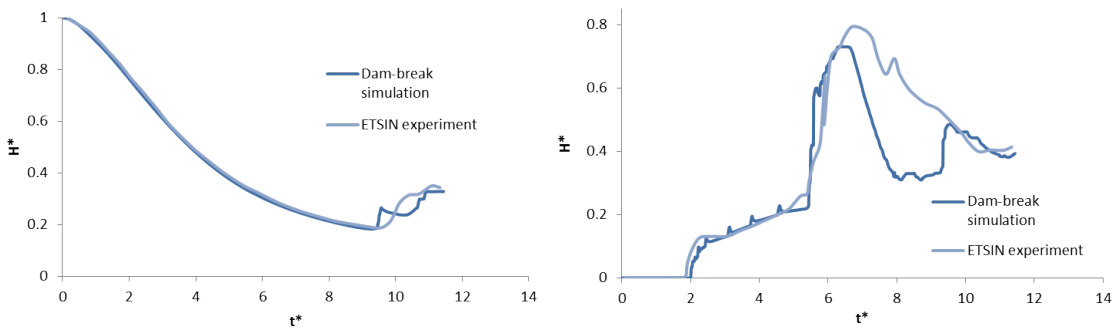


Figure E.2: Continuous lines are experimental results of H1 and H4 [90], dotted lines are simulation results $H = 0.3[m]$.

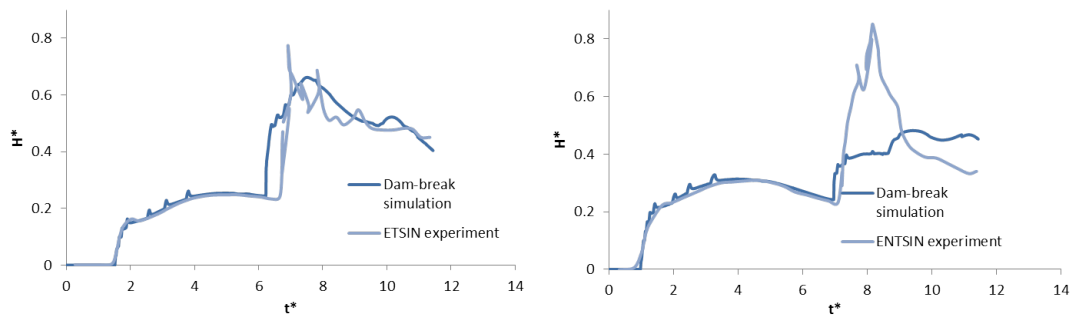


Figure E.3: Continuous lines are experimental results of H2 and H3 [90], dotted lines are simulation results $H = 0.3[m]$.

E.2 Air pocket oscillation

A couple of snapshots are illustrated in fig. E.4 for the case described in section 4.5.6. The pressure p in $[Pa]$ and the fraction F in $[-]$ are illustrated for four time levels. It can be noticed that the entrapped air pocket is pulsating.

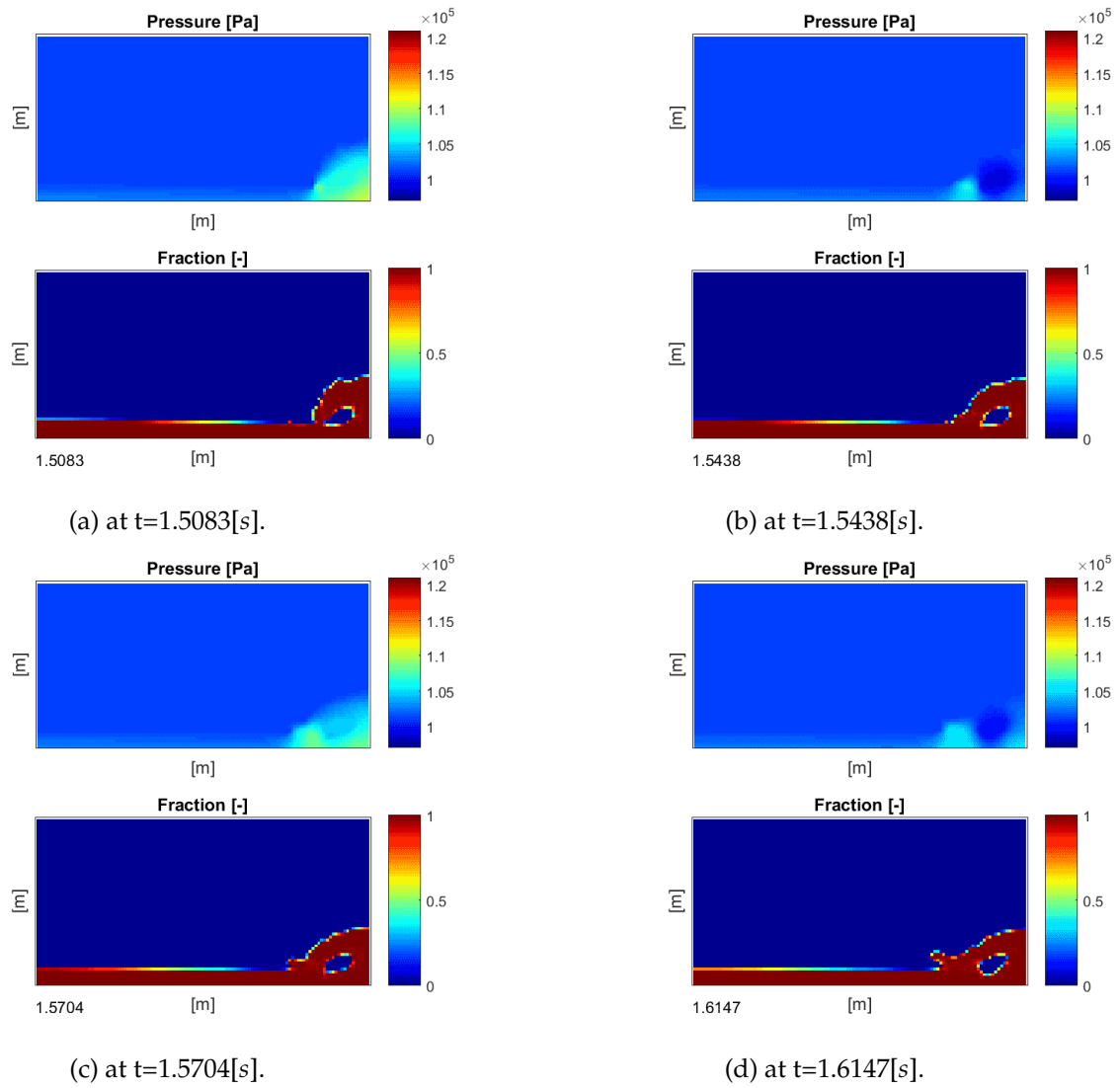


Figure E.4: Illustration of air pocket oscillation.

F | Discretization Multiphase model

In this appendix the numerical method for multiphase flow is fully discretized. This discretization is done by using the conservative momentum equation and the forward Euler timestepping scheme. The sections are ordered based on the fractional step method. The calculation of the auxiliary velocity field is already explained in section 4.3 by simply omitting the pressure term in the momentum equation. With this intermediate the velocity, the pressure of the next time step is solved in appendix F.1. With the new pressure, the new velocity can be calculated in appendix F.2. The discretization is only done for the horizontal momentum

F.1 Poisson equation

In this part the discretization is given of the Poisson equation used for the multiphase model. The general equation for a compressible liquid is:

$$\delta t \nabla \cdot \left(\frac{1}{\rho^n} \nabla p^{n+1} \right) = \frac{1}{\rho^n} \frac{\rho^{n+1} - \rho^n}{\delta t} + \frac{\mathbf{u}^n}{\rho^n} \cdot \nabla \rho^n - \nabla \cdot \left(\frac{\mathbf{u}^n}{\rho^n} (\rho^{n+1} - \rho^n) \right) + \nabla \cdot \tilde{\mathbf{u}}^n, \quad (\text{F.1})$$

where n indicates the timestep and \mathbf{u} is the auxiliary velocity field. Assuming incompressible water:

$$\delta t \nabla \cdot \left(\frac{1}{\rho^n} \nabla p^{n+1} \right) = (1 - F^n) \frac{1}{\rho^n} \left(\frac{\rho_a^{n+1} - \rho_a^n}{\delta t} + \mathbf{u}^n \cdot \nabla \rho_a^n \right) - \nabla \cdot \left(\frac{\mathbf{u}^n}{\rho^n} (\rho^{n+1} - \rho^n) \right) + \nabla \cdot \tilde{\mathbf{u}}^n. \quad (\text{F.2})$$

Where ρ_a^{n+1} is function of p^{n+1} . The equation of state of gaseous phases is used. Further Newton linearization is done, here a mistake is made in the notation by [Wemmenhove et al. \(2015\)](#) by neglecting the second term of the linearization.

$$\delta t \nabla \cdot \left(\frac{1}{\rho^n} \nabla p^{n+1} \right) = (1 - F^n) \frac{1}{\rho^n} \left(\frac{1}{\delta t} \left(\frac{1}{\gamma} \frac{\rho_{a,0}}{p_0^{\frac{1}{\gamma}}} (p^*)^{\frac{1}{\gamma}-1} (p^{n+1} - p^*) + \frac{\rho_{a,0}}{p_0^{\frac{1}{\gamma}}} (p^*)^{1/\gamma} - \rho_a^n \right) + \mathbf{u}^n \cdot \nabla \rho_a^n \right) - \nabla \cdot \left(\frac{\mathbf{u}^n}{\rho^n} (1 - F^n) \left(\frac{\rho_{a,0}}{p_0^{\frac{1}{\gamma}}} (p^*)^{1/\gamma} - \rho_a^n \right) \right) + \nabla \cdot \tilde{\mathbf{u}}^n. \quad (\text{F.3})$$

Replacing the equation of state by the pressure of air.

$$\begin{aligned} \delta t \nabla \cdot \left(\frac{1}{\rho^n} \nabla p^{n+1} \right) = \\ (1 - F^n) \frac{1}{\rho^n} \left(\frac{1}{\delta t} \left(\frac{1}{\gamma} \frac{\rho_a^*}{p^*} (p^{n+1} - p^*) + \rho_a^* - \rho_a^n \right) + \mathbf{u}^n \cdot \nabla \rho_a^n \right) \\ - \nabla \cdot \left(\frac{\mathbf{u}^n}{\rho^n} (1 - F^n) (\rho_a^* - \rho_a^n) \right) + \nabla \cdot \tilde{\mathbf{u}}^n \quad (\text{F.4}) \end{aligned}$$

Note that p^* is the pressure of previous time step. At the free surface we need to use for the equation of state only the gas pressure:

$$\begin{aligned} \nabla \cdot \left(\frac{1}{\rho^n} \nabla p^{n+1} \right) - (1 - F^n) \frac{\rho_a^*}{\rho^n \gamma p^* \delta t^2} p^{n+1} = \\ (1 - F^n) \frac{1}{\rho^n \delta t} \left(\mathbf{u}^n \cdot \nabla \rho_a^n - \frac{1}{\delta t} \left(\frac{\rho_a^*}{\gamma} - \rho_a^* + \rho_a^n \right) \right) \\ - \nabla \cdot \left(\frac{\mathbf{u}^n}{\rho^n \delta t} (1 - F^n) (\rho_a^* - \rho_a^n) \right) + \frac{1}{\delta t} \nabla \cdot \tilde{\mathbf{u}}^n. \quad (\text{F.5}) \end{aligned}$$

The discretization of every term:

$$\int_{V_f} \frac{1}{\delta t} \nabla \cdot (\tilde{\mathbf{u}}^n) dV_f = \oint_{\partial V_f} \frac{1}{\delta t} \tilde{\mathbf{u}} \cdot \mathbf{n}_f dS_f = \frac{1}{\delta t} \left(\frac{(\tilde{u}_{i+\frac{1}{2},j} - \tilde{u}_{i-\frac{1}{2},j})}{\delta x_i} + \frac{(\tilde{v}_{i,j+\frac{1}{2}} - \tilde{v}_{i,j-\frac{1}{2}})}{\delta y_j} \right), \quad (\text{F.6})$$

$$\begin{aligned} \int_{V_f} \nabla \cdot \left(\frac{1}{\rho^n} \nabla p^{n+1} \right) dV_f = \\ \oint_{\partial V_f} \frac{1}{\rho^n} \nabla p^{n+1} \cdot \mathbf{n}_f dS_f = \\ \frac{1}{\rho_{i+\frac{1}{2},j}^n \delta x_i} \frac{p_{i+1,j}^{n+1} - p_{i,j}^{n+1}}{(\delta x_i + \delta x_{i+1})/2} - \frac{1}{\rho_{i-\frac{1}{2},j}^n \delta x_i} \frac{p_{i,j}^{n+1} - p_{i-1,j}^{n+1}}{(\delta x_i + \delta x_{i-1})/2} \\ + \frac{1}{\rho_{i,j+\frac{1}{2}}^n \delta y_j} \frac{p_{i,j+1}^{n+1} - p_{i,j}^{n+1}}{(\delta y_j + \delta y_{j+1})/2} - \frac{1}{\rho_{i,j-\frac{1}{2}}^n \delta y_j} \frac{p_{i,j}^{n+1} - p_{i,j-1}^{n+1}}{(\delta y_j + \delta y_{j-1})/2}, \quad (\text{F.7}) \end{aligned}$$

$$\begin{aligned} \int_{V_f} \nabla \cdot \left(\frac{\mathbf{u}^n}{\rho^n \delta t} (1 - F^n) (\rho_a^* - \rho_a^n) \right) dV_f = \\ \oint_{\partial V_f} \frac{\mathbf{u}^n}{\rho^n \delta t} (1 - F^n) (\rho_a^* - \rho_a^n) \cdot \mathbf{n}_f dS_f = \\ \oint_{\partial V_f} \mathbf{R} \cdot \mathbf{n} dS_f = \frac{(R_{i+\frac{1}{2},j} - R_{i-\frac{1}{2},j})}{\delta x_i} + \frac{(R_{i,j+\frac{1}{2}} - R_{i,j-\frac{1}{2}})}{\delta y_j}, \quad (\text{F.8}) \end{aligned}$$

where the R values are found by cell-averaging the fraction and air density. Note that interpolation is needed to get the pressure, density and volume fraction at the cell edges. The area dV_f is everywhere the same and can be removed. The equations can be reduced to:

$$\int_{V_f} (1 - F^n) \frac{\rho_a^*}{\rho^n \gamma p^* \delta t^2} p^{n+1} dV_f = (1 - F_{i,j}^n) \frac{\rho_{a,i,j}^*}{\rho_{i,j}^n \gamma p_{i,j}^* \delta t^2} p_{i,j}^{n+1}, \quad (\text{F.9})$$

$$\int_{V_f} (1 - F^n) \frac{1}{\rho^n \delta t} \left(\mathbf{u}^n \cdot \nabla \rho_a^n - \frac{1}{\delta t} \left(\frac{\rho_a^*}{\gamma} - \rho_a^* + \rho_a^n \right) \right) dV_f = \int (1 - F^n) \frac{1}{\rho^n \delta t} (R - G) dV_f, \quad (\text{F.10})$$

where $R = \mathbf{u}^n \cdot \nabla \rho_a^n$ and $G = \frac{1}{\delta t} \left(\frac{\rho_a^*}{\gamma} - \rho_a^* + \rho_a^n \right)$:

$$\int_{V_f} (1 - F^n) \frac{1}{\rho^n \delta t} \mathbf{u}^n \cdot \nabla \rho_a^n dV_f = \int (1 - F^n) \frac{1}{\rho^n \delta t} u^n \rho_a^n dy + \int (1 - F^n) \frac{1}{\rho^n \delta t} v^n \rho_a^n dx. \quad (\text{F.11})$$

This results in:

$$(1 - F_{i,j}^n) \frac{1}{\rho_{i,j}^n \delta t} \left(u_{i,j}^n \frac{\rho_{a,i+\frac{1}{2},j}^n - \rho_{a,i-\frac{1}{2},j}^n}{\delta x_i} + v_{i,j}^n \frac{\rho_{a,i,j+\frac{1}{2}}^n - \rho_{a,i,j-\frac{1}{2}}^n}{\delta y_j} \right). \quad (\text{F.12})$$

For the other term G:

$$\int_{V_f} (1 - F^n) \frac{1}{\rho^n \delta t^2} \left(\frac{\rho_a^*}{\gamma} - \rho_a^* + \rho_a^n \right) dV_f = (1 - F_{i,j}^n) \frac{1}{\rho_{i,j}^n \delta t^2} \left(\frac{\rho_{a,i,j}^*}{\gamma} - \rho_{a,i,j}^* + \rho_{a,i,j}^n \right). \quad (\text{F.13})$$

F.2 New velocity

To calculate the new velocity, the pressure term needs to be discretized and summed with the auxiliary velocity field. For this, the control volume in fig. 4.1 is used. To find the new velocity at the cell edges:

$$u^{n+1} = \tilde{u} - \frac{u^n}{\rho_c^n} (\rho_c^{n+1} - \rho_c^n) - \frac{\delta t}{\rho_c^n \delta y_c \delta x_c} (p_e^{n+1} - p_w^{n+1}) \delta y_j. \quad (\text{F.14})$$

G Extended model

In this appendix, the transport equation for fraction A , based on the literature, is derived in appendix G.1. Hereafter, a pseudo code for a CFL-controller is given in appendix G.2. The acoustic properties of the extended model, also based on literature, are derived in appendix G.3. The appendix ends with remaining results of the 2D helium shock bubble case in appendix G.4.

G.1 Derivation transport equation

Compared to the single-phase and multiphase model, the transport equation has to change. The transport equation used for those models are for an incompressible liquid. However, due to the extension, the divergence of the velocity where $F=1$ is not equal to zero anymore.

The new transport equation which is also used by Ma et al. (2014) is derived below using the mass conservation of the mixture [100]. Here it is assumed that the two fluids are isentropic ($\frac{Ds}{Dt}=0$).

$$\begin{aligned} \frac{\partial(A\rho_l)}{\partial t} + \nabla \cdot (A\rho_l \mathbf{u}) &= 0, \\ A \left(\frac{\partial \rho_l}{\partial t} + \mathbf{u} \cdot \nabla \rho_l \right) + A\rho_l \nabla \cdot \mathbf{u} + \rho_l \left(\frac{\partial A}{\partial t} + \mathbf{u} \cdot \nabla A \right) &= 0, \\ \frac{\rho_l}{A} \left(\frac{\partial A}{\partial t} + \mathbf{u} \cdot \nabla A \right) + \rho_l \nabla \cdot \mathbf{u} + \frac{1}{c_l^2} \left(\frac{\partial p}{\partial t} + \mathbf{u} \cdot \nabla p \right) &= 0, \end{aligned} \quad (\text{G.1})$$

The same can be done for the other fluid which results in:

$$-\frac{\rho_a}{(1-A)} \left(\frac{\partial A}{\partial t} + \mathbf{u} \cdot \nabla A \right) + \frac{1}{c_a^2} \left(\frac{\partial p}{\partial t} + \mathbf{u} \cdot \nabla p \right) + \rho_a \nabla \cdot \mathbf{u} = 0. \quad (\text{G.2})$$

Here the material derivative of the pressure, where $p = p(s_l, \rho_l)$ and $p = p(s_a, \rho_a)$ and using the assumption of isentropic flow, is related to the material derivative of the density [80]:

$$\begin{aligned} \frac{Dp}{Dt} &= \left(\frac{\partial p}{\partial \rho_a} \right)_{s_a} \frac{D\rho_a}{Dt} = c_a^2 \frac{D\rho_a}{Dt}, \\ \frac{Dp}{Dt} &= \left(\frac{\partial p}{\partial \rho_l} \right)_{s_l} \frac{D\rho_l}{Dt} = c_l^2 \frac{D\rho_l}{Dt}. \end{aligned} \quad (\text{G.3})$$

Summing the equations for both fluids, like is done to find $\frac{D\rho}{Dt} + \rho \nabla \cdot \mathbf{u} = 0$:

$$\left(\frac{A}{\rho_l} \frac{\partial \rho_l}{\partial p} + \frac{(1-A)}{\rho_a} \frac{\partial \rho_a}{\partial p} \right) \left(\frac{\partial p}{\partial t} + \mathbf{u} \cdot \nabla p \right) + \nabla \cdot \mathbf{u} = 0. \quad (\text{G.4})$$

This equation for the material derivative of the pressure can be substituted in the mass conservation of $A\rho_l$, see eq. (G.1):

$$\frac{\partial A}{\partial t} + \nabla \cdot (A\mathbf{u}) - A\nabla \cdot \mathbf{u} = A(1-A) \left(\frac{\frac{\partial \rho_l}{\partial p} \rho_a - \frac{\partial \rho_a}{\partial p} \rho_l}{A \frac{\partial \rho_l}{\partial p} \rho_a + (1-A) \frac{\partial \rho_a}{\partial p} \rho_l} \right) \nabla \cdot \mathbf{u}, \quad (\text{G.5})$$

where the velocities are known at the cell faces. This equation is derived by assuming pressure equilibrium. The right hand side term assures that the material derivative of the phase entropy is zero in the absence of shockwaves [96]. When neglecting the right hand side term, the transport equation is standard for the fraction A [105].

The equation is quasi-conserving and gives a stabilizing effect [96]. Comparing to the multi-phase model, the extended model is non-conservative. Only the total mass is conserved where the fluids separately are not necessarily conserved.

The method used in Miller et al. (2013) is quite similar to the method used in this report. Neither total mass nor phasic mass are balanced exactly by their method. However, in practice they obtain good results with a reasonable amount of mass error. This may be caused by strongly enforcing the equations of state instead of a weak statement of an energy equation. A slight energy dissipation can give stability to numerical methods. Further, the balance equation is not conservative. The transport equation given in eq. (G.5) can be simplified:

$$\begin{aligned} \frac{\partial A}{\partial t} + \nabla \cdot (A\mathbf{u}) - A\nabla \cdot \mathbf{u} &= A(1-A) \left(\frac{c_a^2 \rho_a - c_l^2 \rho_l}{Ac_a^2 \rho_a + (1-A)c_l^2 \rho_l} \right) \nabla \cdot \mathbf{u}, \\ \frac{\partial A}{\partial t} + \nabla \cdot (A\mathbf{u}) &= \frac{A(1-A)c_a^2 \rho_a - A(1-A)c_l^2 \rho_l + A^2 c_a^2 \rho_a + A(1-A)c_l^2 \rho_l}{Ac_a^2 \rho_a + (1-A)c_l^2 \rho_l} \nabla \cdot \mathbf{u}, \\ \frac{\partial A}{\partial t} + \nabla \cdot (A\mathbf{u}) &= \frac{Ac_a^2 \rho_a}{Ac_a^2 \rho_a + (1-A)c_l^2 \rho_l} \nabla \cdot \mathbf{u}. \end{aligned}$$

G.2 CFL-controller

The CFL-controller is implemented in the following way:

```

if CFL is exceeded
    dt = min(dt/4, CFL*dx/(4*u))
    step = 1
elseif step >= 10 & 2*u*dt/dx < CFL
    dt = 3*dt/2
    step = 1
elseif 2*CFL1 < CFL
    step = step+1
else
    step = 1
end

```

In case of a higher CFL-number than defined, the calculation of that particular timestep needs to be repeated.

G.3 Acoustics of the mixture

The pressure variations by wave impacts can be large. These variations can lead to shock waves in the mixture with a certain speed. This speed of sound for the mixture is validated using the simulation of a 1D shock tube, see section 5.5. In the multiphase model fluids a and w are flowing separately which is also the case for the extended model. However, the extension is made to simulate dispersed air in the fluid w where the acoustic propagation of the mixture has to be represented. In this section this is proved analytically based on the method used by Plumerault (2009).

To find the momentum equation given in eq. (5.1), the assumption is made to average the interface pressure [125]. This gives the relation for the pressure in fluid w ; $p_w = \beta p_a(\rho_a) + (1 - \beta)p_l(\rho_l)$. The definition for the speed of sound of the mixture at atmospheric pressure p_0 is:

$$c_{w,0}^2 = \left. \frac{\partial p_w}{\partial \rho_w} \right|_{\rho_{w,0}}, \quad (\text{G.6})$$

where it is known that $\rho_w = \beta \rho_a + (1 - \beta)\rho_l$. The derivative of the pressure needs to be found to find the speed of sound of the mixture.

$$\begin{aligned} \frac{\partial p_w}{\partial \rho_w} &= \beta \frac{\partial p_a(\rho_a)}{\partial \rho_w} + (1 - \beta) \frac{\partial p_l(\rho_l)}{\partial \rho_w} + p_a(\rho_a) \frac{\partial \beta}{\partial \rho_w} + p_l(\rho_l) \frac{\partial(1 - \beta)}{\partial \rho_w}, \\ \frac{\partial p_w}{\partial \rho_w} &= \beta \frac{\partial p_a(\rho_a)}{\partial \rho_a} \frac{\partial \rho_a}{\partial \rho_w} + (1 - \beta) \frac{\partial p_l(\rho_l)}{\partial \rho_l} \frac{\partial \rho_l}{\partial \rho_w} + (p_a(\rho_a) - p_l(\rho_l)) \frac{\partial \beta}{\partial \rho_w}. \end{aligned} \quad (\text{G.7})$$

Note that the relation between the fluid w and the dispersed air and water is $\beta \rho_a = y \rho_w$ and $(1 - \beta)\rho_l = (1 - y)\rho_w$. Using the quotient rule the derivatives of ρ_a and ρ_l can be found:

$$\begin{aligned} \frac{\partial \rho_a}{\partial \rho_w} &= \frac{\beta y - y \rho_w \frac{\partial \beta}{\partial \rho_w}}{\beta^2}, \\ \frac{\partial \rho_l}{\partial \rho_w} &= \frac{(1 - \beta)(1 - y) + (1 - y) \rho_w \frac{\partial \beta}{\partial \rho_w}}{(1 - \beta)^2}. \end{aligned} \quad (\text{G.8})$$

These derivatives can be substituted. Further, the mass fraction y can be replaced using the relations for ρ_a and ρ_l :

$$\begin{aligned} \frac{\partial p_w}{\partial \rho_w} &= \frac{\partial p_a(\rho_a)}{\partial \rho_a} \frac{\beta y - y \rho_w \frac{\partial \beta}{\partial \rho_w}}{\beta} \\ &\quad + \frac{\partial p_l(\rho_l)}{\partial \rho_l} \frac{(1 - \beta)(1 - y) + (1 - y) \rho_w \frac{\partial \beta}{\partial \rho_w}}{(1 - \beta)} + (p_a(\rho_a) - p_l(\rho_l)) \frac{\partial \beta}{\partial \rho_w}, \\ \frac{\partial p_w}{\partial \rho_w} &= \frac{\partial p_a(\rho_a)}{\partial \rho_a} \rho_a \left(\frac{\beta}{\rho_w} - \frac{\partial \beta}{\partial \rho_w} \right) \\ &\quad + \frac{\partial p_l(\rho_l)}{\partial \rho_l} \rho_l \left(\frac{(1 - \beta)}{\rho_w} + \frac{\partial \beta}{\partial \rho_w} \right) + (p_a(\rho_a) - p_l(\rho_l)) \frac{\partial \beta}{\partial \rho_w}. \end{aligned} \quad (\text{G.9})$$

Using the speed of sound relations for $c_{a,0}^2 = \left. \frac{\partial p_a(\rho_a)}{\partial \rho_a} \right|_{\rho_{a,0}}$ and $c_{l,0}^2 = \left. \frac{\partial p_l(\rho_l)}{\partial \rho_l} \right|_{\rho_{l,0}}$ and the pressure equilibrium (homogeneous mixture) $p_l = p_a$, the pressure derivative relation can be simplified:

$$\frac{\partial p_w}{\partial \rho_w} = c_{a,0}^2 \rho_{a,0} \left(\frac{\beta_0}{\rho_{w,0}} - \frac{\partial \beta_0}{\partial \rho_w} \Big|_{\rho_{w,0}} \right) + c_{l,0}^2 \rho_{l,0} \left(\frac{(1 - \beta_0)}{\rho_{w,0}} + \frac{\partial \beta_0}{\partial \rho_w} \Big|_{\rho_{w,0}} \right), \quad (\text{G.10})$$

where the subscript 0 is used for the reference state. Now an expression for the derivative of the volume fraction $\frac{\partial \beta}{\partial \rho_w} |_{\rho_{w,0}}$ needs to be found. To find this expression, the pressure equilibrium $p_a = p_l$ is used. Using the equation of states in section 5.4.4, the following relation can be found. For this the speed of the fluid l is assumed constant:

$$c_{l,0}^2(\rho_l - \rho_{l,0}) + p_0 = p_0 \left(\frac{\rho_a}{\rho_{a,0}} \right)^{\gamma_a}. \quad (\text{G.11})$$

Substituting the relation for the mass fraction y and taking the derivative $\frac{\partial \beta_0}{\partial \rho_w} |_{\rho_{w,0}}$ using the quotient rule:

$$\begin{aligned} c_{l,0}^2 \left(\frac{(1-y)\rho_w}{(1-\beta)} - \rho_{l,0} \right) + p_0 &= p_0 \left(\frac{y\rho_w}{\beta\rho_{a,0}} \right)^{\gamma_a}, \\ c_{l,0}^2 \frac{(1-y)(1-\beta) + (1-y)\rho_w \frac{\partial \beta}{\partial \rho_w}}{(1-\beta)^2} &= p_0 \gamma_a \left(\frac{y\rho_w}{\beta\rho_{a,0}} \right)^{\gamma_a-1} \frac{y\beta - y\rho_w \frac{\partial \beta}{\partial \rho_w}}{\beta^2}. \end{aligned} \quad (\text{G.12})$$

This equation needs to be rewritten to find the relation for the derivative $\frac{\partial \beta}{\partial \rho_w}$, where $\rho_w = \rho_{w,0}$:

$$\begin{aligned} \frac{\partial \beta_0}{\partial \rho_w} |_{\rho_{w,0}} &= \frac{p_0 \gamma_a y / \beta_0 (y\rho_{w,0} / \beta_0 \rho_{a,0})^{\gamma_a-1} - c_{l,0}^2 (1-y) / (1-\beta_0) \beta_0^2 (1-\beta_0)^2}{c_{l,0}^2 \rho_{w,0} (1-y) / (1-\beta_0)^2 + p_0 \gamma_a y \rho_{w,0} / \beta_0^2 (y\rho_{w,0} / \beta_0 \rho_{a,0})^{\gamma_a-1} \beta_0^2 (1-\beta_0)^2}, \\ \frac{\partial \beta_0}{\partial \rho_w} |_{\rho_{w,0}} &= \frac{p_0 \gamma_a y \beta_0 (1-\beta_0)^2 (y\rho_{w,0} / \beta_0 \rho_{a,0})^{\gamma_a-1} - c_{l,0}^2 (1-y) \beta_0^2 (1-\beta_0)}{c_{l,0}^2 \rho_{w,0} (1-y) \beta_0^2 + p_0 \gamma_a y \rho_{w,0} (1-\beta_0)^2 (y\rho_{w,0} / \beta_0 \rho_{a,0})^{\gamma_a-1}}. \end{aligned} \quad (\text{G.13})$$

Replacing the mass fraction by the relation for the fluid a and substituting the speed of sound $c_{a,0}$:

$$\frac{\partial \beta_0}{\partial \rho_w} |_{\rho_{w,0}} = \frac{\beta_0 (1-\beta_0)^2 c_{a,0}^2 y - c_{l,0}^2 (1-y) \beta_0^2 (1-\beta_0)}{c_{l,0}^2 \rho_{w,0} (1-y) \beta_0^2 + y \rho_{w,0} (1-\beta_0)^2 c_{a,0}^2}. \quad (\text{G.14})$$

To remove all the mass fractions, it is known that $(1-y)\rho_{w,0} = (1-\beta_0)\rho_{l,0}$ and $y\rho_{w,0} = \beta_0\rho_{a,0}$. These relations can be substituted:

$$\begin{aligned} \frac{\partial \beta_0}{\partial \rho_w} |_{\rho_{w,0}} &= \frac{\beta_0 (1-\beta_0)^2 c_{a,0}^2 \beta_0 \rho_{a,0} / \rho_{w,0} - c_{l,0}^2 (1-\beta_0) \rho_{l,0} / \rho_{w,0} \beta_0^2 (1-\beta_0)}{c_{l,0}^2 \rho_{w,0} (1-\beta_0) \rho_{l,0} / \rho_{w,0} \beta_0^2 + \beta_0 \rho_{a,0} / \rho_{w,0} \rho_{w,0} (1-\beta_0)^2 c_{a,0}^2}, \\ \frac{\partial \beta_0}{\partial \rho_w} |_{\rho_{w,0}} &= \frac{1}{\rho_{w,0}} \frac{\beta_0^2 (1-\beta_0)^2 c_{a,0}^2 \rho_{a,0} - c_{l,0}^2 \rho_{l,0} \beta_0^2 (1-\beta_0)^2 / \beta_0 (1-\beta_0)}{c_{l,0}^2 (1-\beta_0) \rho_{l,0} \beta_0^2 + \beta_0 \rho_{a,0} (1-\beta_0)^2 c_{a,0}^2 / \beta_0 (1-\beta_0)}, \\ \frac{\partial \beta_0}{\partial \rho_w} |_{\rho_{w,0}} &= \frac{\beta_0 (1-\beta_0)}{\rho_{w,0}} \frac{c_{a,0}^2 \rho_{a,0} - c_{l,0}^2 \rho_{l,0}}{c_{l,0}^2 \rho_{l,0} \beta_0 + \rho_{a,0} (1-\beta_0) c_{a,0}^2}. \end{aligned} \quad (\text{G.15})$$

This equation can be substituted in eq. (G.10) to find the relation for the sound speed of the mixture $c_{w,0}$:

$$\begin{aligned}
\rho_{w,0}c_{w,0}^2 &= c_{a,0}^2\rho_{a,0}\beta_0 + c_{l,0}^2\rho_{l,0}(1 - \beta_0) \\
&\quad + (c_{l,0}^2\rho_{l,0} - c_{a,0}^2\rho_{a,0})\beta_0(1 - \beta_0)\frac{c_{a,0}^2\rho_{a,0} - c_{l,0}^2\rho_{l,0}}{c_{l,0}^2\rho_{l,0}\beta_0 + \rho_{a,0}(1 - \beta_0)c_{a,0}^2}, \\
\rho_{w,0}c_{w,0}^2(c_{l,0}^2\rho_{l,0}\beta_0 + \rho_{a,0}(1 - \beta_0)c_{a,0}^2) &= (c_{a,0}^2\rho_{a,0}\beta_0 + c_{l,0}^2\rho_{l,0}(1 - \beta_0))(c_{l,0}^2\rho_{l,0}\beta_0 + \rho_{a,0}(1 - \beta_0)c_{a,0}^2) \\
&\quad + (c_{l,0}^2\rho_{l,0} - c_{a,0}^2\rho_{a,0})\beta_0(1 - \beta_0)(c_{a,0}^2\rho_{a,0} - c_{l,0}^2\rho_{l,0}), \\
\rho_{w,0}c_{w,0}^2(c_{l,0}^2\rho_{l,0}\beta_0 + \rho_{a,0}(1 - \beta_0)c_{a,0}^2) &= \rho_l\rho_a c_{l,0}^2 c_{a,0}^2 (\beta_0 + (1 - \beta_0))^2, \\
\rho_{w,0}c_{w,0}^2 &= \frac{\rho_{l,0}\rho_{a,0}c_{l,0}^2c_{a,0}^2}{c_{l,0}^2\rho_{l,0}\beta_0 + \rho_{a,0}(1 - \beta_0)c_{a,0}^2}.
\end{aligned} \tag{G.16}$$

Taking the inverse of the equation results in the Wood (1941) formula, illustrated in eq. (2.8). The equation can be used for any reference state:

$$\frac{1}{\rho_{w,0}c_{w,0}^2} = \frac{\beta_0}{\rho_{a,0}c_{a,0}^2} + \frac{(1 - \beta_0)}{\rho_{l,0}c_{l,0}^2}. \tag{G.17}$$

G.4 Shock bubble

Besides the density field illustrated in the report, also the pressure field and fraction field are compared with the numerical results of Kreeft and Koren (2010). The results are plotted in fig. G.1 and fig. G.2 and show similar results.

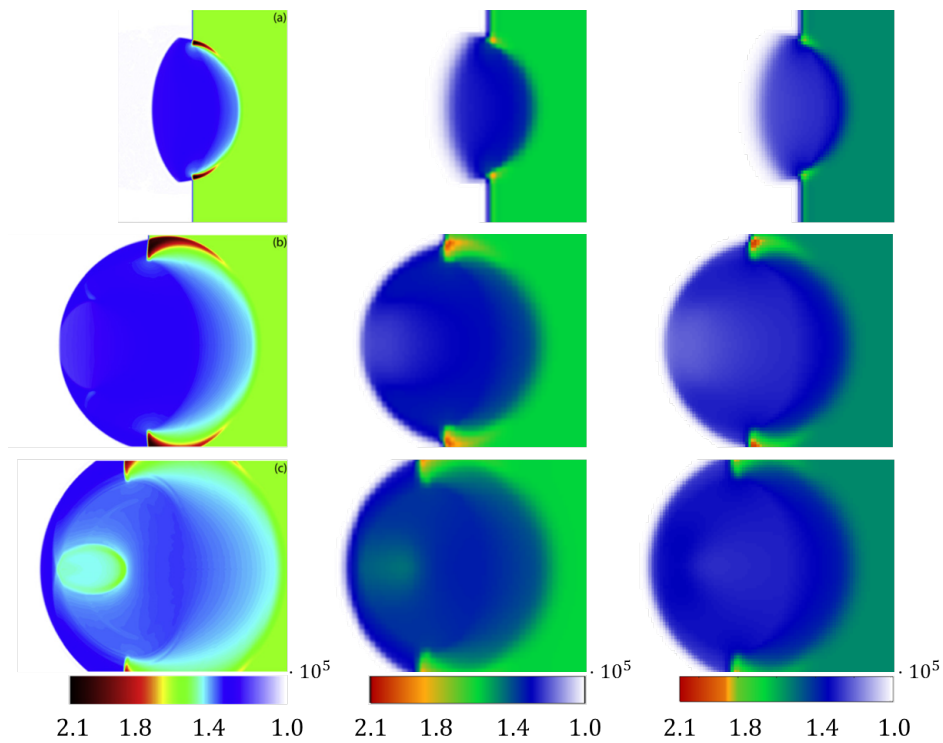


Figure G.1: The pressure field in $[Pa]$ for from left to right; [Quirk and Karni \(1996\)](#) and the present model at time (a) $32[\mu s]$, (b) $62[\mu s]$ and (c) $82[\mu s]$

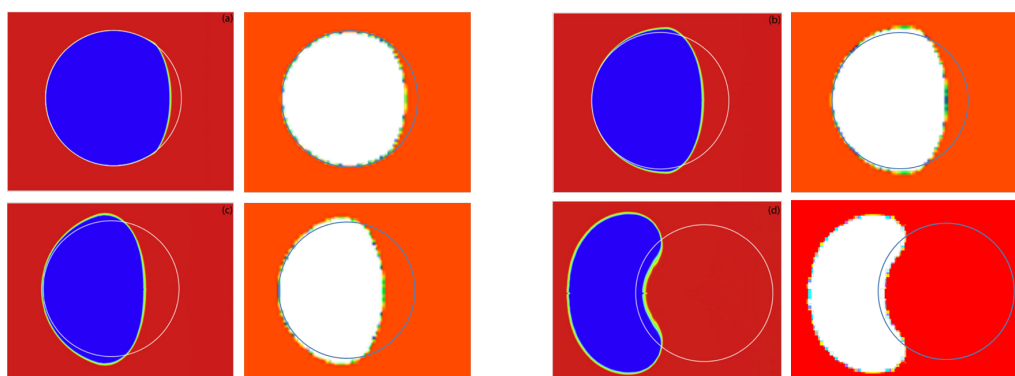


Figure G.2: The fraction field for from left to right; [Quirk and Karni \(1996\)](#) and the present model at time (a) $32[\mu s]$, (b) $62[\mu s]$, (c) $82[\mu s]$ and (d) $230[\mu s]$

Bibliography

- [1] T. Abadie, J. Aubin, and D. Legendre. On the combined effects of surface tension force calculation and interface advection on spurious currents within volume of fluid and level set frameworks. *Journal of Computational Physics*, 297:611–636, 2015.
- [2] R. Abgrall and S. Karni. Computations of compressible multifluids. *Journal of computational physics*, 169(2):594–623, 2001.
- [3] W. Allsop, D. Vicinanza, and J.E. McKenna. Wave forces on vertical and composite breakwaters. 1996.
- [4] J.D. Anderson. *Modern compressible flow: with historical perspective*, volume 12. McGraw-Hill New York, 1990.
- [5] M.R. Baer and J.W. Nunziato. A two-phase mixture theory for the deflagration-to-detonation transition (ddt) in reactive granular materials. *International journal of multiphase flow*, 12(6):861–889, 1986.
- [6] R.A. Bagnold. Interim report on wave-pressure research. *Journal of the Institution of Civil Engineers*, 12(7):202–226, 1939.
- [7] A. Baraldi, M.S. Dodd, and A. Ferrante. A mass-conserving volume-of-fluid method: volume tracking and droplet surface-tension in incompressible isotropic turbulence. *Computers & Fluids*, 96:322–337, 2014.
- [8] X. Bertin, E. Prouteau, and C. Letetrel. A significant increase in wave height in the north atlantic ocean over the 20th century. *Global and Planetary Change*, 106:77–83, 2013.
- [9] B. Biauxser, P. Fraunié, S.T. Grilli, R. Marcer, et al. Numerical analysis of the internal kinematics and dynamics of 3-d breaking waves on slopes. *International Journal of Offshore and Polar Engineering*, 14(04), 2004.
- [10] C.E. Blenkinsopp and J.R. Chaplin. Void fraction measurements and scale effects in breaking waves in freshwater and seawater. *Coastal Engineering*, 58(5):417–428, 2011.
- [11] J.U. Brackbill, D.B. Kothe, and C. Zemach. A continuum method for modeling surface tension. *Journal of computational physics*, 100(2):335–354, 1992.
- [12] H. Bredmose and G.N. Bullock. Scaling of wave-impact pressures in trapped air pockets. In *Proceedings of the 23rd International Workshop on Water Waves and Floating Bodies, Jeju, Korea. IWWWFB*, 2008.
- [13] H. Bredmose, M. Brocchini, D.H. Peregrine, and L. Thais. Experimental investigation and numerical modelling of steep forced water waves. *Journal of Fluid Mechanics*, 490: 217–249, 2003.

-
- [14] H. Bredmose, D.H. Peregrine, and G.N. Bullock. Violent breaking wave impacts. part 2: modelling the effect of air. *Journal of Fluid Mechanics*, 641:389–430, 2009.
- [15] H. Bredmose, G.N. Bullock, and A.J. Hogg. Violent breaking wave impacts. part 3. effects of scale and aeration. *Journal of Fluid Mechanics*, 765:82–113, 2015.
- [16] B. Buchner. On the impact of green water loading on ship and offshore unit design. In *Proceedings of the 6th International Symposium on Practical Design of Ship and Mobile Units*, Sept. 17-22, Seoul, 1995, volume 1, pages 430–443, 1995.
- [17] B. Buchner. Green water from the side of a weathervaning fpso. In *Proc. Conf. Offshore Mechanics and Arctic Engineering*, St. John's, 1999.
- [18] B. Buchner. *Green water on ship-type offshore structures*. PhD thesis, Delft University of Technology Delft, 2002.
- [19] B. Buchner et al. The impact of green water on fpso design. In *Offshore technology conference*. Offshore Technology Conference, 1995.
- [20] M.J. Buckingham. Sound speed and void fraction profiles in the sea surface bubble layer. *Applied Acoustics*, 51(3):225–250, 1997.
- [21] G.N. Bullock, A.R. Crawford, P.J. Hewson, M.J.A. Walkden, and P.A.D. Bird. The influence of air and scale on wave impact pressures. *Coastal Engineering*, 42(4):291–312, 2001.
- [22] G.N. Bullock, C. Obhrai, D.H. Peregrine, and H. Bredmose. Violent breaking wave impacts. part 1: Results from large-scale regular wave tests on vertical and sloping walls. *Coastal Engineering*, 54(8):602–617, 2007.
- [23] W. Bürger, H. Oumeraci, and H.W. Partenscky. Ceohydraulic investigations of rubble mound breakwaters. In *Coastal Engineering 1988*, pages 2242–2256. 1989.
- [24] M. Chai, K. Luo, C. Shao, and J. Fan. An efficient level set remedy approach for simulations of two-phase flow based on sigmoid function. *Chemical Engineering Science*, 172:335–352, 2017.
- [25] R.K-C. Chan and R.L. Street. A computer study of finite-amplitude water waves. *Journal of Computational Physics*, 6(1):68–94, 1970.
- [26] W. Chang, F. Giraldo, and B. Perot. Analysis of an exact fractional step method. *Journal of Computational Physics*, 180(1):183–199, 2002.
- [27] G. Chanteperdrix. *Modélisation et simulation numérique d'écoulements diphasiques à interface libre. Application à l'étude des mouvements de liquides dans les réservoirs de véhicules spatiaux*. PhD thesis, PhD thesis, Ecole Nationale Supérieure de l'Aéronautique et de l'Espace, Toulouse, France (in French), 2004.
- [28] A.J. Chorin. Numerical solution of the navier-stokes equations. *Mathematics of computation*, 22(104):745–762, 1968.
- [29] R. Clift, J.R. Grace, and M.E. Weber. *Bubbles, drops, and particles*. Courier Corporation, 2005.
- [30] R.H. Cole. *Underwater explosions*, 1948.

-
- [31] M.J. Cooker and D.H. Peregrine. Computations of violent motion due to waves breaking against a wall. In *Proceedings of 22nd International Conference on Coastal Engineering, ASCE*, pages 164–176, 1990.
- [32] M.J. Cooker and D.H. Peregrine. Wave impact pressure and its effect upon bodies lying on the sea bed. *Coastal Engineering*, 18(3-4):205–229, 1992.
- [33] M.J. Cooker and D.H. Peregrine. Pressure-impulse theory for liquid impact problems. *Journal of Fluid Mechanics*, 297:193–214, 1995.
- [34] G.B. Deane and M.D. Stokes. Air entrainment processes and bubble size distributions in the surf zone. *Journal of Physical Oceanography*, 29(7):1393–1403, 1999.
- [35] G.B. Deane and M.D. Stokes. Scale dependence of bubble creation mechanisms in breaking waves. *Nature*, 418(6900):839, 2002.
- [36] M.W. Dingemans. *Water Wave Propagation Over Uneven Bottoms: Part 1*. World Scientific, 1997.
- [37] D.G. Dommermuth, D.K.P. Yue, W.M. Lin, R.J. Rapp, E.S. Chan, and W.K. Melville. Deep-water plunging breakers: a comparison between potential theory and experiments. *Journal of Fluid Mechanics*, 189:423–442, 1988.
- [38] S. Downes, A. Knott, and I. Robinson. Towards a shock tube method for the dynamic calibration of pressure sensors. *Phil. Trans. R. Soc. A*, 372(2023):20130299, 2014.
- [39] D.A. Drew. Mathematical modeling of two-phase flow. *Annual review of fluid mechanics*, 15(1):261–291, 1983.
- [40] M. Duval. *Etude du déferlement d'une onde de Stokes et de la dissipation associée par simulation directe*. PhD thesis, Institut National Polytechnique de Toulouse, 2007.
- [41] B. Duz. Wave generation, propagation and absorption in cfd simulations of free surface flows. 2015.
- [42] L. Eça and M. Hoekstra. A procedure for the estimation of the numerical uncertainty of cfd calculations based on grid refinement studies. *Journal of Computational Physics*, 262: 104–130, 2014.
- [43] M. Eijk van der. Volume of fluid method free surface flows: Dam-break & standing wave. Master's thesis, Delft University of Technology, 2018.
- [44] M. Elhimer, N. Jacques, A. El Malki Alaoui, and C. Gabillet. The influence of aeration and compressibility on slamming loads during cone water entry. *Journal of Fluids and Structures*, 70:24–46, 2017.
- [45] R.N. Elias and A.L.G.A. Coutinho. Stabilized edge-based finite element simulation of free-surface flows. *International Journal for Numerical Methods in Fluids*, 54(6-8):965–993, 2007.
- [46] X. Fan, P.H. Diamond, L. Chacón, and H. Li. Cascades and spectra of a turbulent spinodal decomposition in two-dimensional symmetric binary liquid mixtures. *Physical Review Fluids*, 1(5):054403, 2016.
- [47] G. Fekken. Numerical simulation of free-surface flow with moving rigid bodies. 2004.

-
- [48] G. Fekken, A.E.P. Veldman, and B. Buchner. Simulation of green-water loading using the navier-stokes equations. In *Proceedings 7th Intern. Conf. on Numerical Ship Hydrodynamics, Nantes, 1999*.
- [49] D. Feszty and T. Jakubik. Forms of governing equations in cfd. *Computational Fluid Dynamics*.
- [50] ANSYS Fluent. Ansys fluent theory guide. *ANSYS Inc., USA, 15317:724–746, 2011*.
- [51] M.M. Francois, S.J. Cummins, E.D. Dendy, D.B. Kothe, J.M. Sicilian, and M.W. Williams. A balanced-force algorithm for continuous and sharp interfacial surface tension models within a volume tracking framework. *Journal of Computational Physics*, 213(1):141–173, 2006.
- [52] E. Franquet. *Modélisation eulérienne d'écoulements multiphasiques en présence d'ondes de chocs, de détonations et d'interfaces matérielles. Application aux matériaux énergétiques nanostructurés*. PhD thesis, 2006.
- [53] J. Gerrits. *Dynamics of liquid-filled spacecraft: numerical simulation of coupled solid-liquid dynamics*. 2001.
- [54] P. Gorf, N. Barltrop, B. Okan, T. Hodgson, and R. Rainey. Fpso bow damage in steep waves. *Actes De Colloques-Ifremer*, pages 37–46, 2002.
- [55] M. Greco, O.M. Faltinsen, and M. Landrini. Shipping of water on a two-dimensional structure. *Journal of Fluid Mechanics*, 525:309–332, 2005.
- [56] M. Greco, G. Colicchio, and O.M. Faltinsen. Shipping of water on a two-dimensional structure. part 2. *Journal of Fluid Mechanics*, 581:371–399, 2007.
- [57] J-F. Haas and B. Sturtevant. Interaction of weak shock waves with cylindrical and spherical gas inhomogeneities. *Journal of Fluid Mechanics*, 181:41–76, 1987.
- [58] F. Ham and Y-N. Young. A cartesian adaptive level set method for two-phase flows. 2003.
- [59] D.J.E. Harvie, M.R. Davidson, and M. Rudman. An analysis of parasitic current generation in volume of fluid simulations. *Applied mathematical modelling*, 30(10):1056–1066, 2006.
- [60] M. Hattori, A. Arami, and T. Yui. Wave impact pressure on vertical walls under breaking waves of various types. *Coastal Engineering*, 22(1-2):79–114, 1994.
- [61] T. Hayashi and M. Hattori. Pressure of the breaker against a vertical wall. *Coastal Engineering in Japan*, 1(1):25–37, 1958.
- [62] J. Hernández, J. López, P. Gómez, C. Zanzi, and F. Faura. A new volume of fluid method in three dimensions—part i: Multidimensional advection method with face-matched flux polyhedra. *International Journal for Numerical Methods in Fluids*, 58(8):897–921, 2008.
- [63] C. Hirsch. *Numerical computation of internal and external flows: The fundamentals of computational fluid dynamics*. Butterworth-Heinemann, 2007.
- [64] C.W. Hirt and B.D. Nichols. Volume of fluid (vof) method for the dynamics of free boundaries. *Journal of computational physics*, 39(1):201–225, 1981.

-
- [65] T. Hodgson and N. Barltrop. Bp schiehallion full scale bow monitoring. *SAFE-FLOW Project Report*, 2003.
- [66] J. Hoving. Classification of arctic structures. University Lecture, 2017.
- [67] J. Hua and J. Lou. Numerical simulation of bubble rising in viscous liquid. *Journal of Computational Physics*, 222(2):769–795, 2007.
- [68] P. Hull and G. Müller. An investigation of breaker heights, shapes and pressures. *Ocean Engineering*, 29(1):59–79, 2002.
- [69] Delft Hydraulics. Onderzoek watersnood maas. *Hoofdrapport: De Maas meester Investigation of the Meuse Flood. Main report: To master the Meuse*, 1994.
- [70] S-R. Hysing, D. Turek, S. and Kuzmin, N. Parolini, E. Burman, S. Ganesan, and L. Tobiska. Quantitative benchmark computations of two-dimensional bubble dynamics. *International Journal for Numerical Methods in Fluids*, 60(11):1259–1288, 2009.
- [71] M.J. Ivings, D.M. Causon, and E.F. Toro. On riemann solvers for compressible liquids. *International Journal for Numerical Methods in Fluids*, 28(3):395–418, 1998.
- [72] E. Johnsen and T. Colonius. Implementation of weno schemes in compressible multicomponent flow problems. *Journal of Computational Physics*, 219(2):715–732, 2006.
- [73] A.K. Kapila, R. Menikoff, J.B. Bdzil, S.F. Son, and D.S. Stewart. Two-phase modeling of deflagration-to-detonation transition in granular materials: Reduced equations. *Physics of fluids*, 13(10):3002–3024, 2001.
- [74] S. Karni. Multicomponent flow calculations by a consistent primitive algorithm. *Journal of Computational Physics*, 112(1):31–43, 1994.
- [75] C.E. Kees, I. Akkerman, M.W. Farthing, and Y. Bazilevs. A conservative level set method suitable for variable-order approximations and unstructured meshes. *Journal of Computational Physics*, 230(12):4536–4558, 2011.
- [76] H.P. Khadamkar, A.W. Patwardhan, and C.S. Mathpati. Computational fluid dynamics simulations of single drops in confined geometries. *Industrial & Engineering Chemistry Research*, 56(29):8311–8329, 2017.
- [77] M.S. Kirkgöz. Breaking wave impact on vertical and sloping coastal structures. *Ocean Engineering*, 22(1):35–48, 1995.
- [78] K.M.T. Kleefsman, G. Fekken, A.E.P. Veldman, B. Iwanowski, and B. Buchner. A volume-of-fluid based simulation method for wave impact problems. *Journal of computational physics*, 206(1):363–393, 2005.
- [79] S. Koshizuka. A particle method for incompressible viscous flow with fluid fragmentation. *Comput. Fluid Dyn. J.*, 4:29–46, 1995.
- [80] J.J. Kreeft and B. Koren. A new formulation of kapila’s five-equation model for compressible two-fluid flow, and its numerical treatment. *Journal of Computational Physics*, 229(18):6220–6242, 2010.
- [81] P.K. Kundu and I.M. Cohen. Fluid mechanics. 2004. *Elsevier Acad. Press, London*, 199:400, 2008.

-
- [82] W. Lafeber, H. Bogaert, L. Brosset, et al. Comparison of wave impact tests at large and full scale: Results from the sloshel project. In *The Twenty-second International Offshore and Polar Engineering Conference*. International Society of Offshore and Polar Engineers, 2012.
- [83] K.W. Lam. A numerical surface tension model for two-phase flow simulations. *no. August*, 2009.
- [84] E. Lamarre and W.K. Melville. Instrumentation for the measurement of sound speed near the ocean surface. *Journal of Atmospheric and Oceanic Technology*, 12(2):317–329, 1995.
- [85] H. Lamb. *Hydrodynamics*. Cambridge university press, 1932.
- [86] M. Lamnaouer. *Numerical modeling of the shock tube flow fields before and during ignition delay time experiments at practical conditions*. University of Central Florida, 2010.
- [87] Y-G. Lee and J-K. Heo. Simulating nonlinear waves on the free surface in surf zones with two-dimensional sloping beach. *Ocean engineering*, 32(1):57–84, 2005.
- [88] T.G. Leighton. The acoustic bubble. 1994. ISBN: 0-12-44190-8, 1994.
- [89] P. Lin and P.L-F. Liu. A numerical study of breaking waves in the surf zone. *Journal of fluid mechanics*, 359:239–264, 1998.
- [90] L. Lobovsky, E. Botia-Vera, F. Castellana, J. Mas-Soler, and A. Souto-Iglesias. Experimental investigation of dynamic pressure loads during dam break. *Journal of Fluids and Structures*, 48:407–434, 2014.
- [91] G.E. Loots. Fluid-structure interaction in hemodynamics. 2003.
- [92] I.J. Losada, J.L. Lara, E.D. Christensen, and N. Garcia. Modelling of velocity and turbulence fields around and within low-crested rubble-mound breakwaters. *Coastal Engineering*, 52(10-11):887–913, 2005.
- [93] L.B. Lucy. A numerical approach to the testing of the fission hypothesis. *The astronomical journal*, 82:1013–1024, 1977.
- [94] C. Lugni, M. Brocchini, A. Dolcini, F. Palladino, U. Bulgarelli, and O. Faltinsen. An experimental investigation on the flip-through phenomenon. *Proc. 20th International Workshop on Water Waves and Floating Body, Longyearbyen, The University Centre in Svalbard*, 2005.
- [95] H. Lundgren. Wave shock forces: an analysis of deformations and forces in the wave and in the foundation. In *Proc. Symp. Research on Wave Action, Delft*, volume 2, 1969.
- [96] Z.H. Ma, D.M. Causon, L. Qian, C.G. Mingham, H.B. Gu, and P.M. Ferrer. A compressible multiphase flow model for violent aerated wave impact problems. In *Proceedings of the Royal Society of London A: Mathematical, Physical and Engineering Sciences*, volume 470, page 20140542. The Royal Society, 2014.
- [97] M. Marek, W. Aniszewski, and A. Boguslawski. Simplified volume of fluid method (svof) for two-phase flows. *Task Quarterly*, 12(3):255–265, 2008.
- [98] J.C. Martin, W.J. Moyce, A.T. Price, and C.K. Thornhill. Part iv. an experimental study of the collapse of liquid columns on a rigid horizontal plane. *Phil. Trans. R. Soc. Lond. A*, 244 (882):312–324, 1952.
- [99] W.W. Massie. Coastal engineering. volume iii: Breakwater design. 1976.

-
- [100] S.T. Miller, H. Jasak, D.A. Boger, E.G. Paterson, and A. Nedungadi. A pressure-based, compressible, two-phase flow finite volume method for underwater explosions. *Computers & Fluids*, 87:132–143, 2013.
- [101] H. Mitsuyasu. Shock pressure of breaking wave. In *Coastal Engineering 1966*, pages 268–283. 1967.
- [102] N. Mohd, M.M. Kamra, M. Sueyoshi, and C. Hu. Three-dimensional free surface flows modeled by lattice boltzmann method: A comparison with experimental data.
- [103] W.D.M. Morris, J. Millar, and B. Buchner. Green water susceptibility of north sea fpso/fsus. In *Proceedings of the 15th Conference on Floating Production Systems (FPS), London*, 2000.
- [104] G. Muller and G. Wolters. Impact forces on the sea bed created by wave uprush. In *Proceedings of the 4th International Conference on Coasts*, 2000.
- [105] A. Murrone and H. Guillard. A five equation reduced model for compressible two phase flow problems. *Journal of Computational Physics*, 202(2):664–698, 2005.
- [106] R.R. Nourgaliev, T-N. Dinh, and T.G. Theofanous. Adaptive characteristics-based matching for compressible multifluid dynamics. *Journal of Computational Physics*, 213(2):500–529, 2006.
- [107] C. Obhrai, G. Bullock, G. Wolters, G. Müller, H. Peregrine, H. Bredmose, and J. Grüne. Violent wave impacts on vertical and inclined walls: large scale model tests. In *Coastal Engineering 2004: (In 4 Volumes)*, pages 4075–4086. World Scientific, 2005.
- [108] Univeristy of Groningen (RuG). Comflow home page, 2017. URL <http://www.math.rug.nl/~veldman/comflow/comflow.html>.
- [109] S. Osher and J.A. Sethian. Fronts propagating with curvature-dependent speed: algorithms based on hamilton-jacobi formulations. *Journal of computational physics*, 79(1):12–49, 1988.
- [110] H. Oumeraci, H.W. Partenscky, E. Tautenhain, et al. Breaking wave loads on vertical gravity structures. In *The Second International Offshore and Polar Engineering Conference*. International Society of Offshore and Polar Engineers, 1992.
- [111] H. Oumeraci, T. Bruce, P. Klammer, and W.J. Easson. Piv measurement of breaking wave kinematics and impact loading of caisson breakwaters. In *Proceedings International Conference on Coastal and Port Engineering in Developing Countries (COPEDEC)*, pages 2394–2410, 1995.
- [112] D.H. Peregrine and S. Kalliadasis. Filling flows, cliff erosion and cleaning flows. *Journal of Fluid Mechanics*, 310:365–374, 1996.
- [113] D.H. Peregrine and L. Thais. The effect of entrained air in violent water wave impacts. *Journal of Fluid Mechanics*, 325:377–397, 1996.
- [114] D.H. Peregrine, H. Bredmose, D.C. Dunn, T.A. Somerville, G.N. Bullock, C. Obhrai, and G. Wolters. Compressibility of entrained and trapped air in violent water wave impacts. In *Proceedings of the 21st international workshop on water waves and floating bodies*, 2006.

-
- [115] X.P. Pham and K.S. Varyani. Evaluation of green water loads on high-speed containership using cfd. *Ocean Engineering*, 32(5-6):571–585, 2005.
- [116] L-R. Plumerault, D. Astruc, and P. Maron. The influence of air on the impact of a plunging breaking wave on a vertical wall using a multifluid model. *Coastal Engineering*, 62:62–74, 2012.
- [117] L-R. Plumerault, D. Astruc, P. Villedieu, and P. Maron. A numerical model for aerated-water wave breaking. *International Journal for Numerical Methods in Fluids*, 69(12):1851–1871, 2012.
- [118] L.R. Plumerault. Numerical modelling of aerated-water wave impacts on a coastal structure, 2009.
- [119] T.J. Poinsoot and S.K. Lelef. Boundary conditions for direct simulations of compressible viscous flows. *Journal of computational physics*, 101(1):104–129, 1992.
- [120] J.J. Quirk and S. Karni. On the dynamics of a shock–bubble interaction. *Journal of Fluid Mechanics*, 318:129–163, 1996.
- [121] C. Ramkema. A model law for wave impacts on coastal structures. In *Coastal Engineering 1978*, pages 2308–2327. 1978.
- [122] R. Rannacher. On the convergence of the newton-raphson method for strongly nonlinear elliptic problems. *Nonlinear Computational Mechanics*, P. Wriggers and W. Wagner, eds., Springer-Verlag, 1991.
- [123] F. Resch and F. Avellan. Size distribution of oceanic air bubbles entrained in sea-water by wave-breaking. 1982.
- [124] M. Rudman. A volume-tracking method for incompressible multifluid flows with large density variations. *International Journal for numerical methods in fluids*, 28(2):357–378, 1998.
- [125] R. Saurel and R. Abgrall. A multiphase godunov method for compressible multifluid and multiphase flows. *Journal of Computational Physics*, 150(2):425–467, 1999.
- [126] R. Saurel and O. Lemetayer. A multiphase model for compressible flows with interfaces, shocks, detonation waves and cavitation. *Journal of Fluid Mechanics*, 431:239–271, 2001.
- [127] R. Schmidt, H. Oumeraci, and H-W. Partenscky. Impact loads induced by plunging breakers on vertical structures. In *Coastal Engineering 1992*, pages 1545–1558. 1993.
- [128] L.W. Schwartz and J.D. Fenton. Strongly nonlinear waves. *Annual review of fluid mechanics*, 14(1):39–60, 1982.
- [129] J.C. Scott. The role of salt in whitecap persistence. In *Deep Sea Research and Oceanographic Abstracts*, volume 22, pages 653–657. Elsevier, 1975.
- [130] D.E. Slauenwhite and B.D. Johnson. Bubble shattering: Differences in bubble formation in fresh water and seawater. *Journal of Geophysical Research: Oceans*, 104(C2):3265–3275, 1999.
- [131] G.A. Sod. A survey of several finite difference methods for systems of nonlinear hyperbolic conservation laws. *Journal of computational physics*, 27(1):1–31, 1978.

-
- [132] R.M. Sorensen. *Basic wave mechanics: for coastal and ocean engineers*. John Wiley & Sons, 1993.
- [133] J.J. Stoker. *Water waves. the mathematical theory with applications*, interscience publ. Inc., New York, 1957.
- [134] G.G. Stokes. Considerations relative to the greatest height of oscillatory irrotational waves which can be propagated without change of form. *Mathematical and physical papers*, 1:225–228, 1880.
- [135] C.K. Svihla and H. Xu. Simulation of free surface flows with surface tension with ansys cfx. In *2006 International ANSYS Conference, Pittsburg*, 2006.
- [136] S. Takahashi, K. Tanimoto, and S. Miyanaga. Uplift wave forces due to compression of enclosed air layer and their similitude law. *Coastal Engineering in Japan*, 28(1):191–206, 1985.
- [137] H. Tang, L.C. Wrobel, and Z. Fan. Tracking of immiscible interfaces in multiple-material mixing processes. *Computational Materials Science*, 29(1):103–118, 2004.
- [138] S.A. Thorpe. On the clouds of bubbles formed by breaking wind-waves in deep water, and their role in air-sea gas transfer. *Phil. Trans. R. Soc. Lond. A*, 304(1483):155–210, 1982.
- [139] M.K. Tripathi, K.C. Sahu, and R. Govindarajan. Dynamics of an initially spherical bubble rising in quiescent liquid. *Nature communications*, 6:6268, 2015.
- [140] E.F.G. Van Daalen, K.M.T. Kleefsman, J. Gerrits, H.R. Luth, and A.E.P. Veldman. Anti roll tank simulations with a volume of fluid (vof) based navier-stokes solver. In *23rd Symposium on Naval Hydrodynamics*, 2000.
- [141] L. van Wijngaarden. Shock waves in bubbly liquids. *Shock wave science and technology reference library*, 1:1–33, 2007.
- [142] A.E.P. Veldman and K-W. Lam. Symmetry-preserving upwind discretization of convection on non-uniform grids. *Applied Numerical Mathematics*, 58(12):1881–1891, 2008.
- [143] T.M. Vestbstad. Relative wave motion along the side of an fpso hull. In *Proceedings of the 18th Conference on Offshore Mechanics and Arctic Engineering (OMAE'99)*, 1999.
- [144] G.H. Vinesh. Development of volume of fluid (vof) and level set (ls) method code, 2012. URL <https://www.scribd.com/document/115752703/Development-of-Volume-of-Fluid-VOF-and-Level-Set-LS-method-code>.
- [145] HAT Vink. Wave impacts on vertical breakwaters. 1997.
- [146] A.J. Voogt, B. Buchner, and J.L-C. Garcia. Wave impact excitation on ship-type offshore structures in steep fronted waves. In *Proceedings OMAE Speciality Conference on Integrity of Floating Production, Storage & Offloading (FPSO) Systems*, pages 04–0062, 2004.
- [147] G. Wang, S. Tang, Y. Shin, et al. A direct calculation approach for designing a ship-shaped fpso's bow against wave slamming load. In *The Twelfth International Offshore and Polar Engineering Conference*. International Society of Offshore and Polar Engineers, 2002.
- [148] P.R. Wellens. Wave simulation in truncated domains for offshore applications. 2012.

-
- [149] R. Wemmenhove. *Numerical simulation of two-phase flow in offshore environments*. University Library Groningen][Host], 2008.
- [150] R. Wemmenhove, R. Gladsø, B. Iwanowski, M. Lefranc, et al. Comparison of cfd calculations and experiment for the dambreak experiment with one flexible wall. In *The Twentieth International Offshore and Polar Engineering Conference*. International Society of Offshore and Polar Engineers, 2010.
- [151] R. Wemmenhove, R. Luppès, A.E.P. Veldman, and T. Bunnik. Numerical simulation of hydrodynamic wave loading by a compressible two-phase flow method. *Computers & Fluids*, 114:218–231, 2015.
- [152] P.S. Wilson and R.A. Roy. An audible demonstration of the speed of sound in bubbly liquids. *American Journal of Physics*, 76(10):975–981, 2008.
- [153] A.B. Wood. A textbook of sound, 578 pp. *Bell, London*, 1941.
- [154] D.J. Wood, D.H Peregrine, and T. Bruce. Wave impact on a wall using pressure-impulse theory. i: trapped air. *Journal of waterway, port, coastal, and ocean engineering*, 126(4):182–190, 2000.
- [155] Y. Yang and G. Tryggvason. Dissipation of energy by finite-amplitude surface waves. *Computers & fluids*, 27(7):829–845, 1998.
- [156] K. Yokoi. Efficient implementation of thinc scheme: a simple and practical smoothed vof algorithm. *Journal of Computational Physics*, 226(2):1985–2002, 2007.